Chapter 3

Synchrotron Motion

In general, particles gain energy from electric field in longitudinal direction.[1] Since the electric field strength of an electrostatic accelerator is limited by field breakdown and by the length of the acceleration column, electrostatic accelerators have mainly been used for low energy accelerators. Alternatively, a low-loss radio-frequency (rf) cavity operating at a resonance condition can be used to provide accelerating voltage with $V \sin(\phi_s + \omega_{rf}t)$, where V is the amplitude of the rf voltage, ϕ_s is a phase factor, and ω_{rf} is the angular frequency synchronized with the arrival time of beam particles. In this chapter we study particle dynamics in the presence of rf accelerating voltage waves.

Although we can derive a 6D Hamiltonian for both synchrotron and betatron oscillations (see Chap. 2, Sec. IX), here, for simplicity, we will derive the synchrotron Hamiltonian based only on the revolution frequency and energy gain relations. This formalism lacks the essential connection between synchrotron and betatron motions, but it simplifies the choice of synchrotron phase-space coordinates.

A particle synchronized with rf phase $\phi = \phi_s$ at revolution period T_0 and momentum p_0 is called a *synchronous particle*. A synchronous particle will gain or lose energy, $eV \sin \phi_s$, per passage through an rf cavity. Normally the magnetic field is ideally arranged in such a way that the synchronous particle moves on a closed orbit that passes through the center of all magnets. Particles with different betatron amplitudes execute betatron motion around this ideal closed orbit.

A beam bunch consists of particles with slightly different momenta. A particle with momentum p has its own off-momentum closed orbit, $D\delta$, where D is the dispersion function and $\delta = (p - p_0)/p_0$ is the fractional momentum deviation. Since energy gain depends sensitively on the synchronization of rf field and particle arrival time, what happens to a particle with a slightly different momentum when the synchronous particle is accelerated?

---

[1]This statement also applies to charged particle acceleration in the betatron and the induction linac, in which the induced electromotive force is given by the time derivative of the magnetic flux.

The phase focusing principle of synchrotron motion was discovered by McMillan and Veksler [21]: If the revolution frequency f is higher for a higher momentum particle, i.e. $df/d\delta > 0$, the higher energy particle will arrive at the rf gap earlier, i.e. $\phi < \phi_s$. Therefore if the rf wave synchronous phase is chosen such that $0 < \phi_s < \pi/2$, higher energy particles will receive less energy gain from the rf gap. Similarly, lower energy particles will arrive at the same rf gap later and gain more energy than the synchronous particle. This process provides the phase stability of synchrotron motion. In the case of $df/d\delta < 0$, phase stability requires $\pi/2 < \phi_s < \pi$.

The discovery of phase stability paved the way for all modern high energy accelerators, called "synchrotrons," and after half a century of research and development, it remains the cornerstone of modern accelerators. Particle acceleration without phase stability is limited to low energy accelerators, e.g. Cockcroft-Walton, Van de Graaff, betatron, etc. Furthermore, bunched beams can be shortened, elongated, combined, or stacked to achieve many advanced applications by using rf manipulation schemes. Phase-space gymnastics have become essential tools in the operation of high energy storage rings.

In this chapter we study the dynamics of synchrotron motion. In Sec. I, we derive the synchrotron equation of motion in various phase-space coordinates. Section II deals with adiabatic synchrotron motion, where an invariant *torus* corresponds to a constant Hamiltonian value. In Sec. III, we study the perturbation of synchrotron motion resulting from rf phase and amplitude modulation, synchro-betatron coupling through dipole field error, ground vibration, etc. In Sec. IV, we treat non-adiabatic synchrotron motion near transition energy, where the Hamiltonian is not invariant. In Sec. V, we study beam injection, extraction, stacking, bunch rotation, phase displacement acceleration, beam manipulations with double rf systems and barrier rf systems, etc. Section VI treats fundamental aspects of rf cavity design. In Sec. VII, we introduce collective longitudinal instabilities. In Sec. VIII, we provide an introduction to the linac.

I   Longitudinal Equation of Motion

Let the longitudinal electric field at an rf gap be

$$\mathcal{E} = \mathcal{E}_0 \sin(\phi_{\rm rf}(t) + \phi_{\rm s}), \quad \phi_{\rm rf} = h\omega_0 t, \tag{3.1}$$

where $\omega_0 = \beta_0 c/R_0$ is the angular revolution frequency of a reference (synchronous) particle, $\mathcal{E}_0$ is the amplitude of the electric field, $\beta_0 c$ and R_0 are respectively the speed and the average radius of the reference orbiting particle, h is an integer called the harmonic number, and $\phi_{\rm s}$ is the phase angle for a synchronous particle with respect to the rf wave. We assume that the reference particle passes through the cavity gap in time $t \in nT_0 + (-g/2\beta c, g/2\beta c)$ (n = integer), where g is the rf cavity gap width.

The energy gain for the reference particle per passage is

$$\Delta E = e\mathcal{E}_0 \beta c \int_{-g/2\beta_0 c}^{g/2\beta_0 c} \sin(h\omega_0 t + \phi_s) dt = e\mathcal{E}_0 gT \sin\phi_s, \tag{3.2}$$

$$T = \frac{\sin(hg/2R_0)}{(hg/2R_0)}. \tag{3.3}$$

where e is the charge of the circulating particles, and T is the transit time factor. The effective voltage seen by the orbiting particle is $V = \mathcal{E}_0 gT$. The transit time factor arises from the fact that a particle passes through the rf gap within a finite time interval so that the energy gain is the time average of the electric field in the gap during the transit time (see also Exercise 3.1). If the gap length is small, the transit time factor is approximately equal to 1. However, a high electric field associated with a small gap may cause sparking and electric field breakdown.

Since a synchronous particle synchronizes with the rf wave with a frequency of $\omega_{rf} = h\omega_0$, where $\omega_0 = \beta_0 c/R_0$ is the revolution frequency and h is an integer, it encounters the rf voltage at the same phase angle ϕ_s every revolution. The acceleration rate for this synchronous particle is $\dot{E}_0 = \frac{\omega_0}{2\pi} eV \sin\phi_s$, where the dot indicates the derivative with respect to time t.

Now we consider a non-synchronous particle with small deviations of rf parameters from the synchronous particle, i.e.

$$\begin{cases} \omega = \omega_0 + \Delta\omega, & \phi = \phi_s + \Delta\phi, \quad \theta = \theta_s + \Delta\theta, \\ p = p_0 + \Delta p, & E = E_0 + \Delta E. \end{cases}$$

Here $\phi_s, \theta_s, \omega_0, p_0, E_0$ are respectively the rf phase angle, azimuthal orbital angle, angular revolution frequency, momentum, and energy of a synchronous particle, and $\phi, \theta, \omega, p, E$ are the corresponding parameters for an off-momentum particle.

The phase coordinate is related to the orbital angle by $\Delta\phi = \phi - \phi_s = -h\Delta\theta$, or

$$\Delta\omega = \frac{d}{dt}\Delta\theta = -\frac{1}{h}\frac{d}{dt}\Delta\phi = -\frac{1}{h}\frac{d\phi}{dt}. \tag{3.4}$$

The energy gain per revolution for this non-synchronous particle is $eV \sin\phi$, where ϕ is its rf phase angle, and the acceleration rate is $\dot{E} = \frac{\omega}{2\pi} eV \sin\phi$. The equation of motion for the energy-difference becomes[2]

$$\frac{d}{dt}\left(\frac{\Delta E}{\omega_0}\right) = \frac{1}{2\pi} eV (\sin\phi - \sin\phi_s). \tag{3.5}$$

---

[2]We use the relation

$$\frac{1}{\omega}\dot{E} - \frac{1}{\omega_0}\dot{E}_0 = \frac{1}{\omega_0}\dot{\Delta E} - \dot{E}\frac{\Delta\omega}{\omega_0^2} \approx \frac{1}{\omega_0}\dot{\Delta E} + \left[\dot{E}\frac{\Delta(1/\omega_0)}{\Delta E}\right]\Delta E + \cdots = \frac{d}{dt}\left(\frac{\Delta E}{\omega_0}\right).$$

Using the fractional off-momentum variable, we obtain

$$\delta = \frac{\Delta p}{p_0} = \frac{\omega_0}{\beta^2 E}\frac{\Delta E}{\omega_0}, \qquad\qquad \dot{\delta} = \frac{\omega_0}{2\pi\beta^2 E}eV(\sin\phi - \sin\phi_s). \qquad (3.6)$$

The next task is to find the time evolution of the phase angle variable ϕ. Using Eq. (3.4), we find

$$\dot{\phi} = -h(\omega - \omega_0) = -h\Delta\omega. \qquad (3.7)$$

Using the relation $\omega R/\omega_0 R_0 = \beta/\beta_0$ and the result in Chap. 2, Sec. IV, we obtain

$$\frac{\Delta\omega}{\omega_0} = \frac{\beta R_0}{\beta_0 R} - 1. \qquad (3.8)$$

$$R = R_0(1 + \alpha_0\delta + \alpha_1\delta^2 + \alpha_2\delta^3 + \cdots),$$

$$\alpha_c = \frac{1}{R_0}\frac{dR}{d\delta} = \alpha_0 + 2\alpha_1\delta + 3\alpha_2\delta^2 + \cdots \equiv \frac{1}{\gamma_T^2}, \qquad (3.9)$$

where R is the mean radius of a circular accelerator and α_c is the momentum compaction factor,[3] $\gamma_T mc^2$, or simply γ_T, is called the transition energy. Most accelerator lattices have $\alpha_0 > 0$ and the closed-orbit length for a higher energy particle is longer than the reference orbit length. Some specially designed synchrotrons can achieve the condition $\alpha_0 = 0$, where the circumference, up to first order, is independent of particle momentum. Recently, medium energy proton synchrotrons have been designed to have an imaginary γ_T or a negative momentum compaction (see Chap. 2, Sec. IV.8). The orbit length in a negative compaction lattice is shorter for a higher energy particle.

Let $p = mc\beta\gamma = p_0 + \Delta p$ be the momentum of a non-synchronous particle. The fractional off-momentum coordinate δ is

$$\delta = \frac{\Delta p}{p_0} = \frac{\beta\gamma}{\beta_0\gamma_0} - 1. \qquad (3.10)$$

Expressing β and γ in terms of the off-momentum coordinate δ, we find

$$\frac{\gamma}{\gamma_0} = \sqrt{1 + 2\beta_0^2\delta + \beta_0^2\delta^2},$$

$$\frac{\beta}{\beta_0} = \frac{1 + \delta}{\sqrt{1 + 2\beta_0^2\delta + \beta_0^2\delta^2}} = 1 + \frac{1}{\gamma_0^2}\delta - \frac{3\beta_0^2}{2\gamma_0^2}\delta^2 + \frac{\beta_0^2(5\beta_0^2 - 1)}{2\gamma_0^2}\delta^3 + \cdots.$$

Combining Eqs. (3.8) and (3.9), we obtain

$$\frac{\Delta\omega}{\omega_0} = -\eta(\delta)\delta, \qquad (3.11)$$

---

[3]Typically, we have $\alpha_1\gamma_T^2 \approx \frac{1}{\nu_x}\frac{d\nu_x}{d\delta} \approx 1$ for accelerators without chromatic corrections. The α_1 term depends on the sextupole field in the accelerator.

where the phase slip factor is $\eta(\delta) = \eta_0 + \eta_1\delta + \eta_2\delta^2 + \cdots$ with

$$
\begin{cases}
\eta_0 = (\alpha_0 - \frac{1}{\gamma_0^2}), \\
\eta_1 = \frac{3\beta_0^2}{2\gamma_0^2} + \alpha_1 - \alpha_0\eta_0, \\
\eta_2 = -\frac{\beta_0^2(5\beta_0^2-1)}{2\gamma_0^2} + \alpha_2 - 2\alpha_0\alpha_1 + \frac{\alpha_1}{\gamma_0^2} + \alpha_0^2\eta_0 - \frac{3\beta_0^2\alpha_0}{2\gamma_0^2}.
\end{cases}
\tag{3.12}
$$

In linear approximation. we find $\Delta\omega = -\eta_0\omega_0\delta = (\frac{1}{\gamma^2} - \frac{1}{\gamma_T^2})\omega_0\delta$ Below the transition energy $(\gamma < \gamma_T)$ a higher energy particle with $\delta > 0$ has a higher revolution frequency. The speed of the higher energy particle more than compensates the difference in path length. At transition energy, the revolution frequency is independent of particle momentum. The AVF cyclotron operates in this isochronous condition. The nonlinear term in Eq. (3.11) becomes important near transition energy, to be addressed in Sec. IV. Above transition energy $(\gamma > \gamma_T)$ a higher energy particle with $\delta > 0$ has a smaller revolution frequency, i.e. the particle appears to have a "negative mass." Combining Eqs. (3.7) and (3.11), we obtain the phase equation of motion:

$$
\dot{\phi} = h\omega_0\eta\delta = \frac{h\omega_0^2\eta}{\beta^2 E}\left(\frac{\Delta E}{\omega_0}\right),
\tag{3.13}
$$

where $(\phi, \Delta E/\omega_0)$ or equivalently (ϕ, δ) are pairs of conjugate phase-space coordinates. Equations (3.5) and (3.13) form the "synchrotron equation of motion."

I.1 The Synchrotron Hamiltonian

The synchrotron equations of motion (3.5) and (3.13) can be derived from a "Hamiltonian"

$$
\begin{aligned}
H &= \frac{1}{2}\frac{h\eta\omega_0^2}{\beta^2 E}\left(\frac{\Delta E}{\omega_0}\right)^2 + \frac{eV}{2\pi}[\cos\phi - \cos\phi_s + (\phi - \phi_s)\sin\phi_s] \\
&= \frac{1}{2}h\omega_0\eta_0\delta^2 + \frac{\omega_0 eV}{2\pi\beta^2 E}[\cos\phi - \cos\phi_s + (\phi - \phi_s)\sin\phi_s]
\end{aligned}
\tag{3.14}
$$

with time t as an independent variable and for phase-space coordinates $(\phi, \Delta E/\omega_0)$ and (ϕ, δ) respectively. This Hamiltonian, although legitimate, is inconsistent with the "Hamiltonian" for transverse betatron oscillations, where s is the independent coordinate. To simplify our discussion, we will disregard the inconsistency and study synchrotron motion of Eq. (3.14). A fully consistent treatment is needed when we study synchro-betatron coupling resonances.[4]

With this simplified Hamiltonian, we now discuss the stability condition for small amplitude oscillations, where the linearized equation of motion is

$$
\frac{d^2}{dt^2}(\phi - \phi_s) = \frac{h\omega_0^2 eV\eta_0\cos\phi_s}{2\pi\beta^2 E}(\phi - \phi_s).
\tag{3.15}
$$

---

[4]S.Y. Lee, *Phys. Rev.* E**49**, 5706 (1994).

The stability condition for synchrotron oscillation is $\eta_0 \cos \phi_s < 0$, discovered by McMillan and Veksler [21]. Below the transition energy, with $\gamma < \gamma_{\rm T}$ or $\eta_0 < 0$, the synchronous phase angle should be $0 < \phi_s < \pi/2$. Similarly the synchronous phase angle should be shifted to $\pi - \phi_s$ above the transition energy. This can be accomplished by a phase shift of $\pi - 2\phi_s$ to the rf wave. The *angular synchrotron frequency* and *synchrotron tune* (the number of synchrotron oscillations per revolution) are

$$\omega_{\rm s} \;=\; \omega_0 \sqrt{\frac{heV|\eta_0 \cos \phi_s|}{2\pi\beta^2 E}} = \frac{c}{R} \sqrt{\frac{heV|\eta \cos \phi_s|}{2\pi E}}, \tag{3.16}$$

$$Q_{\rm s} \;=\; \frac{\omega_{\rm s}}{\omega_0} = \sqrt{\frac{heV|\eta_0 \cos \phi_s|}{2\pi\beta^2 E}} \equiv \nu_s \sqrt{|\cos \phi_s|}, \quad \text{with} \quad \nu_s = \sqrt{\frac{heV|\eta_0|}{2\pi\beta^2 E}}. \tag{3.17}$$

where c is the speed of light and R is the average radius of synchrotron. The rf bucket at the synchronous rf phase $\phi_s = 0$ or π is called the stationary bucket because there is no net change of beam energy. The synchrotron tune at the stationary bucket is usually denoted by ν_s. The rf buckets with $\phi_s \neq 0$ or π are called running buckets.

Typically the synchrotron tune is of the order of $\sim 10^{-3}$ for proton synchrotrons and 10^{-1} for electron storage rings. Figure 3.1 shows the measured synchrotron tune of the Fermilab Booster in a ramping cycle from 400 MeV to 8 GeV. The inset shows the rf voltage and the corresponding rf synchronous phase during the ramping cycle.
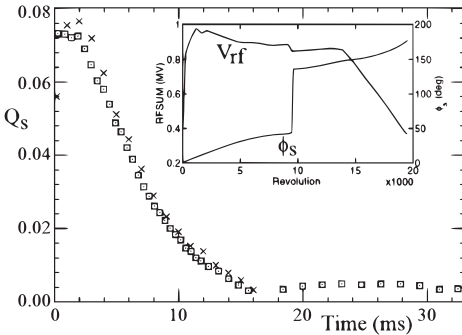

Figure 3.1: The synchrotron tune of a ramping cycle for the Fermilab Booster, which is a rapid cycling accelerator at 15 Hz. At $t = 17$ ms, the beam crosses transition energy. Rectangular symbols are results obtained by the ICA measurement method (see Appendix Sec. III) and ×'s are obtained from spectrum analyzer to a difference signal. The synchrotron tune for a rapid cycling synchrotron at low energy can be large (Courtesy of X. Huang).

The stability of particle motion in rf force potential can be understood from the left plot of Fig. 3.2, where the rf potentials are shown in the left plots for $\phi_s = 0$ and $\phi_s = \pi/6$. The potential well near the synchronous phase angle provides restoring force for quasi-harmonic oscillations. The horizontal dashed line shows the maximum Hamiltonian value for a stable synchrotron orbit. The corresponding stable phase-space (bucket) area is shown in the middle plots in the normalized phase space coordinates $(h|\eta|/\nu_s)\delta_{\rm sx}$ vs ϕ. Particles inside the rf bucket execute stable synchrotron motion, while particles fall outside the bucket will be lost.
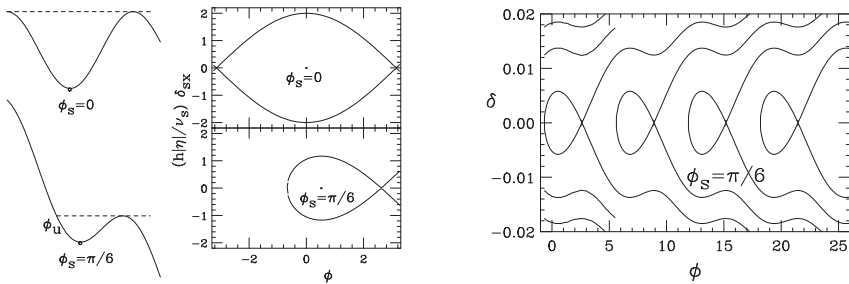
Figure 3.2: Left: schematic drawing of the rf potentials for $\phi_s = 0$ and $\pi/6$. The dashed line shows the maximum "energy" for stable synchrotron motion. Middle: the corresponding separatrix orbits in $(h|\eta|/\nu_s) \times \delta_{\rm sx}$ vs ϕ. The phase ϕ_u is the turning point of the separatrix orbit. Right: an example of stable rf buckets, called fish diagram, in δ vs ϕ at $\phi_s = \pi/6$.

For an accelerator with a harmonic number h, there are h buckets. Particles can fill some of these stable buckets. The filling pattern can be arranged by injection schemes. The right plot of Fig. 3.2 shows a fish diagram of rf buckets at $\phi_s = \pi/6$.

I.2   The Synchrotron Mapping Equation

In Hamiltonian formalism, the rf electric field is considered to be uniformly distributed in an accelerator. In reality, rf cavities are localized in a short section of a synchrotron, the synchrotron motion is more realistically described by the symplectic mapping equation:

$$\begin{cases} \delta_{n+1} = \delta_n + \dfrac{eV}{\beta^2 E}(\sin\phi_n - \sin\phi_s), \\ \phi_{n+1} = \phi_n + 2\pi h\eta(\delta_{n+1})\delta_{n+1}. \end{cases} \tag{3.18}$$

The physics of the mapping equation can be visualized as follows. First, the particle gains or loses energy at its nth passage through the rf cavity, then the rf phase ϕ_{n+1} depends on the new off-momentum coordinate δ_{n+1}. Since the Jacobian of the mapping from (ϕ_n, δ_n) to $(\phi_{n+1}, \delta_{n+1})$ is equal to 1, the mapping preserves phase-space area.

Note that Eq. (3.18) treats the rf cavity as a single lumped element in an accelerator. In reality, the rf cavities may be distributed non-uniformly. The rf phase change between different cavities may not be uniform. Because synchrotron motion is usually slow, Hamiltonian formalism and mapping equations are equivalent. Because of the simplicity of the mapping equations, they are usually used in particle tracking calculations.

I.3   Evolution of Synchrotron Phase-Space Ellipses

The phase-space area enclosed by a trajectory (ϕ, δ) obtained from Eq. (3.18) is independent of energy. Therefore, Eq. (3.18) can not be used in tracking simulations of particle beam in acceleration. During acceleration, the phase-space area in $(\phi, \Delta E/\omega_0)$ is invariant. The phase-space mapping equation for phase-space coordinates $(\phi, \Delta E/\omega_0)$ should be used. The adiabatic damping of phase-space area can be obtained by transforming phase-space coordinates $(\phi, \Delta E/\omega_0)$ to (ϕ, δ).

The separatrix for the rf bucket shown in Fig. 3.2 is a closed curve. In a rapid cycling synchrotron or electron linac where the acceleration gradient is high, the separatrix is not a closed curve. The mapping equations for synchrotron phase-space coordinates $(\phi, \Delta E)$ are

$$\Delta E_{n+1} = \Delta E_n + eV(\sin\phi_n - \sin\phi_s), \tag{3.19}$$

$$\phi_{n+1} = \phi_n + \frac{2\pi h\eta}{\beta^2 E}\Delta E_{n+1}. \tag{3.20}$$

The quantity $\eta/\beta^2 E$ in Eq. (3.20) depends on energy, which is obtained from Eq. (3.19), i.e. $E = E_{0,n+1} = E_{0,n} + eV\sin\phi_s$, $\gamma = E/mc^2$, $\beta = \sqrt{1 - 1/\gamma^2}$, and $\eta = \alpha_c - 1/\gamma^2$. If the acceleration rate is low, the factor $h\eta/\beta^2 E$ is nearly constant, and the separatrix orbit shown in Fig. 3.2 can be considered as a closed curve.

When the acceleration rate is high, tori of the synchrotron mapping equations are not closed curves. Figure 3.3 shows two tori in phase-space coordinates $(\phi, \Delta E/\beta^2 E)$ with parameters $V = 100$ kV, $h = 1$, $\alpha_c = 0.04340$, $\phi_s = 30°$ at 45 MeV proton kinetic energy. Note that the actual attainable rf voltage V is about 200-1000 V in a low energy proton synchrotron. When the acceleration rate is high, the separatrix is not a closed curve. The phase-space tori change from a fish-like to a golf-club-like shape. This is equivalent to the *adiabatic damping* of phase-space area discussed in Chapter 2, Sec. II. Since the acceleration rate for proton (ion) beams is normally low, the separatrix torus shown in Fig. 3.2 is a good approximation. When the acceleration rate is high, e.g. in many electron accelerators, the tori near the separatrix may resemble those in Fig. 3.3.
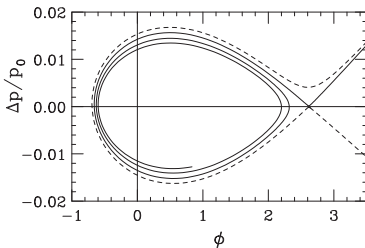

Figure 3.3:   Two tori in phase-space coordinates $(\phi, \Delta E/\beta^2 E)$ obtained from mapping equations (3.19) and (3.20) with parameters $V = 100$ kV, $h = 1$, $\alpha_c = 0.04340$, and $\phi_s = 30°$ at 45 MeV proton kinetic energy. IUCF Cooler Ring has typical rf voltage at about 1–2 kV. Note that the dashed line become the separatrix orbit, while the solid line is trapped into the bucket. This phenomenon is adiabatic damping of synchrotron motion.

I.4   Some Practical Examples

A basic rf cavity requirement for beam acceleration rate is

$$B\rho = \frac{p}{e}, \quad \dot{p} = \frac{1}{\beta c}\dot{E}, \quad f = \frac{\beta c}{2\pi R}, \quad \Longrightarrow \quad V\sin\phi_{\rm s} = 2\pi R\rho\dot{B}. \qquad (3.21)$$

For example, proton acceleration in the IUCF cooler ring from 45 MeV to 500 MeV in one second requires $\dot{B} = \frac{\Delta[B\rho]}{\rho\Delta t} \approx 1.1$ Tesla/sec, and $V\sin\phi_{\rm s} \approx 240$ Volts, where we use $\rho \approx 2.4$ m, $R \approx 14$ m. The result is independent of the harmonic number used.

Similarly, acceleration of protons from 9 GeV to 120 GeV in 1 s at the Fermilab Main Injector would require $\dot{B} \approx 1.6$ Tesla/s. The circumference is 3319.4 m with $\rho = 235$ m. The voltage requirement becomes $V\sin\phi_{\rm s} = 1.2$ MV.

I.5   Summary of Synchrotron Equations of Motion

A. Using t as independent variable

Using time t as an independent variable, the equations of motion and the Hamiltonian are listed as follows.

- Using $(\phi, \Delta E/\omega_0)$ as phase-space coordinates:

$$\frac{d\phi}{dt} = \frac{h\omega_0^2\eta}{\beta^2 E}\left(\frac{\Delta E}{\omega_0}\right), \quad \frac{d\left(\Delta E/\omega_0\right)}{dt} = \frac{1}{2\pi}eV(\sin\phi - \sin\phi_{\rm s}), \quad (3.22)$$

$$H = \frac{1}{2}\frac{h\eta\omega_0^2}{\beta^2 E}\left(\frac{\Delta E}{\omega_0}\right)^2 + \frac{eV}{2\pi}[\cos\phi - \cos\phi_{\rm s} + (\phi - \phi_{\rm s})\sin\phi_{\rm s}]. \quad (3.23)$$

- Using (ϕ, δ) as phase-space coordinates:

$$\frac{d\phi}{dt} = h\omega_0\eta\delta, \quad \frac{d\delta}{dt} = \frac{\omega_0 eV}{2\pi\beta^2 E}(\sin\phi - \sin\phi_{\rm s}), \qquad (3.24)$$

$$H = \frac{1}{2}h\omega_0\eta\delta^2 + \frac{\omega_0 eV}{2\pi\beta^2 E}[\cos\phi - \cos\phi_{\rm s} + (\phi - \phi_{\rm s})\sin\phi_{\rm s}]. \qquad (3.25)$$

- Using $(\phi, \mathcal{P} = -(h|\eta|/\nu_{\rm s})\delta)$ as the normalized phase-space coordinates:

$$\frac{d\phi}{dt} = \omega_0\nu_{\rm s}\mathcal{P}, \quad \frac{d\mathcal{P}}{dt} = \frac{\eta}{|\eta|}\omega_0\nu_{\rm s}(\sin\phi - \sin\phi_{\rm s}), \qquad (3.26)$$

$$H = \frac{1}{2}\omega_0\nu_{\rm s}\mathcal{P}^2 + \frac{\eta}{|\eta|}\omega_0\nu_{\rm s}[\cos\phi - \cos\phi_{\rm s} + (\phi - \phi_{\rm s})\sin\phi_{\rm s}]. \qquad (3.27)$$

- Using $(\tau = (\phi - \phi_s)/h\omega_0, \dot\tau)$ as phase-space coordinates:

$$\frac{d\tau}{dt} = \dot\tau, \quad \frac{d\dot\tau}{dt} = -\frac{\eta\omega_0 eV}{2\pi\beta^2 E}[\sin(\phi_s - h\omega_0\tau) - \sin\phi_s], \tag{3.28}$$

$$H = \frac{1}{2}\dot\tau^2 + \frac{\eta eV}{2\pi h\beta^2 E}[\cos(\phi_s - h\omega_0\tau) - \cos\phi_s - h\omega_0\tau\sin\phi_s]. \tag{3.29}$$

The corresponding normalized phase space is $(\tau, \dot\tau/\omega_s)$.

B. Using longitudinal distance s as independent variable

- Using $(R\phi/h, -\Delta p/p_0)$ as phase-space coordinates, the Hamiltonian is

$$H = -\frac{1}{2}\eta\left(\frac{\Delta p}{p_0}\right)^2 - \frac{\nu_s^2}{h^2|\eta|}[\cos\phi - \cos\phi_s + (\phi - \phi_s)\sin\phi_s], \tag{3.30}$$

where $\nu_s = \sqrt{h|\eta|eV/2\pi\beta^2 E_0}$ is the synchrotron tune at $\phi_s = 0$. This synchrotron Hamiltonian is on an equal footing with the transverse betatron motion. In particular, the negative sign in the first term corresponds to negative mass above the transition energy, where $\eta > 0$.

Exercise 3.1

1. An rf cavity consists of an insulating gap g across which the rf voltage is applied. The gap length is finite and the rf field changes with time during transit time Δt. The total energy gain of a particle passing through the gap is the time average of the rf voltage during the transit time, i.e.

$$\Delta E = \frac{e}{\Delta t}\int_{-\Delta t/2}^{\Delta t/2} V(t)dt, \quad V(t) = V_g\sin(\phi + h\omega_0 t)$$

where V_g is the peak gap voltage, and ϕ the rf phase of the particle. Show that the effective voltage is

$$V = V_g T, \quad T = \frac{\sin(hg/2R)}{(hg/2R)},$$

where R is the mean radius of the accelerator. Thus the transit time factor T is the same for all particles.

2. Show that the relation between the rf frequency of an accelerator and the magnetic flux density $B(t)$ during particle acceleration at a constant radius is given by

$$\omega_{\rm rf} = \frac{hc}{R_0}\left[\frac{B^2(t)}{B^2(t) + (mc^2/ec\rho)^2}\right]^{1/2},$$

where h is the harmonic number, ρ is the bending radius of the dipoles, R_0 is the mean radius of the accelerator, e and m are the charge and mass of the particle, and c is the speed of light.

3. Calculate synchrotron tunes for the proton synchrotrons listed in the following table with $\phi_{\rm s} = 0$.

RF parameters of some proton synchrotrons

P-synchrotron	AGS	RHIC	FNAL-MI	FNAL-BST	SSC	Cooler
K.E. [GeV/u]	0.2	28	8	0.4	2000	0.045
$V_{\rm rf}$ [MV]	0.3	0.3	2	0.95	10	0.0001
h	12	342	588	84	17424	1
γ_T	8.5	24.5	21.8	5.446	140	4.6
C [m]	807.12	3833.84	3319.4	474.2	87120	86.8
$\nu_{\rm s}$						

4. Electrons in storage rings emit synchrotron radiation. The energy loss per turn is given by

$$U_0 = C_\gamma \beta^3 E_0^4 / \rho,$$

where E_0 is the beam energy, βc is the beam velocity, ρ is the bending radius of dipoles, and

$$C_\gamma = 8.85 \times 10^{-5} \text{ m/(GeV)}^3.$$

The energy loss due to synchrotron radiation is compensated by the rf accelerating field, i.e. $U_0 = eV_{\rm rf} \sin \phi_{\rm s}$. Calculate synchrotron tunes for the electron storage rings listed in the following table.

RF parameters of some electron synchrotrons

	LEP	ALS	APS	NLC DR	BEPC	TRISTAN
C [m]	26658.9	196.8	1060	223	240.4	3018
Energy [GeV]	50	1.2	7.0	1.98	2.2	30.
ρ [m]	3096.2	4.01	38.96	4.35	10.35	246.5
$V_{\rm rf}$ [MV]	400	1.5	10	1.0	0.8	400
h	31320	328	1248	531	160	5120
γ_T	50.86	26.44	64.91	46.1	5.0	25.5
ν_x	76.2	14.28	35.22	23.81	6.18	36.8
ν_z	70.2	8.18	14.3	8.62	7.12	38.7
$\phi_{\rm s}$ [deg]						
$Q_{\rm s}$						

5. The synchrotron tune of the Fermilab Booster during the ramping cycle is shown in Fig. 3.1. We note that the rf voltage is ramped from a low value to a high value at injection for adiabatic capture (see Sec. V.2 in Chap. 3).

   (a) Compare the measured synchrotron tune at the injection energy with that obtained from Exercise 5.1.3. Explain the difference.

   (b) At time $t = 17$ ms, what happens to the the measured synchrotron tune? What is the beam energy and what happens to the synchronous phase angle?

   (c) Why the synchronous phase angle is moved to $180°$ at extraction?

6. Compare and discuss the synchrotron mapping equations of Eq. (3.18) vs Eqs. (3.19) and (3.20).

7. Verify Eq. (3.21) of rf voltage requirement during the beam energy ramping process.

8. Find the dimension of phase space area in various phase space coordinates discussed in Sec. I.5

9. Write a computer program to track synchrotron motion near the separatrix, explore the dependence of the separatrix on the acceleration rate, and verify the golf-club-like tori in Fig. 3.3, where the torus of the solid line is captured into the bucket, while the torus of dashed line is outside the bucket.

10. Redefine $y \equiv h|\eta|\delta/\nu_s$.

   (a) Show that Eq. (3.18) of the symplectic mapping equation for a stationary bucket synchrotron motion can be transformed into the standard map:

   $$y_{n+1} = y_n + 2\pi\nu_s(\sin\phi_n - \sin\phi_s),$$
   $$\phi_{n+1} = \phi_n + \frac{\eta}{|\eta|}2\pi\nu_s y_{n+1},$$

   where $\nu_s = \sqrt{h|\eta|eV/2\pi\beta^2 E}$ is the synchrotron tune.

   (b) Write a program to track the phase-space points (ϕ, y) such that $\phi \in [-\pi, \pi]$, $y \in [-2, 2]$. Examine the symmetry of the tracking equation in (ϕ, y) space.

   (c) Explore the phase-space evolution at $\nu_s = \nu_{s,c} = 0.39324366$, where $\nu_{s,c}$ is the critical synchrotron tune for global chaos in the synchrotron phase space.

II Adiabatic Synchrotron Motion

With time t as an independent variable, Hamilton's equations of motion for the synchrotron Hamiltonian for phase-space coordinates (ϕ, δ) shown in Eq. (3.14) are

$$\dot{\phi} = h\eta\omega_0\delta, \qquad \dot{\delta} = \frac{\omega_0 eV}{2\pi\beta^2 E}(\sin\phi - \sin\phi_s), \qquad (3.31)$$

where the over-dots indicate derivatives with respect to time t. For simplicity in notation, hereafter, the subscript of the energy E_0 of the beam has been neglected. If $|\eta| \neq 0$, the small amplitude synchrotron tune is given by Eq. (3.17). The synchrotron period is $T_s = T_0/Q_s$, where T_0 is the revolution period.

The typical synchrotron tune in proton synchrotrons is of the order of 10^{-3}, i.e. it takes about 1000 revolutions to complete one synchrotron oscillation. The typical synchrotron tune in electron storage rings is of the order of 10^{-1}. If the rf parameters V and ϕ_s vary only slowly with time so that the gain in beam energy in each revolution is small, and η differs substantially from 0, the Hamiltonian is time independent or nearly time independent.

During beam acceleration, the Hamiltonian (3.14) generally depends on time. However, if the acceleration rate is low, the Hamiltonian can be considered as quasistatic. This corresponds to adiabatic synchrotron motion, where parameters in the synchrotron Hamiltonian change slowly so that the particle orbit is a torus of constant Hamiltonian value. The condition for adiabatic synchrotron motion is

$$\alpha_{ad} = \left|\frac{1}{\omega_s^2}\frac{d\omega_s}{dt}\right| = \frac{1}{2\pi}\left|\frac{dT_s}{dt}\right| \ll 1, \qquad (3.32)$$

where ω_s is the angular synchrotron frequency and α_{ad} is called the adiabaticity coefficient. Typically, when $\alpha_{ad} \leq 0.05$, the time variation of synchrotron period is small and the trajectories of particle motion can be approximately described by tori of constant Hamiltonian values.

II.1 Fixed Points

The Hamiltonian for adiabatic synchrotron motion has two fixed points $(\phi_s, 0)$ and $(\pi - \phi_s, 0)$, where $\dot{\phi} = 0$ and $\dot{\delta} = 0$. The phase-space point $(\phi_s, 0)$ is the stable fixed point (SFP). Small amplitude phase-space trajectories around the stable fixed point are ellipses. Therefore the SFP is also called an elliptical fixed point.

The phase-space trajectories near the unstable fixed point (UFP) $(\pi - \phi_s, 0)$ are hyperbola. Thus the UFP is also called a hyperbolic fixed point. The torus that passes through the UFP is called the *separatrix*; it separates phase space into regions of bound and unbound oscillations. Figure 3.4 shows the separatrix orbit in the normalized coordinates $(h|\eta|/\nu_s)\delta_{sx}$ vs ϕ for $\eta < 0$ with $\phi_s = 0, \pi/6, \pi/3$ and for $\eta > 0$

with $\phi_s = 2\pi/3, 5\pi/6, \pi$. The synchrotron phase space is divided into stable and unstable regions, and only particles in the stable region can be accelerated to high energy. Particles in synchrotrons are naturally bunched. A beam in which particles are grouped together forming bunches is called a *bunched beam*.
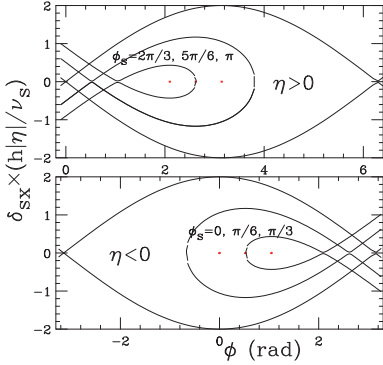

Figure 3.4: Separatrix orbits of the normalized phase space coordinates $(h|\eta|/\nu_s)\delta_{sx}$ vs ϕ for $\eta > 0$ (above transition energy) with $\phi_s = 2\pi/3, 5\pi/6, \pi$, (top) and for $\eta < 0$ (below transition energy) with $\phi_s = 0, \pi/6, \pi/3$ (bottom). The UFP of each separatrix is $\pi - \phi_s$. The phase space area enclosed by the separatrix is called the *bucket area*. The maximum off-momentum deviation of the rf bucket is called *bucket height*. The acceleration rate is zero for a stationary bucket at $\phi_s = 0$ or π. When $\sin \phi_s \neq 0$ or π, the bucket is called a *running bucket*. When an rf system has a harmonic number h applied to an accelerator, there are h identical buckets and a maximum of h bunches can be stored in the accelerator.

For a slowly time-varying Hamiltonian, particle motion adiabatically follows a phase-space ellipse, called a "Hamiltonian torus" at a "constant" Hamiltonian value. The phase-space area enclosed by a Hamiltonian torus is $\tilde{\mathcal{A}} = \oint \delta(\phi)d\phi$. The phase-space area enclosed by the separatrix orbit is called the *bucket area*. The maximum momentum deviation of the separatrix orbit is called the *bucket height*. Particles outside the rf bucket drift along the longitudinal direction, and particles inside the rf bucket execute quasi-harmonic motion within the bucket.

II.2   Bucket Area

The separatrix passes through the unstable fixed point $(\pi - \phi_s, 0)$. Therefore the Hamiltonian value of the separatrix and the phase-space trajectory of the separatrix, where $H = H_{sx}$, are

$$H_{sx} = \frac{\omega_0 eV}{2\pi\beta^2 E} \left[-2\cos\phi_s + (\pi - 2\phi_s)\sin\phi_s\right]. \tag{3.33}$$

$$\delta_{sx}^2 + \frac{eV}{\pi\beta^2 Eh\eta}[\cos\phi + \cos\phi_s - (\pi - \phi - \phi_s)\sin\phi_s] = 0.$$

The separatrix has two turning points, ϕ_u and $\pi - \phi_s$ with $\cos\phi_u + \phi_u\sin\phi_s = -\cos\phi_s + (\pi - \phi_s)\sin\phi_s$. For $\phi_s = 0$, the turning points are $-\pi$ and π.

The phase-space area enclosed by the separatrix is called the bucket area, i.e.

$$\tilde{\mathcal{A}}_B = \oint \delta_{sx}(\phi)d\phi = 16\sqrt{\frac{eV}{2\pi\beta^2 Eh|\eta|}}\ \alpha_b(\phi_s) = \frac{16Q_s}{h|\eta|\sqrt{|\cos\phi_s|}}\ \alpha_b(\phi_s), \tag{3.34}$$

$$\alpha_{\rm b}(\phi_{\rm s}) = \frac{1}{4\sqrt{2}} \int_{\phi_{\rm u}}^{\pi-\phi_{\rm s}} \left[-\frac{|\eta|}{\eta} \left[\cos\phi + \cos\phi_{\rm s} - (\pi - \phi - \phi_{\rm s})\sin\phi_{\rm s} \right] \right]^{1/2} d\phi, \quad (3.35)$$

where the factor $\alpha_{\rm b}(\phi_{\rm s})$ is the ratio of bucket areas of a running bucket ($\phi_{\rm s} \neq 0$) to a stationary bucket ($\phi_{\rm s} = 0$). Table 3.1 lists $\alpha_{\rm b}(\phi_{\rm s})$ as a function of the synchronous phase angle $\phi_{\rm s}$. Naturally $\alpha_{\rm b}(0) = 1$, and $\alpha_{\rm b}(\pi/2) = 0$, i.e. the bucket area vanishes at 90° synchronous phase angle. We note that $\alpha_{\rm b}(\phi_{\rm s}) \approx (1-\sin\phi_{\rm s})/(1+\sin\phi_{\rm s})$.

Table 3.1: Turning point ($\phi_{\rm u}$ in degree), UFP ($\pi - \phi_{\rm s}$ in degree), Bucket length ($\pi - \phi_{\rm s}-\phi_{\rm u}$), bucket height factor $Y(\phi_{\rm s})$ and bucket area factor $\alpha(\phi_{\rm s})$.

$\sin\phi_{\rm s}$	$\phi_{\rm u}$	$\pi - \phi_{\rm s}$	$Y(\phi_{\rm s})$	$\alpha_{\rm b}(\phi_{\rm s})$	$\frac{1-\sin\phi_{\rm s}}{1+\sin\phi_{\rm s}}$
0.00	-180.00	180.00	1.0000	1.0000	1.0000
0.10	-118.90	174.26	0.9208	0.8041	0.8182
0.20	-93.71	168.46	0.8402	0.6611	0.6667
0.30	-73.59	162.54	0.7577	0.5388	0.5385
0.40	-55.66	156.42	0.6729	0.4305	0.4286
0.50	-38.69	150.00	0.5852	0.3333	0.3333
0.60	-21.88	143.13	0.4936	0.2460	0.2500
0.70	-4.48	135.57	0.3967	0.1679	0.1765
0.80	14.59	126.87	0.2919	0.0991	0.1111
0.90	37.77	115.84	0.1731	0.0408	0.0526
1.00	90.00	90.00	0.	0.	0.

The corresponding invariant bucket area in $(\phi, \Delta E/\omega_0)$ phase-space variables,

$$\mathcal{A}_{\rm B,rms} = \frac{\beta^2 E}{\omega_0}\tilde{\mathcal{A}}_{\rm B,rms} = h\pi\sigma_{\Delta t}\sigma_{\Delta E}, \quad (3.36)$$

is the phase-space area of h buckets in accelerator, where Δt is the bucket width in time (s), ΔE is the bucket energy height (eV), and the resulting bucket phase-space area is in eV-s. Table 3.2 lists relevant formulas for rf bucket properties.

Table 3.2: Formula for bucket area in conjugate phase space coordinates

	$\left(\phi, \frac{\Delta E}{\omega_0}\right)$	(ϕ, δ)	$\left(\phi, \frac{h|\eta|}{\nu_{\rm s}}\delta\right)$
Bucket Area	$16\left(\frac{\beta^2 EeV}{2\pi\omega_0^2 h|\eta|}\right)^{1/2}\alpha_{\rm b}(\phi_{\rm s})$	$16\left(\frac{eV}{2\pi\beta^2 Eh|\eta|}\right)^{1/2}\alpha_{\rm b}(\phi_{\rm s})$	$16\,\alpha_{\rm b}(\phi_{\rm s})$
Bucket Height	$2\left(\frac{\beta^2 EeV}{2\pi\omega_0^2 h|\eta|}\right)^{1/2}Y(\phi_{\rm s})$	$2\left(\frac{eV}{2\pi\beta^2 Eh|\eta|}\right)^{1/2}Y(\phi_{\rm s})$	$2\,Y(\phi_{\rm s})$

The bucket length is $|(\pi - \phi_{\rm s}) - \phi_{\rm u}|$, and the bucket height or the maximum momentum width is

$$\delta_{\rm B} = \left(\frac{2eV}{\pi\beta^2 Eh|\eta|}\right)^{1/2} Y(\phi_{\rm s}) = \frac{2Q_{\rm s}}{h|\eta|}\tilde{Y}(\phi_{\rm s}). \quad (3.37)$$

Here bucket height factors $Y(\phi_s)$ and $\tilde{Y}(\phi_s)$ are ratios of the maximum momentum height to that of a stationary bucket, i.e.

$$Y(\phi_s) = \left| \cos\phi_s - \frac{\pi - 2\phi_s}{2}\sin\phi_s \right|^{1/2}, \quad \tilde{Y}(\phi_s) = \left| 1 - \frac{\pi - 2\phi_s}{2}\tan\phi_s \right|^{1/2}. \quad (3.38)$$

Table 3.1 also lists turning point and bucket height factor, $Y(\phi_s)$, of rf bucket.

II.3   Small-Amplitude Oscillations and Bunch Area

The linearized synchrotron Hamiltonian around the SFP is simple harmonic with

$$H = \frac{1}{2}h\omega_0\eta\delta^2 - \frac{\omega_0 eV\cos\phi_s}{4\pi\beta^2 E}\varphi^2,$$

$$\varphi = \hat{\phi}\cos(\omega_s t + \chi), \quad \delta = -\frac{Q_s}{h\eta}\hat{\phi}\sin(\omega_s t + \chi),$$

$$\left(\frac{\delta}{\hat{\delta}}\right)^2 + \left(\frac{\varphi}{\hat{\phi}}\right)^2 = 1, \qquad \frac{\hat{\delta}}{\hat{\phi}} = \left(\frac{eV|\cos\phi_s|}{2\pi\beta^2 Eh|\eta|}\right)^{1/2} = \frac{Q_s}{h|\eta|}, \quad (3.39)$$

where $\varphi = \phi - \phi_s$, and the synchrotron frequency is given by Eq. (3.17) with $\omega_s = Q_s\omega_0$, and $\hat{\delta}$ and $\hat{\phi}$ are maximum amplitudes of the phase-space ellipse. The phase-space area of the ellipse is $\pi\hat{\delta}\hat{\phi}$.

A. Gaussian beam distribution

The equilibrium beam distribution is a function of the invariant ellipse of Eq. (3.39). In many beam applications, we use the normalized Gaussian distribution given by

$$\rho(\delta, \phi) = \frac{1}{2\pi\sigma_\delta\sigma_\phi}\exp\left\{-\frac{1}{2}\left[\frac{\phi^2}{\sigma_\phi^2} + \frac{\delta^2}{\sigma_\delta^2}\right]\right\}, \quad (3.40)$$

where σ_δ and σ_ϕ are rms momentum spread and bunch length respectively. The corresponding rms phase-space area is $\tilde{\mathcal{A}}_{rms} = \pi\sigma_\delta\sigma_\phi$. The phase-space area that contains 95% of the particles in a Gaussian beam distribution is $\tilde{\mathcal{A}}_{95\%} = 6\tilde{\mathcal{A}}_{rms}$, where the factor 6 depends on the distribution function.

The synchrotron phase-space area (or emittance) $\mathcal{A}$, usually measured in eV-s, is defined as the area in the phase space $(\phi/h, \Delta E/\omega_0)$ for **one** bunch,[5] it is related to

---

[5]The energy of a heavy ion beam is usually expressed as [MeV/u] or [GeV/u], the E in the denominator of Eq. (3.41) can be expressed as $A \times (E/A)$, where A is the atomic mass number or the number of nucleons in a nucleus, $E/A = \gamma uc^2$, and $u = 0.931494$ GeV/c^2 is the atomic mass unit. Thus the phase-space area is commonly defined as phase-space area per amu expressed as [eV-s/u] for heavy ion beams. The factors eV and E in this chapter should be modified by ZeV and $A \times (E/A)$ for heavy ion beams, where Z is the ion's charge number, A is the atomic mass number, and E/A is the energy per nucleon.

$\tilde{\mathcal{A}}$ by a factor $h\omega_0/\beta^2 E$. Using Eq. (3.39), we find the maximum momentum width and bunch length of a bunch as

$$\tilde{\mathcal{A}} = \pi\hat{\delta}\hat{\phi} = h\mathcal{A}\left(\frac{\omega_0}{\beta^2 E}\right). \tag{3.41}$$

$$\hat{\delta} = \mathcal{A}^{1/2}\left(\frac{\omega_0}{\pi\beta^2 E}\right)^{1/2}\left(\frac{heV|\cos\phi_s|}{2\pi\beta^2 E|\eta|}\right)^{1/4} = \left(\mathcal{A}\frac{\omega_0 Q_s}{\pi\beta^2 E|\eta|}\right)^{1/2},$$

$$\hat{\theta} = \frac{1}{h}\hat{\phi} = \mathcal{A}^{1/2}\left(\frac{\omega_0}{\pi\beta^2 E}\right)^{1/2}\left(\frac{2\pi\beta^2 E|\eta|}{heV|\cos\phi_s|}\right)^{1/4} = \left(\mathcal{A}\frac{\omega_0|\eta|}{\pi\beta^2 E Q_s}\right)^{1/2},$$

$$\frac{\hat{\delta}}{\hat{\theta}} = \left(\frac{heV|\cos\phi_s|}{2\pi\beta^2 E|\eta|}\right)^{1/2} = \frac{Q_s}{|\eta|}. \tag{3.42}$$

The invariant rms phase-space area for one bunch in eV-s is $\mathcal{A}_{\mathrm{rms}} = \pi\sigma_{\Delta t}\sigma_{\Delta E}$. The scaling properties of bunch length and bunch height of Eq. (3.42) become

$$\hat{\delta} \sim \mathcal{A}^{1/2}V^{1/4}h^{1/4}|\eta|^{-1/4}\gamma^{-3/4}, \qquad \hat{\theta} \sim \mathcal{A}^{1/2}V^{-1/4}h^{-1/4}|\eta|^{1/4}\gamma^{-1/4}, \tag{3.43}$$

where the adiabatic damping is also explicitly shown. As the energy approaches the transition energy with $\eta \to 0$, we expect that $\hat{\delta} \to \infty$, and $\hat{\theta} \to 0$. This is not true because the synchrotron motion around the transition energy is non-adiabatic. It will be discussed in Sec. IV.

Similarly, the invariant phase-space ellipse in (θ, δ) phase space is

$$\left(\frac{\delta^2}{\hat{\delta}}\right)^2 + \left(\frac{\theta}{\hat{\theta}}\right)^2 = 1, \qquad \frac{\hat{\delta}}{\hat{\theta}} = \frac{Q_s}{|\eta|}, \tag{3.44}$$

where $\hat{\delta}$ and $\hat{\theta}$ are the maximum amplitudes of phase-space ellipse. The normalized Gaussian distribution in (θ, δ) space becomes

$$\rho(\delta, \theta) = \frac{1}{2\pi\sigma_\delta\sigma_\theta}\exp\left\{-\frac{1}{2}\left[\frac{\theta^2}{\sigma_\theta^2} + \frac{\delta^2}{\sigma_\delta^2}\right]\right\}. \tag{3.45}$$

Here σ_θ and σ_δ are respectively the rms bunch angular width and rms fractional momentum spread. The bunch length is $\sigma_s = R\sigma_\theta$ in meters, where R is the average radius of the accelerator, or $\sigma_t = \sigma_\theta/\omega_0$ in s.

Now we consider N_B particles distributed in a bunch, where N_B may vary from 10^8 to 10^{14} particles. The line distribution and the peak current (in Amperes) of the bunch are

$$\rho(\phi) = \frac{N_B}{\sqrt{2\pi}\sigma_\phi}e^{-\phi^2/2\sigma_\phi^2} \qquad \text{or} \qquad \rho(\theta) = \frac{N_B}{\sqrt{2\pi}\sigma_\theta}e^{-\theta^2/2\sigma_\theta^2}, \tag{3.46}$$

$$\hat{I} = \frac{N_B\, e}{\sqrt{2\pi}\sigma_t} = \frac{N_B\, e\omega_0}{\sqrt{2\pi}\sigma_\theta} = \left(\frac{2\pi}{\sqrt{2\pi}\sigma_\theta}\right)\frac{N_B\, e}{T_0}, \tag{3.47}$$

where $N_B e/T_0$ is the average current, and $2\pi/(\sqrt{2\pi}\sigma_\theta)$ is the *bunching factor*.

B. Synchrotron motion in reference time coordinates

In collective beam instabilities, we use the particle arrival time τ and its time derivative $\dot{\tau}$ for synchrotron phase-space coordinates, i.e.

$$\tau = -\frac{\theta - \theta_0}{\omega_0}, \quad \text{and} \quad \dot{\tau} = \frac{\Delta\omega}{\omega_0} = +\eta\delta. \tag{3.48}$$

The linearized synchrotron Hamiltonian becomes $H = \frac{1}{2}\left[\dot{\tau}^2 + \omega_s^2 \tau^2\right]$, where ω_s is the angular synchrotron frequency shown in Eq. (3.16). The phase-space ellipse that corresponds to a constant Hamiltonian and the solutions are

$$\tau^2 + \frac{\dot{\tau}^2}{\omega_s^2} = \hat{\tau}^2; \qquad \tau = \hat{\tau}\cos\psi, \quad \frac{\dot{\tau}}{\omega_s} = -\hat{\tau}\sin\psi, \qquad \psi = \psi_0 + \omega_s t, \tag{3.49}$$

where $\hat{\tau}$ and ψ are respectively the synchrotron amplitude and phase. See Eq. (3.273) for its application.

C. Approximate action-angle variables

Expanding the phase coordinate around SFP with $\phi = \phi_s + \varphi$, the synchrotron Hamiltonian becomes (see Exercise 3.2.11)

$$H = \frac{1}{2}h\omega_0\eta\delta^2 + \frac{1}{2h\eta}\omega_0 Q_s^2 \left[\varphi^2 - \frac{1}{3}\tan\phi_s\ \varphi^3 - \frac{1}{12}\ \varphi^4 + \cdots\right], \tag{3.50}$$

where $Q_s = \sqrt{heV|\eta\cos\phi_s|/2\pi\beta^2 E} = \nu_s\sqrt{|\cos\phi_s|}$ is the small amplitude synchrotron tune. For simplicity, we assume $\eta > 0$ in this section.

We would like to transform the phase space coordinates (φ, δ) to action-angle coordinates (ψ, J) by a generating function as:

$$F_1(\varphi, \psi) = -\frac{Q_s}{2h|\eta|}\varphi^2 \tan\psi \implies \varphi = \sqrt{\frac{2h\eta J}{Q_s}}\cos\psi, \ \delta = -\sqrt{\frac{2Q_s J}{h\eta}}\sin\psi. \tag{3.51}$$

With the approximate action-angle variables, the Hamiltonian for synchrotron motion becomes

$$H = \omega_0 Q_s J + \omega_0 \frac{\sqrt{2h\eta Q_s}}{12}\tan\phi_s\ J^{3/2}\left[\cos 3\psi + 3\cos\psi\right] - \omega_0\frac{h\eta}{6}J^2\cos^4\psi. \tag{3.52}$$

If we apply the canonical perturbation method (see Exercise 3.2.11), the averaged synchrotron Hamiltonian and the amplitude dependent synchrotron tune become

$$\langle H \rangle = \omega_0 Q_s J - \frac{\omega_0 h\eta}{16}\left(1 + \frac{5}{3}\tan^2\phi_s\right)J^2 + \cdots$$

$$\tilde{Q}_s(J) \equiv \frac{1}{\omega_0}\frac{\partial\langle H \rangle}{\partial J} \approx Q_s\left[1 - \frac{h\eta}{8Q_s}\left(1 + \frac{5}{3}\tan^2\phi_s\right)J\right]. \tag{3.53}$$

II.4 Small-Amplitude Synchrotron Motion at the UFP

Small amplitude synchrotron motion around an unstable fixed point (UFP) is also of interest in accelerator physics. Expanding the Hamiltonian around the UFP, i.e. $\varphi = \phi - (\pi - \phi_{\mathrm{s}})$, we obtain

$$\dot{\delta} = -\frac{\omega_0 eV \cos\phi_{\mathrm{s}}}{2\pi\beta^2 E}\,\varphi, \qquad \dot{\varphi} = h\eta\omega_0\delta,$$

$$\ddot{\delta} = \omega_{\mathrm{s}}^2\delta, \qquad \ddot{\varphi} = \omega_{\mathrm{s}}^2\varphi. \tag{3.54}$$

The particle motion is hyperbolic around the UFP.

Now, we study the evolution of an elliptical torus of Eq. (3.39) at the UFP. We would like to find the evolution of bunch shape when the center of the beam bunch is instantaneously kicked[6] onto the UFP at time $t = 0$. With normalized coordinates, the solutions of Eq. (3.54) are

$$\tilde{\varphi} = \frac{\varphi}{\hat{\phi}}, \quad \tilde{\delta} = \frac{\delta}{\hat{\delta}}, \qquad \tilde{\varphi} = ae^{\omega_{\mathrm{s}}t} + be^{-\omega_{\mathrm{s}}t}, \quad \tilde{\delta} = ae^{\omega_{\mathrm{s}}t} - be^{-\omega_{\mathrm{s}}t}, \tag{3.55}$$

where a and b are determined from the initial condition. With the constants a and b eliminated, the evolution of the bunch shape ellipse is

$$\tilde{\varphi}^2 - 2\left(\frac{\eta}{|\eta|}\tanh 2\omega_{\mathrm{s}}t\right)\tilde{\varphi}\tilde{\delta} + \tilde{\delta}^2 = (\cosh 2\omega_{\mathrm{s}}t)^{-1}. \tag{3.56}$$

Thus the upright phase-space ellipse will become a tilted phase-space ellipse encompassing the same phase-space area. The width and height of phase-space ellipse increase or decrease at a rate $e^{\pm\omega_{\mathrm{s}}t}$, where t is the length of time that the bunch stays at UFP (see Exercise 3.2.5). This scheme of bunch deformation can be used for bunch rotation or bunch compression. At $\omega_{\mathrm{s}}t \gg 1$, the ellipse becomes a line $\tilde{\varphi} \pm \tilde{\delta} = 0$. However, the nonlinear part of synchrotron Hamiltonian will distort the ellipse.

II.5 Synchrotron Motion for Large-Amplitude Particles

The phase space trajectory of adiabatic synchrotron motion follows a Hamiltonian torus $H(\phi, \delta) = H_0$, where $H(\phi, \delta)$ is the synchrotron Hamiltonian in Eq. (3.14) and the constant Hamiltonian value H_0 is

$$H_0 = \frac{1}{2}h\omega_0\eta\hat{\delta}^2 = \frac{\omega_0 eV}{2\pi\beta^2 E}[\cos\hat{\phi} - \cos\phi_{\mathrm{s}} + (\hat{\phi} - \phi_{\mathrm{s}})\sin\phi_{\mathrm{s}}].$$

---

[6]In reality, the beam does not jump in the phase space; instead, the phase of the rf wave is being shifted so that the UFP is located at the center of a bunch.

Here $\hat{\phi}$ and $\hat{\delta}$ are respectively the maximum phase coordinate and fractional momentum deviation of synchrotron motion. Using Hamilton's equation $\dot{\phi} = h\omega_0 \eta \delta$, we find the synchrotron oscillation period as

$$T = \oint \left(2h\omega_0 \eta \left[H_0 - \frac{\omega_0 eV}{2\pi \beta^2 E} [\cos\phi - \cos\phi_{\rm s} + (\phi - \phi_{\rm s})\sin\phi_{\rm s}] \right] \right)^{-1/2} d\phi, \qquad (3.57)$$

where H_0 is the Hamiltonian value of a torus. The angular synchrotron frequency is $2\pi/T$. The action of the torus is

$$J = \frac{1}{2\pi} \oint \left(\frac{2}{h\omega_0 \eta} [H_0 - \frac{\omega_0 eV}{2\pi \beta^2 E}(\cos\phi - \cos\phi_{\rm s} + (\phi - \phi_{\rm s})\sin\phi_{\rm s})] \right)^{1/2} d\phi. \qquad (3.58)$$

The synchrotron period of Eq. (3.57) can also be derived by differentiating Eq. (3.58) with respect to J, and using $dH_0/dJ = \omega(J)$ to find the synchrotron frequency.

A. Stationary synchrotron motion

For simplicity, we consider the stationary synchrotron motion above the transition energy with $\eta > 0$, or $\phi_{\rm s} = \pi$. The Hamiltonian value for a torus with a maximum phase coordinate $\hat{\phi}$ (or maximum off-momentum coordinate $\hat{\delta}$) is

$$H_0 = \frac{1}{2}h\omega_0 \eta \hat{\delta}^2 = \frac{\omega_0}{h\eta}\nu_{\rm s}^2(1 - \cos\hat{\phi}) \quad \Longrightarrow \quad \hat{\delta} = \frac{2\nu_{\rm s}}{h\eta}\sin\frac{\hat{\phi}}{2}. \qquad (3.59)$$

The maximum off-momentum coordinate $\hat{\delta}$ is related to the maximum phase coordinate $\hat{\phi}$ for a Hamiltonian torus, where the phase space trajectory is given by $(\phi, \pm\delta(\phi))$: $\delta(\phi) = \frac{\nu_{\rm s}}{h\eta}\sqrt{2(\cos\phi - \cos\hat{\phi})}$. The phase space area $\mathcal{A}$, or the action J enclosed by the Hamiltonian torus is

$$\mathcal{A} = 2\pi J = 2\int_{-\hat{\phi}}^{\hat{\phi}} \delta(\phi)d\phi = 16\frac{\nu_{\rm s}}{h\eta}\left[E(k) - (1 - k^2)K(k) \right],$$

$$K(k) = \int_0^{\pi/2} \frac{dw}{\sqrt{1 - k^2\sin^2 w}}, \qquad E(k) = \int_0^{\pi/2} \sqrt{1 - k^2\sin^2 w}\ dw, \qquad (3.60)$$

where $K(k)$ and $E(k)$ are the complete elliptic integrals of the first and second kinds, and $k = \sin(\hat{\phi}/2)$ is the modulus of these integrals.

B. Synchrotron tune

The synchrotron tune of the Hamiltonian torus with maximum phase amplitude $\hat{\phi}$ becomes (see Exercise 3.2.8)

$$\tilde{Q}_{\rm s}(\hat{\phi}) = \frac{\pi\nu_{\rm s}}{2K(\sin(\frac{\hat{\phi}}{2}))} \qquad (3.61)$$

Figure 3.5 compares the theoretical curve of Eq. (3.61) with a measured synchrotron tune at the IUCF Cooler. When the value of the Hamiltonian H_0 approaches that of the separatrix $H_{\rm sx}$ of Eq. (3.33), the synchrotron tune becomes zero and the synchrotron period becomes infinite. In the small angle approximation, we find $\tilde{Q}_{\rm s}(\hat{\phi}) \approx (1 - \frac{1}{16}\hat{\phi}^2)\nu_{\rm s}$, which is identical to Eq. (3.53) at $\phi_{\rm s} = 0$.
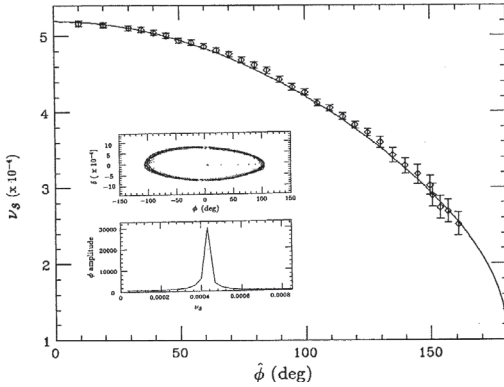

Figure 3.5: The measured synchrotron tune obtained by taking the FFT of the synchrotron phase coordinate is plotted as a function of the maximum phase amplitude of the synchrotron oscillations. The solid line shows the theoretical prediction of Eq. (3.61). The inset shows an example of the synchrotron phase-space map measured at the IUCF Cooler, and the corresponding FFT spectrum. The zero amplitude synchrotron tune was $\nu_{\rm s} = 5.2 \times 10^{-4}$.

Since the synchrotron tune is nonlinear, particles having different synchrotron amplitudes in a beam bunch can have different synchrotron tunes. If the bunch area is a substantial fraction of the bucket area, the synchrotron tune spread may be large. For a mismatched beam bunch, synchrotron tune spread can cause beam *decoherence*, a *filamentation* process, where beam particles spread out in the synchrotron phase space. Beam filamentation causes a mismatched beam bunch to evolve into spirals bounded by a Hamiltonian torus. The final bunch area is determined by the initial beam distribution and parameters of the rf system (see Fig. 3.20 in Sec. V). Filamentation can dilute the phase-space density of the beam. When the beam encounters longitudinal collective beam instability, or mis-injection in the rf bucket, or rf voltage and phase modulations, etc., the mismatched phase-space distribution will decohere and result in beam dilution. This process is important to rf capture in low energy synchrotrons during injection. On the other hand, synchrotron tune spread is useful in providing Landau damping for collective beam instabilities.

II.6 Experimental Tracking of Synchrotron Motion

Experimental measurements of synchrotron phase-space coordinates are important in improving the performance of synchrotrons. For example, a phase detector is needed in implementing a phase feedback loop to damp dipole or higher-order synchrotron modes. In this section we discuss the methods of measuring the off-momentum and rf phase coordinates of a beam.

The fractional off-momentum coordinate of a beam can be derived by measuring the closed orbit of transverse displacement Δx_{co} at a high dispersion function location. The off-momentum coordinate is

$$\frac{\Delta p}{p} = \frac{\Delta x_{\mathrm{co}}}{D}, \tag{3.62}$$

where D is the horizontal dispersion function. Since synchrotron oscillation is relatively slow in proton synchrotrons, the signal-to-noise ratio can be enhanced by using a low-pass filter at a frequency slightly higher than the synchrotron frequency.

The inset in Fig. 3.5 shows a synchrotron phase space ellipse measured at the IUCF Cooler Ring. The phase coordinate is obtained by a phase detector, and the fractional off-momentum coordinate is obtained from the displacement of the beam centroid measured with a beam position monitor (BPM).

The BPM system had an rms position resolution of about 0.1 mm. By averaging the position measurements the stability of the horizontal closed orbit was measured to be within 0.02 mm. The momentum deviation is related to the off-momentum closed orbit, Δx_{co}, by $\Delta x_{\mathrm{co}} = D\delta$, where $\delta = \Delta p/p_0$ is the fractional momentum deviation, and the horizontal dispersion function D is about 4.0 m at a high-dispersion location. The position signals from the BPM were passed through a 3 kHz low-pass filter before digitization to remove effects due to coherent betatron oscillations and high frequency noise. Since the synchrotron frequency at the IUCF Cooler in this experiment was less than 1 kHz for an rf system with $h = 1$, a 3 kHz low-pass filter could be used to average out betatron oscillations of a few hundred kHz.

The synchrotron phase coordinate can be measured by comparing the bunch arrival time with the rf cavity wave. First, we examine the characteristics of beam current signal from a beam position monitor. We assume that the bunch length is much shorter than the circumference of an accelerator. With the beam bunch approximated by an ideal δ-function pulse, the signal from a beam position monitor (BPM) or a wall gap monitor (WGM)[7] is

$$I(t, \tau) = N_{\mathrm{B}} e \sum_{\ell=-\infty}^{\infty} \delta(t + \tau - \ell T_0) = \frac{N_{\mathrm{B}} e}{T_0} \sum_{n=-\infty}^{\infty} e^{in\omega_0(t+\tau)}, \tag{3.63}$$

where N_{B} is the number of particles in a bunch, T_0 is the revolution period, $\omega_0 = 2\pi/T_0$ is the angular revolution frequency, and $\tau = (\theta - \theta_{\mathrm{s}})/\omega_0$ is the arrival time relative to the synchronous particle. Equation (3.63) shows that the periodic delta-function pulse, in time domain, is equivalent to sinusoidal waves at all integer harmonics of the revolution frequency.

---

[7]A wall gap monitor consists of a break in the vacuum chamber. The wall current that flows through a resistor, typically about 50 Ohms with a stray capacitance of about 30 pF, can then be measured. The bandwidth is about 100 MHz.

To measure the phase coordinate or equivalently the relative arrival time τ, we first select a sinusoidal wave by using the band-pass filter, or we select the fundamental harmonic with a low-pass filter including only the fundamental harmonic. The sinusoidal signal is compared with the rf wave; and the phase between the beam and the reference rf wave can be obtained by using phase detectors.[8] Normally, the BPM sum signal or the WGM signal can be used to measure the relative phase of the beam.[9] Since the rf frequency was 1.03 MHz for the 45 MeV protons in this measurement at the IUCF Cooler, the BPM signal was passed through a 1.4 MHz low-pass filter to eliminate high harmonics noise before it was compared with an rf signal in a phase detector.

The phase-space map of synchrotron oscillations can be obtained by plotting $\Delta p/p_0$ vs ϕ in each revolution. Since the synchrotron tune of a proton synchrotron is small, the synchrotron motion can be tracked at N revolution intervals, where $N \ll 1/\nu_s$. The top inset in Fig. 3.5 shows the Poincaré map of the longitudinal phase space at 10 turn intervals; the bottom inset shows the FFT of the phase data. The resulting synchrotron tune as a function of peak phase amplitude is compared with the theoretical prediction in Fig. 3.5.

Exercise 3.2

1. Write a simple program to calculate $\alpha_b(\phi_0)$.

2. This exercise concerns the acceleration of protons in the AGS booster. The injection kinetic energy is 200 MeV from the linac. The circumference of the booster ring is 201.78 m, the transition energy is $\gamma_T = 4.5$, the extraction energy is 1.5 GeV kinetic energy, the acceleration time is 160 ms, and the harmonic number is $h = 3$.

    (a) Find the rf voltage needed for acceleration of a proton bunch in the booster.

    (b) The bunch area is determined by several factors, such as line charge density, microwave instabilities, transition crossing in the AGS, etc. If we need a bunch area of about 1 eV-s per bunch in $(\Delta E/\omega_0, \phi/h)$ phase space, and the bucket area is about 1.2 times as large as the bunch area, what is the minimum rf voltage needed?

    (c) What is the rf frequency swing needed to accelerate protons from 200 MeV to 1.5 GeV?

    (d) How does the rf bucket area change during the acceleration process?

---

[8]See Roland E. Best, *Phase Locked Loops, Theory, Design, and Applications*, pp. 7-9 (McGraw-Hill, New York, 1984). The type II phase detector utilizes XOR logic, and has a range of $\pm 90°$; the type III utilizes the edge triggered JK-master-slave flip-flop circuit, and has a range of $\pm 180°$. The type III has a phase error of about $\pm 10°$ near $0°$, but can adequately measure the synchrotron tune. For more accurate measurement of phase amplitude response, the type II can be used. To extend the range of beam phase detection, a type IV phase detector with a range of $\pm 360°$ can be used.

[9]M. Ellison *et al.*, *Phys. Rev.* **E 50**, 4051 (1994).

3. For a constant rf voltage and synchronous phase angle, show that the rf bucket area in the $(\Delta E/\omega_0, \phi/h)$ phase space has a minimum at $\gamma = \sqrt{3}\gamma_T$.

4. Particle acceleration at a constant bucket is a possible "rf program" in synchrotrons. Find the relation between rf voltage and beam energy.

5. Verify Eq. (3.54). Rotate the phase-space ellipse of Eq. (3.56) into the upright position, show that the width and height of the bunch change by a factor $e^{\pm\omega_s t}$, where t is the time the bunch stays at the UFP, and estimate the time needed to double the bunch height.

6. The anti-protons produced from the Main Injector (Main Ring) pulses have the following characteristics: $p_0 = 8.9$ GeV/c, $\sigma_t = 0.15$ ns, $\sigma_E = 180$ MeV, or $\Delta p/p_0 = \pm 2\%$. The antiprotons are captured in the Debuncher into the 53.1 MHz ($h = 90$) rf bucket with $V = 5$ MV, $\phi_s = 180°$, $\gamma_T = 7.7$, and circumference $C = 505$ m.[10]

   (a) Find the bucket height, synchrotron tune, and synchrotron period of the Debuncher ring with the rf system.

   (b) At 1/4 of the synchrotron period after antiproton injection, the rf voltage is lowered suddenly to match the bunch shape. Show that the final rf voltage V_2 related to the initial voltage V_1 and the final energy spread in this debunching process are respectively

$$\frac{V_2}{V_1} = \left(\frac{\nu_{s1}}{|\eta|}(\omega_0\sigma_{t1})\right)^2\left(\frac{\sigma_{E1}}{\beta^2 E}\right)^{-2}, \qquad \sigma_{E2} = \left[\frac{\nu_{s1}}{|\eta|}(\omega_0\sigma_{t1})\right]\beta^2 E.$$

   Find the final matched rf voltage for the Debuncher and the final energy spread of the antiproton beams.

7. Assuming stationary bucket, fill out the beam properties of the proton synchrotrons in the table below.

P-synchrotron	AGS	RHIC	FNAL-MI	FNAL-BST	Cooler
K.E. [GeV]	25	250	120	8	0.045
V_{rf} [MV]	0.3	0.3	2	0.95	0.0001
h	12	342	588	84	1
γ_T	8.5	24.5	21.8	5.446	4.6
C [m]	807.12	3833.84	3319.4	474.2	86.8
$\mathcal{A}_{rms}$ [eV-s]	1.5	0.5	0.15	0.15	0.0001
σ_E [MeV]					
σ_t [ns]					

8. Show that the synchrotron tune of a particle with phase amplitude $\hat{\phi}$ in a stationary bucket is

$$Q_s(\hat{\phi}) = \pi\nu_s/2K(\sin\frac{\hat{\phi}}{2}),$$

where $K(x)$ is the complete elliptical integral of the first kind given in Eq. (3.60).

---

[10]See A.V. Tollestrup and G. Dugan, p. 954 in Ref. [17] (1983). Note that 5 MV is the maximum voltage that the Debuncher rf system can deliver.

9. Define $p_\phi = h\omega\eta\delta$, and show that the synchrotron equations of motion become

$$\dot{\phi} = p_\phi, \quad \dot{p}_\phi = \frac{\eta}{|\eta|}\omega_s^2(\sin\phi - \sin\phi_s),$$

where $\omega_s = \omega_0\sqrt{h|\eta|eV/2\pi\beta^2 E}$, and the overdot indicates the derivative with respect to time t. The Hamiltonian for a stationary rf system with ϕ_s becomes

$$H = \frac{1}{2}p_\phi^2 + \frac{\eta}{|\eta|}\omega_s^2(\cos\phi - 1).$$

(a) Using the generating function show that phase-space coordinates are

$$F_1 = -\frac{\omega_s}{2}\phi^2\tan\psi \implies \phi = \sqrt{2J/\omega_s}\cos\psi, \quad p_\phi = -\sqrt{2J\omega_s}\sin\psi,$$

where J and ψ are action-angle coordinates. Show that the Hamiltonian below the transition energy becomes

$$H = \omega_s J + \omega_s^2\left[1 - \frac{J}{\omega_s}\cos^2\psi - \cos\left(\sqrt{\frac{2J}{\omega_s}}\cos\psi\right)\right].$$

(b) Using the phase averaging method, show that the synchrotron tune is approximately given by

$$Q_s(J) = \nu_s\left[\frac{1}{2} + \frac{J_1(w)}{w}\right], \quad w = \sqrt{\frac{2J}{\omega_s}},$$

where $J_1(w)$ is the Bessel function.

(c) Compare the accuracy of the above approximated synchrotron tune to that of the exact formula given by Exercise 3.2.8.

10. Let $\hat{\phi}$ be the maximum synchrotron phase amplitude. Show that the maximum off-momentum deviation is

$$\hat{\delta} = \frac{\sqrt{2}Q_s}{h|\eta|}\left[-1 + \frac{\cos\hat{\phi}}{\cos\phi_s} + (\hat{\phi} - \phi_s)\tan\phi_s\right].$$

11. Expanding the phase coordinate around the SFP with $\phi = \phi_s + \varphi$, the synchrotron Hamiltonian becomes

$$H = \frac{1}{2}h\omega_0\eta\delta^2 + \frac{1}{2h\eta}\omega_0 Q_s^2\left[\varphi^2 - \frac{1}{3}\tan\phi_s\varphi^3 - \frac{1}{12}\varphi^4 + \cdots\right],$$

$$Q_s = \sqrt{\frac{heV|\eta\cos\phi_s|}{2\pi\beta^2 E}} = \nu_s\sqrt{|\cos\phi_s|}.$$

For simplicity, we assume $\eta > 0$ in this exercise.

(a) Using the generating function to transform (φ, δ) to angle-action (ψ, J) coordinates, show that the coordinate transformation and the resulting Hamiltonian in action-angle are

$$F_1(\phi, \psi) = -\frac{Q_s}{2h\eta}\varphi^2 \tan \psi$$

$$\varphi = \sqrt{2h\eta J/Q_s} \cos \psi, \ \ \delta = -\sqrt{2Q_s J/h\eta} \sin \psi,$$

$$H = \omega_0 Q_s J - \frac{\omega_0 \sqrt{2h\eta Q_s}}{12} \tan \phi_s \, J^{3/2} \left[\cos 3\psi + 3 \cos \psi\right] - \frac{\omega_0 h\eta}{6} J^2 \cos^4 \psi.$$

(b) Using the generating function

$$F_2(\psi, I) = \psi I + G_3(I) \sin 3\psi + G_1(I) \sin \psi,$$

show that terms proportional to $J^{3/2}$ in the Hamiltonian can be canceled if G_3 and G_1 are chosen to be

$$G_3 = \frac{\sqrt{2h\eta}}{36\sqrt{Q_s}} \tan \phi_s \, I^{3/2}, \quad G_1 = \frac{\sqrt{2h\eta}}{4\sqrt{Q_s}} \tan \phi_s \, I^{3/2}.$$

Finding new canonical variables to cancel low-order perturbation terms is called the *canonical perturbation technique*.

(c) Show that the new Hamiltonian is

$$\begin{aligned}
H &= \omega_0 Q_s I - \frac{\omega_0 h\eta}{6} I^2 \cos^4 \psi \\
&\quad - \frac{\omega_0 \sqrt{2h\eta Q_s}}{8} \tan \phi_s I^{1/2} [\cos 3\psi + 3\cos \psi][3G_3 \cos 3\psi + G_1 \cos \psi].
\end{aligned}$$

Now the perturbation in the new action variable is proportional to I^2.

(d) Show that the average Hamiltonian and thus the synchrotron tune for a particle with a synchrotron amplitude are

$$\langle H \rangle = \omega_0 Q_s I - \frac{\omega_0 h\eta}{16} \left(1 + \frac{5}{3} \tan^2 \phi_s\right) I^2 + \cdots.$$

$$\tilde{Q}(\hat{\varphi}) = Q_s \left[1 - \frac{1}{16} \left(1 + \frac{5}{3} \tan^2 \phi_s\right) \hat{\varphi}^2\right],$$

where $\hat{\varphi}$ is the maximum synchrotron amplitude in the quasi-harmonic approximation. Compare your result with that of Eq. (3.61) for $\phi_s = 0$.

12. The natural rms fractional momentum spread of electron beams in a storage ring is $\sigma_E/E = \sqrt{C_q \gamma^2 / \mathcal{J}_E \rho}$, where $C_q = 3.83 \times 10^{-13}$ m, ρ is the bending radius, and $\mathcal{J}_E \approx 2$ is the damping partition. In the NLC damping ring (DR) parameter list shown in Exercise 3.1.3, the rms fractional momentum spread of the electron beam is $\sigma_\delta = 0.000813$. Find the bunch length and rms phase-space area in eV-s.

13. The equilibrium distribution in linearized synchrotron phase space is a function of the invariant ellipse given by Eq. (3.44), where $\hat{\theta} = |\eta|\hat{\delta}/\nu_{\rm s}$. When a mismatched Gaussian beam

$$\rho(\delta, \theta) = \frac{N_{\rm B}e}{2\pi\sigma_\delta\sigma_\theta} \exp\left\{-\frac{1}{2}\left[\frac{\theta^2}{\sigma_\theta^2} + \frac{\delta^2}{\sigma_\delta^2}\right]\right\}$$

is injected into the synchrotron at time $t = 0$, what is the time evolution of the beam? Here σ_θ and σ_δ are respectively the initial rms bunch angular width and fractional momentum spread, and the mismatch condition for the linearized synchrotron motion is given by $\sigma_\theta \neq |\eta|\sigma_\delta/\nu_{\rm s}$.

   (a) Show that the projection of the beam distribution function onto the θ axis is[11]

   $$\rho(\theta, t) = \frac{N_{\rm B}e}{\sqrt{2\pi}\tilde{\sigma}}e^{-\theta^2/2\tilde{\sigma}^2} \qquad \tilde{\sigma}^2 = \sigma_\theta^2 \cos^2\omega_{\rm s}t + (|\eta|\sigma_\delta/\nu_{\rm s})^2 \sin^2\omega_{\rm s}t.$$

   Show that the peak current is $\hat{I}(t) = N_{\rm B}e\omega_0/\sqrt{2\pi}\tilde{\sigma}$.

   (b) For a weakly mismatched beam, show that

   $$\sigma_\theta^2 \approx \sigma_0^2(1 - \Delta V/2V), \quad (\eta\sigma_\delta/\nu_{\rm s})^2 \approx \sigma_0^2(1 + \Delta V/2V),$$

   where $\sqrt{2}\sigma_0 = \sqrt{\sigma_\theta^2 + (\eta\sigma_\delta/\nu_{\rm s})^2}$ is the matched rms beam width, ΔV is the mismatched voltage, and V is the voltage for the matched beam profile. Show that the peak current for the weakly mismatched beam is

   $$\hat{I}(t) \approx \frac{N_{\rm B}e\omega_0}{\sqrt{2\pi}\sigma_0^2}\left(1 - \frac{\Delta V}{4V} \cos 2\omega_{\rm s}t\right).$$

   Discuss your result. Because the bunch tumbles at twice the synchrotron frequency, the resulting coherent beam motion is called the quadrupole synchrotron mode. The nonlinear synchrotron tune will cause the mismatched injection to filament and the resulting phase-space area will be larger.

14. An off momentum particle executes synchrotron motion with $\delta = \hat{\delta}\sin\omega_s t$, where ω_s is the synchrotron tune, $\hat{\delta}$ is the amplitude of synchrotron motion. Show that the accumulated betatron phase advance in a half-synchrotron period

$$\Delta\Phi_\beta = 4\pi\frac{C\hat{\delta}}{\omega_s T_0} = \frac{C\omega_0}{\eta}2\hat{\tau},$$

where C is the chromaticity, $2\hat{\tau} = 2\eta\hat{\delta}/\omega_s$ is the time width of synchrotron motion, and η is the phase slip factor. Note that the accumulated betatron phase shift is proportional to the synchrotron time-width. The quantity $C\omega_0/\eta$ is the betatron frequency shift from the head to tail for all particle. If $C/\eta < 0$, the frequency shift is negative, and beam may sample impedance in the negative frequency and cause transverse head-tail instability.

---

[11]Transform the (θ, δ) coordinate system into the normalized coordinate system ($x = \theta$ and $p = |\eta|\delta/\nu_{\rm s}$), where the matched beam profile is a circle. Make coordinate transformation into the synchrotron rotating frame. The beam profile in the x plane is equal to $\rho(x) = \int \rho(x, p)dp$.

III   RF Phase and Voltage Modulations

Particle motion in accelerators experiences perturbations from rf phase and ampli-
tude noise, power supply ripple, wakefields, etc. These perturbation sources cause rf
phase or voltage modulations. In general, the frequency spectrum of rf noise may con-
tain high frequency arising from random thermal (white) noise, low frequency from
power supply ripple and ground motion, and medium frequency from mechanical vi-
bration etc. In this section, we study the effects of a single frequency sinusoidal rf
phase and voltage modulation on particle motion and beam distribution. Physics of
beam response to a single frequency modulation can be applied to more complicated
multi-frequency perturbations. In Sec. III.1, the longitudinal phase space coordinates
$(\phi, \Delta p/p)$ will be expanded in action-angle variables (J, ψ). With these results, the
perturbed Hamiltonian of phase and voltage modulation can easily be expressed in
action-angle variables (see Secs. III.2 and III.5). Once this is accomplished, effects of
rf phase and voltage modulation can be readily obtained.

III.1   Normalized Phase-Space Coordinates

Using normalized momentum deviation coordinate $\mathcal{P} = -(h|\eta|/\nu_s)(\Delta p/p)$, the Hamil-
tonian for a stationary synchrotron motion is

$$H_0 = \frac{1}{2}\nu_s \mathcal{P}^2 + 2\nu_s \sin^2 \frac{\phi}{2}, \tag{3.64}$$

where $\nu_s = \sqrt{h|\eta|eV/2\pi\beta^2 E}$ is the synchrotron tune at $|\cos\phi_s| = 1$, the orbital
angle θ is the independent variable, and $(\phi, \mathcal{P})$ are normalized conjugate phase-space
coordinates. The Hamiltonian has fixed points at

$$(\phi, \mathcal{P})_{\text{SFP}} = (0, 0) \quad \text{and} \quad (\phi, \mathcal{P})_{\text{UFP}} = (\pi, 0).$$

The synchrotron Hamiltonian is autonomous (time independent), and thus the Hamil-
tonian value is a constant of motion.

Expressing the synchrotron coordinates in parameters k and w as

$$\sin \frac{\phi}{2} = k \sin w, \quad \frac{\mathcal{P}}{2} = k \cos w, \tag{3.65}$$

we obtain $H_0 = 2\nu_s k^2$, where $k = 0$ corresponds to the SFP and $k = 1$ corresponds
to the separatrix orbit that passes through the UFP. The action is

$$J = \frac{1}{2\pi} \oint \mathcal{P} d\phi = \frac{8}{\pi} \left[E(k) - (1 - k^2)K(k) \right], \tag{3.66}$$

where the complete elliptical function integrals are [30]

$$E(k) = \int_0^{\pi/2} \sqrt{1 - k^2 \sin^2 w} \; dw, \quad K(k) = \int_0^{\pi/2} \frac{1}{\sqrt{1 - k^2 \sin^2 w}} \; dw.$$

In the normalized phase-space coordinates, the maximum action ($k = 1$) is $J_{\max} = 8/\pi$, and the maximum bucket area is $\mathcal{A} = 2\pi J_{\max} = 16$ (see Table 3.2).

For synchrotron motion with a small action, the power series expansions of elliptical integrals are

$$
\begin{aligned}
K(k) &= \frac{\pi}{2}\left[1 + (\frac{1}{2})^2 k^2 + (\frac{1 \cdot 3}{2 \cdot 4})^2 k^4 + (\frac{1 \cdot 3 \cdot 5}{2 \cdot 4 \cdot 6})^2 k^6 + \cdots\right], \\
E(k) &= \frac{\pi}{2}\left[1 - (\frac{1}{2})^2\frac{k^2}{1} - (\frac{1 \cdot 3}{2 \cdot 4})^2\frac{k^4}{3} - (\frac{1 \cdot 3 \cdot 5}{2 \cdot 4 \cdot 6})^2\frac{k^6}{5} - \cdots\right].
\end{aligned}
$$

The action is related to the parameter k by

$$J = 2k^2(1 + \frac{1}{8}k^2 + \frac{3}{64}k^4 + \cdots), \tag{3.67}$$

$$2k^2 = J(1 - \frac{1}{16}J - \frac{1}{256}J^2 - \cdots). \tag{3.68}$$

In terms of the action, the Hamiltonian is $H_0(J)$. The *synchrotron tune* becomes

$$\tilde{Q}_{\mathrm{s}}(J) = \frac{\partial H_0}{\partial J} = \frac{\pi\nu_{\mathrm{s}}}{2K(k)} = \nu_{\mathrm{s}}(1 - \frac{J}{8} - \frac{3J^2}{256} - \cdots), \tag{3.69}$$

where we have used the identities

$$2k^2\frac{dE(k)}{dk^2} = E(k) - K(k), \quad 2k^2\frac{dK(k)}{dk^2} = \frac{1}{1 - k^2}E(k) - K(k).$$

Using the generating function to transform from (ϕ, δ) to (ψ, J), i.e.

$$F_2(\phi, J) = \int_0^\phi \mathcal{P}(\tilde{\phi})\,d\tilde{\phi}, \quad \Longrightarrow \quad \psi = \frac{\partial F_2}{\partial J} = \frac{\tilde{Q}_{\mathrm{s}}(J)}{\nu_{\mathrm{s}}}\int_0^\phi \frac{d\tilde{\phi}}{\mathcal{P}(\tilde{\phi})}. \tag{3.70}$$

The angle variable ψ, conjugate to the action J, can also be obtained by integrating Hamilton's equation Eq. (3.69):

$$\psi = \frac{\pi\nu_{\mathrm{s}}}{2K}\theta + \psi_0. \tag{3.71}$$

The next task is to express the normalized off-momentum coordinate $\mathcal{P}$, and the synchrotron phase coordinate ϕ, in Fourier harmonics of the conjugate angle parameter ψ. First, using Hamilton's equation $\dot{\phi} = \nu_{\mathrm{s}}\mathcal{P}$, we can relate the orbital angle θ to the w parameter of Eq. (3.65) as

$$\nu_{\mathrm{s}}(\theta - \theta_0) = \int_{\phi_0}^\phi \frac{d\phi}{\mathcal{P}} = u - u_0,$$

where

$$u = \int_0^w \frac{1}{\sqrt{1 - k^2 \sin^2 w}} \, dw, \quad u_0 = \int_0^{w_0} \frac{1}{\sqrt{1 - k^2 \sin^2 w}} \, dw.$$

The Jacobian elliptical functions, cn and sn, are then defined as

$$\sin w = \mathrm{sn}(u|k), \quad \cos w = \mathrm{cn}(u|k), \tag{3.72}$$

and the synchrotron phase-space coordinates are related to the Jacobian elliptical function by

$$\mathcal{P} = 2k \, \mathrm{cn}(u|k), \quad \sin \frac{\phi}{2} = k \, \mathrm{sn}(u|k). \tag{3.73}$$

Thus the expansion of $\mathcal{P}$ and $\sin(\phi/2)$ in Fourier harmonics of ψ is equivalent to the expansion of $\mathrm{cn}(u|k)$ and $\mathrm{sn}(u|k)$ in $\psi = \pi u/2K$. This can be achieved by using Eq. (16.23.2) in Ref. [30], i.e.

$$\begin{aligned}
\mathcal{P} &= 2k\mathrm{cn}(u|k) = \frac{4\pi\sqrt{k}}{K(k)} \sum_0^\infty \frac{q^{n+1/2}}{1 + q^{2n+1}} \cos(2n+1)\psi \\
&\approx (2J)^{1/2} \cos\psi + \frac{(2J)^{3/2}}{64} \cos 3\psi + \frac{(2J)^{5/2}}{4096} \cos 5\psi + \cdots, \tag{3.74}
\end{aligned}$$

where ψ is the synchrotron phase with the q parameter given by

$$q = e^{-\pi K'/K} = \frac{k^2}{16} + 8\left(\frac{k^2}{16}\right)^2 + 84\left(\frac{k^2}{16}\right)^3 + 992\left(\frac{k^2}{16}\right)^4 + \cdots,$$

with $K' = K(\sqrt{1 - k^2})$. Similarly, using the identity $k^2\mathrm{sn}^2(u|k) = 1 - \mathrm{dn}^2(u|k)$, we obtain

$$2\sin^2 \frac{\phi}{2} = \sum_{n=-\infty}^\infty G_n(J)e^{jn\psi} \approx -\frac{J}{2}\cos 2\psi - \frac{J^2}{32}\cos 4\psi + \cdots, \tag{3.75}$$

$$G_n(J) = \frac{1}{2\pi} \int_0^{2\pi} (1 - \cos\phi)e^{-jn\psi} \, d\psi, \tag{3.76}$$

where $G_{-n} = G_n^*$. Because $1 - \cos\phi$ is an even function, $G_n = 0$ for odd n. The expansion of normalized coordinates in action-angle variables is useful for evaluating the effect of perturbation on synchrotron motion, discussed below.

Sum rule theorem

The solutions of many dynamical systems can be obtained by expanding the perturbation potential in action angle variables. For the case of rf phase modulation, the expansion of the normalized off-momentum coordinate is

$$\mathcal{P} = \sum_{n=-\infty}^\infty f_n(J)e^{in\psi}, \tag{3.77}$$

where $f_{-n} = f_n^*$ and, from Eq. (3.74), the strength functions f_n are

$$f_{2m+1} = \frac{2\pi\sqrt{k}q^{m+1/2}}{K(k)(1+q^{2m+1})}, \quad f_{2m} = 0.$$

Because $\mathcal{P}$ is an odd function, only odd harmonics exist. Furthermore, the sum of all strength functions is (see Exercise 3.3.2)

$$\sum_{n=-\infty}^{\infty} |f_n|^2 = \frac{\tilde{Q}_s(J)}{\nu_s}J. \tag{3.78}$$

We observe that the strength functions are zero at the center of the rf bucket where $J = 0$ and at the separatrix where $\tilde{Q}_s(J_{sx}) = 0$.

III.2 RF Phase Modulation and Parametric Resonances

If the phase of the rf wave changes by an amount $\varphi(\theta)$, where $\theta = \omega_0 t$ is the orbiting angle serving as time coordinate, the synchrotron mapping equation is

$$\phi_{n+1} = \phi_n + 2\pi h\eta\delta_n + \Delta\varphi(\theta), \tag{3.79}$$

$$\delta_{n+1} = \delta_n + \frac{eV}{\beta^2 E}(\sin\phi_{n+1} - \sin\phi_s), \tag{3.80}$$

where $\Delta\varphi(\theta) = \varphi(\theta_n + 2\pi) - \varphi(\theta_n)$ is the difference in rf phase error between successive turns in the accelerator. In this section, we consider only a sinusoidal rf phase modulation with[12]

$$\varphi = a\sin(\nu_m\theta + \chi_0),$$

where ν_m is the modulation tune, a is the modulation amplitude, and χ_0 is an arbitrary phase factor. The resulting rf phase difference in every revolution is $\Delta\varphi = 2\pi\nu_m a\cos(\nu_m\theta + \chi_0)$.

For simplicity, we consider the case of a stationary bucket with $\phi_s = 0$ for $\eta < 0$. Using the normalized off-momentum coordinate $\mathcal{P} = -(h|\eta|/\nu_s)\delta$, we obtain the perturbed Hamiltonian

$$H = H_0 + H_1 = \frac{1}{2}\nu_s\mathcal{P}^2 + 2\nu_s\sin^2\frac{\phi}{2} + \nu_m a\mathcal{P}\cos(\nu_m\theta + \chi_0), \tag{3.81}$$

where the perturbation potential of rf phase modulation is

$$H_1 = \nu_m a\mathcal{P}\cos(\nu_m\theta + \chi_0). \tag{3.82}$$

---

[12]M. Ellison *et al.*, *Phys. Rev. Lett.* **70**, 591 (1993); M. Syphers *et al.*, *Phys. Rev. Lett.* **71**, 719 (1993); H. Huang *et al.*, *Phys. Rev.* E **48**, 4678 (1993); Y. Wang *et al.*, *Phys. Rev.* E **49**, 1610 (1994).

Expressing the phase-space coordinate $\mathcal{P}$ in action-angle coordinates with Eq. (3.74), we can expand the perturbation in action-angle variables

$$
\begin{aligned}
H_1 &= \nu_{\mathrm{m}} a \sqrt{J/2}\, \left[\cos(\psi + \nu_{\mathrm{m}}\theta + \chi_0) + \cos(\psi - \nu_{\mathrm{m}}\theta - \chi_0)\right] \\
&\quad + \nu_{\mathrm{m}} a \frac{(2J)^{3/2}}{128} \left[\cos(3\psi + \nu_{\mathrm{m}}\theta + \chi_0) + \cos(3\psi - \nu_{\mathrm{m}}\theta - \chi_0)\right] + \dots, \quad (3.83)
\end{aligned}
$$

where J and ψ are conjugate action-angle variables. The rf phase error generates only odd order parametric resonances because $\mathcal{P}$ is an odd function. However, two nearby strong parametric resonances can drive secondary and tertiary resonances. For example, the 1:1 and 3:1 parametric resonances driving by a strong phase modulation can produce a secondary 4:2 resonance at $\nu_{\mathrm{m}} \approx 2\nu_{\mathrm{s}}$. In the following, we discuss only the primary parametric resonances, particularly the 1:1 dipole mode.

A. Effective Hamiltonian near a parametric resonance

When the modulation tune is near an odd multiple of synchrotron sideband, i.e. $\nu_{\mathrm{m}} = (2m + 1)\nu_{\mathrm{s}}$, stationary phase condition exists for a parametric resonance term. We neglect all non-resonance terms in H_1 to obtain an approximate synchrotron Hamiltonian

$$
H \approx \nu_{\mathrm{s}} J - \frac{1}{16}\nu_{\mathrm{s}} J^2 + \nu_{\mathrm{m}} f_{2m+1} J^{m+1/2} \cos\left((2m+1)\psi - \nu_{\mathrm{m}}\theta - \chi_0\right), \quad (3.84)
$$

where $f_1 = a/\sqrt{2}$, $f_3 = a/32\sqrt{2}$, etc. The effect of rf phase modulation on phase-space distortion can be solved by using the effective parametric resonance Hamiltonian, that resembles the Hamiltonian for 1-D betatron resonances discussed in Sec. VII, Chap. 2. This primary parametric resonance is called $(2m+1){:}1$ resonance. In this section, we consider only the dominant dipole mode below.

B. Dipole mode

If the phase modulation amplitude is small, the dominant contribution arises from the $m = 0$ sideband. Near the first-order synchrotron sideband with $\nu_{\mathrm{m}} \approx \nu_{\mathrm{s}}$, the Hamiltonian for the dipole mode is

$$
H \approx \nu_{\mathrm{s}} J - \frac{1}{16}\nu_{\mathrm{s}} J^2 + \frac{\nu_{\mathrm{s}} a}{\sqrt{2}} J^{1/2} \cos(\psi - \nu_{\mathrm{m}}\theta - \chi_0). \quad (3.85)
$$

The Hamiltonian can be transformed into the resonance rotating frame:

$$
\begin{aligned}
F_2(\psi, I) &= (\psi - \nu_{\mathrm{m}}\theta - \chi_0 - \pi)\, I, \\
\chi &= \psi - \nu_{\mathrm{m}}\theta - \chi_0 - \pi, \quad I = J; \\
\tilde{H} &= (\nu_{\mathrm{s}} - \nu_{\mathrm{m}}) I - \frac{1}{16}\nu_{\mathrm{s}} I^2 - \nu_{\mathrm{s}}\frac{a}{\sqrt{2}} I^{1/2} \cos\chi. \quad (3.86)
\end{aligned}
$$

where (ψ, J) are transformed to the new phase-space coordinates (χ, I). Since the new Hamiltonian $\tilde{H}$ is "time" independent in the resonance rotating frame, a torus of particle motion will follow a constant Hamiltonian contour, where Hamilton's equations of motion are

$$\dot{\chi} = \nu_{\mathrm{s}} - \nu_{\mathrm{m}} - \frac{1}{8}\nu_{\mathrm{s}}I - \nu_{\mathrm{s}}\frac{a}{2\sqrt{2I}}\cos\chi, \qquad \dot{I} = -\nu_{\mathrm{s}}\frac{a}{2}\sqrt{2I}\sin\chi. \qquad (3.87)$$

The fixed points of the Hamiltonian, which characterize the structure of resonant islands, are given by the solution of $\dot{I} = 0$, $\dot{\chi} = 0$. Using $g = \sqrt{2J}\cos\chi$, with $\chi = 0$ or π, to represent the phase coordinate of a fixed point, we obtain the equation for g as

$$g^3 - 16\left(1 - \frac{\nu_{\mathrm{m}}}{\nu_{\mathrm{s}}}\right)g + 8a = 0. \qquad (3.88)$$

When the modulation tune is below the *bifurcation tune* ν_{bif} given by[13]

$$\nu_{\mathrm{m}} \le \nu_{\mathrm{bif}} = \nu_{\mathrm{s}}\left[1 - \frac{3}{16}(4a)^{2/3}\right], \qquad (3.89)$$

Eq. (3.88) has three solutions:

$$\begin{cases} g_a(x) = -\dfrac{8}{\sqrt{3}}x^{1/2}\cos\dfrac{\xi}{3}, & (\psi = \pi) \\[2mm] g_b(x) = \dfrac{8}{\sqrt{3}}x^{1/2}\sin(\dfrac{\pi}{6} - \dfrac{\xi}{3}), & (\psi = 0) \\[2mm] g_c(x) = \dfrac{8}{\sqrt{3}}x^{1/2}\sin(\dfrac{\pi}{6} + \dfrac{\xi}{3}), & (\psi = 0) \end{cases} \qquad (3.90)$$

where

$$x = 1 - \nu_{\mathrm{m}}/\nu_{\mathrm{s}}, \quad x_{\mathrm{bif}} = 1 - \nu_{\mathrm{bif}}/\nu_{\mathrm{s}}, \quad \xi = \arctan\sqrt{\left(\frac{x}{x_{\mathrm{bif}}}\right)^3 - 1}, \quad x_{\mathrm{bif}} = \frac{3}{16}(4a)^{2/3}.$$

Here g_a and g_b are respectively the outer and the inner stable fixed points (SFPs) and g_c is the unstable fixed point (UFP). The reason that g_a and g_b are SFPs and g_c is the UFP will be discussed shortly. Particle motion in the phase space can be described by tori of constant Hamiltonian around SFPs. The lambda-shaped phase amplitudes of the SFPs ($|g_a|$ and $|g_b|$, solid lines) and UFP ($|g_c|$, dashed line) shown in the left plot of Fig. 3.6 vs the modulation frequency is a characteristic property of the dipole mode excitation with nonlinear detuning. In the limit $\nu_{\mathrm{m}} \ll \nu_{\mathrm{bif}}$, we have $\xi \to \pi/2$, thus $g_a \to -4x^{1/2}$, $g_c \to 4x^{1/2}$, and $g_b \to 0$.

The Hamiltonian tori in phase space coordinates $\mathcal{P} = -\sqrt{2I}\sin\chi$ vs $X = \sqrt{2I}\cos\chi$ are shown in the right plot of Fig. 3.6. The actual Hamiltonian tori rotate about the

---

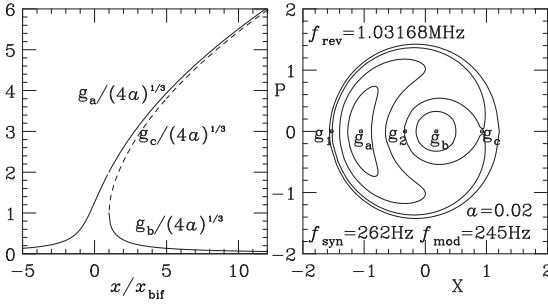[13]Find the root of the discriminant of the cubic equation (3.88).

Figure 3.6: Left: fixed point amplitudes $|g_a|$, $|g_b|$, and $|g_c|$ (in unit of $(4a)^{1/3}$). Right: Poincaré surfaces of section for $f_m = 245$ Hz and $f_s = 262$ Hz at $a = 0.02$. The SFPs are g_a and g_b, and the UFP is g_c.

center of the phase space at the modulation tune ν_m, i.e. the phase space ellipses return to this structure in $1/\nu_m$ revolutions. The torus passing through the UFP is the separatrix, which separates the phase space into two stable islands. The intercept of the the separatrix with the phase axis is denoted by g_1 and g_2.

When the modulation frequency approaches the bifurcation frequency from below $(x/x_{bif} > 1)$, the UFP and the outer SFP move in and the inner SFP moves out. At the bifurcation frequency, where $x = x_{bif}$ and $\xi = 0$, the UFP collides with the inner SFP with $g_b = g_c = (4a)^{1/3}$; and they disappear together. Beyond the bifurcation frequency, $\nu_m > \nu_{bif}$ $(x < x_{bif})$, there is only one real solution to Eq. (3.88):

$$g_a(x) = -(4a)^{1/3}\left[\left(\sqrt{1 - \left(\frac{x}{x_{bif}}\right)^3} + 1\right)^{1/3} - \left(\sqrt{1 - \left(\frac{x}{x_{bif}}\right)^3} - 1\right)^{1/3}\right]. \quad (3.91)$$

In particular, $g_a = -(8a)^{1/3}$ at $x = 0$ $(\nu_m = \nu_s)$, and $g_a = -2(4a)^{1/3}$ at $x = x_{bif}$. The characteristics of bifurcation appear in all orders of resonances with nonlinear detuning. As the modulation tune approaches the bifurcation tune, resonance islands can be created or annihilated.

C. Island tune

Let y, p_y be the local coordinates about a fixed point of the Hamiltonian, i.e.

$$y = \sqrt{2I}\cos\chi - g, \qquad p_y = -\sqrt{2I}\sin\chi, \quad (3.92)$$

where g is a fixed point of the Hamiltonian. With a local coordinate expansion, the Hamiltonian (3.86) becomes

$$H_{island} = \frac{\nu_s a}{4g}(1 - \frac{g^3}{4a})y^2 + \frac{\nu_s a}{4g}p_y^2 + \cdots. \quad (3.93)$$

Therefore the fixed point g is a stable fixed point if $(1 - g^3/4a) \geq 0$. Because $g_a^3/4a \leq 0$ and $0 \leq g_b^3/4a \leq 1$, g_a and g_b are SFPs. Since $g_c^3/4a \geq 1$, g_c is the

UFP. The equilibrium beam distribution (see Appendix A, Sec. II.3), which satisfies the Fokker-Planck-Vlasov equation, is generally a function of the local Hamiltonian, Eq. (3.93) can also provide information on the local distortion of the bunch profile.

The island tune for the small-amplitude oscillations is

$$\nu_{\text{island}} = \left| \nu_{\text{s}} \left(1 - \frac{g^2}{16} \right) - \nu_{\text{m}} \right| \left(1 - \frac{g^3}{4a} \right)^{1/2}. \tag{3.94}$$

The island tune around the inner SFP given by g_b at $\nu_{\text{m}} \ll \nu_{\text{bif}}$ is approximately given by $\nu_{\text{island}} \approx |\nu_{\text{s}}(1 - \frac{1}{16}g^2) - \nu_{\text{m}}|$. This means that the solution of the equations of motion can be approximated by a linear combination of the solution of the homogeneous equation with tune $\nu_{\text{s}}(1 - \frac{1}{16}g^2)$ and the particular solution with tune ν_{m}.[14] Thus *the island tune is the beat frequency between these two solutions.* When the modulation tune ν_{m} approaches ν_{bif}, with $(1 - g_b^3/4a)^{1/2} \to 0$, the island tune for small-amplitude oscillation about the inner SFP approaches 0 and the small-amplitude island tune for the outer SFP at $\nu_{\text{m}} = \nu_{\text{bif}}$ is $\nu_{\text{island}} = 3|\nu_{\text{s}}(1 - \frac{1}{16}g^2) - \nu_{\text{m}}|$. In this region of the modulation frequency, the linear superposition principle fails. When the modulation frequency becomes larger than the bifurcation frequency so that $[1 - (g^3/4a)]^{1/2} \to 1$, we obtain again $\nu_{\text{island}} = |\nu_{\text{s}}(1 - \frac{1}{16}g^2) - \nu_{\text{m}}|$, and the linear superposition principle is again applicable. The island tune for large-amplitude motion about a SFP can be obtained by integrating the equation of motion along the corresponding torus of the Hamiltonian in Eq. (3.86).

D. Separatrix of resonant islands

The Hamiltonian torus that passes through the UFP is the separatrix. With the UFP g_c substitutes into the Hamiltonian (3.86), the separatrix torus is

$$H(J, \psi) = \nu_{\text{s}} \left[\frac{1}{2} x g_c^2 - \frac{1}{64} g_c^4 - \frac{1}{2} a g_c \right], \tag{3.95}$$

where $x = 1 - \nu_{\text{m}}/\nu_{\text{s}}$. The separatrix orbit intersects the phase axis at g_1 and g_2. These intercepts, shown in Figs. 3.6 and 3.7, are useful in determining the maximum phase amplitude of synchrotron motion with external phase modulation. With the notation $h_i = g_i/(4a)^{1/3}$, the intercepts of the separatrix are

$$h_1 = -h_c - \frac{2}{\sqrt{h_c}}, \quad h_2 = -h_c + \frac{2}{\sqrt{h_c}}.$$

The intercepts of the separatrix with the phase axis, h_1 and h_2, and the fixed points, h_a, h_b and h_c are shown in 3.7.

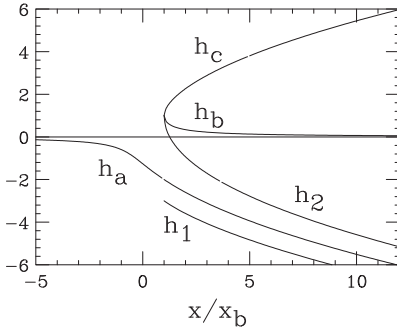[14]M. Ellison *et al.*, *Phys. Rev. Lett.* **70**, 591 (1993).

Figure 3.7: The fixed points in units of $(4a)^{1/3}$ are plotted as a function of the modulation frequency in x/x_{bif}, where $x = 1 - \nu_m/\nu_s$ and $x_{\text{bif}} = \frac{3}{16}(4a)^{2/3}$ with a as the amplitude of the phase modulation. The SFPs are $h_a = g_a/(4a)^{1/3}$ and $h_b = g_b/(4a)^{1/3}$ and the UFP is $h_c = g_c/(4a)^{1/3}$. The intercepts of the separatrix with the phase axis are shown as $h_1 = g_1/(4a)^{1/3}$ and $h_2 = g_2/(4a)^{1/3}$.

III.3   Measurements of Synchrotron Phase Modulation

Here we discuss an example of experimental measurements of rf phase modulation at the IUCF Cooler. The experimental procedure started with a single bunch of about 3×10^8 protons with kinetic energy 45 MeV. The corresponding revolution period was 969 ns with an rf frequency of 1.03148 MHz. The cycle time was 10 s. The injected beam was electron-cooled for about 3 s. The full width at half maximum bunch length was about 5.4 m (or 60 ns). The low-frequency rf system of the IUCF Cooler at $h = 1$ was used in this experiment.

For the longitudinal rf phase shift, the beam was kicked longitudinally by a phase shifter and the data acquisition system was started 2000 turns before the phase kick. The principle of the phase shifter used is as follows. The rf signal from an rf source is split into a 90° phase shifted channel and a non-phase shifted channel. A separate function generator produces two modulating voltages, each proportional to the sine and cosine of the intended phase shift φ_{mod}. As a result of the amplitude modulation, the two rf channels are multiplied by $\sin\varphi_{\text{mod}}$ and $\cos\varphi_{\text{mod}}$ respectively. These two modulated signals were added, using an rf power combiner, resulting in an rf phase shift φ_{mod} in the rf wave. The control voltage versus actual phase shift linearity was experimentally calibrated. Both the phase error due to control nonlinearity and the parasitic amplitude modulation of the IUCF Cooler rf systems were controlled to less than 10%.

The phase lock feedback loop was switched off in our experiment. The response time of the step phase shift was limited primarily by the inertia of the resonant cavity. At 1 MHz, the quality factor Q of the rf cavity was about 40, resulting in a half-power bandwidth of about 25 kHz. The corresponding response time for a step rf phase shift was about 40~50 revolutions. In this experiment, the synchrotron oscillation frequency was chosen to be about 540 Hz, or about 1910 revolutions (turns) in the accelerator. Measurements of subsequent beam-centroid displacements have been discussed in Chap. 3, Sec. II.6.

A. Sinusoidal rf phase modulation

When the bunch, initially at $\phi_i = 0$, $\delta_i = 0$, experiences the rf phase sinusoidal modulation with $\varphi_{\mathrm{mod}} = a \sin \nu_{\mathrm{m}} \theta$, where ν_{m} is the modulation tune and a the modulation amplitude with $a \ll 1$. The synchrotron motion, in terms of a differential equation, is

$$\dot{\phi} = h\eta\delta + \nu_{\mathrm{m}} a \cos \nu_{\mathrm{m}} \theta, \quad \dot{\delta} = \frac{eV}{2\pi\beta^2 E} \sin \phi - \lambda\delta, \tag{3.96}$$

where ϕ is the particle phase angle relative to the modulated rf phase, the overdot indicates the derivative with respect to the variable θ, and λ is the damping decrement due to electron cooling. Thus the synchrotron equation of motion becomes

$$\ddot{\phi} + \frac{2\alpha}{\omega_0}\dot{\phi} + \nu_{\mathrm{s}}^2 \sin \phi = -a\nu_{\mathrm{m}}^2 \sin \nu_{\mathrm{m}}\theta + \frac{2\alpha}{\omega_0}\nu_{\mathrm{m}} a \cos \nu_{\mathrm{m}}\theta. \tag{3.97}$$

The measured damping coefficient α at the IUCF Cooler was $\alpha = \omega_0\lambda/4\pi \approx 3 \pm 1$ s^{-1}. Since the measurement time was typically within 150 ms after the phase kick or the start of rf phase modulation, the effect of electron cooling was not important in these measurements.

The subsequent beam centroid phase-space coordinates are tracked at 10 revolution intervals. The left plots of Fig. 3.8 show examples of measured ϕ and $\mathcal{P} = \frac{h\eta}{\nu_{\mathrm{s}}}\frac{\Delta p}{p}$ vs turn number at 10-turn intervals for an rf phase modulation amplitude of 1.45° after an initial phase kick of 42° at modulation frequencies of 490 Hz (upper) and 520 Hz (lower). The resulting response can be characterized by the beating amplitude and period. The beating period is equal to $T_0/\nu_{\mathrm{island}}$, where T_0 is the revolution period and ν_{island} is the island tune, and the beating amplitude is equal to the maximum intercept of Poincaré surface of section with the phase axis.

B. Action angle derived from measurements

For small-amplitude synchrotron motion, Eq. (3.51) can be used to deduce the action and angle variables, i.e.[15]

$$J = \frac{1}{2}(\phi^2 + \mathcal{P}^2), \qquad \tan\psi = -\frac{\mathcal{P}}{\phi} \tag{3.98}$$

in the $(\phi, \mathcal{P})$ phase space.

For large-amplitude synchrotron motion, we need to use the following procedure to deduce the action-angle variables from the measured synchrotron phase-space coordinates. This procedure can improve the accuracy of data analysis.

---

[15]Note that the action in the (ϕ, δ) phase space is related to the action in the $(\phi, \mathcal{P})$ space by a constant factor $h|\eta|/(\nu_{\mathrm{s}}\sqrt{|\cos\phi_{\mathrm{s}}|})$.
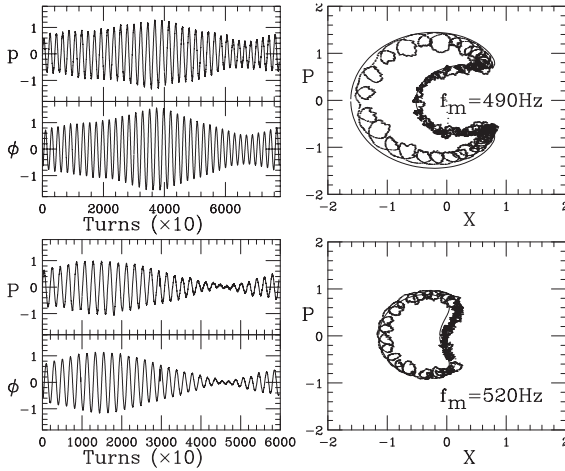
Figure 3.8: Left plots: normalized off-momentum coordinate $\mathcal{P}$ and the phase ϕ vs revolutions at 10-turn intervals. Right plots: the corresponding Poincaré surfaces of section. The upper and lower plots correspond to $f_{\mathrm{m}} = 490$ and 520 Hz respectively. The modulation amplitude was $a = 1.45°$, and the initial phase kick amplitude was $45°$. The solid line shows the Hamiltonian torus of Eq. (3.85).

1. The k value at the phase-space coordinates $(\phi, \mathcal{P})$ is

$$k^2 = \frac{\mathcal{P}^2}{4} + \sin^2\frac{\phi}{2}. \tag{3.99}$$

The action can be obtained from Eq. (3.66) or Eq. (3.67).

2. The synchrotron phase, ψ, can be obtained from the expansion

$$\frac{\mathcal{P}}{2\sin\frac{\phi}{2}} = \frac{\pi}{2K}\tan(\frac{\pi}{2} - \psi) - \frac{2\pi}{K}\sum_{n=1}^{\infty}\frac{q^{2n}}{1+q^{2n}}\sin 2n\psi. \tag{3.100}$$

For synchrotron motion with relatively large k, a better approximation for data analysis can be obtained through polynomial approximation of Eqs. (17.3.34) and (17.3.36) of Ref. [30] to evaluate $K(k), E(k)$ and q functions and obtain J and ψ. For each data point $(\phi, \mathcal{P})$, Eq. (3.99) is used to calculate k, and finally, the action J is obtained from Eq. (3.66). The corresponding angle variable ψ is obtained from Eq. (3.100).

C. Poincaré surface of section

The Poincaré map in the resonance frame is formed by phase-space points in

$$(\sqrt{2J}\cos(\psi - \nu_{\mathrm{m}}\theta), -\sqrt{2J}\sin(\psi - \nu_{\mathrm{m}}\theta)).$$

The resulting invariant tori are shown in the right plots in Fig. 3.8. It becomes clear that the measured response period corresponds to the period of island motion

around a SFP, and the response amplitude is the intercept of the invariant torus with the phase axis. The trajectory of a beam bunch in the presence of external rf phase modulation traces out a torus determined by the initial phase-space coordinates of the bunch. Since the torus, which passes through fixed initial phase-space coordinates, depends on the rf phase modulation frequency, the measured tori depend on the driven frequency. Figure 3.8 shows invariant tori deduced from experimental data. The solid lines are invariant Hamiltonian tori of Eq. (3.86), where the synchrotron frequency was fitted to be about 535 ± 3 Hz.

III.4   Effects of Dipole Field Modulation

Ground motion of quadrupoles and power supply ripple in dipoles can cause dipole field modulation. Equation (2.102) in Chap. 2, Sec. III, shows that the change of path length of a reference orbit is $\Delta C = D_x \theta$, where θ is angular kick resulting from dipole field errors and D_x is the dispersion function. If the dipole field is modulated, the path length and thus the arrival time at rf cavities of particles are also modulated. This effect is equivalent to rf phase modulation, which gives rise to parametric resonances in synchrotron motion. The effect is a special type of "synchro-betatron coupling" that may limit the performance of high energy colliders.

Here we discuss experimental measurements of dipole field modulation at the IUCF Cooler. For this experiment, the harmonic number was $h = 1$, the phase slip factor was $\eta \approx -0.86$, the stable phase angle was $\phi_0 = 0$, and the revolution frequency was $f_0 = 1.03168$ MHz at 45 MeV proton kinetic energy. The rf voltage was chosen to be 41 V to obtain a synchrotron frequency of $f_s = \omega_s/2\pi = 262$ Hz in order to avoid harmonics of the 60 Hz ripple. The synchrotron tune was $\nu_s = \omega_s/\omega_0 = 2.54 \times 10^{-4}$. We chose $\nu_x = 3.828$, $\nu_z = 4.858$ to avoid nonlinear betatron resonances. The corresponding smallest horizontal and vertical betatron sideband frequencies were 177 and 146 kHz respectively.

With horizontal dipole (vertical field) modulation at location s_0, the horizontal closed-orbit deviation is $x_{co}(s, s_0, t) = G(s, s_0)\theta(t)$ (see Chap. 2, Sec. III), where $G(s, s_0)$ is the Green's function, $\theta(t) = \hat{\theta}\sin(\omega_m t + \chi_0)$, $\hat{\theta} = \hat{B}_m \ell / B\rho$, and $\hat{B}_m$ is the peak modulation dipole field. Furthermore, if the dispersion function at the modulating dipole location is not zero, the path length is also modulated. The change in the circumference is

$$\Delta C = D_x \theta(t) = D_x \hat{\theta} \, \sin(\omega_m t + \chi_0), \tag{3.101}$$

where D_x is the dispersion function at the modulation dipole location. The corresponding rf phase difference becomes $\Delta\phi = 2\pi h(\Delta C/C)$, where $C = 86.82$ m is the circumference of the IUCF Cooler. In our experiment, the maximum rf phase shift per turn $\hat{\Delta\phi}$ was $0.78 \times 10^{-5}\hat{B}_m$ radians, where the magnetic field $\hat{B}_m$ is in Gauss.

The longitudinal phase-space coordinates $(\phi, \Delta p/p_0)$ at the nth and $(n + 1)$th revolutions are transformed according to mapping equations:

$$\phi_{n+1} = \phi_n + 2\pi h\eta \left(\frac{\Delta p}{p}\right)_n + \Delta\phi, \tag{3.102}$$

$$\left(\frac{\Delta p}{p}\right)_{n+1} = \left(\frac{\Delta p}{p}\right)_n + \frac{eV}{\beta^2 E}\sin\phi_{n+1} - \lambda\left(\frac{\Delta p}{p}\right)_n, \tag{3.103}$$

where the fractional momentum deviation of particles $(\Delta p/p_0)$ is the conjugate coordinate to synchrotron phase angle ϕ, and λ is the phase-space damping parameter related to electron cooling. Thus the synchrotron equation of motion, in the presence of transverse dipole field modulation, becomes

$$\frac{d^2\phi}{dt^2} + 2\alpha\frac{d\phi}{dt} + \omega_s^2\sin\phi = \omega_m^2 a\cos\omega_m t + 2\alpha\omega_s a\sin\omega_m t, \tag{3.104}$$

where the damping coefficient is $\alpha = \lambda\omega_0/4\pi$. With an electron current of 0.75 A, the damping time for 45 MeV protons was measured to be about 0.33 ± 0.1 s or $\alpha = 3 \pm 1$ s^{-1}, which was indeed small compared with $\omega_s = 1646$ s^{-1}.

Because the synchrotron frequency is much smaller than the revolution frequency in proton storage rings, the phase errors of each turn accumulate. The equivalent phase modulation amplitude is enhanced by a factor $\omega_0/2\pi\omega_m$, i.e. the effective phase modulation amplitude parameter a is

$$a = \frac{h\omega_0 D_x\hat{\theta}}{\omega_m C} = \frac{\omega_0}{2\pi\omega_m}\hat{\Delta}\phi. \tag{3.105}$$

Although the cooling was weak, the transient solution of Eq. (3.104) was damped out by the time of measurement. We therefore measured the steady state solution, in contrast to the experiment discussed in the previous section, where we measured the transient solutions. Let the steady state solution of the nonlinear parametric dissipative resonant system, Eq. (3.104), be

$$\phi \approx g\sin(\omega_m t - \chi), \tag{3.106}$$

where we used the approximation of a single harmonic. Expanding the term $\sin\phi$ in Eq. (3.104) up to the first harmonic, we obtain the equation for the modulation amplitude g and the phase χ as

$$\left[-\omega_m^2 g + 2\omega_s^2 J_1(g)\right]^2 + [2\alpha\omega_m g]^2 = [\omega_m\omega_s a]^2 + [2\alpha\omega_s a]^2 \tag{3.107}$$

$$\chi = \arctan\left[\frac{g\omega_m(\omega_m^2 + 4\alpha^2) - 2\omega_s^2\omega_m J_1(g)}{4\alpha\omega_s^2 J_1(g)}\right], \tag{3.108}$$

where J_1 is the Bessel function [30] of order 1. Steady state solutions of Eq. (3.107) are called *attractors* for the dissipative system. The existence of a unique phase

factor χ for solutions of the dissipative parametric resonant equation implies that the attractor is a single phase-space point rotating at modulation frequency ω_{m}.

When the modulation frequency is below the bifurcation frequency, ω_{bif}, which is given by

$$\frac{\partial \omega_{\mathrm{m}}}{\partial g}\bigg|_{\omega_{\mathrm{m}}=\omega_{\mathrm{bif}}} = 0,$$

Eq. (3.107) has three solutions. A stable solution with a large phase amplitude g_a and phase factor $\chi_a \approx \pi/2$ is the outer attractor. The stable solution at a smaller phase amplitude g_b with $\chi_b \approx -\pi/2$ is the inner attractor. The third solution g_c with $\chi_c \approx -\pi/2$ corresponds to the unstable (hyperbolic) solution, which is associated with the UFP of the effective non-dissipative Hamiltonian. When the damping parameter α is small, these two stable solutions are nearly equal to the SFPs of the effective Hamiltonian, and are almost opposite to each other in the synchrotron phase space, as shown in Fig. 3.6. They rotate about the origin at the modulation frequency [see Eq. (3.106)]. When the damping parameter α is increased, the stable solution (g_a, χ_a) and the unstable solution (g_c, χ_c) approach each other. At a large damping parameter, they collide and disappear, i.e. the outer attractor solution disappears. When the modulation frequency is larger than the bifurcation frequency, only the outer attractor solution exists.

When the modulation frequency is far from the bifurcation frequency, the response amplitude for the inner attractor at $\omega_{\mathrm{m}} \ll \omega_{\mathrm{bif}}$, or for the outer attractor at $\omega_{\mathrm{m}} \gg \omega_{\mathrm{bif}}$, can be approximated by solving the linearized equation (3.107), i.e.

$$g = \left(\frac{(\omega_{\mathrm{m}}\omega_{\mathrm{s}})^2 + (2\alpha\omega_{\mathrm{s}})^2}{(\omega_{\mathrm{s}}^2 - \omega_{\mathrm{m}}^2)^2 + (2\alpha\omega_{\mathrm{m}})^2} \right)^{1/2} a. \tag{3.109}$$

A. Chaotic nature of parametric resonances

In the presence of a weak damping force, *fixed points of the time-averaged Hamiltonian become attractors.* A weak damping force does not destroy the resonance island created by external rf phase modulation. Because of phase-space damping, these fixed points of the Hamiltonian become attractors. Particles in the phase space are damped incoherently toward these attractors, while the attractors rotate about the center of the bucket at the modulation frequency. As the damping force becomes larger, the outer SFP and the UFP may collide and disappear.

Numerical simulations based on Eq. (3.103) were done to demonstrate the coherent and incoherent nature of the single particle dynamics of the parametric resonance system. One of the results is shown in Fig. 3.9, where each black dot corresponds to initial phase-space coordinates that converge toward the outer attractor. Complementary phase-space coordinates converge mostly to the inner attractor except for

a small patch of phase-space coordinates located on the boundary of the separatrix, which will converge toward two attractors located near the separatrix.
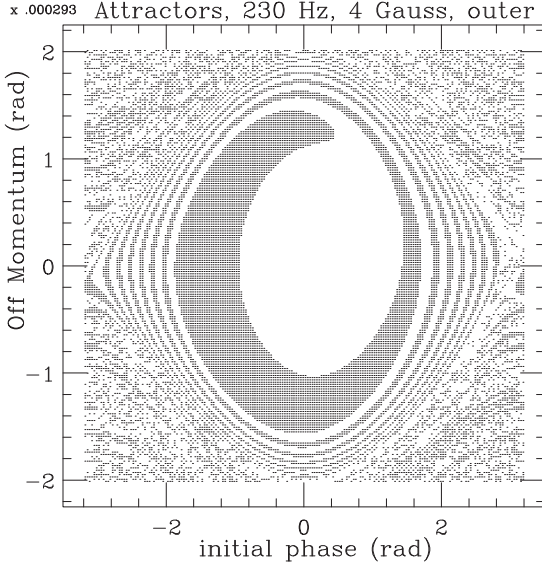

Figure 3.9: Initial normalized phase-space coordinates, obtained from a numerical simulation of Eq. (3.103), which converge to the outer attractor are shown for $\hat{B}_m = 4$ Gauss and $f_m = 230$ Hz. The synchrotron frequency is 262 Hz. The number of phase-space points that converge to the inner or the outer attractors can be used to determine the beamlet intensity.

The basin of attraction for the inner and the outer attractors forms non-intersecting intervolving spiral rings. To which attractor a particle will converge depends sensitively on the initial phase-space coordinates, especially for particles outside the bucket. The orientation of initial phase-space coordinates converging toward the inner or the outer attractor depends on the initial driving phase χ_0 of the dipole field in Eq. (3.101). Numerical simulations indicate that all particles located initially inside the rf bucket will converge either to the inner or to the outer attractor. However, initial phase-space coordinates in a small patch located at the separatrix of the rf bucket converge toward two attractors moving along the separatrix.

B. Observation of attractors

Since the injected beam from the IUCF K200 AVF cyclotron is uniformly distributed in the synchrotron phase space within a momentum spread of about $(\Delta p/p) \approx \pm 3 \times 10^{-4}$, all attractors can be populated. The phase coordinates of these attractors could be measured by observing the longitudinal beam profile from BPM sum signals on an oscilloscope. Figure 3.10 shows the longitudinal beam profile accumulated through many synchrotron periods with modulation field $\hat{B}_m = 4$ G for modulation frequencies of 210, 220, 230, 240, 250, and 260 Hz; it also shows the rf waveform for reference.
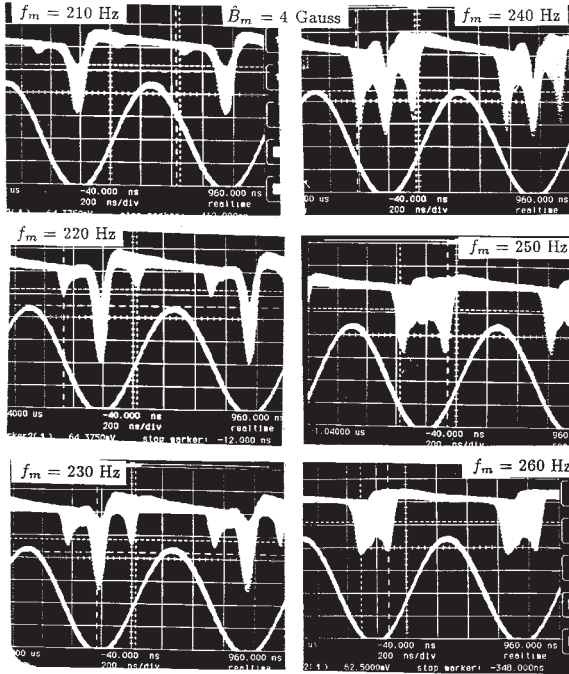
Figure 3.10: Modulation frequencies of left panel: 210, 220, 230 Hz; of right panel: 240, 250, 260 Hz. Synchrotron frequency is 262 Hz. Oscilloscope traces of accumulated BPM sum signals showing the splitting of a beam bunch into beamlets below the bifurcation frequency. The modulation amplitude was $\hat{B}_{\mathrm{m}} = 4$ G. The sine waves are the rf waveform. The relative populations of the inner and outer attractors can be understood qualitatively from numerical simulations of the attractor basin.

It was puzzling at first why the longitudinal profile exhibited gaps in time domain, as if there were no synchrotron motion for the beam bunch located at a relatively large phase amplitude. However, using a fast sampling digital oscilloscope (HP54510A) for a single trace, we found that the beam profile was not made of particles distributed in a ring of large synchrotron amplitude, but was composed of two beamlets. Both beamlets rotated in the synchrotron phase space at the modulating frequency, as measured from the fast Fourier transform (FFT) of the phase signal. If the equilibrium distribution of the beamlet was elongated, then the sum signal, which measured the peak current of the beam, would show a large signal at both extremes of its phase coordinate, where the peak current was large. When the beamlet rotated to the central position in the phase coordinate, the beam profile became flat with a smaller peak current. Therefore the profile observed with the oscilloscope offered an opportunity to study the equilibrium distribution of charges in these attractors.

If we assume an equilibrium elliptical beamlet profile with Gaussian distribution, the current density distribution function becomes

$$\rho(\phi, t) = \frac{\rho_1}{\sqrt{2\pi}\sigma_1} e^{-[\phi - \phi_1(t)]^2 / 2\sigma_1^2} + \frac{\rho_2}{\sqrt{2\pi}\sigma_2} e^{-[\phi - \phi_2(t)]^2 / 2\sigma_2^2}, \qquad (3.110)$$

where ρ_1 and ρ_2 represent the populations of the two beamlets with $\rho_1 + \rho_2 = 1$. Since

each particle in the two beamlets rotates in the phase space at modulating frequency ω_{m}, the parameters $\phi_{1,2}$ and $\sigma_{1,2}$ are

$$\phi_1(t) = g_a \sin(\omega_{\mathrm{m}}t - \chi_a), \quad \phi_2(t) = g_b \sin(\omega_{\mathrm{m}}t - \chi_b),$$

and

$$\sigma_1^2 = \sigma_{10}^2(1 + r_1 \sin^2 \omega_{\mathrm{m}}t), \quad \sigma_2^2 = \sigma_{20}^2(1 + r_2 \sin^2 \omega_{\mathrm{m}}t).$$

Here $g_{a,b}$ and $\chi_{a,b}$ are the amplitudes and phases of the two beamlets, obtained by solving Eqs. (3.107) and (3.108). Since the profile observed on the oscilloscope was obtained by accumulation through many synchrotron periods, it did not depend on the parameters $\chi_{a,b}$, i.e. these profiles were not sensitive to the relative positions of the two beamlets. The eccentricity parameters r_1 and r_2 signify the aspect ratio of the two beamlets, and σ_{10} and σ_{20} represent the average rms bunch length. For example, the aspect ratio, given by $1 : 1 + r_1$ of the outer beamlet at modulation frequency 220 Hz was found to be about 1:3 from the profile in Fig. 3.10. This means that the peak current for the outer beamlet was reduced by a factor of 3 when this beamlet rotated to the center of the phase coordinate. The relative populations of the two beamlets was about 75% for the inner and 25% for the outer, obtained by fitting the data. As the modulating frequency increased toward the synchrotron frequency, the phase amplitude of the outer beamlet became smaller and its population increased. When the modulating frequency was higher than the bifurcation frequency ω_{bif}, the center peak disappeared (see 260 Hz data of Fig. 3.10).

C. The hysteretic phenomena of attractors

The phase amplitudes of attractors shown in Fig. 3.11 also exhibited hysteresis phenomena. When the modulation frequency, which was initially above the bifurcation frequency, was ramped downward, the phase amplitude of the synchrotron oscillations increased along the outer attractor solution. When it reached a frequency far below the bifurcation frequency, the phase amplitude jumped from the outer attractor to the inner attractor solution. On the other hand, if the modulation frequency, originally far below the bifurcation frequency, was ramped up toward the bifurcation frequency, the amplitude of the phase oscillations followed the inner attractor solution. At a modulation frequency near the bifurcation frequency, the amplitude of the synchrotron oscillations jumped from the inner to the outer attractor solution.

The hysteresis depended on beam current and modulation amplitude a. Since a large damping parameter could destroy the outer attractor, the hysteresis depended also on the dissipative force. The observed phase amplitudes were found to agree well with the solutions of Eq. (3.107). Similar hysteretic phenomena have been observed in electron-positron colliders, related to beam-beam interactions, where the amplitudes

of the coherent π-mode oscillations showed hysteretic phenomena.[16] At a large beam-beam tune shift, the vertical beam size exhibited a flip-flop effect with respect to the relative horizontal displacement of two colliding beams.[17]

D. Systematic property of parametric resonances

The formalism discussed so far seems complicated by the transformation of phase-space coordinates into action-angle variables. However, the essential physics is rather simple. In this section, we will show that the global property of parametric resonances can be understood simply from Hamiltonian dynamics.

The circles in Fig. 3.11 show a compilation of beamlet phase amplitude vs modulation frequency for four different experimental phase modulation amplitudes. The solid lines show the synchrotron tune and its third harmonic. We note that the bifurcation of the 1:1 resonance islands follows the tune of the *unperturbed* Hamiltonian system, and the measured third order 3:1 resonance islands fall on the curve of the third harmonic of the synchrotron tune. The sideband around the first order synchrotron tune corresponds to the 60 Hz power supply ripple. Because the rf phase modulation does not excite 2:1 resonance, we did not find parametric resonances at the second synchrotron harmonic.
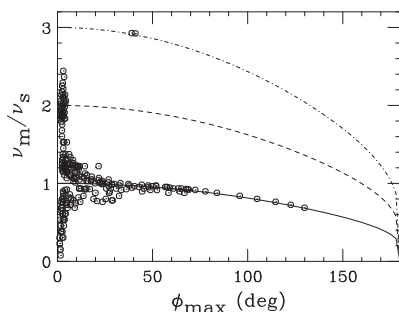

Figure 3.11: The phase amplitudes of beamlets excited by rf phase modulation, measured from the oscilloscope trace, are compared with the theoretical synchrotron tune. The bifurcation of the resonance islands follows the unperturbed tune of the synchrotron Hamiltonian, shown as the lower solid line (see also Fig. 3.6 on the bifurcation of 1:1 parametric resonance). The third order resonance island falls also on the third harmonic of the synchrotron tune.

When an external time dependence perturbation is applied to a Hamiltonian system, the perturbed Hamiltonian contains a perturbing term similar to that in Eq. (3.83). On the basis of the Kolmogorov-Arnold-Moser (KAM) theorem, many Hamiltonian tori are mildly perturbed and survived, while some tori encountering resonance condition are destroyed. Thus the external perturbation excites only particles locally in the phase space where the amplitude dependent synchrotron tune falls exactly at the modulation tune, where the particle motion can be described by the

[16]See T. Ieiri and K. Hirata, *Proc. 1989 Part. Accel. Conf.* p. 926 (IEEE, New York, 1989).
[17]See M.H.R. Donald and J.M. Paterson, *IEEE Trans. Nucl. Sci.* **NS-26**, 3580 (1979); G.P. Jackson and R.H. Siemann, *Proc. 1987 Part. Accel. Conf.* p. 1011 (IEEE, New York, 1987).

effective parametric resonance Hamiltonian (3.84).[18] The size of a resonance island
depends on the slope of tune vs amplitude, strength function $g_n(J)$, and amplitude
of perturbation.

In fact, the external perturbation creates a local minimum in the potential energy
at the SFP locations. When a weak damping force is applied to the dynamical system,
the SFP becomes an attractor, and the local potential well becomes the basin for
stable particle motion. Thus a beam inside an rf bucket can split into beamlets.

When the modulation frequency is varied, SFPs (attractors) are formed along the
tune of the unperturbed Hamiltonian, i.e.

$$\nu_{\mathrm{m}} = n\tilde{Q}_{\mathrm{s}}(J_{\mathrm{SFP}}). \tag{3.111}$$

The measurement of attractor amplitude vs modulation tune is equivalent to the mea-
surement of synchrotron tune vs synchrotron amplitude, as clearly seen in Fig. 3.11.
Since the rf phase modulation does not excite even synchrotron harmonics, we do
not observe a 2:1 attractor in Fig. 3.11. If, however, a stronger phase modulation is
applied to the dynamical system, a 2:1-like (4:2) parametric resonance can be formed
by 1:1 and 3:1 resonances through second order perturbation.

An important implication of the above parametric excitation theorem is that chaos
at the separatrix orbit is induced by overlapping parametric resonances. This can be
understood as follows. Let $Q(J)$ be the tune of a dynamical system, where the tune
is zero at the separatrix, i.e. $Q(J_{\mathrm{sx}}) = 0$. Now a time dependent perturbation can
induce a series of parametric resonances in the perturbed Hamiltonian. These para-
metric resonances, located at $nQ(J)$ with integer n, can be excited by time dependent
perturbation. Since $nQ(J_{\mathrm{sx}}) \approx 0$ for all n near the separatrix, a perturbation with low
frequency modulation can produce many overlapping parametric resonances near the
separatrix and lead to local chaos. This result can be applied to synchrotron motion
as well as to betatron motion, where higher order nonlinear resonances serve as the
source of time dependent modulation.

Now, we apply this result to evaluate the effect of low frequency modulations on
particle motion. If the amplitude of low frequency modulation is not large, it will
induce overlapping parametric resonances only near the separatrix. If the beam size
is relatively small, the stochasticity at the separatrix will do little harm to the beam
motion. However, when the modulation frequency approaches the tune of particles at
the center of the bucket, particle orbits near the center of the bucket will be strongly
perturbed, forming islands within the bucket.

In reality, the perturbation arising from wakefields, rf phase error, dipole field
error, ground vibration, etc., consists of a spectrum of frequency distributions. The

---

[18]The remaining terms play the role of time dependent perturbations to the effective Hamiltonian
of Eq. (3.84). Based on KAM theorem, many higher order resonance islands exist within each
parametric resonance island.

mean field of the perturbation gives rise to the effect called potential well distortion, which, solved self-consistently in the Vlasov equation, modifies the unperturbed tune of the system. The remaining time dependent perturbation can generate further bunch deformation, bunch splitting, hysteresis, etc., depending on its frequency spectrum. The complicated collective instability phenomenon is in fact closely related to nonlinear beam dynamics. A series of *beam transfer function* measurements were made at electron storage rings. Sweeping the rf phase modulation frequency and measuring the response by measuring either the centroid of the beam, or the beam profile from a synchrotron light monitor using a streak camera, the response of the beam to external rf phase modulation can be obtained.[19]

III.5   RF Voltage Modulation

The beam lifetime limitation due to rf noise has been observed in many synchrotrons, e.g., the super proton synchrotron (SPS) in CERN.[20] There has been some interest in employing rf voltage modulation to induce super slow extraction through a bent crystal for very high energy beams,[21] rf voltage modulation to stabilize collective beam instabilities, rf voltage modulation for extracting beam with a short bunch length, etc. Since the rf voltage modulation may be used for enhancing a desired beam quality, we will study the physics of synchrotron motion with rf voltage modulation, that may arise from rf noise, power supply ripple, wakefields, etc. Beam response to externally applied rf voltage modulation has been measured at the IUCF Cooler.[22]

A. The equation of motion with rf voltage modulation

In the presence of rf voltage modulation, the synchrotron equations of motion are

$$\phi_{n+1} = \phi_n - 2\pi\nu_s \frac{\eta}{|\eta|}\mathcal{P}_n, \tag{3.112}$$

$$\mathcal{P}_{n+1} = \mathcal{P}_n - 2\pi\nu_s[1 + b\sin(\nu_m\theta_{n+1} + \chi)]\sin\phi_{n+1} - \frac{4\pi\alpha}{\omega_0}\mathcal{P}_n, \tag{3.113}$$

where $\mathcal{P} = -h|\eta|\delta/\nu_s$ is the normalized off-momentum coordinate conjugate to ϕ; $\delta = \Delta p/p_0$ is the fractional momentum deviation from the synchronous particle; η is the phase slip factor; $\nu_s = \sqrt{h|\eta|eV/2\pi\beta^2 E_0}$ is the synchrotron tune at zero

[19]See e.g. M.H. Wang, *et al.*, *Proc. 1997 Part. Accel. Conf.* (1997); J. Byrd, *ibid.* (1997); M.G. Minty *et al.*, *ibid.* (1997); D. Rice, private communications.

[20]D. Boussard, *et al.*, *IEEE Trans. Nucl. Sci.* **NS-26**, 3484 (1979); D. Boussard, *et al.*, *Proc. 11th Int. Conf. on High Energy Accelerators*, p. 620 (Birkhauser, Basel, 1980); G. Dôme, CERN **87-03**, p. 370 (1987); S. Krinsky and J.M. Wang, *Part. Accel.* **12**, 107 (1982).

[21]H.J. Shih and A.M. Taratin, SSCL-389 (1991); W. Gabella, J. Rosenzweig, R. Kick, and S. Peggs, *Part. Accel.* **42**, 235 (1993).

[22]D. Li *et al.*, *Phys. Rev.* E **48**, R1638 (1993); D.D. Caussyn *et al.*, *Proc. Part. Acc. Conf.* p. 29 (IEEE, Piscataway, NJ, 1993); D. Li *et al.*, *Nucl. Instrum. Methods* A **364**, 205 (1995).

amplitude; E_0 is the beam energy; $b = \Delta V/V$ is the fractional rf voltage modulation strength ($b > 0$); ν_{m} is the rf voltage modulation tune; χ is a phase factor; θ is the orbital angle used as time variable; $\omega_0 = 2\pi f_0$ is the angular revolution frequency; and α is the phase-space damping factor resulting from phase-space cooling.

At the IUCF Cooler, the phase-space damping rate was measured to be about $\alpha \approx 3.0 \pm 1.0$ s^{-1}, which is much smaller than $\omega_0\nu_{\mathrm{s}}$, typically about 1500 s^{-1} for the $h = 1$ harmonic system. Without loss of generality, we discuss the case for a particle energy below the transition energy, i.e. $\eta < 0$.

Neglecting the damping term, i.e. $\alpha = 0$, the equation of motion for phase variable ϕ is

$$\ddot{\phi} + \nu_{\mathrm{s}}^2[1 + b\sin(\nu_{\mathrm{m}}\theta + \chi)]\sin\phi = 0, \tag{3.114}$$

where the overdot indicates the time derivative with respect to θ. In linear approximation with $\sin\phi \approx \phi$, Eq. (3.114) reduces to Mathieu equation. By choosing $\chi = -\pi/2$ and $z = \frac{1}{2}\nu_{\mathrm{m}}\theta$, $p = 4\nu_{\mathrm{s}}^2/\nu_{\mathrm{m}}^2$, and $q = 2b\nu_{\mathrm{s}}^2/\nu_{\mathrm{m}}^2$, we can linearize Eq. (3.114) into Mathieu's equation [30]

$$\frac{d^2\phi}{dz^2} + (p - 2q\cos 2z)\phi = 0. \tag{3.115}$$

In accelerator physics applications, p and q are real with $q \ll 1$. The stable solutions of Mathieu's equation are obtained with the condition that the parameter p is bounded by the characteristic roots $a_r(q)$ and $b_{r+1}(q)$, where $r = 0, 1, 2, \cdots$. In other words, unstable solutions are in the region $b_r(q) \leq p \leq a_r(q)$, where $r = 1, 2, \cdots$. The first order unstable region and the second order unstable region respectively

$$2\nu_{\mathrm{s}}(1 - \frac{1}{4}b) \leq \nu_{\mathrm{m}} \leq 2\nu_{\mathrm{s}}(1 + \frac{1}{4}b). \tag{3.116}$$

$$\nu_{\mathrm{s}}(1 - \frac{5}{24}b^2) \leq \nu_{\mathrm{m}} \leq \nu_{\mathrm{s}}(1 + \frac{1}{24}b^2),$$

which can be obtained from the second order perturbation theory.[23] The width of the instability decreases rapidly with increasing order for small b. In our application, we need to consider only the lowest order Mathieu instability. Since synchrotron motion is nonlinear, the linear Mathieu instability analysis can be extended to nonlinear synchrotron motion as follows.

B. The perturbed Hamiltonian

The synchrotron equation of motion with rf voltage modulation can be derived from the Hamiltonian $H = H_0 + H_1$ with

$$H_0 = \frac{1}{2}\nu_{\mathrm{s}}\mathcal{P}^2 + \nu_{\mathrm{s}}(1 - \cos\phi), \tag{3.117}$$

$$H_1 = \nu_{\mathrm{s}}b\,\sin(\nu_{\mathrm{m}}\theta + \chi)\,[1 - \cos\phi], \tag{3.118}$$

[23]L.D. Landau and E.M. Lifschitz, *Mechanics*, 3rd. ed. (Pergamon Press, Oxford, 1976).

where H_0 is the unperturbed Hamiltonian and H_1 the perturbation. For a weakly perturbed Hamiltonian system, we expand H_1 in action-angle coordinates of the unperturbed Hamiltonian

$$H_1 = \nu_\mathrm{s} b \sum_{n=-\infty}^{\infty} |G_n(J)| \ \sin(\nu_\mathrm{m}\theta - n\psi - \gamma_n), \tag{3.119}$$

where we choose $\chi = 0$ for simplicity, and $|G_n(J)|$ is the Fourier amplitude of the factor $(1 - \cos\phi)$ with γ_n its phase, defined in Eq. (3.76).

Since $(1 - \cos\phi)$ is an even function of ψ in $[-\pi, \pi]$, the Fourier integral for G_n from Eq. (3.76) is zero except for n even with $G_{-n} = G_n^*$. Thus rf voltage modulation generates only even-order synchrotron harmonics in H_1. Expanding $G_n(J)$ in power series, we obtain

$$G_0 \approx \frac{1}{2}J + \frac{1}{2048}J^3 + \cdots \quad \Longrightarrow \quad \Delta\tilde{Q}_\mathrm{s} \approx \frac{1}{2}\nu_\mathrm{s}b\sin\nu_\mathrm{m}\theta.$$

$$G_2 \approx -\frac{1}{4}J + \frac{1}{128}J^2 + \cdots, \quad G_4 \approx -\frac{1}{64}J^2 + \frac{1}{2048}J^3 + \cdots, \quad G_6 \approx \frac{3}{4096}J^3 + \cdots.$$

Note that the $G_0(J)$ term in the perturbation contributes to synchrotron tune modulation ΔQ_s.

C. Parametric resonances

When the modulation frequency is near an even harmonic of the synchrotron frequency, i.e. $\nu_\mathrm{m} \approx nQ_\mathrm{s}$ ($n = $ even integers), particle motion can be coherently perturbed by the rf voltage modulation resulting from a resonance driving term (stationary phase condition). The resonances, induced by the external harmonic modulation of the rf voltage, are called parametric resonances. Using the generating function

$$F_2 = (\psi - \frac{\nu_\mathrm{m}}{n}\theta + \frac{\gamma_n}{n} + \frac{\pi}{2n})\tilde{J},$$

we obtain the Hamiltonian in a resonance rotating frame as

$$\tilde{H} = E(\tilde{J}) - \frac{\nu_\mathrm{m}}{n}\tilde{J} + \nu_\mathrm{s}b|G_n(\tilde{J})|\cos n\tilde{\psi} + \Delta\tilde{H}(\tilde{J}, \tilde{\psi}, \theta), \tag{3.120}$$

where the remaining small time dependent perturbation term ΔH oscillates at frequencies $\nu_\mathrm{m}, 2\nu_\mathrm{m}, \cdots$. In the time average, we have $\langle\Delta\tilde{H}\rangle \approx 0$. Thus the time averaged Hamiltonian $\langle\tilde{H}\rangle$ for the nth order parametric resonance becomes

$$\langle\tilde{H}\rangle = E(\tilde{J}) - \frac{\nu_\mathrm{m}}{n}\tilde{J} + \nu_\mathrm{s}b|G_n(\tilde{J})|\cos n\tilde{\psi}. \tag{3.121}$$

The phase-space contour may be strongly perturbed by a parametric resonance. Since $|G_{n+2}/G_n| \sim J$ for $n > 0$, the resonance strength is greatest at the lowest harmonic for particles with small phase amplitude. The system is most sensitive to the rf voltage modulation at the second synchrotron harmonic.

D. Quadrupole mode

When the rf voltage modulation frequency is near the second harmonic of synchrotron frequency, particle motion is governed by the $n = 2$ parametric resonance Hamiltonian

$$\langle \tilde{H} \rangle = (\nu_{\mathrm{s}} - \frac{\nu_{\mathrm{m}}}{2})\tilde{J} - \frac{\nu_{\mathrm{s}}}{16}\tilde{J}^2 + \frac{\nu_{\mathrm{s}}}{4}b\tilde{J}\cos 2\tilde{\psi} \qquad (3.122)$$

in the resonance rotating frame. Since the Hamiltonian (3.122) is autonomous, Hamiltonian is a constant of motion. For simplicity, we drop the tilde notations. Hamilton's equations are

$$\dot{J} = \frac{\nu_{\mathrm{s}}}{2}bJ\sin 2\psi, \qquad (3.123)$$

$$\dot{\psi} = \nu_{\mathrm{s}} - \frac{\nu_{\mathrm{m}}}{2} - \frac{\nu_{\mathrm{s}}}{8}J + \frac{\nu_{\mathrm{s}}}{4}b\cos 2\psi. \qquad (3.124)$$

The fixed points that determine the locations of islands and separatrix of the Hamiltonian are obtained from $\dot{J} = 0$, $\dot{\psi} = 0$. The stable fixed points (SFPs) ($\psi = 0$ and π) and the unstable fixed points (UFPs) ($\psi = \pi/2$ and $3\pi/2$) are

$$J_{\mathrm{SFP}} = \begin{cases} 8(1 - \frac{\nu_{\mathrm{m}}}{2\nu_{\mathrm{s}}}) + 2b, & \text{if } \nu_{\mathrm{m}} \leq 2\nu_{\mathrm{s}} + \frac{1}{2}b\nu_{\mathrm{s}} \\ 0, & \text{if } \nu_{\mathrm{m}} > 2\nu_{\mathrm{s}} + \frac{1}{2}b\nu_{\mathrm{s}} \end{cases} \qquad (3.125)$$

$$J_{\mathrm{UFP}} = \begin{cases} 8(1 - \frac{\nu_{\mathrm{m}}}{2\nu_{\mathrm{s}}}) - 2b, & \text{if } \nu_{\mathrm{m}} \leq 2\nu_{\mathrm{s}} - \frac{1}{2}b\nu_{\mathrm{s}} \\ 0, & \text{if } 2\nu_{\mathrm{s}} - \frac{1}{2}b\nu_{\mathrm{s}} \leq \nu_{\mathrm{m}} \leq 2\nu_{\mathrm{s}} + \frac{1}{2}b\nu_{\mathrm{s}} \end{cases} \qquad (3.126)$$

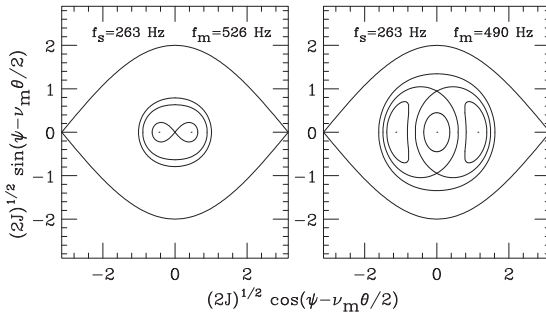Examples of Hamiltonian Tori around SFPs are shown in Fig. 3.12.

Figure 3.12: The separatrix and tori of the Hamiltonian (3.122) in the resonance rotating frame. The synchrotron frequency is $f_{\mathrm{s}} = 263$ Hz, the voltage modulation amplitude is $b = 0.05$, and the modulation frequencies are $f_{\mathrm{m}} = 526$ Hz (left plot) and $f_{\mathrm{m}} = 490$ Hz (right plot).

We note that the second harmonic rf voltage modulation can induce an instability at $J_{\mathrm{UFP}} = 0$ in the frequency domain $2\nu_{\mathrm{s}} - \frac{1}{2}b\nu_{\mathrm{s}} \leq \nu_{\mathrm{m}} \leq 2\nu_{\mathrm{s}} + \frac{1}{2}b\nu_{\mathrm{s}}$. This is the first order Mathieu resonance of Eq. (3.116). Nonlinear synchrotron motion extends the instability to lower modulation frequency at larger synchrotron amplitude, according to

$$\nu_{\mathrm{m}} = 2\nu_{\mathrm{s}}(1 - \frac{J_{\mathrm{UFP}}}{8}) - \frac{1}{2}\nu_{\mathrm{s}}b, \qquad (3.127)$$

which is a nonlinear extension of Mathieu instability.

Modulation of rf voltage at the second harmonic of the synchrotron tune had been found useful in damping the multi-bunch instabilities for the damping ring at the Stanford linear collider (SLC), and stabilizing coupled bunch instabilities induced by parasitic rf cavity modes with high brightness beams at the Taiwan Light Source.[24] By adjusting the amplitude and phase of the rf voltage modulation, the collective instability of high brightness electron beams in the SLC damping ring can be controlled. The damping mechanism may be understood as follows. When the voltage modulation at $\nu_\mathrm{m} = 2\nu_\mathrm{s}$ is applied, the Mathieu resonance gives rise to an UFP at the origin of the phase space and the SFP is displaced to $J_\mathrm{SFP} = 2b$. Since electrons are damped incoherently into the SFP by the synchrotron radiation damping, the beam distribution becomes dumbbell-shaped in phase space, rotating in the longitudinal phase space at half the modulation frequency, i.e. the synchrotron frequency. The size and orientation of the dumbbell can be controlled by parameter b and phase χ.

E. The separatrix

The separatrix torus, which passes through the UFPs, is given by

$$H(J, \psi) = H(J_\mathrm{UFP}, \psi_\mathrm{UFP}). \tag{3.128}$$

The separatrix intersects the phase axis at the actions J_1 and J_2 given by

$$J_1 = \begin{cases} J_\mathrm{SFP} + \sqrt{J_\mathrm{SFP}^2 - J_\mathrm{UFP}^2} & \text{if } \nu_\mathrm{m} \leq 2\nu_\mathrm{s} - \frac{1}{2}b\nu_\mathrm{s} \\ 2J_\mathrm{SFP} & \text{if } 2\nu_\mathrm{s} - \frac{1}{2}b\nu_\mathrm{s} \leq \nu_\mathrm{m} \leq 2\nu_\mathrm{s} + \frac{1}{2}b\nu_\mathrm{s} \end{cases} \tag{3.129}$$

and

$$J_2 = \begin{cases} J_\mathrm{SFP} - \sqrt{J_\mathrm{SFP}^2 - J_\mathrm{UFP}^2} & \text{if } \nu_\mathrm{m} \leq 2\nu_\mathrm{s} - \frac{1}{2}b\nu_\mathrm{s} \\ 0 & \text{if } 2\nu_\mathrm{s} - \frac{1}{2}b\nu_\mathrm{s} \leq \nu_\mathrm{m} \leq 2\nu_\mathrm{s} + \frac{1}{2}b\nu_\mathrm{s}. \end{cases} \tag{3.130}$$

The intercepts can be used to determine the maximum synchrotron phase oscillation due to rf voltage modulation. Figure 3.12 shows also the intercepts of separatrix with phase axis. The island size $\Delta\phi_\mathrm{island}$ is $\sqrt{2J_1} - \sqrt{2J_2}$.

F. The amplitude dependent island tune of 2:1 parametric resonance

For an autonomous dynamical system governed by the Hamiltonian (3.122), the Hamiltonian is a constant of motion. The Hamiltonian value is $E_\mathrm{s} = \frac{1}{16}\nu_\mathrm{s}J_\mathrm{SFP}^2$ at SFP, and $E_\mathrm{u} = \frac{1}{16}\nu_\mathrm{s}J_\mathrm{UFP}^2$ at UFP. Using Hamilton's equations of motion, we obtain $\dot{J} = f(J, E)$, where

$$f(J, E) = 2\nu_\mathrm{s}\sqrt{\left[\frac{J^2}{16} + \frac{E}{\nu_\mathrm{s}} - (1 - \frac{\nu_\mathrm{m}}{2\nu_\mathrm{s}} - \frac{b}{4})J\right]\left[(1 - \frac{\nu_\mathrm{m}}{2\nu_\mathrm{s}} + \frac{b}{4})J - \frac{E}{\nu_\mathrm{s}} - \frac{J^2}{16}\right]}. \tag{3.131}$$

---

[24]M.H. Wang, and S.Y. Lee, *Journal of Applied Physics*, **92**, 555 (2002); J.D. Fox and P. Corredoura, *Proc. European Part. Accel. Conf.* p. 1079 (Springer-Verlag, Heidelberg, 1992).

For a given Hamiltonian value E, the action J is limited by $J_{\min}$ and $J_{\max}$ given by

$$J_{\min} = (1 - \sqrt{1-x})J_{\text{SFP}}, \quad J_{\max} = (1 + \sqrt{1-x})J_{\text{SFP}},$$

where $x = E/E_s$, with $x \in [J_{\text{UFP}}^2/J_{\text{SFP}}^2\,, 1]$. Note that $J_{\text{SFP}} = \frac{1}{2}(J_{\min} + J_{\max})$. The island tune becomes

$$Q_{\text{island}} = \frac{2\pi}{\oint d\theta} = 2\pi \left[\oint \frac{dJ}{f(J,E)} \right]^{-1} = \frac{\pi\nu_s\sqrt{2bJ_{\text{SFP}}}}{8K(k)}x^{1/4}, \qquad (3.132)$$

$$k = \frac{1}{\sqrt{2}}\sqrt{1 - \frac{xJ_{\text{SFP}} - J_{\text{UFP}}}{\sqrt{x}(J_{\text{SFP}} - J_{\text{UFP}})}},$$

where $K(k)$ is the complete elliptical integral of the first kind [30]. At $x = 1$, the island tune becomes $\nu_s\sqrt{bJ_{\text{SFP}}/8}$. At the separatrix with $x = J_{\text{UFP}}^2/J_{\text{SFP}}^2$, the island tune is zero.

III.6   Measurement of RF Voltage Modulation

We describe here an rf voltage modulation measurement at the IUCF Cooler. The experiment started with a single bunch of about 5×10^8 protons with kinetic energy 45 MeV. The cycle time was 10 s, with the injected beam electron-cooled for about 3 s, producing a full width at half maximum bunch length of about 9 m (or 100 ns) depending on rf voltage. The low frequency rf system used in the experiment was operating at harmonic number $h = 1$ with frequency 1.03168 MHz.

A. Voltage modulation control loop

The voltage control feedback of the IUCF Cooler rf system works as follows. The cavity rf voltage is picked up and rectified into DC via synchronous detection. The rectified DC signal is compared to a preset voltage. The error found goes through a nearly ideal integrator that has very high DC gain. The integrated signal is then used to control an attenuator regulating the level of rf signal being fed to rf amplifiers. Because of the relatively low Q of the cavity at the IUCF Cooler, the effect of its inertia can be ignored if the loop gain is rolled off to unity well before $f_0/2Q$, where f_0 is the resonant frequency of the rf cavity and $Q \approx 50$ is the cavity Q value. Thus, no proportional error feedback is needed to stabilize the loop. The overall loop response exhibits the exponential behavior prescribed by a first order differential equation, i.e. $dV/dt = -V/\tau$, where V is the rf voltage and the characteristic relaxation time τ is about $10 - 200\ \mu$ s.

The amplitude modulation is summed with the reference and compared to the cavity sample signal. The modulation causes a change in the error voltage sensed by the control loop and results in modulation of the attenuator around a preset cavity

voltage. The maximum modulation rate is limited by the loop response time of about 10 kHz. The modulation rates in our experiments are well within this limit. The modulation amplitude was measured and calibrated.
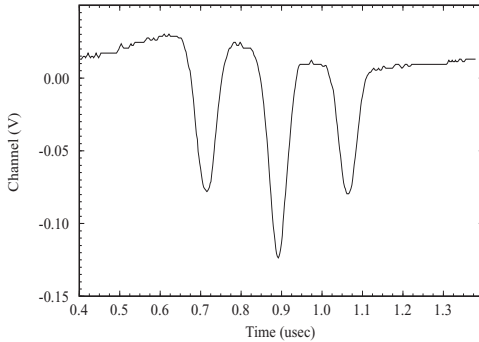

Figure 3.13: The beam bunch was observed to split into three beamlets in a single rf bucket measured from a fast sampling scope in (μs). The voltage modulation amplitude is $b = 0.05$ at modulation frequency $f_m = 480$ Hz with synchrotron tune $f_s = 263$ Hz. Note that the outer two beamlets rotated around the center beamlet at a frequency equal to half the modulation frequency.

B. Observations of the island structure

Knowing that the beam bunch will be split into beamlets, as shown in Sec. III.2, we first measured the phase oscillation amplitude of the steady state solution by using the oscilloscope. The beam was injected, the rf voltage was modulated, and the beam was cooled with electron current 0.75 A. Then the steady state bunch distribution was measured. Figure 3.13 shows that the sum signals from a beam position monitor (BPM) on a fast oscilloscope triggered at the rf frequency exhibited two peaks around a central peak. A fast 1×10^9 sample per second oscilloscope was used to measure the profile of the beam in a single pass. The profile shown in Fig. 3.13 indicated that there were three beamlets in the $h = 1$ rf bucket. The beam particles were damped to attractors of the dissipative parametric resonant system. Thus the phase amplitude of the outer peaks measured from the oscilloscope can be identified as the phase amplitude of the SFP.

Since the attractors (or islands) rotate around the origin of the rf bucket with half the modulation frequency, the observed beam profile in an oscilloscope is a time average of the BPM sum signal. Because the equilibrium beamlet distribution in a resonance island has a large aspect ratio in the local phase-space coordinates, the resulting beam profile will exhibit two peaks at the maximum phase amplitude, resembling that in Fig. 3.13. This implies that when a beamlet rotates to the upright position in the phase coordinate, a larger peak current can be observed. On the other hand, when a beamlet rotates to the flat position, where the SFPs are located on the $\mathcal{P}$ axis, the aspect ratio becomes small and the line density is also small.

The measured action J of the outer beamlets as a function of modulation frequency is shown in Fig. 3.14, where J_{SFP} of the Hamiltonian (3.122) is also shown
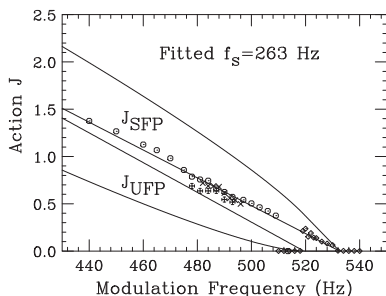
Figure 3.14: The measured action J of outer beamlets as a function of modulation frequency. Here $J \approx \frac{1}{2}\hat{\phi}^2$ with $\hat{\phi}$ as the peak phase amplitude of attractors. Different symbols correspond to measurements at different times for an almost identical rf voltage. The solid line for J_{SFP} obtained from Eq. (3.125) fits data with $f_s = 263$ Hz. The actions of UFP J_{UFP} and intercepts J_1 and J_2 of the separatrix with the phase axis are also shown.

for comparison. Experimentally, we found that the action of the outer attractor varied linearly with modulation frequency. Similarly, J_{SFP} is also a linear function of modulation frequency, where the slope depends sensitively on synchrotron frequency. Using this sensitivity, the synchrotron frequency was determined more accurately to be about 263 ± 1 Hz for this run. Our experimental results agreed well with the theoretical prediction except in the region $f_{\mathrm{m}} \in [510, 520]$ Hz, where we did not observe beam splitting. A possible explanation is that the actual beam size was larger than the separation of islands. In this case, the SFPs were about 100 ns from the center of the bucket. Once f_{m} reached $2f_{\mathrm{s}} - \frac{1}{2}bf_{\mathrm{s}} \approx 520$ Hz, where $J_{\mathrm{UFP}} = 0$, the beam was observed to split into only two beamlets. It was also clearly observed that all parametric resonance islands ceased to exist at $f_{\mathrm{m}} = 2f_{\mathrm{s}} + \frac{1}{2}bf_{\mathrm{s}} \approx 532$ Hz.

Exercise 3.3

1. Prove the identity of the action integral in Eq. (3.66).

2. We consider a general Hamiltonian

$$H = \frac{1}{2}\nu_{\mathrm{s}}\mathcal{P}^2 + V(\phi),$$

    where $(\phi, \mathcal{P})$ are conjugate phase-space variables with orbiting angle θ as time variable, ν_{s} is the small amplitude synchrotron tune, and $V(\phi)$ is the potential.[25] The action is $J = (1/2\pi) \oint \mathcal{P}d\phi$. Using the generating function

$$F_2 = \int_0^\phi \mathcal{P}d\phi,$$

    show that the coordinate transformation between phase variable ψ and coordinate ϕ is

$$d\psi = \frac{Q(J)}{\nu_{\mathrm{s}}}d\phi,$$

---

[25]In linear approximation, the potential can be expressed as $V(\phi) = \frac{1}{2}\nu_{\mathrm{s}}\phi^2 + \cdots$. However, small amplitude behavior of the potential is not a necessary condition for the sum rule theorem stated in this exercise.

where ψ is the conjugate phase variable to the action J. Expanding $\mathcal{P}$ in action-angle variables with

$$\mathcal{P} = \sum_{n=-\infty}^{\infty} f_n e^{in\psi},$$

prove the sum rule theorem

$$\sum_{n=-\infty}^{\infty} |f_n|^2 = \frac{Q(J)}{\nu_s} J.$$

3. From Exercise 2.4.8, we find that the change of orbit length due to a modulating dipole kicker is given by

$$\Delta C = D(s_0)\,\theta(t) = D(s_0)\,\hat{\theta}\,\sin(\omega_m t + \chi_0),$$

where $D(s_0)$ is the dispersion function at the dipole location, $\hat{\theta}$ is the maximum dipole kick angle, ω_m is the modulating angular frequency, and χ_0 is an arbitrary initial phase. The modulating tune is $\nu_m = \omega_m/\omega_0$, where ω_0 is the angular revolution frequency.

(a) Show that the modulating dipole field produces an equivalent rf phase error

$$\Delta\phi = \frac{2\pi h D(s_0)\hat{\theta}}{C}\,\sin(\omega_m t + \chi_0) = \hat{\Delta\phi}\sin(\omega_m t + \chi_0),$$

where C is the circumference of the synchrotron, and h is the harmonic number.

(b) Show that the amplitude of the equivalent rf wave phase error is

$$a = \hat{\Delta\phi}/2\pi\nu_m.$$

Give a physical argument that the amplitude of the equivalent rf wave phase error a is amplified as the modulation tune ν_m becomes smaller.

(c) Evaluate the effective rf modulation amplitude a for the accelerators listed in the table below, where C is the circumference, $\Delta B\ell$ is the integrated dipole field error, f_{mod} is the modulation frequency, D is the dispersion function at the dipole, γ is the Lorentz relativistic factor, and h is the harmonic number.

	IUCF Cooler	RHIC	MI	Recycler
C (m)	86.8	3833.8	3319.4	3319.4
$\Delta B\ell$ (Gm)	1	1	1	1
f_{mod} (Hz)	262	60	60	4
D (m)	4	1	1	1
γ	1.04796	24	21.8	9.5
h	1	342	588	1
a				

4. Using the conjugate phase space coordinates

$$Q = \sqrt{2J}\cos(\psi - \tfrac{1}{2}\nu_{\mathrm{m}}\theta), \qquad P = -\sqrt{2J}\sin(\psi - \tfrac{1}{2}\nu_{\mathrm{m}}\theta),$$

show that the Hamiltonian (3.122) for the quadrupole mode is

$$H = \frac{1}{2}(\delta + \frac{\nu_{\mathrm{s}}b}{4})Q^2 + \frac{1}{2}(\delta - \frac{\nu_{\mathrm{s}}b}{4})P^2 - \frac{\nu_{\mathrm{s}}}{64}(Q^2 + P^2)^2,$$

where $\delta = \nu_{\mathrm{s}} - (\nu_{\mathrm{m}}/2)$ and, without loss of generality, we assume $b > 0$. Show that the fixed points of the Hamiltonian are located at

$$
\begin{array}{llr}
P_{\mathrm{SFP}} = 0, & Q_{\mathrm{SFP}} = 0 & (\nu_{\mathrm{m}} > 2\nu_{\mathrm{s}} + \nu_{\mathrm{s}}b/2) \\
P_{\mathrm{SFP}} = 0, \quad Q_{\mathrm{SFP}} = \sqrt{16(1 - \nu_{\mathrm{m}}/2\nu_{\mathrm{s}}) + 4b} & & (\nu_{\mathrm{m}} > 2\nu_{\mathrm{s}} + \nu_{\mathrm{s}}b/2) \\
Q_{\mathrm{UFP}} = 0, \quad P_{\mathrm{UFP}} = 0 & & (2\nu_{\mathrm{s}} - \nu_{\mathrm{s}}b/2 \le \nu_{\mathrm{m}} \le 2\nu_{\mathrm{s}} + \nu_{\mathrm{s}}b/2) \\
Q_{\mathrm{UFP}} = 0, \quad P_{\mathrm{UFP}} = \sqrt{16(1 - \nu_{\mathrm{m}}/2\nu_{\mathrm{s}}) - 4b} & & (\nu_{\mathrm{m}} \le 2\nu_{\mathrm{s}} - \tfrac{1}{2}\nu_{\mathrm{s}}b).
\end{array}
$$

Compare this result with Eqs. (3.125) and (3.126). Show that the separatrix for $\nu_{\mathrm{m}} \le 2\nu_s - \nu_s b/2$ is given by two circles

$$(Q - Q_{\mathrm{c}})^2 + P^2 = r^2, \qquad (Q + Q_{\mathrm{c}})^2 + P^2 = r^2$$

with

$$Q_{\mathrm{c}} = \sqrt{4b}, \qquad r = \sqrt{16\delta/\nu_s}.$$

The separatrix in the betatron phase space for slow beam extraction that employs a half integer stopband is identical to that given in this exercise. Quadrupoles are used to provide resonance driving term b, and octupoles are used to provide nonlinear detuning α_{xx}. The resulting effective Hamiltonian is

$$H_{\mathrm{eff}} = \nu_x J_x + \frac{1}{2}\alpha_{xx}J_x^2 + bJ_x\cos(\psi_x - \frac{\ell}{2}\theta),$$

where $\alpha_{xx} = (-1/16\pi B\rho)\oint \beta_x^2 B_3 ds$ is the detuning parameter, B_3 is the octupole strength, and b is the half integer stopband width.

5. Show that the equation of motion for rf dipole on betatron motion in Eq. (2.107) near a betatron sideband can be cast into an effective Hamiltonian

$$H_{\mathrm{eff}} = \nu J + \frac{1}{2}\alpha J^2 + gJ^{1/2}\cos(\psi - \nu_{\mathrm{m}}\theta + \chi),$$

where ν, (J, ϕ), α are the tune, the action-angle coordinates, and the detuning parameter of the betatron motion, g is proportional to the rf dipole field strength, and ν_{m} is the rf dipole modulation tune. Find the fixed points of the Hamiltonian and discuss the dependence of the fixed point on parameters $\nu_{\mathrm{m}} - \nu$, and α.

IV Nonadiabatic and Nonlinear Synchrotron Motion

Transition energy has been both a nuisance in machine operation and a possible blessing for attaining beam bunches with some desired properties, such as enhanced beam separation for filtering ion beams having nearly equal charge to mass ratios, and beam bunches with ultra-small beam width.[26] However, the synchrotron frequency spread vanishes at transition energy, and the circulating beams can suffer microwave instabilities and other collective instabilities for lack of Landau damping, to be discussed in Sec. VII.

Near the transition energy region, the adiabaticity condition (3.32) is not satisfied, i.e. the Hamiltonian is time dependent and is not a constant of motion. This results in non-adiabatic synchrotron motion, where the bucket area increases dramatically, and the phase-space area occupied by the beam bunch is a small fraction of the bucket area. The linearized rf potential is a good approximation. If the phase slip factor is independent of the off-momentum variable, we will obtain analytic solutions for the linearized synchrotron motion near transition energy in Sec. IV.1. The integral of the linearized Hamiltonian is also an ellipse, and the action is a constant of motion. We will discuss the scaling properties of the beam at the transition energy crossing.

However, when the phase slip factor η_0 of Eq. (3.11) becomes small, the nonlinear phase slip factor term η_1 can be important. This again raises another nonlinear problem in synchrotron motion, i.e. parts of a beam bunch can encounter a defocusing force during transition energy crossing. In Sec. IV.2 we study nonlinear synchrotron motion due to nonlinearity in phase slip factor. Although the action of a Hamiltonian flow is invariant, the torus is highly distorted and particles in a beam may be driven out of the rf bucket after crossing the transition energy. In Sec. IV.3 we examine beam manipulation techniques for particle acceleration through transition energy. In Sec. IV.4 we study the effects of nonlinear phase slip factor and examine the properties of the so-called α-bucket, and in Sec. IV.5 we study problems associated with quasi-isochronous (QI) storage rings, which may provide beam bunches with ultra-short bunch length.

---

[26]Since the bunch width becomes very short and the momentum spread becomes large at transition energy, transition energy may be used to generate short bunches. See e.g., R. Cappi, J.P. Delahye, and K.H. Reich, *IEEE Trans. Nucl. Sci.* **NS-28**, 2389 (1981). Using the sensitivity of the closed orbit to beam momentum at transition energy, one can filter beam momentum from nearly identical Z/A (charge to mass ratio) ion beams. Oxygen and sulfur ions have been filtered at transition energy in the CERN PS.

IV.1   Linear Synchrotron Motion Near Transition Energy

Since the energy gain per revolution in rf cavities is small, we assume $\gamma = \gamma_{\mathrm{T}} + \dot{\gamma} t$, where $\dot{\gamma} = d\gamma/dt$ is the acceleration rate, and t is the time coordinate. The phase slip factor becomes

$$\eta_0 = \alpha_0 - \gamma^{-2} \approx \frac{2\dot{\gamma} t}{\gamma_{\mathrm{T}}^3}. \tag{3.133}$$

Here we have neglected the dependence of the phase slip factor on the off-momentum coordinate δ, and assume that all particles in a bunch pass through transition energy at the same time. Substituting Eq. (3.133) into Eq. (3.17), we obtain

$$\omega_{\mathrm{s}}^2 = \frac{|t|}{\tau_{\mathrm{ad}}^3}, \qquad \tau_{\mathrm{ad}} = \left(\frac{\pi \beta^2 m c^2 \gamma_{\mathrm{T}}^4}{\dot{\gamma} \omega_0^2 h e V |\cos\phi_{\mathrm{s}}|} \right)^{1/3}. \tag{3.134}$$

Here τ_{ad} is the *adiabatic time*. At $|t| \gg \tau_{\mathrm{ad}}$, the adiabaticity condition (3.32) is satisfied. At $|t| \geq 4\tau_{\mathrm{ad}}$ the adiabatic condition is approximately fulfilled because $\alpha_{\mathrm{ad}} = |d(\omega_{\mathrm{s}}^{-1})/dt| = \frac{1}{2}(\tau_{\mathrm{ad}}/|t|)^{3/2} \approx 0.06$. Table 3.3 lists the adiabatic time for some proton synchrotrons. Typically τ_{ad} is about 1–10 ms. Note that the beam parameters for RHIC correspond to those of a typical gold beam injected from the AGS with charge number $Z = 79$, and atomic mass number $A = 197$. The injection energy for proton beams in RHIC is above transition energy.

Table 3.3: The adiabatic and nonlinear times of some proton synchrotrons.

	FNAL Booster	FNAL MI	AGS	RHIC	KEKPS	CPS
C (m)	474.2	3319.4	807.12	3833.8	339.29	628.32
V (kV)	950	4000	300	300	90	200
h	84	588	12	360	9	6–20
γ_{T}	5.4	20.4	8.5	22.5	6.76	6.5
$\dot{\gamma}$ (s^{-1})	200	190	70	1.6	40	60
$\mathcal{A}$ (eVs/u)	0.04	0.04	1.	0.3	0.3	0.5
$\hat{\delta}$ ($\times 10^{-3}$)	6.4	2.5	6.7	4.5	5.4	6.6
τ_{ad} (ms)	0.2	2.0	2.5	36	1.8	1.5
τ_{nl} (ms)	0.13	0.19	0.61	63	0.7	0.5

In linear approximation, the synchrotron equations of motion near the transition energy region become

$$\dot{\delta} = \frac{\omega_0 e V}{2\pi \beta^2 E} \cos\phi_{\mathrm{s}}(\Delta\phi), \qquad (\dot{\Delta\phi}) = \frac{2 h \omega_0 \dot{\gamma}}{\gamma_{\mathrm{T}}^3} t\, \delta, \tag{3.135}$$

where the overdot indicates the derivative with respect to time t, and $\delta = \Delta p/p_0$ and $\Delta\phi = \phi - \phi_s$ are the fractional off-momentum and phase coordinates of a particle. Taking into account the synchronous phase change from ϕ_s to $\pi - \phi_s$ across transition energy, we obtain

$$\frac{d}{dt}\left(\frac{\tau_{ad}^3}{|t|}\frac{d}{dt}\Delta\phi\right) + \Delta\phi = 0. \tag{3.136}$$

Defining a new time variable y as

$$y = \int_0^x x^{1/2}dx = \frac{2}{3}x^{3/2} \qquad \text{with} \qquad x = \frac{|t|}{\tau_{ad}}, \tag{3.137}$$

Eq. (3.136) can be transformed into Bessel's equation of order $2/3$,

$$\varphi'' + \frac{1}{y}\varphi' + (1 - \frac{(2/3)^2}{y^2})\varphi = 0, \tag{3.138}$$

where $\varphi = y^{-2/3}\Delta\phi$, and the primes indicate derivatives with respect to time variable y. The solution of Eq. (3.138) can be written readily as

$$\Delta\phi = bx\left[\cos\chi\, J_{2/3}(y) + \sin\chi\, N_{2/3}(y)\right], \tag{3.139}$$

where χ and b are constants to be determined from the initial condition. Here the Neumann function is $N_\nu(z) = [J_\nu(z)\cos\pi\nu - J_{-\nu}(z)]/\sin\pi\nu$. It is also called the Bessel function of the second kind. In Ref. [30], the notation is $Y_\nu(z)$. The off-momentum coordinate δ can be obtained from Eq. (3.135), i.e.

$$\dot{\Delta\phi} = \frac{2h\omega_0\dot\gamma t}{\gamma_T^3}\delta = \frac{\Delta\phi}{\tau_{ad}x} + \frac{bx^{2/3}}{\tau_{ad}}\left(\cos\chi\left[\frac{2J_{2/3}}{3y} - J_{5/3}\right] + \sin\chi\left[\frac{2N_{2/3}}{3y} - N_{5/3}\right]\right).$$

Combining this with Eq. (3.139), we obtain the constant of motion

$$\alpha_{\phi\phi}(\Delta\phi)^2 + 2\alpha_{\phi\delta}\Delta\phi\delta + \alpha_{\delta\delta}\delta^2 = 1, \tag{3.140}$$

where

$$\alpha_{\phi\phi} = \frac{\pi^2}{9b^2x^2}\left[\left(\frac{3}{2}yN_{5/3} - 2N_{2/3}\right)^2 + \left(2J_{2/3} - \frac{3}{2}yJ_{5/3}\right)^2\right],$$

$$\alpha_{\phi\delta} = \frac{\pi^2}{9b^2}\left(\frac{2h\dot\gamma\omega_0\tau_{ad}^2}{\gamma_T^3}\right)\left[N_{2/3}\left(\frac{3}{2}yN_{5/3} - 2N_{2/3}\right) - J_{2/3}\left(2J_{2/3} - \frac{3}{2}yJ_{5/3}\right)\right],$$

$$\alpha_{\delta\delta} = \frac{\pi^2}{9b^2}x^2\left(\frac{2h\dot\gamma\omega_0\tau_{ad}^2}{\gamma_T^3}\right)^2[J_{2/3}^2 + N_{2/3}^2].$$

There is no surprise that the constant of motion for a time dependent *linear* Hamiltonian is an ellipse. In (ϕ, δ) phase-space coordinates, the shape of the ellipse

changes with time. The phase-space area enclosed in the ellipse of Eq. (3.140) is a
constant of motion given by

$$\tilde{\mathcal{A}} = \frac{\pi}{\sqrt{\alpha_{\phi\phi}\alpha_{\delta\delta} - \alpha_{\phi\delta}^2}} = \frac{3b^2\gamma_{\mathrm{T}}^3}{2h\dot{\gamma}\omega_0\tau_{\mathrm{ad}}^2} = h\mathcal{A}\frac{\omega_0}{\beta^2\gamma_{\mathrm{T}}mc^2}, \tag{3.141}$$

where $\mathcal{A}$ is the phase-space area of the bunch in eV-s. Thus the parameter b is

$$b = \left(\frac{2\mathcal{A}h^2\omega_0^2\dot{\gamma}\tau_{\mathrm{ad}}^2}{3mc^2\beta^2\gamma_{\mathrm{T}}^4}\right)^{1/2}. \tag{3.142}$$

A. The asymptotic properties of the phase space ellipse

The phase-space ellipse is tilted in the transition energy region. Using a Taylor series
expansion around $y = 0$, we obtain

$$\alpha_{\phi\phi} = \frac{\pi^2}{9b^2}\frac{4}{3^{1/3}[\Gamma(\frac{2}{3})]^2}, \tag{3.143}$$

$$\alpha_{\phi\delta} = -\frac{\pi^2}{9b^2}\left(\frac{2h\dot{\gamma}\omega_0\tau_{\mathrm{ad}}^2}{\gamma_{\mathrm{T}}^3}\right)\frac{\sqrt{3}}{\pi}, \tag{3.144}$$

$$\alpha_{\delta\delta} = \frac{\pi^2}{9b^2}\left(\frac{2h\dot{\gamma}\omega_0\tau_{\mathrm{ad}}^2}{\gamma_{\mathrm{T}}^3}\right)^2\frac{3^{4/3}[\Gamma(\frac{2}{3})]^2}{\pi^2}. \tag{3.145}$$

The tilt angle, the maximum momentum spread, and the maximum bunch width of
the ellipse are

$$\psi = \frac{1}{2}\tan^{-1}\frac{2\alpha_{\phi\delta}}{\alpha_{\phi\phi} - \alpha_{\delta\delta}}, \tag{3.146}$$

$$\hat{\delta}\Big|_{\gamma=\gamma_{\mathrm{T}}} = \frac{\gamma_{\mathrm{T}}}{3^{1/6}\beta\tau_{\mathrm{ad}}\Gamma(\frac{2}{3})}\left(\frac{2\mathcal{A}}{3mc^2\dot{\gamma}}\right)^{1/2} \approx 0.502\frac{\gamma_{\mathrm{T}}}{\beta\tau_{\mathrm{ad}}}\left(\frac{\mathcal{A}}{mc^2\dot{\gamma}}\right)^{1/2}, \tag{3.147}$$

$$\hat{\phi}\Big|_{\gamma=\gamma_{\mathrm{T}}} = \sqrt{\frac{\alpha_{\delta\delta}}{\alpha_{\phi\phi}\alpha_{\delta\delta} - \alpha_{\phi\delta}^2}} = \frac{3^{2/3}\Gamma(\frac{2}{3})}{\pi}\left(\frac{2\mathcal{A}h^2\omega_0^2\dot{\gamma}\tau_{\mathrm{ad}}^2}{3mc^2\beta^2\gamma_{\mathrm{T}}^4}\right)^{1/2}. \tag{3.148}$$

Note that $\hat{\delta}$ is finite at $\gamma = \gamma_{\mathrm{T}}$ for a nonzero acceleration rate. At a higher acceler-
ation rate, the maximum momentum width of the beam will be smaller. Substituting
the adiabatic time τ_{ad} of Eq. (3.134) into Eq. (3.147), we obtain the following scaling
property:

$$\hat{\delta}\Big|_{\gamma=\gamma_{\mathrm{T}}} \sim h^{1/3}V^{1/3}\mathcal{A}^{1/2}\dot{\gamma}^{-1/6}\gamma_{\mathrm{T}}^{-1/3}. \tag{3.149}$$

The scaling property is important in the choice of operational conditions.

In the adiabatic region where $x \gg 1$, we can use asymptotic expansion of Bessel functions to obtain

$$\alpha_{\phi\phi} \to \frac{\pi^2}{3b^2}x^{-1/2}, \quad \alpha_{\phi\delta} \to 0, \quad \alpha_{\delta\delta} \to \frac{\pi^2}{3b^2}\left(\frac{2h\dot{\gamma}\omega_0\tau_{\text{ad}}^2}{\gamma_{\text{T}}^3}\right)^2 x^{1/2}.$$

The phase-space ellipse is restored to the upright position.

B. The Gaussian distribution function at transition energy

The distribution function that satisfies the Vlasov equation is a function of the invariant ellipse (3.140). Using the Gaussian distribution function model, we obtain

$$
\begin{aligned}
\Psi_0(\Delta\phi, \delta) &= \frac{3N_{\text{B}}(\alpha_{\phi\phi}\alpha_{\delta\delta} - \alpha_{\phi\delta}^2)^{1/2}}{\pi} e^{-3[\alpha_{\phi\phi}(\Delta\phi)^2 + 2\alpha_{\phi\delta}\delta(\Delta\phi) + \alpha_{\delta\delta}\delta^2]} \\
&= N_{\text{B}}G_1(\Delta\phi)G_2(\delta), \tag{3.150}
\end{aligned}
$$

where N_{B} is the number of particles in the bunch, the factor 3 is chosen to ensure that the phase-space area $\mathcal{A}$ of Eq. (3.141) corresponds to 95% of the beam particles, and the normalized distribution functions $G_1(\Delta\phi)$ and $G_2(\delta)$ are

$$G_1(\Delta\phi) = \sqrt{\frac{3(\alpha_{\phi\phi}\alpha_{\delta\delta} - \alpha_{\phi\delta}^2)}{\pi\alpha_{\delta\delta}}} \exp\{-\frac{3(\alpha_{\phi\phi}\alpha_{\delta\delta} - \alpha_{\phi\delta}^2)}{\alpha_{\delta\delta}}(\Delta\phi)^2\}$$

$$G_2(\delta) = \sqrt{\frac{3\alpha_{\delta\delta}}{\pi}} \exp\{-3\alpha_{\delta\delta}(\delta + \frac{\alpha_{\phi\delta}}{\alpha_{\delta\delta}}\Delta\phi)^2\}.$$

Note here that $G_1(\Delta\phi)$ is the line charge density, and the peak current is still located at $\Delta\phi = 0$. Using the ellipse of Eq. (3.140), we can evaluate the evolution of the peak current at the transition energy crossing.

IV.2   Nonlinear Synchrotron Motion at $\gamma \approx \gamma_{\text{T}}$

In Sec. IV.1, all particles were assumed to cross transition energy at the same time. This is not true, because the phase slip factor depends on the off-momentum coordinate δ. Near the transition energy region, the nonlinear phase slip factor of Eq. (3.11) becomes quite important. Expanding the phase slip factor up to first order in δ, the synchrotron equations of motion become

$$\dot{\Delta\phi} = h\omega_0\left(\frac{2\dot{\gamma}t}{\gamma_{\text{T}}^3} + \eta_1\delta\right)\delta, \qquad \dot{\delta} = \frac{\omega_0 eV\cos\phi_{\text{s}}}{2\pi\beta^2 E}(\Delta\phi), \tag{3.151}$$

where the synchronous particle crosses transition energy at time $t = 0$, and, to a good approximation, the phase slip factor has been truncated to second order in δ. At time
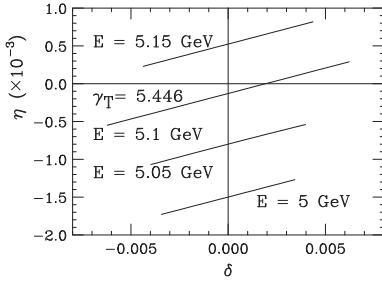
Figure 3.15: Schematic plot of η vs δ near the transition energy region for the Fermilab Booster, where $\gamma_{\mathrm{T}} = 5.446$, $\gamma_{\mathrm{T}}^2 \alpha_1 = 0.5$, and a phase-space area of 0.05 eV-s are used to calculate $\eta(\delta)$ for the beam. A beam bunch is represented by a line of $\eta(\delta)$ vs δ. The synchrotron motion corresponds to particle motion along this line. At the beam synchronous energy of $E = 5.1$ GeV, which is below the transition energy of 5.11 GeV, particles at $\delta > 0.0018$ will experience unstable synchrotron motion due to the nonlinear phase slip factor.

$t = 0$, the synchronous phase is also shifted from ϕ_{s} to $\pi - \phi_{\mathrm{s}}$ in order to achieve stable synchrotron motion.

Figure 3.15 shows the phase slip factor η vs the fractional off-momentum coordinate δ near transition energy for a beam in the Fermilab Booster. A beam bunch with momentum width $\pm\hat{\delta}$ is represented by a short tilted line. At a given time (or beam energy), particles are projected onto the off-momentum axis represented by this line. Since the phase slip factor is nonlinear, the line is tilted. When the beam is accelerated (or decelerated) toward transition energy, a portion of the beam particles can cross transition energy and this leads to unstable synchrotron motion, as shown in the example at 5.1 GeV beam energy in Fig. 3.15. Since the synchrotron motion is slow, we hope that the unstable motion does not give rise to too much bunch distortion before particles are recaptured into a stable bucket.

To characterize nonlinear synchrotron motion, we define the *nonlinear time* τ_{nl} as the time when the phase slip factor changes sign for the particle at the maximum momentum width $\hat{\delta}$ of the beam, i.e. $\eta_0 + \eta_1\hat{\delta} = -(2\dot{\gamma}\tau_{\mathrm{nl}}/\gamma_{\mathrm{T}}^3) + \eta_1\hat{\delta} = 0$, or

$$\tau_{\mathrm{nl}} = \gamma_{\mathrm{T}}^3 \frac{\eta_1}{2\dot{\gamma}}\hat{\delta} = \gamma_{\mathrm{T}} \frac{\frac{3}{2}\beta_0^2 + \gamma_{\mathrm{T}}^2\alpha_1}{2\dot{\gamma}}\hat{\delta}, \tag{3.152}$$

where $\hat{\delta}$ is the maximum fractional momentum spread of the beam, η_1 is obtained from Eq. (3.11), and the α_1 term can be adjusted by sextupoles. For a lattice without sextupole correction, we typically have $\gamma_{\mathrm{T}}^2\alpha_1 \approx 1$. Within the nonlinear time $\pm\tau_{\mathrm{nl}}$, some portions of the beam could experience unstable synchrotron motion. Note that the nonlinear time depends on the off-momentum width of the beam. Table 3.3 lists the nonlinear time of some accelerators, where $\alpha_1 = 0$ is assumed. Note that the nonlinear time for RHIC is particularly long because superconducting magnets can tolerate only a slow acceleration rate.

When the beam is accelerated toward transition energy to within the range

$$\gamma_{\mathrm{T}} - \dot{\gamma}\tau_{\mathrm{nl}} \leq \gamma \leq \gamma_{\mathrm{T}} + \dot{\gamma}\tau_{\mathrm{nl}},$$

the phase equation begins to change sign for particles at higher momenta while the phase angle ϕ_s has not yet been shifted. Therefore these particles experience defocusing synchrotron motion. After the synchronous energy of the bunch reaches transition energy and the synchronous phase has also been shifted from ϕ_s to $\pi - \phi_s$, lower momentum portions of the bunch will experience defocusing synchrotron motion. The problem is most severe for accelerators with a slow acceleration rate.

The relative importance of non-adiabatic and nonlinear synchrotron motions depends on the adiabatic time of Eq. (3.134) that governs the adiabaticity of the synchrotron motion, and the nonlinear time τ_{nl}, within which some portion of the beam particles experiences unstable synchrotron motion. Using Eq. (3.151), we obtain

$$\delta'' = -x\delta + \frac{\tau_{nl}}{\tau_{ad}}\frac{\delta^2}{\hat{\delta}}, \tag{3.153}$$

where the primes indicate derivatives with respect to $x = |t|/\tau_{ad}$. Note that when the nonlinear time τ_{nl} vanishes, the solution of Eq. (3.153) is an Airy function, discussed in Sec. IV.1. Since the solution of the nonlinear equation is not available, we estimate the growth of momentum width by integrating the unstable exponent. The growth factor is

$$G = \exp\left\{\int_0^{\tau_{nl}/\tau_{ad}} \left(-x + \frac{\tau_{nl}}{\tau_{ad}}\right)^{1/2} dx\right\} = \exp\left\{\frac{2}{3}\left(\frac{\tau_{nl}}{\tau_{ad}}\right)^{3/2}\right\} \tag{3.154}$$

for a particle with $\delta = \hat{\delta}$. The maximum momentum height is increased by the growth factor G, which depends exponentially on τ_{nl}/τ_{ad}. Depending on the adiabatic and nonlinear times, important beam dynamics problems are nonlinear synchrotron motion and of microwave instability to be discussed in Sec. VII.

We have seen that the momentum width will increase due to the nonlinear phase slip factor. However, we should bear in mind that the synchrotron motion can be derived from a Hamiltonian

$$H = \frac{1}{2}h\omega_0\left[\eta_0 + \frac{2}{3}\eta_1\delta\right]\delta^2 - \frac{\omega_0 eV}{4\pi^2\beta^2 E}\cos\phi_s(\Delta\phi)^2, \tag{3.155}$$

where $\eta_0 = 2\dot{\gamma}t/\gamma_T^3$. Expressing Hamilton's equation as a difference mapping equation, we can easily prove that the Jacobian is 1. Therefore the area of the phase-space ellipse of each particle is conserved, and the 1D dynamical system is integrable. The action integral is a distorted curve in phase-space coordinates. When the bunch is accelerated through transition energy, some portions of the phase-space torus may lie outside the stable ellipse of the synchrotron Hamiltonian. They may be captured by other empty buckets of the rf system, or may be lost because of the aperture limitation. For a modern high intensity hadron facility, the loss would cause radiation problems; therefore efforts to eliminate transition energy loss are important.

IV.3   Beam Manipulation Near Transition Energy

Near the transition energy, the revolution frequencies of all particles are nearly identical, i.e. the beam is isochronous or quasi-isochronous. Since there is no frequency spread for Landau damping, the beam can suffer microwave instability. The tolerance of microwave instability near transition energy will be discussed in Sec. VII.

The nonlinear phase slip factor can cause defocusing synchrotron motion for a portion of the bunch. The growth of the bunch area is approximately $G^2 = \exp\{\frac{4}{3}(\tau_{\mathrm{nl}}/\tau_{\mathrm{ad}})^{3/2}\}$ shown in Eq. (3.154). The 5% beam loss at transition energy found for proton synchrotrons built in the 60's and 70's may arise mainly from this nonlinear effect. Bunched beam manipulation are usually needed to minimize beam loss and uncontrollable emittance growth. Minimizing both τ_{ad} and τ_{nl} provides cleaner beam acceleration through the transition energy.

A. Transition energy jump

By applying a set of quadrupoles, transition energy can be changed suddenly in order to attain fast transition energy crossing (see Chap. 2, Sec. IV.8). The effective γ_{T} crossing rate is $\dot{\gamma}_{\mathrm{eff}} = \dot{\gamma} - \dot{\gamma}_{\mathrm{T}}$. For example, if γ_{T} is changed by one unit in 1 ms,[27] the effective transition energy crossing rate is 1000 s^{-1}, which is much larger than the beam acceleration rates listed in Table 3.3.

Transition γ_{T} jump has been employed routinely in the CERN PS. The scheme has also been studied in the Fermilab Booster and Main Injector, the KEK PS, and the AGS. The minimum γ_{T} jump width is

$$\Delta\gamma_{\mathrm{T}} = 2\dot{\gamma} \times \mathrm{Max}(\tau_{\mathrm{ad}}, \tau_{\mathrm{nl}}). \tag{3.156}$$

B. Momentum aperture for faster beam acceleration

The synchronization of dipole field with synchronous energy is usually accomplished by a "radial loop," which provides a feedback loop for rf voltage and synchronous phase angle. In most accelerators, the maximum $\dot{B}$ is usually limited, but the rf voltage and synchronous phase angle can be adjusted to move the beam across the momentum aperture. The radial loop can be programmed to keep the beam closed orbit inside the nominal closed orbit below transition energy, and to attain faster acceleration across transition energy so that the beam closed orbit is outside the nominal closed orbit above transition energy. For an experienced machine operator to minimize the beam loss with a radial loop, the essential trick is to attain a faster transition energy crossing rate.

---

[27]The γ_{T} jump time scale is non-adiabatic with respect to synchrotron motion. However, the time scale can be considered as adiabatic in betatron motion so that particles adiabatically follow the new betatron orbit.

C. Flatten the rf wave near transition energy

Near transition energy, partial loss of focusing force in synchrotron motion can be alleviated by flattening the rf wave. This can be done by choosing $\phi_s = \pi/2$ or employing a second or third harmonic cavity.[28] In the flattened rf wave, all particles gain an equal amount of energy each turn, and thus δ of each particle is approximately constant in a small energy range. The solution of Eq. (3.151) with $\dot{\delta} = 0$ is

$$\Delta\phi = \Delta\phi_1 + \frac{h\omega_0\dot{\gamma}\delta}{\gamma_T^3}(t^2 - t_1^2) + \eta_1 h\omega_0\delta^2 \ (t - t_1), \qquad (3.157)$$

where t_1 is the rf flattening period, $(\Delta\phi_1, \delta_1)$ are the initial phase-space coordinates of the particle, and $\delta = \delta_1$.

Figure 3.16 shows the evolution of the phase-space torus when the rf wave is flattened across the transition energy region; the parameters used in this calculations are $\gamma_T = 22.5$, $\omega_0 = 4.917 \times 10^5$ rad/s, $\dot{\gamma} = 1.6$ s^{-1}, $h = 360$, $t_1 = -63$ ms, and $\gamma_T^2\eta_1 \approx 2$. Note that the ellipse evolves into a boomerang shaped distribution function with an equal phase-space area. The rf flattening scheme is commonly employed in isochronous cyclotrons.
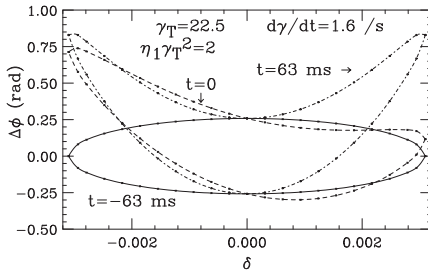
Figure 3.16: The evolution of a phase-space ellipse in the flattened rf wave near the transition energy region. Note that the off-momentum coordinates of each particle are unchanged, while the bunch length elongates along the ϕ axis.

IV.4   Synchrotron Motion with Nonlinear Phase Slip Factor

In the production of secondary beams, very short proton bunches are needed for attaining small emittance. Very short electron bunches, e.g. sub-millimeter in bunch length, have many applications such as time resolved experiments with synchrotron light sources, coherent synchrotron radiation, and damping rings for the next linear colliders. Since the ratio of bunch length to bunch height is proportional to $\sqrt{|\eta|}$, a possible method of producing short bunches is to operate the accelerator in an

---

[28]See e.g., C.M. Bhat *et al.*, *Phys. Rev.* E **55**, 1028 (1997). The AVF cyclotron has routinely employed this method for beam acceleration. This concept was patented by G.B. Rossi, U.S. Patent 2778937 (1954).

isochronous condition for proton synchrotrons, or to reduce the momentum compaction factor for electron storage rings. Because of its potential benefit of the low η condition, we carefully study the physics of the QI dynamical system.[29]

Table 3.2 and Eq. (3.43) show that the synchrotron bucket height and momentum spread become very large when $|\eta|$ is small. This requires careful examination because when the phase slip factor η is small, its dependence on the fractional momentum deviation δ becomes important. The synchrotron Hamiltonian needs to take into account the effects of nonlinear phase slip factor.

Expanding the phase slip factor as $\eta = \eta_0 + \eta_1 \delta + \cdots$ and using the orbiting angle θ as the independent variable, we obtain the Hamiltonian for synchrotron motion as

$$H = \frac{1}{2}h\left(\eta_0 + \frac{2}{3}\eta_1\delta\right)\delta^2 + \frac{eV}{2\pi\beta^2 E}[\cos\phi - \cos\phi_s + (\phi - \phi_s)\sin\phi_s], \qquad (3.158)$$

where we have truncated the phase slip factor to the second order in δ. The fixed points of the nonlinear synchrotron Hamiltonian are

$$(\phi,\delta)_{\text{SFP}} = (\phi_s, \ 0), \qquad (\pi - \phi_s, \ -\eta_0/\eta_1), \qquad (3.159)$$

$$(\phi,\delta)_{\text{UFP}} = (\pi - \phi_s, \ 0), \quad (\phi_s, \ -\eta_0/\eta_1). \qquad (3.160)$$

Note that the nonlinear phase slip factor introduces another set of fixed points in the phase space. The fixed points with $\delta_{\text{FP}} = 0$ are the nominal fixed points. The fixed points with $\delta_{\text{FP}} = -\eta_0/\eta_1$ arising from the nonlinear-phase-slip factor are called nonlinear-phase-slip-factor (NPSF) fixed points. These fixed points play important role in determining the dynamics of synchrotron motion.

We define $\nu_s = \sqrt{h|\eta_0|eV/2\pi\beta^2 E}$ for small amplitude synchrotron tune, and use the normalized phase space coordinates ϕ and $\mathcal{P} = (h\eta_0/\nu_s)\delta$. The Hamiltonian of synchrotron motion becomes

$$H = \frac{1}{2}\nu_s\mathcal{P}^2 + \frac{1}{2y}\nu_s\mathcal{P}^3 + \nu_s[\cos\phi - \cos\phi_s + (\phi - \phi_s)\sin\phi_s]. \qquad (3.161)$$

The parameter

$$y = 3h\eta_0^2/2\eta_1\nu_s \qquad (3.162)$$

signifies the relative importance of the linear and nonlinear parts of the phase slip factor. If $|y| \gg 1$, the nonlinear phase slip factor is not important, and if $|y|$ is small, the phase space tori will be deformed.

---

[29] A. Riabko et al., Phys. Rev. E**54**, 815 (1996); D. Jeon et al., Phys. Rev. E**54**, 4192 (1996); M. Bai et al., Phys. Rev. E**55**, 3493 (1997); C. Pellegrini and D. Robin, Nucl. Inst. Methods, A **301**, 27 (1991); D. Robin, et. al., Phys. Rev. E**48**, 2149 (1993); H. Bruck et al., IEEE Trans. Nucl. Sci. **NS20**, 822 (1973); L. Liu et al., Nucl. Instru. Methods, **A329**, 9 (1993); H. Hama, S. Takano and B. Isoyama, Nucl. Instru. Methods, **A329**, 29 (1993); S. Takano, H. Hama and G. Isoyama, Japan J. Appl. Phys. **32**, 1285 (1993); A. Nadji et al., Proc. EPAC94 p. 128 (1994); D. Robin, H. Hama, and A. Nadji, LBL-37758 (1995).

Figure 3.17 shows the separatrix of the nonlinear Hamiltonian in normalized phase space coordinates for $\phi_s = 150°$ and $180°$ respectively, where, without loss of generality, we have assumed $\eta_0 > 0$ and $\eta_1 > 0$. The separatrix that passes through the nominal fixed points are nominal separatrix. When the nominal separatrix crosses the unstable NPSF fixed point, the separatrix of two branches will become one (see the middle plots of Fig. 3.17 and Exercise 3.4.6). This condition occurs at $y = y_{cr}$, given by

$$y_{cr} = \sqrt{27[(\pi/2 - \phi_s)\sin\phi_s - \cos\phi_s]}. \tag{3.163}$$

For $y \gg y_{cr}$, the stable buckets of the upper and lower branches are separated by a distance of $\Delta\mathcal{P} = 2y/3$. Particle motion can be well described by neglecting the $\mathcal{P}^3$ term in the Hamiltonian.
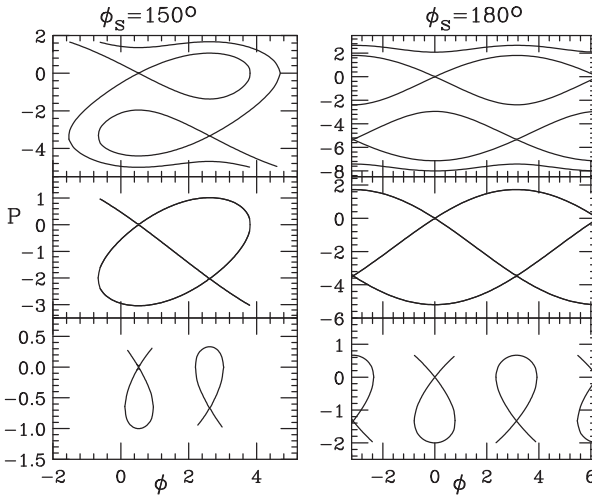
Figure 3.17: Left: Separatrix in the normalized phase space (ϕ, $P = \mathcal{P}$) for the synchrotron Hamiltonian with parameters $\phi_s = 150°$ and $y = 5$ (top), $y = y_{cr} = 3.0406$ (middle) and 1 (bottom); Right: Separatrix with parameters $\phi_s = 180°$ and $y = 8$ (top), $y = y_{cr} = 5.1962$ (middle), and 3 (bottom). In this example, we assume $\eta_0 > 0$ and $\eta_1 > 0$. Note the dependence of the Hamiltonian tori on the parameter y.

For $y < y_{cr}$, the separatrix ("fish") is deformed into up-down shape (see lower plots). They are called "α-bucket." Since the α-bucket is limited in a small region of the phase coordinate ϕ, small angle expansion is valid. The particle motion inside such a quasi-isochronous (QI) dynamical system can be analytically solved as follows.

IV.5 The QI Dynamical Systems

The synchrotron equation of motion for the rf phase coordinate ϕ of a particle is

$$\dot{\phi} = h\eta\delta, \qquad \eta = \eta_0 + \eta_1\delta + \cdots, \tag{3.164}$$

where h is the harmonic number, $\delta = \Delta p/p_0$ is the fractional momentum deviation from a synchronous particle, the overdot indicates the derivative with respect to the

orbiting angle $\theta = s/R_0$, and η is the phase slip factor, η_0 and η_1 are the first order and second order phase slip factors. In many storage rings, truncation of the phase slip factor at the η_1 term is a good approximation. Similarly, the equation of motion for the fractional off-momentum deviation is

$$\dot{\delta} = \frac{eV_0}{2\pi\beta^2 E_0}[\sin(\phi + \phi_s) - \sin\phi_s] \approx \frac{eV_0\cos\phi_s}{2\pi\beta^2 E}\,\phi, \qquad (3.165)$$

where V_0 and ϕ_s are the rf voltage and synchronous phase angle, βc is the speed, and E_0 is the energy of the beam. Here, the linearized phase coordinate in Eq. (3.165) is a good approximation because the (up-down) synchrotron bucket is limited in a small range of the phase coordinate (see Fig. 3.17).

With $t = \nu_s\theta$ as the time variable, where $\nu_s = \sqrt{heV_0|\eta_0\cos\phi_s|/2\pi\beta^2 E_0}$ is the small amplitude synchrotron tune, and with (x,p) as conjugate phase-space coordinates, where

$$x = -\frac{\eta_1}{\eta_0}\frac{\Delta p}{p_0}, \quad p = \frac{\nu_s\eta_1}{h\eta_0^2}\phi, \qquad (3.166)$$

the synchrotron Hamiltonian for particle motion in QI storage rings becomes

$$H_0 = \frac{1}{2}p^2 + V(x), \qquad V(x) = \frac{1}{2}x^2 - \frac{1}{3}x^3. \qquad (3.167)$$

This universal Hamiltonian is autonomous and the Hamiltonian value E is a constant of motion with $E \in [0, \frac{1}{6}]$ for particles inside the bucket.

The equation of motion for the QI Hamiltonian with $H_0 = E$ is the standard Weierstrass equation,

$$\left(\frac{d\wp(u)}{du}\right)^2 = 4(\wp - e_1)(\wp - e_2)(\wp - e_3), \qquad (3.168)$$

where $u = t/\sqrt{6}$, $\wp = x$, and the turning points are

$$e_1 = \frac{1}{2} + \cos(\xi), \quad e_2 = \frac{1}{2} + \cos(\xi - 120°), \quad e_3 = \frac{1}{2} + \cos(\xi + 120°)$$

with $\xi = \frac{1}{3}\arccos(1 - 12E)$. The ξ parameter for particles inside the bucket varies from 0 to $\pi/3$. Figure 3.18 shows the separatrix of the QI bucket QI potential, and the turning points, where e_2 and e_3 are turning points for stable particle motion.

The Weierstrass elliptic $\wp$-function is a single valued doubly periodic function of a single complex variable. For particle motion inside the separatrix, the discriminant $\Delta = 648E(1 - 6E)$ is positive, and the Weierstrass $\wp$ function can be expressed in terms of the Jacobian elliptic function [30]

$$x(t) = e_3 + (e_2 - e_3)\,\text{sn}^2\left(\sqrt{\frac{e_1 - e_3}{6}}t|m\right), \qquad (3.169)$$

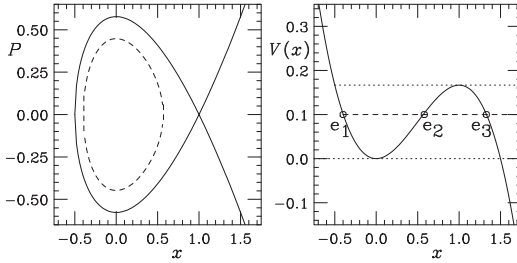$$k = \frac{e_2 - e_3}{e_1 - e_3} = \frac{\sin\xi}{\sin(\xi + 60°)}. \qquad (3.170)$$

Figure 3.18: Schematic plots of the QI bucket (left) and the QI potential (right). The dotted lines are the lower and upper limits of the "energy" 0 and 1/6 respectively. The turning points e_1, e_2, and e_3 are also shown for energy $E = 0.1$, associated with the dashed-line beam bunch at the left plot. The separatrix of the QI bucket is one of the separatrix, plotted side-way, shown in Fig. 3.17.

The separatrix orbit, which corresponds to $k = 1$, is

$$x_{\text{sx}}(t) = 1 - \frac{3}{\cosh t + 1}, \quad p_{\text{sx}}(t) = \frac{3 \sinh t}{(\cosh t + 1)^2}. \tag{3.171}$$

The tune of the QI Hamiltonian is

$$Q(E) = \frac{\pi[\sqrt{3}\sin(\xi + 60°)]^{1/2}}{\sqrt{6}K(k)}, \tag{3.172}$$

where $K(k)$ is the Jacobian Elliptical function. The normalized tune of the QI Hamiltonian is compared with that of the normal synchrotron Hamiltonian in Fig. 3.19.
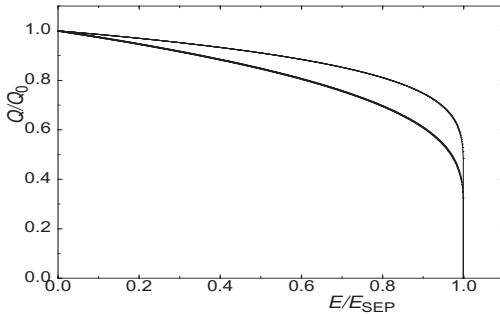
Figure 3.19: The synchrotron tune of the QI dynamical system (upper curve) is compared with that of the nominal rf potential (lower curve); plotted in relative Hamiltonian value, or "energy" E/E_{sep}. Note that the sharp drop of the QI synchrotron tune at the separatrix can cause chaotic motion for particles with large synchrotron amplitudes under the influence of the low-frequency time-dependent perturbation.

Here, we note that the synchrotron tune decreases to zero very sharply near the separatrix. Because of the sharp decrease in synchrotron tune, time dependent perturbation will cause overlapping parametric resonances and chaos near the separatrix.[30]

[30]H. Huang, et al., Phys. Rev. E**48**, 4678 (1993); M. Ellison, et al., Phys. Rev. Lett. **70**, 591 (1993); M. Syphers, et al., Phys. Rev. Lett. **71**, 719 (1993); Y. Wang, et al., Phys. Rev. **E49**, 1610 (1994). D. Li, et al., Phys. Rev. **E48**, R1638 (1993); D. Li, et al., Nucl. Inst. Methods, **A364**, 205 (1995).

The action of a torus is

$$J = \frac{1}{2\pi} \oint p\,dx = \frac{1}{8}\sqrt{\frac{2}{3}}(e_2 - e_3)^2(e_1 - e_3)^{1/2} F\left(\frac{3}{2}, -\frac{1}{2}; 3; k\right), \qquad (3.173)$$

where F is the hypergeometric function [30]. The action of the separatrix orbit is $J_{\mathrm{sx}} = 3/5\pi$, or equivalently the bucket area is $6/5$. Using the generating function

$$F_2(x, J) = \int_{e_3}^{x} p\,dx, \qquad (3.174)$$

the angle variable is $\psi = \partial F_2/\partial J = Qt$. The resulting Hamiltonian is

$$H_0(J) \approx J - \frac{5}{12}J^2 + \cdots.$$

Because of the synchrotron radiation damping, the equation of motion for QI electron storage rings is $x'' + Ax' + x - x^2 = 0$, where the effective damping coefficient is

$$A = \frac{\lambda}{\nu_{\mathrm{s}}} = \frac{U_0 J_E}{2\pi E_0 \nu_{\mathrm{s}}}. \qquad (3.175)$$

Here λ is the damping decrement, U_0 is the energy loss per revolution, and J_E is the damping partition number. In QI storage rings, the effective damping coefficient is enhanced by a corresponding decrease in synchrotron tune, i.e. $A \sim |\eta_0|^{-1/2}$, where the value of A can vary from 0 to 0.5.

Including the rf phase noise, the Hamiltonian in normalized phase-space coordinates is

$$H = \frac{p^2}{2} + \frac{1}{2}x^2 - \frac{1}{3}x^3 + \omega_{\mathrm{m}} B x \cos \omega_{\mathrm{m}} t, \qquad (3.176)$$

where

$$B = \frac{\eta_1 a}{\eta_0 \nu_{\mathrm{s}}} \qquad (3.177)$$

is the effective modulation amplitude, a is the rf phase modulation amplitude, $\omega_{\mathrm{m}} = \nu_{\mathrm{m}}/\nu_{\mathrm{s}}$ is the normalized modulation tune, and ν_{m} is the modulation tune of the original accelerator coordinate system. Note that the effective modulation amplitude B is greatly enhanced for QI storage rings by the smallness of η_0, i.e. $B \sim |\eta_1|/|\eta_0|^{3/2}$. Including the damping force, the equation of motion becomes

$$x'' + A x' + x - x^2 = -\omega_{\mathrm{m}} B \cos \omega_{\mathrm{m}} t. \qquad (3.178)$$

The stochasticity of such a dynamical system has been extensively studied.[31] Experimental verification of the QI dynamical system has not been fully explored. Detailed discussions of this topic is beyond this introductory textbook.

---

[31] A. Riabko *et al.*, *Phys. Rev.* E**54**, 815 (1996); D. Jeon *et al.*, *Phys. Rev.* E**54**, 4192 (1996); M. Bai *et al.*, *Phys. Rev.* E**55**, 3493 (1997).

Exercise 3.4

1. Verify the adiabatic time, the nonlinear time, and the momentum spread of the beam $\hat{\delta}$ at $\gamma = \gamma_T$ for the accelerators listed in Table 3.3.

2. Show that Eq. (3.135) can be reduced to

$$\delta'' + x\delta = 0$$

   where the primes indicate derivatives with respect to the variable $x = |t|/\tau_{\mathrm{ad}}$, where τ_{ad} is the adiabatic time of Eq. (3.134).

   (a) Express the solution in terms of Airy functions and find the equation for the invariant torus.

   (b) Verify Eq. (3.140).

3. Show that $\tau_{\mathrm{nl}}/\tau_{\mathrm{ad}} \propto \dot{\gamma}^{-5/6}\gamma_{\mathrm{T}}^{-2/3}$. Discuss the effects of high vs low γ_{T} lattices on the dynamics of synchrotron motion near the transition energy.

4. The Fermilab Main Injector accelerates protons from 8.9 GeV to 120 GeV in 1 s. Assuming $\gamma_T = 20.4$, calculate the characteristic time and the maximum momentum spread for a phase space area of 0.04 eV-s.

5. Show that the phase space area enclosed by $(\Delta\phi, \delta)$ of Eq. (3.157) is equal to the phase space area enclosed by $(\Delta\phi_1, \delta_1)$ of the initial ellipse.

6. Using the normalized phase space coordinates ϕ and $\mathcal{P}$, show that the Hamiltonian (3.158) with nonlinear phase slip factor depends only on a single parameter $y = 3h\eta_0^2/2\nu_s\eta_1$. Show that the separatrices of the Hamiltonian are

$$\nu_s \mathcal{P}^3 + y\mathcal{P}^2 + 2y[\cos\phi + \cos\phi_{\mathrm{s}} + (\phi + \phi_{\mathrm{s}} - \pi)\sin\phi_{\mathrm{s}}] = 0,$$

$$\nu_s \mathcal{P}^3 + y\mathcal{P}^2 + 2y[\cos\phi - \cos\phi_{\mathrm{s}} + (\phi - \phi_{\mathrm{s}})\sin\phi_{\mathrm{s}}] - \frac{4}{27}y^3 = 0.$$

   Show that when $y = y_{\mathrm{cr}}$ of Eq. (3.163) the separatrix of the upper branch passes through the UFP of the lower branch.

7. Show that the QI Hamiltonian can be reduced to Eq. (3.167) and that the solution is given by the Weierstrass elliptical function.

V   Beam Manipulation in Synchrotron Phase Space

A charged particle beam is usually produced by an intense ion source, pre-accelerated by an electrostatic Cockcroft-Walton or an RFQ, prebunched and injected into a linac to reach an injection energy for low energy synchrotrons, called booster synchrotrons or boosters. The beam is accumulated, phase-space painted, stacked in a low energy booster, and accelerated toward higher energies by a chain of synchrotrons of various sizes. The reasons for this complicated scheme are economics and beam dynamics issues. Since dipole and quadrupole magnets have low and high field operational limits, the range of beam energy for a synchrotron is limited. The mean-field Coulomb force can also have a large effect on the stability of low energy beams in boosters, where the space-charge tune shift, proportional to circumference of the synchrotron, is limited to about 0.3–0.4.

For the acceleration of ion beams, the fractional change of beam velocity in low energy boosters can be large. The rf frequency for a low energy booster has to be tuned in a wide range. The rf voltage requirement is determined by technical issues such as rf cavity design, rf power source, and the requirements in the momentum aperture and phase-space area. During beam acceleration, phase-space area is normally conserved. The beam distribution function can thus be manipulated to some desirable properties for experiments. Careful consideration is thus needed to optimize the operation and construction costs of accelerators.

On the other hand, electrons are almost relativistic at energies above 10 MeV, and the required range of rf frequency change is small. However, electrons emit synchrotron radiation, which must be compensated by the longitudinal rf electric field in a storage ring. Since synchrotron radiation power depends on particle energy, and the mean energy loss of a beam is compensated by the rf field, particle motion in synchrotron phase-space is damped. The synchrotron radiation emitted by a relativistic electron is essentially concentrated in a cone with an angular divergence of $1/\gamma$ along its path, and the energy compensation of the rf field is along the longitudinal direction; the betatron motion is also damped. Equilibrium is reached when the quantum fluctuation due to the emission of photons and the synchrotron radiation damping are balanced. The resulting momentum spread is independent of the rf voltage, and the transverse emittance depends essentially on the lattice arrangement.

In this section we examine applications of the rf systems in the bunched beam manipulations, including phase displacement acceleration, phase-space stacking, adiabatic capture, bucket to bucket transfer, bunch rotation, and debunching. We carefully study the double rf systems, that have often been applied in the space charge dominated beams and high brilliance electron storage rings for providing a larger tune spread for Landau damping. We also study the barrier rf systems that have been proposed for low energy proton synchrotrons. In general, innovative bunched beam manipulation schemes can enhance beam quality for experiments.

V.1 RF Frequency Requirements

Particle acceleration in synchrotrons requires synchronism between rf frequency and particle revolution frequency. Thus the rf frequency is an integer multiple of the revolution frequency $\omega_{\text{rf}} = h\omega_0(B, R_0)$, where h is the harmonic number, and the angular revolution frequency ω_0 is a function of the magnetic field B and the average radius of the synchrotron R_0. The momentum p_0 of a particle is related to the magnetic field by $p_0 = e\rho B$, where ρ is the bending radius, and e is the particle's charge. Thus the rf frequency is

$$\omega_{\text{rf}} = h\frac{\beta c}{R_0} = \frac{he\rho B}{R_0 \gamma m} = \frac{hc}{R_0}\left[\frac{B^2(t)}{B^2(t) + (mc^2/ec\rho)^2}\right]^{1/2}, \qquad (3.179)$$

$$\frac{mc^2}{ec\rho} = \begin{cases} 3.1273/\rho\,[\text{m}]\ \text{Tesla} & \text{for protons,} \\ 0.001703/\rho\,[\text{m}]\ \text{Tesla} & \text{for electrons,} \end{cases}$$

where m is the particle's mass. The rf frequency is a function of the dipole magnetic field, particularly particularly important for low energy proton or ion accelerators. In low to medium energy synchrotrons, the rf system is usually limited by the range of required frequency swing. Table 3.4 lists parameters of some proton synchrotrons.

Table 3.4: RF parameters of some proton synchrotrons

	AGS BST	AGS	RHIC	FNALBST	FNALMI
Inj. K.E. [GeV/u]	0.001/0.2	0.2(1.5)	12	0.2(0.4)	8.0
Acc. Rate [GeV/s]	100	60	3.7	200	100
Max. K.E. [GeV]	1.5	30	250	8	500
f_{rf} [MHz]	0.18–4.1	2.4–4.6	26.68–26.74	30.0–52.8	52.8–53.1
Av. Radius [m]	$(1/4)R_{\text{ags}}$	128.457	$(19/4)R_{\text{ags}}$	75.47	528.30
h	1–3 (2)	12 (8)	6×60	84	7×84
V_{rf} [kV]	90	300	300	950	4000

In some applications, the magnetic field can be ramped linearly as $B = a + bt$, or resonantly as $B = (\hat{B}/2)(1 - \cos\omega t) = \hat{B}\sin^2(\omega t/2)$, with ramping frequency $\omega/2\pi$ varying from 1 Hz to 50 Hz; the rf frequency should follow the magnetic field ramp according to Eq. (3.179), for which cavities with ferrite tuners are usually used. On the other hand, electrons are nearly relativistic at all energies, and the rf frequency swing is small. High frequency pill-box-like cavities are usually used. Normally the frequency range can be in the 200, 350, 500, and 700 MHz regions, where rf power sources are readily available. In recent years, wideband solid state rf power sources and narrowband klystron power sources have been steadily improved. New methods of beam manipulation can be employed.

Requirements of rf systems depend on their applications. To achieve high beam power in meson factories and proton drivers for spallation neutron sources, a fast acceleration rate is important. For example, the ISIS at the Rutherford Appleton Laboratory has a 50 Hz ramp rate, whereas the rf systems in the Spallation Neutron Source (SNS) provide only beam capture. On the other hand, acceleration rate is less important in storage rings used for internal target experiments.

A. The choice of harmonic number

The harmonic number determines the bunch spacing and the maximum number of particles per bunch obtainable from a given source, which can be important for colliding beam facilities. The harmonic numbers are related by the mean radii of the chain of accelerators needed to reach an efficient box-car injection scheme, which is equivalent to bucket to bucket transfer from one accelerator to another. For example, the average radius of the AGS Booster is 1/4 that of the AGS, and the ratio of harmonic numbers is 4. Similar reasoning applies to the chain of accelerators.

Since the damping time of electron beams in electron storage rings (see Table 4.2, Chap. 4, Sec. I.4) is short, the injection scheme of damping accumulation at full energy is usually employed in high performance electron storage rings. The choice of harmonic number for high energy electron storage rings is determined mainly by the availability of the rf power source, efficient high quality cavity design, and the size of the machine. Since rf power sources are available at 200, 350, 500, 700 MHz regions, most of the rf cavities of electron storage rings are operating at these frequencies. The harmonic number is then determined by the rf frequency and circumference of the storage ring.

B. The choice of rf voltage

High intensity beams usually require a larger bunch area to control beam instabilities. Since the rf bucket area and height are proportional to $\sqrt{V_{\rm rf}}$, a minimum voltage is needed to capture and accelerate charged particles efficiently.

In electron storage rings, the choice of rf voltage is important in determining the beam lifetime because of quantum fluctuation and Touschek scattering, a large angle Coulomb scattering process converting the horizontal momenta of two electrons into longitudinal momenta.

In general, the rf voltage is limited by the rf power source and the Kilpatrick limit of sparking at the rf gap. The total rf voltage of synchrotrons and storage rings is usually limited by the available space for the installation of rf cavities.

V.2 Capture and Acceleration of Proton and Ion Beams

At low energy, the intensity and brightness of an injected beam are usually limited by space-charge forces, intrabeam scattering, microwave instability, etc.; phase-space painting for beam distribution manipulation can be used to alleviate some of these problems (see Chap. 2, Sec. III.8, for transverse phase-space painting).

Since the injected beam from a linac normally has a large energy spread, the rf voltage requirement in booster synchrotrons needs enough bucket height for beam injection. The peak voltage is usually limited by the power supply and electric field breakdown at the rf cavity gap. A debuncher or a bunch rotator in the transfer line can be used to lower the momentum width of injected beams. The resulting captured beam brightness depends on the rf voltage manipulation. The following example illustrates the difference between adiabatic capture and non-adiabatic capture processes.

A. Adiabatic capture

During multi-turn injection (transverse or longitudinal phase-space painting or charge exchange strip injection), very little beam loss in the synchrotron phase-space can theoretically be achieved by adiabatically ramping the rf voltage with $\phi_{\mathrm{s}} = 0$. The right plots, (e) to (h), of Fig. 3.20 show an example of adiabatic capture in the IUCF cooler injector synchrotron (CIS). The proton beam was accelerated from 7 to 200 MeV at 1 Hz repetition rate, and the rf voltage $V_{\mathrm{rf}}(t)$ was increased from a small value to 240 V adiabatically, plots (e) and (f), while the synchronous phase was kept at zero. The adiabaticity coefficient of Eq. (3.21) becomes

$$\alpha_{\mathrm{ad}} = \frac{T_{\mathrm{s}}}{4\pi V_{\mathrm{rf}}} \frac{dV_{\mathrm{rf}}}{dt} = \frac{T_{\mathrm{s}}}{2\pi \mathcal{A}_{\mathrm{B}}} \frac{d\mathcal{A}_{\mathrm{B}}}{dt}, \tag{3.180}$$

where T_{s} is the synchrotron period and $\mathcal{A}_{\mathrm{B}}$ is the bucket area. In order to satisfy the adiabatic condition, the initial rf voltage should have a small finite initial voltage V_0, and the rf voltage is ramped to a final voltage smoothly (see also Exercise 3.5.1).

After beam capture, the synchronous phase was ramped adiabatically to attain a desired acceleration rate. Good acceleration efficiency requires adiabatic ramping of V and ϕ_{s} while providing enough bucket area during beam acceleration. In this numerical example, we find that the capture efficiency is about 99.6%. In reality, the momentum spread of the injected beam is about 0.5% instead of 0.1% shown in this example. The maximum voltage is only barely able to hold the momentum spread of the injected beam from linac. The actual capture efficiency is much lower. A possible solution is to install a debuncher in the injection transfer line for lowering the momentum spread of the injected beam.
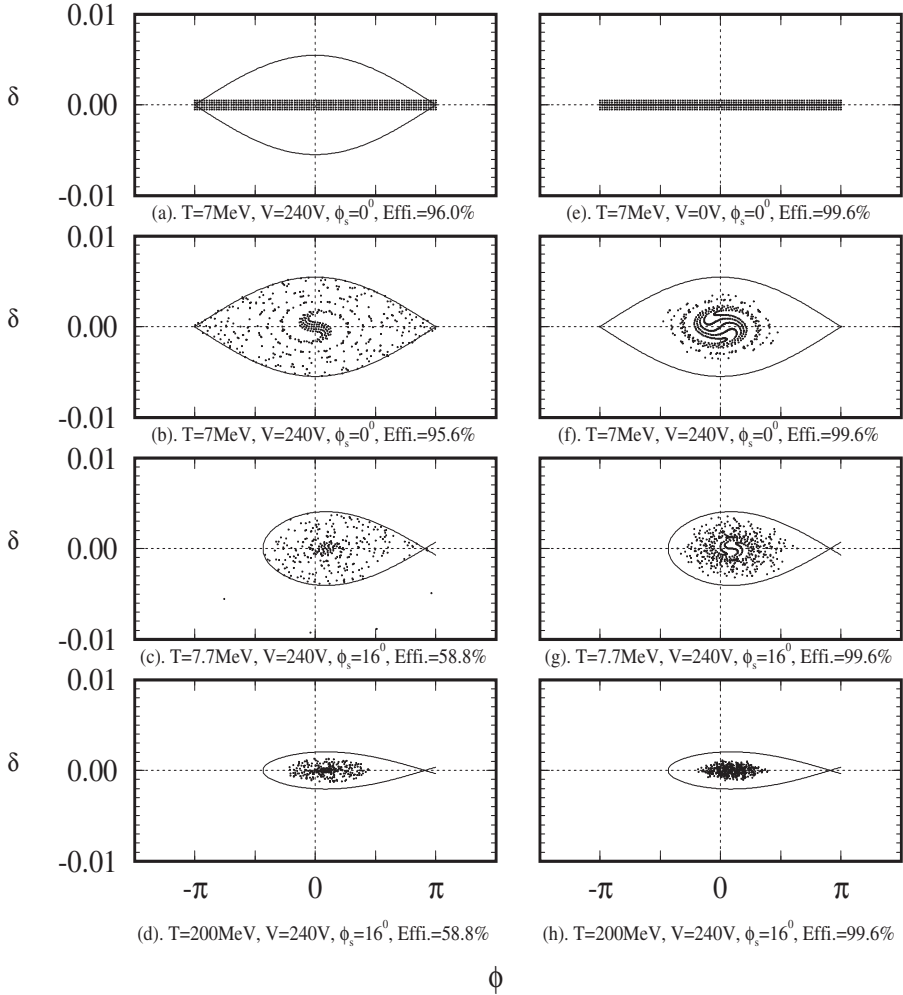
Figure 3.20: The left plots, (a) to (d), show non-adiabatic beam capture during injection and acceleration. The right plots, (e) to (h), show adiabatic capture of the injected beam: the rf voltage is ramped from 0 to 240 V adiabatically to capture the injected beam with a momentum spread of 0.1%. The rf synchronous phase is then ramped adiabatically to achieve the required acceleration rate. The actual momentum spread of the injected beam is about ±0.5%, and thus the actual adiabatic capture efficiency is substantially lower. Space-charge force and microwave instability are not included in the calculation. This calculation was done by X. Kang (Ph.D. Thesis, Indiana University, 1998).

B. Non-adiabatic capture

The left plots, (a) to (d), of Fig. 3.20 show an example of non-adiabatic capture with nonzero initial rf voltage. When the rf voltage is set to 240 V to capture the injected beam, the beam fills up the entire phase-space, as shown in plot (b). Beam loss occurs during acceleration, the final phase-space area is larger, and the capture efficiency is low. With microwave instability and space-charge effects included, the capture efficiency may be even lower.

As seen in plots (b) and (f), the injected beam particles decohere and fill up the entire bucket area because of synchrotron tune spread. The decoherence results in emittance growth.

C. Chopped beam at the source

Many fast cycling synchrotrons require nonzero rf voltage and nonzero rf synchronous phase $\phi_s > 0$ to achieve the desired acceleration rate. In this case, capture efficiency is reduced by the nonadiabatic capture process. To circumvent low efficiency, a beam chopper consisting of mechanical or electromagnetic deflecting devices, located at the source, can be used to paint the phase-space of the injected beam and eliminate beam loss at high energy.

V.3   Bunch Compression and Rotation

When a bunch is accelerated to its final energy, it may be transferred to another accelerator or used for research. When the beam is transferred from one accelerator to another, the beam profile matching condition is

$$
\left[\frac{\hat{\delta}}{R\hat{\theta}} \right]_{\text{acc.1}} = \left[\frac{\hat{\delta}}{R\hat{\theta}} \right]_{\text{acc.2}}, \quad \text{or} \quad \left[\frac{1}{R} \sqrt{\frac{hV}{|\eta|}} \right]_{\text{acc.1}} = \left[\frac{1}{R} \sqrt{\frac{hV}{|\eta|}} \right]_{\text{acc.2}}. \tag{3.181}
$$

This matching condition may be higher than the limit of a low frequency rf system. Similarly, the bunch length of a beam may need to be shortened in many applications. A simple approach is to raise the voltage of the accelerator rf system. However, the peak voltage of an rf system is limited by the breakdown of electric field at the acceleration gap. According to the empirical Kilpatrick criterion, the rf frequency f [MHz] is related to the peak electric field gradient E_K [MV/m] by

$$
f = 1.64 \, E_K^2 \, e^{-8.5/E_K}. \tag{3.182}
$$

Because of this limitation, we have to use different beam manipulation techniques such as bunch compression by rf gymnastics, etc.

Bunched beam gymnastics are particularly important for shortening the proton bunch before the protons hit their target in antiproton or secondary beam production.

Generally, the emittance of secondary beams is equal to the product of the momentum aperture of the secondary-beam capture channel and the bunch length of the primary beam. When the bunch length of a primary proton beam is shortened, the longitudinal emittance of the secondary antiproton beam becomes smaller. The antiproton beam can be further debunched through phase-space rotation in a debuncher by converting momentum spread to phase spread, and the final antiproton beam is transported to an accumulator for cooling accumulation (see Exercise 3.5.3).

Beam bunch compression is also important in shortening the electron bunch in order to minimize the beam breakup head-tail instabilities in a linac (see Sec. VIII). A few techniques of bunch compression are described below.

A. Bunch compression by rf voltage manipulation

The first step it to lower the rf voltage adiabatically, e.g. $V_0 \to V_1$, so that the bucket area is about the same as the bunch area. Then the rf voltage is increased non-adiabatically from V_1 to V_2. The unmatched beam bunch rotates in synchrotron phase-space. At 1/4 or 3/4 of the synchrotron period, a second rf system at a higher harmonic number is excited to capture the bunch, or a kicker is fired to extract beams out of the synchrotron. Figure 3.21 shows schematic phase-space ellipses during the bunch compression process. The lower-left plot shows the final phase-space ellipse in an idealized linear synchrotron motion. In reality, the maximum attainable rf voltage is limited, and the final phase-space ellipse is distorted by the nonlinear synchrotron motion that causes emittance dilution.
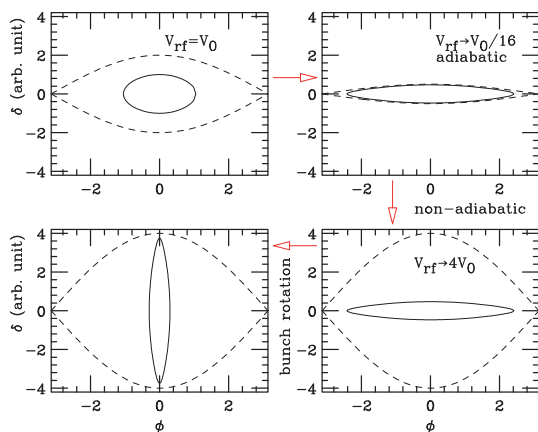

Figure 3.21: Schematic drawings (clockwise) of bunch compression scheme using rf voltage manipulation. The bunch area is initially assumed to be about 1/5 of the bucket area (top-left). The voltage is adiabatically reduced by 16 times so that the bunch is almost fill the bucket area (top-right). As the voltage is non-adiabatically raised to four times the original rf voltage, the mismatched bunch begins to rotate. When the bunch length is shortened (lower-left) at 1/4 of the synchrotron period, a kicker can be fired to extract the beam.

For a given bunch area, the rms bunch width and height are obtained from Eq. (3.42) during the adiabatic rf voltage compression from V_0 to V_1. After the rf voltage is jumped to V_2, the bunch height will become bunch width according to

Eq. (3.42). The maximum bunch compression ratio, defined as the ratio of the bunch lengths at $(V_0 = V_2) \rightarrow V_1 \rightarrow V_2$, becomes

$$r_{\rm c} = \frac{\sigma_{\phi,{\rm i}}}{\sigma_{\phi,{\rm f}}} = \left(\frac{V_2}{V_1}\right)^{1/4} = \left(\frac{\mathcal{A}_{\rm bucket,max}}{\mathcal{A}_{\rm bunch}}\right)^{1/2} = \frac{2\sqrt{2}}{\sqrt{3\pi}\sigma_\phi}, \qquad (3.183)$$

where we have used the properties that the bunch area supposedly fills up the bucket area at $V_{\rm rf} = V_1$, and the fact that the bucket area is 16 (see Table 3.2), and the bunch area containing 95% of the beam is $6\pi\sigma_\phi^2$ in the normalized synchrotron phase space coordinates.

B. Bunch compression using unstable fixed point

If the rf phase is shifted so that the unstable fixed point (UFP) is located at the center of the bunch, the bunch will begin compressing in one direction and stretching in the other direction along the separatrix orbit (see Sec. II.4 and Exercise 3.2.5). In linear approximation, the bunch length and bunch height change according to $\exp\{\pm\omega_{\rm s}t_{\rm ufp}\} = \exp\{\pm 2\pi t_{\rm ufp}/T_{\rm s}\}$, where $\omega_{\rm s}$ is the small amplitude synchrotron angular frequency, $T_{\rm s}$ is the synchrotron period, and $t_{\rm ufp}$ is the time-duration that the bunch stays at the UFP. The length of stay at the UFP can be adjusted to attain a required aspect ratio of the beam ellipse.

When the SFP of the rf potential is shifted back to the center of the bunch. The mis-matched bunch profile will begin to execute synchrotron motion. At 3/8 of the synchrotron period, the bunch can be captured by a matched high frequency rf system or kicked out of the accelerator by fast extraction.

We now derive the ultimate bunch compression ratio for the rf phase shift method as follows. In the normalized phase-space coordinates, ϕ and $\mathcal{P} = -(h|\eta|/\nu_{\rm s})(\Delta p/p)$, the Hamiltonian for stationary synchrotron motion is given by Eq. (3.64).

Near the UFP, the separatrix of the Hamiltonian in Eq. (3.64) can be approximated by two straight lines crossing at 45° angles with the horizontal axis ϕ. When the rf phase is shifted so that the beam sits on the UFP, the bunch width and height will stretch and compress along the separatrix. The rate of growth is equal to $\exp(\omega_s t_{\rm ufp})$. The maximum rf phase coordinate $\phi_{\rm max}$ that a bunch width can increase and still stay within the bucket after the rf phase is shifted back to SFP is given approximately by

$$\frac{1}{2}\phi_{\rm max}^2 + 2\sin^2(\frac{\phi_{\rm max}}{2}) \approx 2, \qquad (3.184)$$

where we assume linear approximation for particle motion near SFP. Thus we obtain $\phi_{\rm max} \approx \sqrt{2}$. Using Liouville's theorem, conservation of phase-space area, we find

$$\pi\sigma_{\phi,{\rm i}}^2 = \pi\sigma_{\mathcal{P},{\rm f}}\sigma_{\phi,{\rm f}}. \qquad (3.185)$$

Assuming that 95% of the beam particles reach $\phi_{\max} = \sqrt{2}$ so that $\sigma_{\mathcal{P},\mathrm{f}} = \frac{\sqrt{2}}{\sqrt{6}}\phi_{\max} = \sqrt{2/3}$, we find the compression ratio as

$$r_{\mathrm{c,max}}^{\mathrm{p}} = \frac{\sigma_{\phi,\mathrm{i}}}{\sigma_{\phi,\mathrm{f}}} = \frac{\sigma_{\mathcal{P},\mathrm{f}}}{\sigma_{\phi,\mathrm{i}}} \approx \frac{\sqrt{2}}{\sqrt{3}\sigma_{\phi,\mathrm{i}}}, \tag{3.186}$$

The time needed to reach this maximum compression ratio is

$$\omega_{\mathrm{s}}\hat{t}_{\mathrm{ufp}} = \ln\frac{1}{\sigma_{\phi,\mathrm{i}}} - 0.203. \tag{3.187}$$

A difficulty associated with bunch compression using rf phase-shift is that the rf voltage may remain at a relatively low value during the bunch rotation stage. The effect of non-linear synchrotron motion will be more important because the ratio of bucket-area to the bunch-area is small.

The difficulty of nonlinear synchrotron motion in the final stage of bunch rotation can be solved by using the buncher in the transport line. After proper bunch compression, the beam is kicked out of the synchrotron and the R_{56} transport matrix element will compress bunch, i.e. lower energy particles travel shorter path, and the higher energy particle travel a longer path. However, the resulting compression ratio is reduced by a factor of $1/\sqrt{2}$. Since there is no constraint that the final bunch size should fit into the bucket, one can regain the factor of $\sqrt{2}$ in staying longer at the UFP.

C. Bunch rotation using buncher/debuncher cavity

The principle of bunch rotation by using a buncher/debuncher cavity is based on the correlation of the time and off-momentum coordinates (the transport element R_{56}). By employing a cavity to accelerate and decelerate parts of the beam bunch, the bunch length and the momentum spread can be adjusted. This method is commonly used in the beam transfer line. For example, a simple debuncher used to decrease the energy spread of a non-relativistic beam out of a linac can function as follows. First, let the beam drift a distance L so that higher energy particles are ahead of lower energy particles. A cavity that decelerates leading particles and accelerates trailing particles can effectively decrease the energy spread of the beam.

For relativistic particles, a drift space can not provide the correlation for the transport element R_{56} because all particles travel at almost the same speed. It requires bending magnets for generating local dispersion functions so that the path length is correlated with the off-momentum coordinate.[32] A buncher/debuncher cavity can then be used to shorten or lengthen the bunch.

---

[32]See e.g., T. Raubenheimer, P. Emma, and S. Kheifets, *Proc. 1993 PAC*, p. 635 (1993).

V.4   Debunching

When rf systems are non-adiabatically turned off, particles drift and fill up the entire ring because the rotation frequency depends on the off-momentum variable. The debunching rate is $\dot{\phi} = h\omega_0\eta\delta$. Neglecting synchrotron radiation loss, the momentum spread will not change. The bunch shape will be distorted because particles of higher and lower momenta drift in different directions. The debunching time can be expressed as

$$T_{\rm db} = 2\pi/h\omega_0\eta\hat{\delta}, \tag{3.188}$$

where $\hat{\delta}$ is the maximum momentum spread of a beam. Note that the momentum spread of the entire beam remains the same in this non-adiabatic debunching process.

To reduce the momentum spread in the debunching process, we can adiabatically lower the rf voltage. In this case, the resulting debunched beam has a smaller momentum spread. The phase-space area remains the same if we can avoid collective beam instability.

V.5   Beam Stacking and Phase Displacement Acceleration

The concept of beam stacking is that groups of particles are accelerated to a desired energy and left to circulate in a fixed magnetic field; and subsequent groups are accelerated and deposited adjacent to each other. The accumulated beam will overlap in physical space at special locations, e.g. small β and zero $D(s)$ locations, which increases the density and the collision rate. In a successful example of beam stacking in the ISR pp collider, a single beam current of 57.5 A was attained. To accomplish phase-space stacking, phase displacement acceleration is usually employed.[33]

In a Hamiltonian system, particles can not cross the separatrix, therefore particles outside the bucket can not be captured during acceleration. Since the magnetic field depends on rf frequency, only particles inside the stable rf bucket are accelerated toward high energy. Particles outside the rf bucket are lost in the vacuum chamber because of the finite magnet aperture.

What happens to the unbunched coasting beam outside the separatrix when an empty moving bucket is accelerated through the beam? Since the beam is outside the separatrix, it may not be captured into the bucket if the rf bucket acceleration is adiabatic. Particles flow along lines of constant action, and their energies are lowered. The change in energy is $\Delta E = \omega_0 A/2\pi$. Similarly, when a bucket is decelerated toward lower energy, the beam energy will be displaced upward in phase-space, i.e. accelerated. Phase displacement acceleration has been used to accelerate coasting beams

---

[33]K.R. Symon and A.M. Sessler, *Methods of radio-frequency acceleration in fixed field accelerators with applications to high current and intersecting beam accelerators*, p. 44, CERN Symp. 1956; L.W. Jones, C.H. Pruett, K.R. Symon and K.M. Terwilliger, in *Proc. of Int. Conf. on High-Energy Accelerators and Instrumentation*, p. 58 (CERN, 1959).

in the Intersecting Storage Ring (ISR) at CERN[34] and to compensate synchrotron radiation loss in electron storage rings.

In a storage rings with electron cooling or stochastic cooling, a newly injected beam accelerated by phase displacement can be moved toward the cooling stack to achieve a high cooling rate. This method has been successfully used to accumulate polarized protons at low energy cooling storage rings, and to accumulate antiprotons at antiproton accumulators. For example, the cooling stacking method can enhance polarized proton intensity by a factor of 1000 in the IUCF Cooler.[35] Similarly, with phase displacement acceleration, antiprotons can be moved to the cooling stack for cooling accumulation.

V.6   Double rf Systems

Space charge has been an important limitation to beam intensity in many low energy proton synchrotrons. Space charge induces potential well distortion and generates coherent and incoherent betatron tune shifts, which may lower the thresholds for transverse and longitudinal collective instabilities. Fast beam loss may occur during accumulation and storage when the peak beam current exceeds a threshold value.

To increase the threshold beam intensity, a double rf system has often been used to increase the synchrotron frequency spread, which enhances Landau damping in collective beam instabilities. As early as 1971, an attempt was made to increase Landau damping by installing a cavity operating at the third harmonic of the accelerating frequency in the Cambridge Electron Accelerator (CEA).[36] This technique was also successfully applied to cure coupled bunch mode instabilities at ISR, where an additional cavity was operated at the sixth harmonic of the primary rf frequency.[37]

Adding a higher harmonic rf voltage to the main rf voltage can flatten the potential well. Since the equilibrium beam profile follows the shape of the potential well, a double rf system can provide a smaller *bunching factor*, defined as the fraction of the circumference occupied by a beam or the ratio of peak current to average current, than that of a single rf system. Therefore, for a given DC beam current in a synchrotron, the peak current and consequently the incoherent space-charge tune shift are reduced. For example, a double rf system with harmonics 5 and 10 was successfully used in

[34]A high current stack at the ISR has a momentum spread of about 3%, that can be handled by a low power rf system in the ISR. By employing the phase displacement acceleration, the circulating beams in ISR were accelerated from 26 GeV to 31.4 GeV without loss of luminosity. The installation of low-β superconducting quadrupoles in 1981 brought a record luminosity of 1.4×10^{32} cm^{2}s^{-1}. The machine stopped operation in December 1983, giving its way to a fully operational SP$\bar{\text{P}}$S, that observed its first $p\bar{p}$ collision at the center of mass energy of 540 GeV on July 10, 1981.

[35]A. Pei, Ph.D. Thesis, Indiana University (1993).

[36]R. Averill *et al.*, *Proc. 8th Int. Conf. on High Energy Accelerators*, p. 301 (CERN 1971).

[37]P. Bramham *et al.*, *Proc. 9th Int. Conf. on High Energy Accel.* (CERN, 1974); P. Bramham *et al.*, *IEEE Trans. Nucl. Sci.* **NS-24**, 1490 (1977).

the Proton Synchrotron Booster (PSB) at CERN to increase the beam intensity by
$25 - 30\%$ when the coherent longitudinal sextupole and decapole mode instabilities
were suppressed by beam feedback systems.[38] At the Indiana University Cyclotron
Facility (IUCF), a recent beam dynamics experiment showed that with optimized
electron cooling the beam intensity in the cooler ring was quadrupled when two rf
cavities were used.[39]

A. Synchrotron equation of motion in a double rf system

For a given particle at angular position θ relative to the synchronous angle $\theta_{\rm s}$, the
phase angle of the primary rf system can be expressed as

$$\phi = \phi_{1\rm s} - h_1(\theta - \theta_{\rm s}), \tag{3.189}$$

where ϕ is the phase coordinate relative to the primary rf cavity, $\phi_{1\rm s}$ is the phase
angle for the synchronous particle, and h_1 is the harmonic number for the primary rf
system. Similarly, the rf phase angle for the second rf system is

$$\phi_2 = \phi_{2\rm s} - h_2(\theta - \theta_{\rm s}) = \phi_{2\rm s} + \frac{h_2}{h_1}(\phi - \phi_{1\rm s}), \tag{3.190}$$

where h_2 is the harmonic number for the second rf system and $\phi_{2\rm s}$ is the corresponding
synchronous phase angle. The equation of motion becomes

$$\dot{\delta} = \frac{\omega_0 e V_1}{2\pi \beta^2 E} \left\{ \sin\phi - \sin\phi_{1\rm s} + \frac{V_2}{V_1} \left(\sin\left[\phi_{2\rm s} + \frac{h_2}{h_1}(\phi - \phi_{1\rm s})\right] - \sin\phi_{2\rm s} \right) \right\}, \tag{3.191}$$

where the overdot is the derivative with respect to orbiting angle θ, and V_1 and V_2 are
the voltages of the rf cavities. Equations (3.13) and (3.191) are Hamilton's equations
of motion for a double rf system.

Using the normalized momentum coordinate $\mathcal{P} = -(h_1|\eta|/\nu_{\rm s})(\Delta p/p_0)$, the Hamil-
tonian is

$$\begin{aligned}
H &= \frac{1}{2}\nu_{\rm s}\mathcal{P}^2 + V(\phi), \tag{3.192}\\
V(\phi) &= \nu_{\rm s}\{(\cos\phi_{1\rm s} - \cos\phi) + (\phi_{1\rm s} - \phi)\sin\phi_{1\rm s} \\
&\quad - \frac{r}{h}\left[\cos\phi_{2\rm s} - \cos\left(\phi_{2\rm s} + h(\phi - \phi_{1\rm s})\right) - h(\phi - \phi_{1\rm s})\sin\phi_{2\rm s}\right]\}.
\end{aligned}$$

Here $\nu_{\rm s} = \sqrt{h_1 e V_1 |\eta|/2\pi\beta^2 E_0}$ is the synchrotron tune at zero amplitude for the
primary rf system, $h = h_2/h_1$, $r = -V_2/V_1$, and $\phi_{1\rm s}$ and $\phi_{2\rm s}$ are the corresponding rf

[38]See J.M. Baillod *et al.*, *IEEE Trans. Nucl. Sci.* **NS-30**, 3499 (1983); G. Galato *et al*, *Proc. PAC*, p. 1298 (1987).

[39]See S.Y. Lee *et al.*, *Phys. Rev.* E**49**, 5717 (1994); J.Y. Liu *et al.*, *Phys. Rev.* E**50**, R3349 (1994); J.Y. Liu *et al.*, *Part. Accel.* **49**, 221-251 (1995).

phase angles of a synchronous particle. Here, the conditions $r = 1/h$ and $h \sin \phi_{2s} = \sin \phi_{1s}$ are needed to obtain a flattened potential well. For $r > 1/h$, there are two inner buckets on the ϕ axis. The effective acceleration rate for the beam is $\Delta E = eV_1(\sin \phi_{1s} - r \sin \phi_{2s})$ per revolution.

Because the rf bucket is largest at the lowest harmonic ratio, we study the double rf system with $h = 2$. To simplify our discussion, we study a stationary bucket with $\phi_{1s} = \phi_{2s} = 0°$. However, the method presented in this section can be extended to more general cases with $\phi_{1s} \neq 0$ and $\phi_{2s} \neq 0$.

B. Action and synchrotron tune

When the synchrotron is operating at $\phi_{1s} = \phi_{2s} = 0$, the net acceleration is zero and the Hamiltonian becomes

$$H = \frac{\nu_s}{2}\mathcal{P}^2 + \nu_s \left[(1 - \cos \phi) - \frac{r}{2}(1 - \cos 2\phi) \right]. \tag{3.193}$$

The fixed points $(\phi_{\mathrm{FP}}, \mathcal{P}_{\mathrm{FP}})$ are listed in Table 3.5.

Table 3.5: SFP and UFP of a double rf system.

	SFP	UFP
$0 \leq r \leq \frac{1}{2}$	(0,0)	$(\pi, 0)$
$\frac{1}{2} < r$	$(\pm \arccos(\frac{1}{2}), 0)$	$(0, 0),\ (\pm\pi, 0)$

Since the Hamiltonian is autonomous, the Hamiltonian value E is a constant of motion with $E/\nu_s \in [0, 2]$. The action is

$$J(E) = \frac{1}{\pi} \int_{-\hat{\phi}}^{\hat{\phi}} \mathcal{P}\, d\phi, \tag{3.194}$$

where $\hat{\phi}$ is the maximum phase angle for a given Hamiltonian torus. The value E is related to $\hat{\phi}$ by $E = 2\nu_s(1 - 2r \cos^2(\hat{\phi}/2)) \sin^2(\hat{\phi}/2)$; the phase-space area is $2\pi J$; and the synchrotron tune is $Q_s = (\partial J/\partial E)^{-1}$. The bucket area $\mathcal{A}_b$ is

$$\mathcal{A}_b = 2\pi \hat{J} = 8 \left[\sqrt{1 + 2r} + \frac{1}{\sqrt{2r}} \ln(\sqrt{1 + 2r} + \sqrt{2r}) \right], \tag{3.195}$$

which is a monotonic increasing function of the ratio r. The corresponding bucket area for the single rf system is $\mathcal{A}_b(r \to 0) = 16$ (see Table 3.2).

C. The $r \leq 0.5$ case

Changing the variables with

$$t = \tan\frac{\phi}{2}, \quad d\phi = \frac{2}{1+t^2}dt, \quad t_0 = \tan\frac{\hat{\phi}}{2}, \quad \tau = \frac{t}{t_0},$$

we obtain

$$\frac{\partial J}{\partial E} = \frac{2(1+t_0^2)}{\pi\nu_s t_0[1+(1+2r)t_0^2]^{1/2}} \int_0^1 \left[(1-\tau^2)\left(\frac{1-2r+t_0^2}{t_0^2[1+(1+2r)t_0^2]} + \tau^2 \right) \right]^{-1/2} d\tau. \tag{3.196}$$

Thus the synchrotron tune becomes [31]

$$\frac{Q_s}{\nu_s} = \frac{\pi\sqrt{(1-2r)+2t_0^2+(1+2r)t_0^4}}{2(1+t_0^2)K(k_1)}, \tag{3.197}$$

where $K(k_1)$ is the complete elliptic integral of the first kind with modulus

$$k_1 = \frac{t_0\sqrt{1+(1+2r)t_0^2}}{\sqrt{(1-2r)+2t_0^2+(1+2r)t_0^4}}. \tag{3.198}$$

In fact, this formula is also valid for $r > 0.5$ and $\hat{\phi} > \phi_b$, where ϕ_b is the intercept of the inner separatrix with the phase axis.

D. The $r > 0.5$ case

For $r > 0.5$, the origin of phase-space $\mathcal{P} = \phi = 0$ becomes a UFP of the unperturbed Hamiltonian. Two SFPs are located at $\mathcal{P} = 0$ and $\phi = \pm\phi_f$, where $\cos(\phi_f/2) = 1/2r$. The inner separatrix, which passes through the origin, intersects the phase axis at $\pm\phi_b$ with $\cos(\phi_b/2) = 1/\sqrt{2r}$. Figure 3.22 shows ϕ_b and ϕ_f and some phase space ellipses for $r = 0.6$.
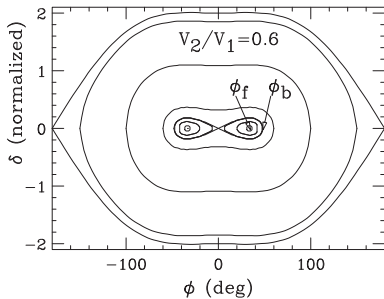
Figure 3.22: RF bucket and phase space ellipses for a double rf system with $h_2/h_1 = 2$ and $r = V_2/V_1 = 0.6$. Two stable fixed points are located at $(\pm\phi_f, 0)$, where $\phi_f = \cos^{-1}(1/2r)$. The maximum phase amplitude of the inner separatrix is $\phi_b = \cos^{-1}(1/\sqrt{2r})$. For $r \gg 1$, the SFP $\phi_f \to \pm\frac{\pi}{2}$, and the bucket is split into 2.

A given torus inside the inner bucket corresponds to a Hamiltonian flow of constant Hamiltonian value. Let ϕ_l and ϕ_u be the lower and upper intercepts of a torus with the

phase axis, where $\phi_\mathrm{u} = \hat{\phi}$ and $\sin(\phi_\mathrm{l}/2) = \sqrt{\sin^2(\phi_\mathrm{b}/2) - \sin^2(\phi_\mathrm{u}/2)}$. The derivative of the action with respect to the energy for the torus becomes

$$\frac{\partial J}{\partial E} = \frac{\sqrt{(1+t_\mathrm{u}^2)(1+t_\mathrm{l}^2)}}{\pi\nu_\mathrm{s}\sqrt{2r}} \int_{t_\mathrm{l}}^{t_\mathrm{u}} \frac{dt}{\sqrt{(t_\mathrm{u}^2 - t^2)(t^2 - t_\mathrm{l}^2)}}, \tag{3.199}$$

where $t_\mathrm{u} = \tan(\phi_\mathrm{u}/2)$, $t_\mathrm{l} = \tan(\phi_\mathrm{l}/2)$, $t = \tan(\phi/2)$, and $d\phi = 2dt/(1+t^2)$. Thus the synchrotron tune is

$$\frac{Q_\mathrm{s}}{\nu_\mathrm{s}} = \frac{\sqrt{2r}\pi t_\mathrm{u}}{\sqrt{(1+t_\mathrm{u}^2)(1+t_\mathrm{l}^2)}} \frac{1}{K(k_2)}, \tag{3.200}$$

where modulus $k_2 = \sqrt{t_\mathrm{u}^2 - t_\mathrm{l}^2}/t_\mathrm{u}$.

Figure 3.23 shows the synchrotron tune as a function of the amplitude of synchrotron oscillation for various voltage ratios. At $r = 0$, the system reduces to a single primary rf cavity, where the synchrotron tune is $Q_\mathrm{s}/\nu_\mathrm{s} = 1$ at zero amplitude. As r increases, the derivative of synchrotron tune vs action becomes large near the origin. Since large tune spread of the beam is essential for Landau damping of collective beam instabilities, an optimal rf voltage ratio is $r = 0.5$, where the synchrotron tune spread of the beam is maximized for a given bunch area.

At $r = 0.5$, the synchrotron tune becomes

$$\frac{Q_\mathrm{s}}{\nu_\mathrm{s}} = \frac{\pi t_0}{\sqrt{2(1+t_0^2)}K(k)} = \frac{\pi(E/2\nu_\mathrm{s})^{1/4}}{\sqrt{2}K(k)} \tag{3.201}$$

with modulus

$$k = \sqrt{\frac{1}{2}\left(1 + \frac{t_0^2}{1+t_0^2}\right)} = \sqrt{\frac{1}{2}\left(1 + \sqrt{\frac{E}{2\nu_\mathrm{s}}}\right)},$$

where $t_0 = \tan(\hat{\phi}/2)$. For small amplitude synchrotron motion, $t_0 = 0$ and $k_0 = 1/\sqrt{2}$. In this case, the maximum synchrotron tune is $\hat{Q}_\mathrm{s} = 0.7786\nu_\mathrm{s}$, located at $\hat{\phi} = 117°$ (or $E = 1.057\nu_\mathrm{s}$). Near this region, $\partial Q_\mathrm{s}/\partial\hat{\phi}$ is very small or zero. When the voltage ratio is $r > 0.5$, a dip in $Q_\mathrm{s}(J)$ appears at the inner separatrix of inner buckets, and two small potential wells are formed inside the inner separatrix.

E. Action-angle coordinates

Although analytic solutions for action-angle variables, presented in this section, are valid only for the case with $r = 0.5$, the method can be extended to obtain similar solutions for other voltage ratios. With the generating function, the angle coordinate becomes

$$F_2(\phi, J) = \int_{\hat{\phi}}^{\phi} \mathcal{P}(\phi')d\phi', \tag{3.202}$$

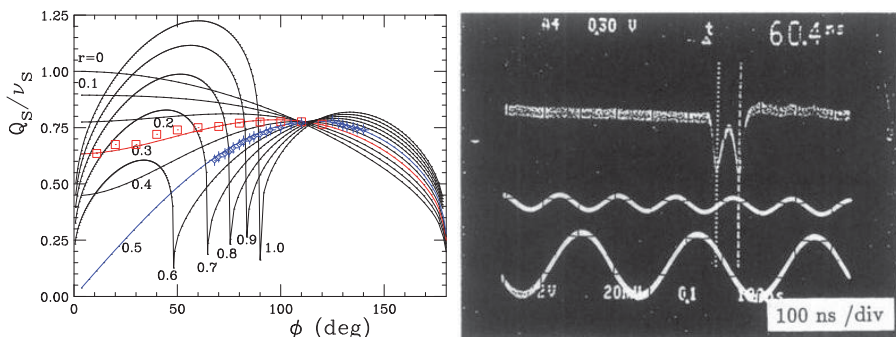Figure 3.23: Left: The normalized synchrotron tune as a function of the peak phase $\phi = \hat{\phi}$ for various values of voltage ratio r. The rectangular and star symbols are data measured at the IUCF Cooler Ring. Note that when $r > 0.5$, the center of the bucket becomes an UFP. Two SFPs are located at the phase amplitude $\phi = \arccos(1/2r)$, where the synchrotron tune is maximum. Right: Beam profile of a proton beam bunch that was cooled by electron-cooling system and damped to 2 beamlets at stable fixed points. The separation between beamlets can be used to calibrate voltage ratio of 2 rf systems resulting $r = 0.6$ in this experiment.

$$
\begin{aligned}
\psi &= \frac{\partial F_2}{\partial J} = \frac{\partial E}{\partial J} \int_{\hat{\phi}}^{\phi} \frac{\partial \mathcal{P}}{\partial E} d\phi' = \frac{Q_s}{\nu_s} \int_{\hat{\phi}}^{\phi} \frac{d\phi}{\mathcal{P}} \\
&= \frac{Q_s}{\nu_s} \frac{(1+t_0^2)}{t_0 \sqrt{1+2t_0^2}} \int_1^{\tau} \left((1-\tau^2)(\frac{1}{1+2t_0^2} + \tau^2) \right)^{-1/2} d\tau = \frac{Q_s}{\sqrt{2}\nu_s} \frac{\sqrt{1+t_0^2}}{t_0} u,
\end{aligned}
$$

where

$$
u = \int_1^{\mathrm{cn}u} \frac{dx}{\sqrt{(1-x^2)(k'^2 + k^2 x^2)}}, \quad k = \sqrt{(1+2t_0^2)/[2(1+t_0^2)]}, \quad k' = \sqrt{1-k^2},
$$

and the Jacobian elliptical function $\mathrm{cn}u$ is

$$
\mathrm{cn}u = \frac{\tan(\phi/2)}{\tan(\hat{\phi}/2)} = \frac{2\pi}{kK(k)} \sum_{n=0}^{\infty} \frac{q^{n+1/2}}{1+q^{2n+1}} \cos[(2n+1)\psi], \tag{3.203}
$$

with $q = e^{-\pi K'/K}$, $K' = K(\sqrt{1-k^2})$, and

$$
\psi = \frac{Q_s}{\nu_s} \frac{\sqrt{1+t_0^2}}{\sqrt{2}t_0} u = \frac{\pi u}{2K(k)}, \tag{3.204}
$$

From Eq. (3.203), we obtain

$$
\phi = 2\arctan\left(\tan\frac{\hat{\phi}}{2} \, \mathrm{cn}u \right), \quad \text{or} \quad \tan\frac{\phi}{2} = \tan\frac{\hat{\phi}}{2}\mathrm{cn}u, \tag{3.205}
$$

and from Hamilton's equation of motion, we get

$$
\mathcal{P} = -2\sqrt{2}\sin\left(\frac{\hat{\phi}}{2}\right)\tan\left(\frac{\hat{\phi}}{2}\right)\frac{\operatorname{sn}u\ \operatorname{dn}u}{1 + [\tan(\hat{\phi}/2)\operatorname{cn}u]^2}. \tag{3.206}
$$

When the voltage ratio is not 0.5, Eqs. (3.204) to (3.206) remain valid provided that the modulus is replaced by k_1 of Eq. (3.198) or k_2 of Eq. (3.200).

Thus the transformation of the phase-space coordinates $(\phi, \mathcal{P})$ to the action-angle variables (J, ψ) can be accomplished by using Eqs. (3.205) and (3.206) or equivalently

$$
\sin\frac{\phi}{2} = \frac{\xi^{1/4}\ \operatorname{cn}u}{\sqrt{1 - \xi^{1/2}\ \operatorname{sn}^2 u}}, \qquad \frac{\mathcal{P}}{2} = \pm\xi^{1/2}\sqrt{1 - \frac{\operatorname{cn}^4 u}{(1 - \xi^{1/2}\ \operatorname{sn}^2 u)^2}}, \tag{3.207}
$$

where $\xi = E/2\nu_{\mathrm{s}}$.

F. Small amplitude approximation

A tightly bunched beam occupies a small phase-space area. The formulas for small amplitude approximation are summarized as follows:

$$
J \approx \frac{8\sqrt{2}K}{3\pi}\left(\frac{E}{2\nu_{\mathrm{s}}}\right)^{3/4} = \frac{8\sqrt{2}K}{3\pi}\sin^3\frac{\hat{\phi}}{2}, \tag{3.208}
$$

$$
\frac{Q_{\mathrm{s}}}{\nu_{\mathrm{s}}} \approx \frac{\pi}{\sqrt{2}K}\sin\frac{\hat{\phi}}{2},
$$

$$
\phi \approx \hat{\phi}\frac{2\pi}{kK}\sum_{n=0}^{\infty}\frac{q^{n+1/2}}{1 + q^{2n+1}}\cos(2n+1)\psi,
$$

$$
\mathcal{P} = -\hat{\phi}^2\frac{\pi^2}{\sqrt{2}kK^2}\sum_{n=0}^{\infty}\frac{(2n+1)q^{n+1/2}}{1 + q^{2n+1}}\sin(2n+1)\psi, \tag{3.209}
$$

where $k \approx 1/\sqrt{2}$, $K = K(k) \approx 1.8541$, and $q \approx e^{-\pi}$.

Let $\mathcal{A}$ be the rms phase-space area of the bunch, and $\sigma_{\mathcal{P}}$ and σ_{ϕ} the rms conjugate phase-space coordinates. We then obtain

$$
\sigma_{\phi} = \left(\frac{3\mathcal{A}}{2\sqrt{2}K}\right)^{1/3}, \quad \sigma_{\mathcal{P}} = \left(\frac{3\mathcal{A}}{8K}\right)^{2/3}. \tag{3.210}
$$

The rms tune spread of the beam is then

$$
\Delta Q = \frac{\pi}{\sqrt{2}K}\left(\frac{3\mathcal{A}}{16\sqrt{2}K}\right)^{1/3}\nu_{\mathrm{s}}. \tag{3.211}
$$

G. Sum rule theorem and collective instabilities

The perturbing potential due to rf phase modulation is linearly proportional to $\mathcal{P}$ of Eq. (3.206). Expanding $\mathcal{P}$ in action-angle coordinates as $\mathcal{P} = \sum_n f_n(J)e^{jn\psi}$, we find that the strength functions $f_n(J)$ satisfy the sum rule shown in Eq. (3.78). The sum rule can be used to identify the region of phase-space that is sensitive to rf phase modulation (see Exercise 3.3.1).

Since $dQ/dJ = 0$ occurs inside the bucket, it may be of concern that large amplitude particles can become unstable against collective instabilities. When an rf phase or voltage noise is applied to beams in a double rf system, particle motion near the center of the bucket may become chaotic because of overlapping resonances. However, the chaotic region is bounded by invariant tori, and the effect on beam dilution may not be important. A most critical situation arises when the synchrotron amplitude of the beam reaches the region where Q_s is maximum or near the rf bucket boundary, where the tune spread is small. The beam may be susceptible to collective instabilities, and feedback systems may be needed for a high intensity beam that occupies a sizable phase-space area.

V.7 The Barrier RF Bucket

Bunch beam gymnastics have been important in antiproton production, beam coalescence for attaining high bunch intensity, multi-turn injection, accumulation, phase-space painting, etc. The demand for higher beam brightness in storage rings and higher luminosity in high energy colliders requires intricate beam manipulations at various stages of beam acceleration. In particular, a flattened rf wave form can be employed to shape the bunch distribution in order to alleviate space-charge problems in low energy proton synchrotrons and to increase the tune spread in electron storage rings. The extreme of the flattened rf wave form is the barrier bucket.[40]

For achieving high luminosity in the Fermilab TeV collider Tevatron, a Recycler has been built, which would recycle unused antiprotons from the Tevatron. The recycled antiprotons can be cooled by stochastic cooling or electron cooling to attain high phase-space density. At the same time, the Recycler would also accumulate newly produced, cooled antiprotons from the antiproton Accumulator. To maintain the antiproton bunch structure, a barrier rf wave form can be used to confine the beam bunch and shape the bunch distribution waiting for the next collider refill. The required bunch length and the momentum spread of the beam can be adjusted more easily by gymnastics with barrier rf waves than with the usual rf cavities.

---

[40]See J. Griffin, C. Ankenbrandt, J.A. MacLachlan, and A. Moretti, *IEEE Trans. Nucl Sci.* **NS-30**, 3502 (1983); V.K. Bharadwaj, J.E. Griffin, D.J. Harding, and J.A. MacLachlan, *IEEE Trans. Nucl. Sci.* **NS-34**, 1025 (1987); S.Y. Lee and K.Y. Ng, *Phys. Rev.* E**55**, 5992 (1997); M. Fujieda *et al.*, PRSTAB **2**, 122001 (1999).

The barrier rf wave is normally generated by a solid state power amplifier, which has intrinsic wide bandwidth characteristics. An arbitrary voltage wave form can be generated across a wideband cavity gap. Figure 3.24 shows some possible barrier rf waves with half sine, triangular, and square function forms. These wave forms are characterized by voltage amplitude $V(\tau)$, pulse duration T_1, pulse gap T_2 between positive and negative voltage pulses, and integrated pulse strength $\int V(\tau)d\tau$. For example, the integrated pulse strength for a square wave form is $V_0 T_1$. The rf wave form is applied to a wideband cavity with frequency $h f_0$, where h is an integer, and f_0 is the revolution frequency of synchronous particles. The effect on the beam depends mainly on the integrated voltage of the rf pulse. Acceleration or deceleration of the beam can be achieved by employing a biased voltage wave in addition to the bunch-confining positive and negative voltage pulses.
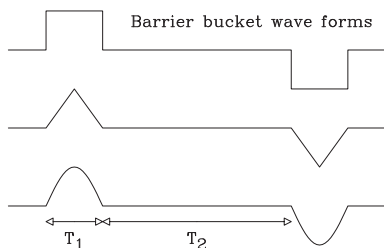
Figure 3.24: Possible wave forms for the barrier bucket. The barrier rf wave is characterized by a voltage height $V(\tau)$, a pulse width T_1, and a pulse gap T_2.

Most of the time, orbiting particles see no cavity field in passing through the cavity gap. When a particle travels in the time range where the rf voltage is not zero, its energy can increase or decrease depending on the sign of the voltage it encounters. In this way, the accelerator is divided into stable and unstable regions. Thus the wide bandwidth rf wave can create a barrier bucket to confine orbiting particles.

A. Equation of motion in a barrier bucket

For a particle with energy deviation ΔE, the fractional change of the orbiting time $\Delta T/T_0$ is

$$\frac{\Delta T}{T_0} = \eta \frac{\Delta E}{\beta^2 E_0}, \qquad (3.212)$$

where η is the phase slip factor, βc and E_0 are the speed and the energy of a synchronous particle, and T_0 is its revolution period. Without loss of generality, we consider here synchrotron motion with $\eta < 0$. For $\eta > 0$, the wave form of the barrier bucket is reversed.

The time coordinate for an off-momentum particle $-\tau$ is given by the difference between the arrival time of this particle and that of a synchronous particle at the center of the bucket. The equations of motion for the phase-space coordinate τ and

particle energy deviation are

$$\frac{d\tau}{dt} = -\eta \frac{\Delta E}{\beta^2 E_0} , \qquad \frac{d(\Delta E)}{dt} = \frac{eV(\tau)}{T_0} . \tag{3.213}$$

The equations of particle motion in a barrier rf wave are governed by Eq. (3.213).

B. Synchrotron Hamiltonian for general rf wave form

From the equations of motion (3.213), we obtain the general synchrotron Hamiltonian for an arbitrary barrier rf wave form:

$$H = -\frac{\eta}{2\beta^2 E_0}(\Delta E)^2 - \frac{1}{T_0}\int_0^\tau eV(\tau)d\tau. \tag{3.214}$$

Thus the maximum off-energy bucket height can be easily derived:

$$\Delta E_{\rm b} = \left(\frac{2\beta^2 E_0}{|\eta|T_0}\left|\int_{T_2/2}^{T_2/2+T_1} eV(\tau)d\tau\right|\right)^{1/2} , \tag{3.215}$$

where T_1 is the width of the barrier rf wave form. Since the barrier rf Hamiltonian is time independent, an invariant torus has a constant Hamiltonian value. We define the W parameter for a torus from the equation below:

$$\frac{|\eta|}{2\beta^2 E_0}(\hat{\Delta E})^2 = \frac{1}{T_0}\left|\int_{T_2/2}^{T_2/2+W} eV(\tau)d\tau\right|. \tag{3.216}$$

The synchrotron period of a Hamiltonian torus becomes

$$T_{\rm s} = 2\frac{T_2}{|\eta|}\left(\frac{\beta^2 E_0}{|\hat{\Delta E}|}\right) + 4T_{\rm c} , \tag{3.217}$$

$$T_{\rm c} = \frac{\beta^2 E_0}{|\eta|}\int_0^W\left[(\hat{\Delta E})^2 - \frac{2\beta^2 E_0}{|\eta|T_0}\int_{T_2/2}^{T_2/2+\tau} eV(\tau')d\tau'\right]^{-1/2} d\tau, \tag{3.218}$$

where $4T_{\rm c}$ is the time for a particle to be reflected in the potential well. Clearly, all physical quantities depend essentially on the integral $\int V(\tau)d\tau$. Thus, the essential physics is independent of the exact shape of the barrier rf wave.

C. Square wave barrier bucket

Since the effect of the barrier rf wave on particle motion depends essentially on the integrated rf voltage wave, we consider only the square wave forms with voltage heights $\pm V_0$ and pulse width T_1 in time, separated by a gap of T_2. When the particle

passes through the cavity gap at voltage $\pm V_0$, it gains (loses) an equal amount of energy eV_0, i.e. $d(\Delta E)/dt = \pm eV_0/T_0$ every turn. The number of cavity passages before the particle loses all its off-energy value $\hat{\Delta E}$ is

$$N = \frac{|\hat{\Delta E}|}{eV_0}. \tag{3.219}$$

Thus the phase-space trajectory for a particle with maximum off-energy $\hat{\Delta E}$ is

$$(\Delta E)^2 = \begin{cases} (\hat{\Delta E})^2 & \text{if } |\tau| \leq T_2/2 \\ (\hat{\Delta E})^2 - \left(|\tau| - \dfrac{T_2}{2}\right) \dfrac{\omega_0 \beta^2 E_0 eV_0}{\pi|\eta|} & \text{if } T_2/2 \leq |\tau| \leq (T_2/2) + T_1, \end{cases} \tag{3.220}$$

where $\omega_0 = 2\pi f_0$ is the angular revolution frequency of the beam. The phase-space ellipse is composed of a straight line in the rf gap region and a parabola in the square rf wave region. The phase-space area of the invariant phase-space ellipse is

$$\mathcal{A} = 2T_2 \hat{\Delta E} + \frac{8\pi|\eta|}{3\omega_0 \beta^2 E_0 eV_0}(\hat{\Delta E})^3. \tag{3.221}$$

The maximum energy deviation or the barrier height that a barrier rf wave can provide is

$$\Delta E_{\text{b}} = \left(\frac{eV_0 T_1}{T_0} \frac{2\beta^2 E_0}{|\eta|}\right)^{1/2}, \tag{3.222}$$

where T_1 is the pulse width of the rf voltage wave, and T_0 is the revolution period of the beam. The bucket height depends on $V_0 T_1$, which is the integrated rf voltage strength $\int V(\tau)d\tau$. The synchrotron period is

$$T_{\text{s}} = 2\frac{T_2}{|\eta|}\left(\frac{\beta^2 E_0}{|\hat{\Delta E}|}\right) + 4\frac{|\hat{\Delta E}|}{eV_0}T_0 \tag{3.223}$$

for particles inside the bucket. The mathematical minimum synchrotron period of Eq. (3.223) and the corresponding maximum synchrotron tune are

$$T_{\text{s,min}} = \left(\frac{32 T_0 T_2 \beta^2 E_0}{|\eta| eV_0}\right)^{1/2}, \qquad \nu_{\text{s,max}} = \left(\frac{T_0}{T_2} \frac{|\eta| eV_0}{32\beta^2 E_0}\right)^{1/2}. \tag{3.224}$$

Note here that $\pi T_0/(16 T_2)$ plays the role of harmonic number h of a regular rf system. The synchrotron tune is a function of the off-energy parameter $\hat{\Delta E}$ given by

$$\nu_{\text{s}} = 4\nu_{\text{s,max}}\sqrt{\frac{T_1}{T_2}}\frac{\hat{\Delta E}}{\Delta E_b}\left(1 + 4\left[\frac{\hat{\Delta E}}{\Delta E_b}\right]^2 \frac{T_1}{T_2}\right)^{-1}. \tag{3.225}$$

Note that when the rf pulse gap width decreases to $T_2/T_1 < 4$, the synchrotron tune becomes peaked at an amplitude within the bucket height. This feature is similar to that of a double rf system. Figure 3.25 shows ν_s vs ΔE with Fermilab Recycler parameters $E_0 = 8.9$ GeV, $\gamma_T = 20.7$, $f_0 = 89.8$ kHz, $T_1 = 0.5$ μs, $V_0 = 2$ kV, and $T_2/T_1 = 1, 2, 4,$ and 8. For example, $\nu_{s,\text{max}} = 3.7 \times 10^{-5}$ for $T_2 = T_1$, i.e. the synchrotron frequency is 3.3 Hz.
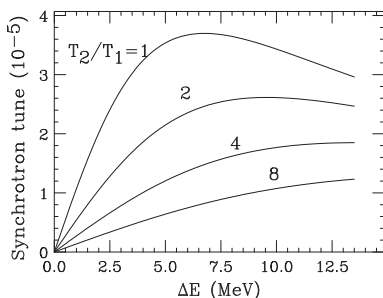
Figure 3.25: Synchrotron tune vs off-energy parameter ΔE. Parameters used are $E_0 = 8.9$ GeV, $f_0 = 89.8$ kHz, $V_0 = 2$ kV, $\gamma_T = 20.7$, and $T_1 = 0.5$ μs. Note that if $T_2 > 4T_1$, the synchrotron tune is a monotonic function of ΔE. On the other hand, if $T_2 < 4T_1$, the synchrotron tune is peaked at an off-energy ΔE smaller than the bucket height ΔE_b.

D. Hamiltonian formalism

The Hamiltonian for the phase-space coordinates $(\tau, \Delta E)$ is

$$H_0 = \frac{\eta}{2\beta^2 E_0}(\Delta E)^2 + \frac{\omega_0 e V_0 T_1}{2\pi} f_0(\tau, T_1, T_2), \qquad (3.226)$$

where

$$
\begin{aligned}
f_0(\tau, T_1, T_2) &= -1 + \frac{1}{T_1}\left[(\tau + T_1 + \frac{T_2}{2})\theta(\tau + T_1 + \frac{T_2}{2}) - (\tau + \frac{T_2}{2})\theta(\tau + \frac{T_2}{2})\right. \\
&\quad \left. -(\tau - \frac{T_2}{2})\theta(\tau - \frac{T_2}{2}) + (\tau - T_1 - \frac{T_2}{2})\theta(\tau - T_1 - \frac{T_2}{2})\right]. \quad (3.227)
\end{aligned}
$$

Here $\theta(x)$ is the standard step function with $\theta(x) = 1$ for $x > 0$ and $\theta(x) = 0$ for $x < 0$.

For a constant T_1, T_2 and V_0, the Hamiltonian H_0 is a constant of motion. The action of a Hamiltonian torus is

$$J = \frac{1}{2\pi}\oint \Delta E d\tau = \frac{1}{2\pi}\sqrt{\frac{\omega_0 \beta^2 E_0 e V_0}{\pi|\eta|}}\oint \sqrt{W + f_0(\tau, T_1, T_2)}d\tau. \qquad (3.228)$$

The parameter W with a dimension of time is related to the Hamiltonian value by

$$H_0 = -\frac{\omega_0 e V_0}{2\pi}W = \frac{\eta}{2\beta^2 E_0}\left(\hat{\Delta E}\right)^2. \qquad (3.229)$$

For a given Hamiltonian torus, W has the physical meaning that it is equal to the maximum phase excursion $|\tau|$ in the rf wave region. Therefore $W = 0$ corresponds to an on-momentum particle, and $W = T_1$ is associated with particles on the bucket boundary.

The action for a particle torus inside the bucket and the bucket area of the maximum action with $W = T_1$ are

$$J = \frac{1}{2\pi} \sqrt{\frac{\omega_0 \beta^2 E_0 eV_0}{\pi |\eta|}} \left[2T_2 \sqrt{W} + \frac{8}{3} W^{3/2} \right] = \frac{1}{2\pi} \left[2T_2 + \frac{8}{3} W \right] \hat{\Delta E},$$

$$\mathcal{B} = 2\pi \hat{J} = \left(2T_2 + \frac{8}{3} T_1 \right) \Delta E_{\rm b}. \tag{3.230}$$

The bucket area depends only on the integrated rf voltage strength $\int V(\tau) d\tau = V_0 T_1$.

E. Action-angle coordinates

Canonical transformation from the phase-space coordinates $(\tau, \Delta E)$ to the action-angle variable can be achieved by using the generating function:

$$F_2(J, \tau) = \int_{-\hat{\tau}}^{\tau} \Delta E \, d\tau, \qquad \psi = \frac{\partial F_2}{\partial J} = \frac{\pi \sqrt{W}}{T_2 + 4W} \int_{-\hat{\tau}}^{\tau} \frac{d\tau}{\sqrt{W + f_0}}. \tag{3.231}$$

where $\hat{\tau} = W + (T_2/2)$. The integral can be evaluated easily to obtain

$$\psi = \begin{cases} \dfrac{2\pi \sqrt{W}}{T_2 + 4W} \sqrt{W + \dfrac{1}{2} T_2 + \tau} & \text{if } -W - \tfrac{1}{2} T_2 \le \tau \le -\tfrac{1}{2} T_2, \ \Delta E > 0 \\[2ex] \psi_c + \dfrac{\pi}{T_2 + 4W} \left(\tau + \dfrac{1}{2} T_2 \right) & \text{if } -\tfrac{1}{2} T_2 \le \tau \le \tfrac{1}{2} T_2, \ \Delta E > 0 \\[2ex] 2\psi_c + \psi_s - \dfrac{2\pi \sqrt{W}}{T_2 + 4W} \sqrt{W + \dfrac{1}{2} T_2 - \tau} & \text{if } \tfrac{1}{2} T_2 \le \tau \le W + \tfrac{1}{2} T_2, \ \Delta E > 0 \\[2ex] 2\psi_c + \psi_s + \dfrac{2\pi \sqrt{W}}{T_2 + 4W} \sqrt{W + \dfrac{1}{2} T_2 - \tau} & \text{if } \tfrac{1}{2} T_2 \le \tau \le W + \tfrac{1}{2} T_2, \ \Delta E < 0 \\[2ex] 3\psi_c + \psi_s + \dfrac{\pi}{T_2 + 4W} \left(\dfrac{1}{2} T_2 - \tau \right) & \text{if } -\tfrac{1}{2} T_2 \le \tau \le \tfrac{1}{2} T_2, \ \Delta E < 0 \\[2ex] 4\psi_c + 2\psi_s - \dfrac{2\pi \sqrt{W}}{T_2 + 4W} \sqrt{W + \dfrac{1}{2} T_2 + \tau} & \text{if } -W - \tfrac{1}{2} T_2 \le \tau \le -\tfrac{1}{2} T_2, \ \Delta E < 0, \end{cases}$$

where

$$\psi_c = \frac{2\pi W}{T_2 + 4W}, \qquad \psi_s = \frac{\pi T_2}{T_2 + 4W} \tag{3.232}$$

are respectively the synchrotron phase advances for a half orbit in the rf wave region and in the region between two rf pulses. Note that $2\psi_c + \psi_s = \pi$ for one half of

the synchrotron orbit, and that the motion of a stable particle orbit in the barrier bucket with $\eta < 0$ is clockwise. We choose the convention of $\dot{\psi} > 0$ corresponding to a clockwise motion in synchrotron phase-space.

When a perturbation, such as rf noise, is applied to the barrier rf system, stable bucket area may be reduced. The resonance strength functions and their associated sum rules can be derived analytically. The resonance strength function decreases slowly with mode number. The rf phase and voltage modulation can severely dilute bunch area if the modulation frequency is near the top of the synchrotron tune and its harmonics. The rf phase modulation due to orbit length modulation resulting from ground vibration can be important. Because the solid state amplifier is a low power device, it is important to avoid a large reduction of stable phase-space area. Active compensation may be used to compensate the effect of rf phase modulation.[41]

V.8   Beam-stacking in Longitudinal Phase space

Beam intensity is limited by space-charge effects at low energies. Rapid cycling synchrotrons (RCS) can be used to increase beam power. However, RCS is usually limited by its achievable energy and a second-stage accelerator is required to increase both energy and beam power. Slip-stacking injection may be used to double the beam power. The idea of slip-stacking was first proposed by F.E. Mills, where he studied the stability of particle motion under the influence of two rf systems at a nearby frequency.[42] During the slip stacking process, both systems are at the stationary phase condition. The Hamiltonian of the two-rf system in the normalized phase space coordinates is (see Eq. (3.192))

$$H = \frac{\nu_s \mathcal{P}^2}{2} + \nu_s \{[1 - \cos\phi] + [1 - \cos(\phi - \nu_{\text{slip}}\theta)]\}, \qquad (3.233)$$

where $\mathcal{P}$ and ϕ are the normalized phase-space coordinates, $\nu_s = \sqrt{h|\eta|eV_{\text{rf}}/2\pi\beta^2 E}$ is the small-amplitude synchrotron tune, V_{rf} is the rf voltage, and βc and E are the nominal speed and energy of the beam particles, $\nu_{\text{slip}} = f_{\text{slip}}/f_0$ is the *slip-tune*, f_{slip} is the slip frequency, and f_0 is the revolution frequency of the stacking-Ring. All physical quantities represent parameters of the slip-stacking ring. The rf phase ϕ and the normalized off-momentum $\mathcal{P}$ are conjugate canonical coordinates, while θ represents the independent 'time' variable, which increases by 2π in each revolution around the stacking-ring.

In order for slip-stacking to work, these two rf systems must generate buckets which slip by exactly one train or one batch of rf buckets in consecutive injections from the rapid-cycling booster synchrotron. This condition fixes the rf frequency difference to $f_{\text{slip}} = h_{\text{B}}f_{\text{B}}$, where f_{B} is the repetition frequency of the RCS and h_{B} is

---

[41]See S.Y. Lee and K.Y. Ng, *Phys. Rev.* E**55**, 5992 (1997).
[42]F.E. Mills, BNL 15936 (1971).

its rf harmonics. For Fermilab, the RCS is the Booster with $h_B = 84$ and $f_B = 15$ Hz. The Recycler ring serves as the stacking ring with the harmonic number $h_R = 588$.

We assume that these two rf systems have the same total rf cavity voltage $V_{\rm rf}$. One of the beam bunches that synchronize the rf system $(1 - \cos\phi)$, while the train of buckets that synchronize with the rf system $(1 - cos(\phi - \nu_{\rm slip}\theta))$ is moving at a different momentum. These to beams bunches slip against each other at the slip tune of $\nu_{\rm slip}$. If the phase-slip factor is $\eta < 0$, the rf buckets generated by the rf system corresponding to $\cos(\phi - \nu_{\rm slip}\theta)$ are at a slightly lower energy than the buckets generated by the rf system of $\cos\phi$ in the Hamiltonian, i.e. the lower-energy bucket series slips forward at the rate of $\Delta\phi = \nu_{\rm slip}\theta$.

The fractional momentum that separates the upper and lower bucket series is

$$\Delta\delta_{\rm sep} \equiv \frac{\Delta P_{\rm sep}}{P_0} = \frac{\nu_{\rm slip}}{h|\eta|} = \frac{h_B f_B}{h_R|\eta|f_0}, \qquad (3.234)$$

where $\Delta P_{\rm sep}$ is the momentum difference of the two slip-stacking beams, P_0 is the nominal momentum of the beams, and η is the phase slip-factor of the slip-stacking ring. Once the repetition rate of the RCS, the phase-slip factors, and the revolution frequency of the slip-stacking ring are designed, the momentum separation of the two bucket series, $\Delta\delta_{\rm sep}$, is fixed. In terms of the normalized off-momentum coordinate $\mathcal{P}$, the separation of the centers of the upper and lower buckets is

$$\Delta\mathcal{P}_{\rm sep} = \frac{h|\eta|\Delta\delta_{\rm sep}}{\nu_s} = \frac{\nu_{\rm slip}}{\nu_s} \equiv \alpha_s, \qquad (3.235)$$

where α_s is called the *slip-stacking parameter*. The unperturbed bucket height is $|\mathcal{P}| \leq 2$ for stationary bucket (see Table 3.2 and the bucket of Fig. 3.12). The unperturbed rf buckets of the two rf systems just touch each other at $\alpha_s = 4$. The two unperturbed rf buckets are separated from each other when $\alpha_s > 4$, and they overlap when $\alpha_s < 4$.

Slip-stacking had been tried in the CERN SPS to accumulate beams from the CERN PS, successfully applied in the Fermilab Tevatron Run IIB to increase antiproton production, and employed in the Fermilab Recycler Ring to increase the proton beam power for neutrino production.[43] Because of the presence of the two rf systems, the two series of rf buckets, upper and lower, are mutually perturbing each other. The stable bucket areas become smaller than those of the unperturbed rf buckets. When the upper and lower series of buckets overlap, resonance islands can be generated in-between the two series of rf buckets usually around $p = 0$ and $\phi = 0$ and $\pm\pi$. In addition, chaotic regions may be created, which can reduce the stable region of the rf buckets significantly.

[43]D. Boussard and Y. Mizumachi, IEEE Trans. Nucl. Sci. **NS-26**, 3623 (1979); K. Seiya, *et al.* PAC2005 347, (2005); I. Kourbanis, IPAC2014, 904, (2014).

Overlapping resonances can be avoided if the upper and lower buckets are widely separated or if $\alpha_s \gg 4$. Bigger α_s, however, implies smaller rf voltage and therefore smaller unperturbed bucket areas (in δ-ϕ coordinates), which may not be large enough to accommodate the beam injected from the RCS. On the other hand, smaller α_s implies larger rf voltage. One may think that there would be bigger unperturbed bucket areas to accept the beam injected from the RCS. When $\alpha_s < 4$, these two bucket series can produce strong overlapping resonances and chaos so that the stable parts of the buckets become smaller than the unperturbed buckets. Careful choice of the rf parameters provide successful doubling of beam intensity.

Numerical simulations can be carried out to analyze the interaction of these two rf buckets. Transforming the phase space into the Poincaré map, where the particles in the slipping bucket are shifted backward in the time coordinate, we will observe stationary resonance islands in the Poincaré map. Figure 3.26 shows the Poincaré maps with parameter $\alpha_s = 4.1$ (left) and 6.0 (right) respectively.
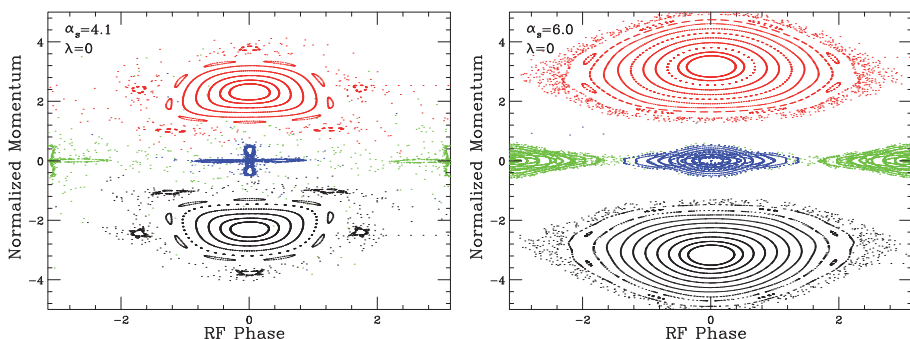
Figure 3.26: Left: Phase-space structure with slip-stacking parameter $\alpha_s = 4.1$; Right: phase-space structure with slip-stacking parameter $\alpha_s = 6.0$. Parametric resonances are excited by the mutual interaction between these two rf systems.

Note that there is little perturbation at $\alpha_s = 6$ in comparison with that of $\alpha_s = 4.1$. Furthermore, We note that there is a prominent 5th order resonance at $\alpha_s = 4.1$ and the 7th order resonance at $\alpha_s = 6.0$. These parametric resonances are produced by mutual interaction between these two rf systems discussed in Sec. III in Chapter 3.

For beam particles in one of the buckets, the other slip-stacking rf system produces a time-dependent modulation at the tune of $\nu_{\mathrm{slip}} = \alpha_s \nu_s$, which is a combination of phase and voltage modulations. If the modulation tune is equal to an integer multiple of the particle tune, the parametric resonance occurs. The synchrotron tune of a particle in the bucket depends on its synchrotron amplitude, i.e., the synchrotron tune is ν_s at small amplitude and decreases to zero at the separatrix of the synchrotron phase space, as shown in Fig. 3.27. Resonances will occur at different phase-space
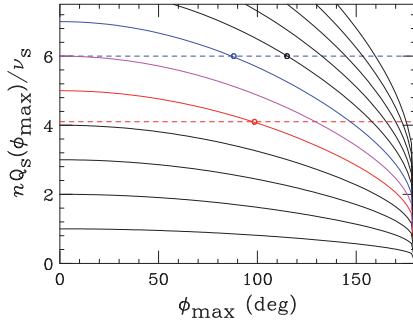
Figure 3.27: The harmonics of the synchrotron tune of a stationary rf system system versus the rf phase amplitude $\phi_{\max}$. The horizontal dashed lines correspond to the modulation tunes at slip-stacking parameters of $\alpha_s = 4.1$ and 6 of Fig. 3.26. When the slip-stacking modulation tune cut through an nth harmonic of the synchrotron tune, the nth-order resonance will occur at that phase-space amplitude, evidently seen in Fig. 3.26.

locations as the slip-tune $\alpha_s \nu_s$ changes.

If the modulation (slip-stacking) tune cuts through the nth harmonic of the synchrotron tune, the nth-order resonance, called the $n{:}1$ parametric resonance, will appear at the corresponding phase-space location. For example, the horizontal red dashed line in Fig. 3.27 corresponding to $\alpha_s = 4.1$ cuts through the 5th harmonic of the synchrotron tune to produce a 5th-order resonance at the maximum rf phase amplitude $\phi_{\max} \sim 95°$. Similarly, the $\alpha_s = 6$ line cut through the 7 times the synchrotron tune line will produce the 7th order parametric resonance at its phase amplitude.

Two strong resonances can also concatenate into a second-order resonance, for example, the 4:1 and 5:1 resonances can interact to produce a 9:2 resonance at the phase space in between these two first-order resonances, evidently shown at the Left plot of Fig. 3.26. The size of the resonance islands depend on the resonance strength and the slope of the n-harmonic synchrotron tune versus amplitude.

We also note that the phase space region between the upper and lower buckets in Fig. 3.26 can cause overlapping resonances phase space region near the separatrix. Using the second canonical perturbation method, one can find a cavity to compensate the interaction between these two bucket at the overlapping region.[44]

Exercise 3.5

1. The Cooler Injector Synchrotron (CIS) accelerates protons from 7 MeV to 200 MeV in 1.0 Hz. The circumference is 17.364 m. The rf system operates at $h = 1$ with a maximum voltage 240 V. The momentum compaction factor is $\alpha_c = 0.6191$. The momentum spread of the injection linac is about $\pm 5.0 \times 10^{-3}$.

    (a) Assuming that the rf voltage is ramped according to

    $$V_{\mathrm{rf}}(t) = V_0 + (V_1 - V_0)\left(3\frac{t^2}{T_1^2} - 2\frac{t^3}{T_1^3}\right), \quad t \in [0, T_1],$$

---

[44]J. Eldred, Ph.D. Thesis, Department of Physics, Indiana University, Bloomington, IN, December 2015; FERMILAB-THESIS-2015-31; J. Eldred and R. Zwaska, Phys. Rev. ST Accel. Beams **19**, 104001 (2016); S.Y. Lee and K.Y. Ng, PRAB, **20**, 064202 (2017).

where V_0 and $V_1 = 240$ V are the initial and the maximum final rf voltages, T_1 is the voltage ramp time. Calculate the adiabaticity coefficient of Eq. (3.21), and the rf bucket height during the rf voltage ramping as functions of time t with $V_0 = 10$ V and $T_1 = 10$ ms. Change these parameters to see the variation of the adiabaticity coefficient.

(b) If the magnetic field of a proton synchrotron is ramped according to

$$B(t) = B_0 + \left(3\frac{t^2}{t_1^2} - 2\frac{t^3}{t_1^3}\right)(B_1 - B_0), \quad t \in [0, t_1]$$

where B_0 and B_1 are magnetic field at the injection and at the flat top, and $t = 0$ and $t = t_1$ are the time at the beginning of ramp and at the flat top, find the frequency ramping relation of the rf cavity, and find the maximum $\dot{B}$.

2. In proton accelerators, the rf gymnastics for bunch rotation is performed by adiabatically lowering the voltage from V_1 to V_2 and suddenly raising the voltage from V_2 to V_1 (see also Exercise 3.2.6). Using Eq. (3.42) and conservation of phase-space area, show that the bunch length in the final step is

$$\hat{\theta}_{\text{final}} = \left(\frac{\nu_{s2}}{\nu_{s1}}\right)^{1/2} \hat{\theta}_{\text{initial}},$$

where $\hat{\theta}_{\text{initial}}$ is the initial bunch length in orbital angle variable, and ν_{s1} and ν_{s2} are the synchrotron tune at voltages V_1 and V_2. Apply the bunch rotation scheme to proton beams at $E = 120$ GeV in the Fermilab Main Injector, where the circumference is 3319.4 m, the harmonic number is $h = 588$, the transition energy is $\gamma_T = 21.8$, and the phase-space area is $\mathcal{A} = 0.05$ eV-s for 6×10^{10} protons. Find the voltage V_2 such that the final bunch length is 0.15 ns with an initial voltage $V_1 = 4$ MV. The energy of the secondary antiprotons is 8.9 GeV. If the acceptance of the antiproton beam is $\pm 3\%$, what is the phase-space area of the antiproton beams? If the antiproton production efficiency is 10^{-5}, what is the phase-space density of the antiproton beams?

3. Neglecting wakefield and other diffusion mechanisms, the momentum spread of an electron beam in a storage ring is determined mainly by the equilibrium between the quantum fluctuation of photon emission and the radiation damping. For an isomagnetic ring, it is given by

$$\left(\frac{\sigma_E}{E}\right)^2 = C_q \frac{\gamma^2}{\mathcal{J}_s \rho}, \qquad C_q = \frac{3C_u\hbar}{4mc} = \frac{55}{32\sqrt{3}}\frac{\hbar}{mc} = 3.83 \times 10^{-13} \text{ m},$$

where $\mathcal{J}_s$ is the damping partition number with $\mathcal{J}_s \approx 2$ for separate function machines. Using the electron storage ring parameters listed in Exercise 3.1.6, calculate the phase-space area in eV-s.

4. Verify Eq. (3.191) and derive the Hamiltonian for the double rf system. For a flattened potential well in the double rf system with $\phi_{1s} = \phi_{2s} = 0$, show that the Hamiltonian for small amplitude synchrotron motion is

$$H \approx \frac{1}{2}\mathcal{P}^2 + \nu_s b\phi^4,$$

where $b = (h^2 - 1)/24$, h is the ratio of the harmonic numbers, and the independent "time" variable is the orbital angle θ. We solve the synchrotron motion for the quartic potential below.

(a) Since the Hamiltonian is time independent, the Hamiltonian value E is a constant of motion. Show that the action variable is related to the Hamiltonian value by

$$J = \frac{4K}{3\pi b^{1/4}}\left(\frac{E}{\nu_s}\right)^{3/4} = \frac{4K}{3\pi}b^{1/2}\hat{\phi}^3,$$

where $K = K(\sqrt{\frac{1}{2}}) = 1.85407468$ is the complete elliptical integral with modulus $k = 1/\sqrt{2}$, $\hat{\phi}$ is the amplitude of the phase oscillation.

(b) Show that the synchrotron tune is

$$\frac{Q_s(J)}{\nu_s} = \frac{\pi}{K}b^{1/4}\left(\frac{E}{\nu_s}\right)^{1/4} = \frac{3^{1/3}\pi^{4/3}b^{1/3}}{4^{1/3}K^{4/3}}J^{1/3} = \frac{\pi}{K}b^{1/2}\hat{\phi}.$$

(c) Define the generating function

$$F_2(\phi, J) = \int_0^\phi \mathcal{P}d\phi,$$

and show that the solution of the synchrotron motion is given by

$$\phi = \hat{\phi}\,\operatorname{cn}\left(\frac{2K}{\pi}\psi|\frac{1}{2}\right),$$

$$\mathcal{P} = -\sqrt{2}\hat{\mathcal{P}}\,\operatorname{sn}\left(\frac{2K}{\pi}\psi|\frac{1}{2}\right)\,\operatorname{dn}\left(\frac{2K}{\pi}\psi|\frac{1}{2}\right),$$

where cn, sn, and dn are elliptical functions with modulus $k = 1/\sqrt{2}$. Compare your results with that of Eq. (3.209) for the $h = 2$ case.

5. Two strong resonances can interact to create a secondary resonance located in the phase space between these two primary resonance as shown in Exercise 2.7.8, where 3:1 and 1:1 resonances produce a 4:2 resonance. The slip-stacking rf buckets of Eq. (3.233 can also produce resonances at the phase space in the middle of the two buckets, besides the parametric resonances shown in Fig. 3.26. These secondary resonances can overlap with the primary parametric resonances so that the bucket overlapping region becomes chaotic. One can use the canonical perturbation method to understand these secondary resonance. This exercise explore the canonical perturbation technique.

(a) To simplify the derivation, symmetrize the Hamiltonian to a frame with the upper and lower buckets centered at $p = +\frac{1}{2}\alpha_s$, or with frames moving at $+\frac{1}{2}\nu_{\text{slip}}\theta$. Using the generating function

$$F_2(\phi, \tilde{p}) = \left(\phi - \frac{\nu_{\text{slip}}\theta}{2}\right)\left(\tilde{p} + \frac{\alpha_s}{2}\right),$$

show that the new Hamiltonian is

$$H = \frac{\nu_s\tilde{p}^2}{2} + \nu_s\left[2 - \cos\left(\tilde{\phi} + \frac{\nu_{\text{slip}}\theta}{2}\right) - \cos\left(\tilde{\phi} - \frac{\nu_{\text{slip}}\theta}{2}\right)\right]$$

where $\tilde{p}$ and $\tilde{\phi}$ are the conjugate canonical coordinates of the symmetrized slip-stacking rf systems, and we ignore a constant term $+\frac{\nu_s \alpha_s^2}{8}$ from the Hamiltonian. This Hamiltonian represents the upper and lower buckets moving at $\Delta\phi = \mp\nu_{\text{slip}}\theta/2$ respectively, while the structures in-between the two buckets centered at $\tilde{p} = 0$ is stationary.

(b) Resonances due to the interaction of these bucket occurs at the phase space near $\tilde{p} = 0$, Because we wish to study the phase space structure in-between the upper and lower rf buckets, we perform a canonical transformation to cancel the potential-energy part of the Hamiltonian using the generating function

$$F_2(\tilde{\phi}, \bar{p}) = \phi\bar{p} + a(\bar{p})\sin(\tilde{\phi} + \frac{\nu_{\text{slip}}}{2}\theta) + b(\bar{p})\sin(\tilde{\phi} - \frac{\nu_{\text{slip}}}{2}\theta),$$

where $a(\bar{p})$ and $b(\bar{p})$ are two functions of $\bar{p}$ to be determined, show that the new Hamiltonian is

$$H = \frac{1}{2}\nu_s\bar{p}^2 + \frac{2}{\alpha_s^2 - 4\bar{p}^2}\nu_s\left(1 - \cos(2\bar{\phi})\right) + ...$$

where the ... represents either constants or time dependent terms that are average to zero in the new Hamiltonian, and we have chosen

$$a(\bar{p}) = \frac{2}{\alpha_s + 2\bar{p}} \qquad \text{and} \qquad b(\bar{p}) = -\frac{2}{\alpha_s - 2\bar{p}},$$

to cancel the primary rf bucket potentials. The combined effect of two rf systems is a 2nd order bucket located at the phase space of these two rf buckets. The strength of this bucket is $2/\alpha_s^2$ of that of the primary bucket. A cavity at the frequency $2hf_0 + f_s lip$ at the voltage of $-\frac{2}{\alpha_s^2}V_0$ can be used to cancel the 2nd order bucket induced by two primary cavities, and help to eliminate the chaos near the separatrices of these two primary buckets.

VI   Fundamentals of RF Systems

The basic function of rf cavities is to provide a source of electric field for beam manipulations, including acceleration, deceleration, bunching and debunching, and deflection. The longitudinal electric field must be synchronized with the particle arrival time. Resonance cavities, where only electromagnetic fields at resonance frequencies can propagate, are a natural choice in rf cavity design.

Cavities are classified according to their operational frequencies. For cavities operating at a few hundred MHz or higher, pillbox cavities with nose-cone or disk loaded geometry can be used. At lower frequencies, coaxial geometry is commonly employed. Some fundamental parameters of cavities are transit time factor, shunt impedance, and quality factor.

The transit time factor of Eq. (3.3) reflects the finite passage time for a particle to traverse the rf cavity, while the accelerating field varies with time. The transit time factor reduces the effective voltage seen by passing particles. We may reduce the accelerating voltage gap to increase the transit time factor, but a smaller gap can cause electric field breakdown due to the Kilpatrick limit (see Sec. V.3).

The quality factor (Q-factor) depends on the resistance of the cavity wall and the characteristic impedance of the rf cavity structure. It is defined as the ratio of the rf power stored in the cavity to the power dissipated on the cavity wall. The shunt impedance, defined as the ratio of the square of the rf voltage seen by the beam to the dissipated power, is an important figure of merit in cavity design. Generally, the ratio of shunt impedance to Q-factor depends only on the geometry of the cavity and the characteristic impedance, i.e. a higher Q-factor cavity has a higher shunt impedance.

In this section we examine some basic principles in cavity design. Properties of pillbox and coaxial-geometry cavities will be discussed. Some fundamental characteristic parameters, the shunt impedance, the Q-factor, and the filling time, of a resonance cavity will be defined and discussed. At a given resonance frequency, we will show that a resonance cavity can be well approximated by an equivalent RLC circuit. Beam loading and Robinson dipole-mode instability will be addressed. High frequency cavities of linacs will be discussed in Sec. VIII.

VI.1   Pillbox Cavity

We first consider a cylindrically symmetric pillbox cavity [22] of radius b and length ℓ (left plot of Fig. 3.28). Maxwell's equations (see Appendix B Sec. IV) for electromagnetic fields inside the cavity are

$$\nabla \cdot \vec{B} = 0, \quad \nabla \times \vec{B} = \mu\epsilon\frac{\partial \vec{E}}{\partial t}, \quad \nabla \cdot \vec{E} = 0, \quad \nabla \times \vec{E} = -\frac{\partial \vec{B}}{\partial t}, \qquad (3.236)$$

where ϵ and μ are dielectric permittivity and permeability of the medium. The EM waves in the cavity can conveniently be classified into transverse magnetic (TM)

mode, for which the longitudinal magnetic field is zero, and transverse electric (TE) mode, for which the longitudinal electric field is zero. The TM modes are of interest for beam acceleration in the rf cavity, while the TE modes can be used for beam deflection.
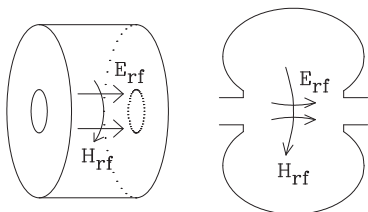

Figure 3.28: Schematic drawings of high frequency cavities. Left: pill-box cavity with disk load; right: nose-cone cavity. Although their names and shapes are different, these high frequency cavities have similar basic features.

An an ideal conducting surface with infinite conductivity, the electromagnetic fields satisfy $\hat{n} \times \vec{E} = 0$ and $\hat{n} \cdot \vec{H} = 0$, where $\hat{n}$ is the vector normal to the conducting surface. There is *no tangential component of electric field*, and *no normal component of magnetic field*. Assuming a time dependence factor $e^{j\omega t}$ for electric and magnetic fields, the TM standing wave modes in cylindrical coordinates (r, ϕ, s) are (see Appendix B Sec. IV)

$$\begin{cases} E_s = A\,k_r^2\,J_m(k_r r)\cos m\phi \cos ks \\ E_r = -A\,kk_r\,J'_m(k_r r)\cos m\phi \sin ks \\ E_\phi = A\,(mk/r)J_m(k_r r)\sin m\phi \sin ks \\ B_s = 0 \\ B_r = -jA\,(m\omega/c^2 r)\,J_m(k_r r)\sin m\phi \cos ks \\ B_\phi = -jA\,(\omega k_r/c^2)\,J'_m(k_r r)\cos m\phi \cos ks \end{cases} \tag{3.237}$$

where A is a constant, $s = 0$ and ℓ correspond to the beginning and end of the pillbox cavity, m is the azimuthal mode number, k, k_r are wave numbers in the longitudinal and radial modes, and $\omega/c = \sqrt{k^2 + k_r^2}$. The standing wave can be decomposed into traveling waves in the $+\hat{s}$ and $-\hat{s}$ directions. The solution is chosen so that $E_r = 0$ and $E_\phi = 0$ at $s = 0$.

The longitudinal wave number k is determined by the boundary condition that $E_r = 0$ and $E_\phi = 0$ at $s = 0$ and ℓ, and the radial wave number is determined by the boundary condition with $E_s = 0$ and $E_\phi = 0$ at $r = b$, i.e.

$$k_{s,p} = \frac{p\pi}{\ell}, \quad p = 0, 1, 2, \cdots, \qquad k_{r,mn} = \frac{j_{mn}}{b}, \tag{3.238}$$

where j_{mn}, listed in Table B.1, are zeros of Bessel functions $J_m(j_{mn}) = 0$. The resonance wave number k for mode number (m, n, p) is

$$k_{mnp} = \sqrt{k_{r,mn}^2 + k_{s,p}^2} = \sqrt{\frac{j_{mn}^2}{b^2} + \frac{p^2\pi^2}{\ell^2}} = \frac{\omega_{mnp}}{c} = \frac{2\pi}{\lambda_{mnp}}. \tag{3.239}$$

The lowest frequency mode is usually called the fundamental mode. Other resonance frequencies are called high order modes (HOM). A good cavity design is to damp HOMs without affecting the fundamental mode. The EM field of the lowest mode TM_{010} ($k_{s,p} = 0$) is

$$E_s = E_0 J_0(kr), \quad B_\phi = j\frac{E_0}{c} J_1(kr), \quad k_{010} = \frac{2.405}{b}, \quad \lambda = \frac{2\pi b}{2.405}. \tag{3.240}$$

For example, a 3 GHz structure corresponds to $\lambda = 10$ cm and $b = 3.8$ cm. Such a structure is usually used for high frequency cavities. Since $k_{s,p} = 0$ for the TM_{010} mode, the phase velocity $\omega/k_{s,p} = \infty$. Thus beam particles traveling at speed $v \leq c$ can not synchronize with the electromagnetic wave and receive net acceleration.

To slow down the phase velocity, the cavity is loaded with one beam hole with an array of cavity geometries and shapes. Figure 3.28 shows high frequency cavities with disk and nose-cone loaded geometries. Many different geometric shapes are used in the design of high frequency cavities, but their function and analysis are quite similar. All cavities convert TEM wave energy into TM mode to attain a longitudinal electric field. We will return to this subject in Sec. VIII.

VI.2   Low Frequency Coaxial Cavities

Lower frequency rf systems usually resemble coaxial wave guides, where the length is much larger than the width. Figure 3.29 shows an example of a coaxial cavity. The TEM wave in the coaxial wave guide section is converted to the TM mode at the cavity gap through the capacitive load. When the cavity is operating in 50 to 200 MHz range, it requires a very small amount of ferrite for tuning.[45] When the cavity is operating at a few MHz range, ferrite rings in the cavity are needed to slow down EM waves. The ferrite is biased with magnetic field bias frequency tuning.[46]
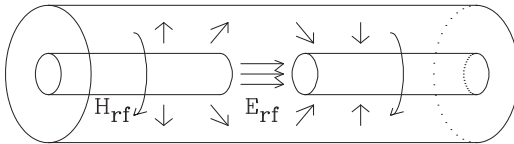

Figure 3.29: Schematic drawing of a low frequency coaxial cavity. Note that the TEM wave is matched to a TM wave at the capacitive loaded gap for the acceleration electric field.

Using the wave guide transmission line theory, characteristic properties of rf systems can be analyzed. Let r_1 and r_2 be the inner and outer radii of a wave guide.

---

[45]Ferrite is magnetic ceramic material that combines the property of high magnetic permeability and high electric resistivity. The material is made of double oxide spinel Fe_2O_3MO, where M can be Mn, Zn, Cr, Ni, etc. Ferrites are commonly used in frequency synthesis devices, Touch-Tone telephone, low loss microwave devices, etc. Application in accelerator can be found in induction linac, frequency tuning for rf cavities, kickers, etc.

[46]W.R. Smythe, *IEEE Trans. Nucl. Sci.*, **NS-30**, 2173 (1983).

The inductance $\tilde{L}$ and the capacitance $\tilde{C}$ per unit length of the concentric coaxial wave guides are

$$\tilde{L} = \frac{\mu}{2\pi} \ln \frac{r_2}{r_1} + \frac{\mu_c \delta_{\text{skin}}}{4\pi} (\frac{1}{r_1} + \frac{1}{r_2}), \qquad \tilde{C} = \frac{2\pi\epsilon}{\ln(r_2/r_1)}, \tag{3.241}$$

where μ_c is the permeability of the conductor, $\delta_{\text{skin}} = \sqrt{2/\omega\mu_c\sigma}$ is the skin depth of flux penetration. The inductance and capacitance of the coaxial cavity structure are respectively $L = \tilde{L}\ell$ and $C = \tilde{C}\ell$, where ℓ the length of the structure. Neglecting the flux penetration in the conductor, the resonating frequency and the cavity length for the quarter-wave mode are

$$v = \frac{\omega}{k} = \frac{1}{\sqrt{\tilde{L}\tilde{C}}} = \frac{1}{\sqrt{\epsilon\mu}}, \qquad \ell = \frac{\lambda}{4} = \frac{v}{4f} = \frac{75}{f[\text{MHz}]} \frac{v}{c} \text{ [m]}. \tag{3.242}$$

To shorten the length of the cavity ℓ, we need to slow down the wave speed by the ferrite materials. For a cavity operating beyond 20 MHz, ferrite can be used only for tuning purposes. At frequencies below tens of MHz, the rf cavities must be ferrite loaded in order to fit into the available free space in an accelerator. Typically the permittivity and magnetic permeability of ferrite are about $10 \epsilon_0$ and $10 - 500 \mu_0$. When a biased field is applied to the ferrite core, the magnetic permeability can be tuned to match the change of the particle revolution frequency.

To understand the capacitive loading that converts the TEM wave into the TM wave at the cavity gap, we study the rf electromagnetic wave in the wave guide. The characteristic impedance of a wave guide is

$$Z_c = R_c = \sqrt{\frac{L}{C}} \approx \frac{1}{2\pi} \sqrt{\frac{\mu}{\epsilon}} \ln \frac{r_2}{r_1}. \tag{3.243}$$

Now, we consider an ideal lossless transmission line, where the electromagnetic field has no longitudinal component. Assuming a time dependent factor $e^{j\omega t}$, the current and voltage across the rf structure are (see Exercise 3.6.3)

$$I(s,t) = I_0 \cos ks - j(V_0/R_c) \sin ks, \quad V(s,t) = V_0 \cos ks - jI_0 R_c \sin ks, \tag{3.244}$$

where $k = \frac{2\pi}{\lambda} = \frac{\omega}{v}$ is the wave number of the line, $v = 1/\sqrt{\epsilon\mu}$ is wave speed in the medium, s is the distance from one end of the transmission line, V_0 and I_0 are the voltage and current at the cavity gap.

For a standing wave, where the end of the transmission line is shorted, the boundary condition at the shorted side is $V = 0$. we find $V_0 \cos k\ell - jI_0 R_c \sin k\ell = 0$, and the current at the shorted side is $I_\ell = I_0/\cos(k\ell)$. The resulting rf current and voltage become $I(s,t) = I_\ell \cos[k(s - \ell)]$ and $V(s,t) = -jI_\ell R_c \sin[k(s - \ell)]$. The line input impedance at the gap becomes

$$Z_{\text{in}} = \frac{V(0,t)}{I(0,t)} = +jR_c \tan k\ell. \tag{3.245}$$

The line impedance is inductive if $k\ell < \pi/2$. The length of the line is chosen to match the gap capacitance at a required resonance frequency, i.e.

$$Z_{\text{in}} + Z_{\text{gap}} = 0, \quad \text{or} \quad \cot k\ell_{\text{r}} = \omega C_{\text{gap}} R_{\text{c}} \equiv g, \tag{3.246}$$

where $Z_{\text{gap}} = -j/(\omega C_{\text{gap}})$ is the gap impedance, C_{gap} is the capacitance of a half gap, and g is the capacitive coupling factor of the cavity, For example, a total capacitance of 10 pF implies that $C_{\text{gap}} = 20$ pF. The length ℓ_{r} of one-half cavity, the gap capacitance, the biased current, and the external loading capacitance can be designed to attain a resonance condition for a given frequency range. A load capacitor may be shunted to decrease the resonance frequency or minimize the cavity length. The effective capacitance is $C_{\text{gap}} + C_{\text{load}}$.

In principle, for a given $\ell_{\text{r}}, R_{\text{c}}$, and C_{gap}, there are many resonance frequencies that satisfy Eq. (3.246). The lowest frequency is called the fundamental TEM mode. If the loading capacitance is small, the resonance condition of Eq. (3.246) becomes $k\ell_{\text{r}} = \pi/2$, i.e. $\ell_{\text{r}} = \lambda/4$: the length of the coaxial cavity is equal to 1/4 of the wavelength of the TEM wave in the coaxial wave guide. Such a structure is also called a quarter-wave cavity. The gap voltage of the coaxial cavity is

$$V_{\text{rf}} = +jI_{\ell}R_{\text{c}} \sin k\ell_{\text{r}} = +j\frac{I_{\ell}R_{\text{c}}}{\sqrt{1+g^2}}. \tag{3.247}$$

A. Shunt impedance and Q-factor

The surface resistivity R_{s} of the conductor and the resistance R of a transmission line are

$$R_{\text{s}} = \sqrt{\frac{\mu_c \omega}{2\sigma}}, \quad R = \frac{R_{\text{s}}\ell}{2\pi}(\frac{1}{r_1} + \frac{1}{r_2}), \tag{3.248}$$

where σ is the conductivity of the material, ω is the rf frequency, r_1 and r_2 are the inner and outer radii of the transmission line, and ℓ is the length. Thus the quality factor becomes

$$Q = \frac{R_{\text{c}}}{R} = \frac{\omega L}{R} \approx \frac{2r_1 r_2}{(r_1+r_2)\delta_{\text{skin}}} \frac{\mu}{\mu_c} \ln\frac{r_2}{r_1}. \tag{3.249}$$

Table 3.6 lists typical Q-factors for a copper cavity as a function of cavity frequency, where we have used $\ln(r_2/r_1) \approx 1$ and $r_1 \approx 0.05$ m, and $\sigma_{\text{Cu}} \approx 5.8 \times 10^7$ $[\Omega\text{m}]^{-1}$ at room temperature.

An important quantity in the design and operation of rf cavities is the shunt impedance. This is the resistance presented by the structure to the beam current at the resonance condition. The total power of dissipation P_{d} of the transmission line cavity and the shunt impedance become

$$P_{\text{d}} = \frac{I_{\ell}^2 R}{2} \int_0^{k\ell_{\text{r}}} \cos^2 x \, dx = \frac{I_{\ell}^2 R}{4(1+g^2)}[(1+g^2)\cot^{-1} g + g], \tag{3.250}$$

Table 3.6: Some characteristic properties of coaxial RF cavities made of copper.

f [MHz]	1	10	100
δ_{skin} [μm]	66.	21.	6.6
r_1	0.05	0.05	0.05
Q	1100	3500	11000

$$R_{\text{sh}} = \frac{|V_{\text{rf}}|^2}{2P_{\text{d}}} \qquad \text{or} \qquad \frac{R_{\text{sh}}}{Q} = \left\{ \frac{4}{\pi} \frac{\pi/2}{(1+g^2)\cot^{-1}g + g} \right\} R_{\text{c}} \qquad (3.251)$$

The expression in brackets is a shunt-impedance geometry factor due to the equivalent gap capacitance loading, i.e. $C_{\text{eq}} = C_{\text{gap}} + C_{\text{load}}$. Figure 3.30 shows the geometry factor (solid) and the phase advance $k\ell_r$ vs the the capacitive coupling factor g.
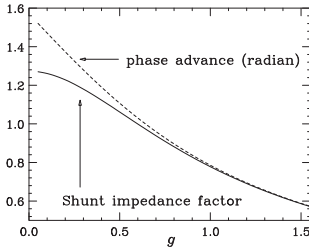
Figure 3.30: The shunt-impedance geometric factor of the bracket in Eq. (3.251) (solid) and the phase advance $k\ell_r = \arctan(1/g)$ (dashed) vs the capacitive coupling factor. As the gap capacitance increases, the shunt impedance decreases.

From the transmission-line point of view, the cavity gap presents a capacitance and resistive load shown in Fig. 3.31, where $Z_{\text{in}} = j\omega L_{\text{eq}}$, and $C_{\text{eq}} = C_{\text{gap}} + C_{\text{load}}$. The matching condition of Eq. (3.246) implies that the reactance of the cavity is zero on resonance, and the effective impedance is R_{sh}. The resonance frequency and the Q-factor of the equivalent RLC-circuit are $\omega_r = 1/\sqrt{L_{\text{eq}}C_{\text{eq}}}$ and $Q = R_{\text{sh}}\sqrt{C_{\text{eq}}/L_{\text{eq}}}$.
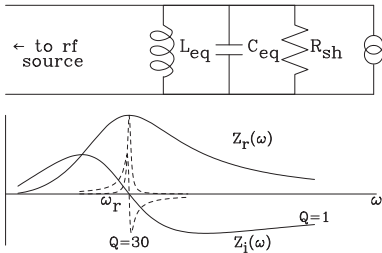
Figure 3.31: Top: Schematic drawing of an equivalent circuit of a cavity. The input impedance of the wave guide is represented by an equivalent inductance. The wave guide is loaded with capacitive cavity-gap and real shunt impedance. Bottom: Plot of the impedance of Eq. (3.252). The solid lines are the real and the imaginary parts of a resonance impedance with Q=1, and the dashed lines are the corresponding parts at Q=30.

The impedance of the rf system, represented by a parallel RLC circuit, is

$$Z = \left(\frac{1}{R_{\text{sh}}} + j\omega C_{\text{eq}} + \frac{1}{j\omega L_{\text{eq}}} \right)^{-1} = \frac{R_{\text{sh}}}{1 + jQ(\frac{\omega}{\omega_r} - \frac{\omega_r}{\omega})} \approx R_{\text{sh}}\cos\psi\, e^{-j\psi}, \qquad (3.252)$$

$$\psi = \tan^{-1}\frac{2Q(\omega - \omega_r)}{\omega_r}, \qquad \omega_r = \frac{1}{\sqrt{L_{\text{eq}}C_{\text{eq}}}}, \qquad Q = R_{\text{sh}}\sqrt{\frac{C_{\text{eq}}}{L_{\text{eq}}}} = \frac{R_{\text{sh}}}{R_{\text{c}}},$$

where L_{eq} and C_{eq} are the equivalent inductance and capacitance, ψ is the cavity detuning angle, and R_c is the characteristic impedance. At the resonance frequency ω_r particles see a pure resistive load with an effective resistance R_{sh}. The rf system becomes capacitive at $\omega > \omega_r$, and inductive at $\omega < \omega_r$. The bottom plot of Fig. 3.31 shows the real and imaginary parts of Eq. (3.252) for Q=1 and Q=30.

Accelerator cavities usually contain also many parasitic HOMs. Each HOM has its shunt impedance and Q-value. If the frequency of one of the HOMs falls on a synchrotron or betatron sideband, the beam can be strongly affected by the parasitic rf driven resonance. Correction, detuning, and lowering the Q-factor of these sidebands are very important in rf cavity design and operation.

B. Filling time

The quality factor defined in Eq. (3.249) is equal to the ratio of the stored power P_{st} to the dissipated power P_d, Using energy conservation, we find

$$Q = \frac{P_{st}}{P_d} = \frac{\omega W_s}{P_d}, \tag{3.253}$$

$$\frac{dW_s}{dt} = -P_d = -\frac{\omega}{Q} W_s,$$

$$W_s = W_{s0} e^{-\omega t/Q} = W_{s0} e^{-2t/T_{f0}}, \qquad T_{f0} = \frac{2Q}{\omega}. \tag{3.254}$$

where W_s is the stored energy and the unloaded *filling time* T_{f0} is equal to the time for the electric field or voltage to decay to $1/e$ of its original value.

C. Qualitative feature of rf cavities

Qualitatively, the rf voltage is the time derivative of the total magnetic flux linking orbit (Faraday's law of induction). We assume that a sinusoidal time dependent magnetic flux density with $1/r$ dependence in a coaxial cavity structure. The induced voltage is

$$V_{rf} = \frac{\Delta\Phi}{\Delta t} = f_{rf}\ell \int_{r_1}^{r_2} B(r)dr = f_{rf}B_1[\ell r_1 \ln\frac{r_2}{r_1} \approx f_{rf}B_1 A, \tag{3.255}$$

where $A = \ell r_1 \ln(r_2/r_1) \approx \ell(r_2 - r_1)$ is the effective area of the ferrite core and B_1 is the peak magnetic flux at $r = r_1$. Because of the logarithmic dependence on r_2, it is inefficient to increase the outer radius of the ferrite core to increase the rf voltage. The peak magnetic flux in Eq. (3.255) depends on the ferrite material.

The quality factor Q is the ratio of stored power to the dissipated power. When there are many dissipative power sources, the loaded Q-factor is

$$\frac{1}{Q_L} = \frac{P_d}{P_{st}} = \frac{1}{Q_1} + \frac{1}{Q_2} + \frac{1}{Q_3} + \cdots,$$

where P_{st} is the power stored in the cavity and P_d is the total dissipated power. The shunt impedance of an rf structure is the resistance presented to the beam current at the resonance condition, i.e.

$$R_{sh} = \frac{|V_{rf}|^2}{2P_d} = \frac{R_c P_{st}}{P_d} \approx R_c Q_L. \tag{3.256}$$

The quality factor Q of the ferrite loaded cavity is dominated by the Q value of the ferrite material itself, i.e. $Q_{ferrite} \approx 10 - 300$, which alone is not adequate for the required frequency tuning range. Frequency tuning can be achieved by inducing a shunt capacitor and a DC magnetic field in the ferrite core. With an external magnet or bias current that encircles the ferrite without contributing a net rf flux, the effective permeability for rf field can be changed.

Since the Q-value of ferrite is relatively low, power dissipation in ferrite is important. The dissipation power is

$$P_d = \frac{f_{rf}}{Q} \left[\frac{\ell}{2\mu} \int_{r_1}^{r_2} B^2(r) 2\pi r dr \right] = \frac{\pi r_1 f_{rf} B_1^2 A}{\mu Q} \approx \frac{\pi r_1 V_{rf}^2}{A \left[\mu f_{rf} Q \right]} \tag{3.257}$$

where the bracket is the average magnetic energy dissipated in each cycle. The power dissipation in a ferrite cavity is inversely proportional to $(\mu f_{rf} Q)$, which characterizes ferrite materials. Since the power is inversely proportional to the effective area A, we need a large volume of ferrite to decrease the flux density in order to minimize energy loss for achieving high rf voltage at low frequencies,

At rf frequencies above tens of MHz, the cavity size (normally 1/2 or 1/4 wavelength) becomes small enough that a resonant structure containing little or no ferrite may be built with significantly lower power loss at $Q \approx 10^4$ with a narrower bandwidth. At frequencies of a few hundred MHz, where adequate and efficient rf power sources are commercially available, the main portion of the rf cavity can be made of copper or aluminum with a small amount of ferrite used for tuning. The cavity can still be considered as a coaxial wave guide, and Eqs. (3.241) to (3.255) remain valid. The characteristic impedance R_c of Eq. (3.243) is about 60 Ω. The stored power is $I^2 R_c$ and the power dissipation is $I^2 R$, where I is the surface current and R of Eq. (3.248) is the surface resistance of the structure. At frequencies above a few hundred MHz, resonance frequency can be tuned only by a slotted tuner or by physically changing the size of the cavity.

D. The rf cavity of the IUCF cooler injector synchrotron

The IUCF cooler injector synchrotron (CIS) is a low energy booster for the IUCF cooler ring. It accelerates protons (or light ions) from 7 MeV to 225 MeV. The cavity is a quarter-wave coaxial cavity with heavy capacitance loading.To make the cavity length reasonably short and to achieve rapid tuning, required for synchrotron

acceleration, ten Phillips 4C12 type ferrite rings are used. The μ of the ferrite material is changed by a superimposed DC magnetic field provided by an external quadrupole magnet. The ferrite rings return the magnet flux between the two adjacent quadrupole tips (Fig. 3.32).
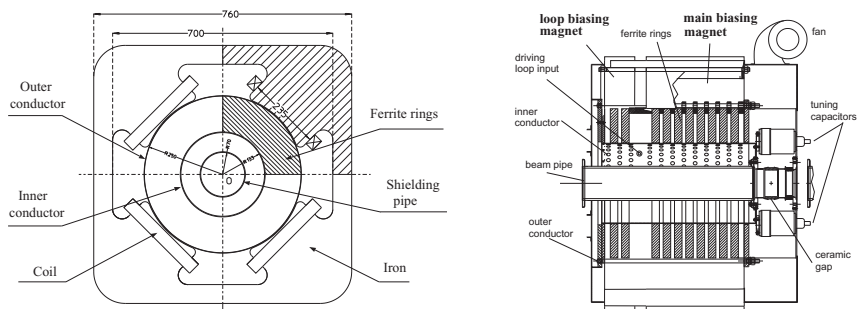

Figure 3.32: The cross section (left) and the longitudinal view of the CIS rf cavity. The external quadrupole magnet provides biased field in ferrite rings to change the effective permeability (courtesy of Alex Pei).

Analysis of such a field shows that the field direction is mostly parallel to the rf field, i.e. along the azimuthal direction, except near the tips of the quadrupole, where the biased fields in the ferrite rings are perpendicular to the rf field. In the working region of the ferrite biasing strength, the effect of the perpendicular component on ferrite rf-μ is small. The effective rf-μ, to first order in wave propagation, is determined by dB/dH, as in parallel biasing analysis, rather than B/H, as in perpendicular analysis. The phenomenon of gyromagnetic resonance associated with perpendicular biasing, however, needs to be considered and avoided in the design of the cavity.

The advantages of using an external biasing magnet include making it possible to separate the rf field from the biasing elements, and the rf field in the cavity will not be affected by the biasing structure. As many windings of the bias coils as practical can be used — resulting in a smaller amperage requirement for the bias supply. In CIS and the IUCF cooler ring, the bias supplies for these external quadrupole biasing magnet type cavities are rated at only 20 A. If the biasing field is to be produced only by a bias winding threaded through the rf cavity, the number of windings is usually limited to no more than a few turns because of possible resonance and arcing. It usually takes 1000 A or more to bias such a cavity.

As the frequency changes, the power loss in ferrite material varies (usually increasing as frequency increases). As a result, it has been difficult to feed the rf generator power to the cavity efficiently because of the high voltage standing wave ratio (VSWR) caused by impedance mismatch (see Appendix B.IV.3). In the CIS cavity this problem was solved by dividing the ferrite rings into two sections; the strength of the biasing magnet in each section can be adjusted by the coupling loop.

The coupling coefficient can be used to compensate the change in the gap impedance, and the input impedance can be maintained constant to match the transmission line impedance of the rf amplifier. The CIS cavity is thus able to operate with a 10:1 frequency ratio with high efficiency, due to the higher impedance of a resonant structure and optimized amplifier coupling.

The loading capacitor can further reduce the length requirement of coaxial cavities and can also be used conveniently to switch frequency bands. For example, the CIS cavity can be operated at $0.5 - 5$ MHz or $1 - 10$ MHz by varying its loading capacitor. Including the load capacitance, C_{load}, the circuit matching (resonance) condition of Eq. (3.246) becomes $\cot(k\ell_r) = R_c\omega(C_{gap} + C_{load})$.

E. Wake-function and impedance of an RLC resonator model

If we represent a charged particle of charge q by $I(t) = q\delta(t) = (1/2\pi)\int qe^{j\omega t}d\omega$, the energy loss due to the passage of an rf gap, represented by an RLC resonator model, is

$$\Delta U = \int |I(\omega)|^2 Z(\omega)d\omega = 2k_r q^2, \qquad k_r = \frac{\omega_r R_{sh}}{4\pi Q}, \qquad (3.258)$$

where k_r is the *loss factor* of the impedance at frequency ω_r. This means that the passing particle loses energy and induces a wakefield in the cavity.

The longitudinal impedance is the Fourier transform of the wake function, and thus the wake function is the inverse Fourier transform of the impedance, For the RLC resonator model, the wake function becomes (see Exercise 3.6.5)

$$Z(\omega) = \int_0^\infty W(t)e^{-j\omega t}dt = \int_{-\infty}^\infty W(t)e^{-j\omega t}dt,$$

$$W(t) = \frac{1}{2\pi}\int Z(\omega)e^{j\omega t}d\omega = 4\pi k_r \left[\cos\tilde{\omega}_r t - \frac{1}{\tilde{\omega}_r T_{f0}}\sin\tilde{\omega}_r t\right]e^{-t/T_{f0}}\,\Theta(t), \quad (3.259)$$

where $\Theta(t) = 1$ if $t > 0$, and 0 if $t < 0$; $T_{f0} = 2Q/\omega_r$ is unloaded filling time defined in Eq. (3.254); and $\tilde{\omega}_r = \omega_r\left(1 - (1/4Q^2)\right)^{1/2}$. If the filling time is long, then the wake potential is a sinusoidal function with angular frequency $\tilde{\omega}_r$, i.e.

$$W(t) \approx 4\pi k_r e^{-t/T_{f0}}\cos\omega_r t.$$

Thus the filling time corresponds also to the wakefield decay time. When beams pass repetitively through the cavity, the effective voltage is the sum of the voltage supplied by the generator current and the wakefields of all beams. Beam loading is important in the design and operation of rf cavities.

VI.3 Beam Loading

A passing beam charge can induce wakefield in an rf cavity. The beam induced rf voltage can alter the effective voltage at the rf gap. Without proper compensation,

the resulting rf voltage acting on the passing beam may cause beam deceleration in an uncontrollable manner. Thus beam loading needs to be considered in the operation of rf cavities.

A. Phasor

The sinusoidal electromagnetic fields and voltages in a standing wave rf structure can be expressed as complex quantities, i.e. $V = V_0 e^{j(\omega t + \theta)}$, where ω is the frequency, θ is a phase angle, and V_0 is the amplitude of the rf voltage. The rf voltage seen by the beam is the projection of the rotating vector on the real axis. Now, we choose a coordinate system that rotates with the rf frequency, and thus the rf voltage is stationary in this rotating coordinate system. In the rotating coordinate system, the voltage vector is called a phasor: $\tilde{V} = V e^{j\theta}$ with $V_0 \cos\theta = V_0 \sin\phi_s$, where ϕ_s is the synchronous phase angle. Phasors are manipulated by using usual rules of complex vector algebra. The properties of rf fields can be studied by using graphic reconstruction in phasor diagrams.

B. Fundamental theorem of beam loading

The cavity provides a longitudinal electric field for particle acceleration. However, when a charged particle passes through the cavity, the image current on the cavity wall creates an electric field that opposes the particle motion. The question arises: what fraction of the electric field or voltage created by the beam affects the beam motion? The question can be addressed by the fundamental theorem of beam loading due to Wilson [see P. B. Wilson, *AIP Conf. Proc.* **87**, 452 (1981).]: *A charged particle sees exactly $\frac{1}{2}$ of its own induced voltage.*

To prove this fundamental theorem, we assume that the stored energy in a cavity in any given mode is $W = \alpha V^2$. We assume that a fraction f of the induced voltage is seen by the inducing particle, and the effective voltage is $V_e = f V_b$, where V_b is the induced voltage in each passage. We assume further that the induced voltage lies at phase angle χ with respect to the inducing current or charge.

Now, we consider two identical charged particles of charge q, separated by phase angle θ, passing through the cavity. The total energy deposited in the cavity and the energy loss by these two particles are respectively

$$W_c = \alpha |\tilde{V}_b(1) + \tilde{V}_b(2)|^2 = \alpha \left(2V_b \cos\frac{\theta}{2} \right)^2 = 2\alpha V_b^2 (1 + \cos\theta),$$

$$\Delta U = [qV_e] + [qV_e + qV_b \cos(\chi + \theta)],$$

where the first and second brackets are the energy losses due to the first and second particles respectively. From the conservation of energy, $\Delta U = W_c$, we obtain

$$\chi = 0, \quad V_b = \frac{q}{2\alpha}, \quad V_e = \frac{1}{2}V_b, \quad f = \frac{1}{2}. \tag{3.260}$$

The result can be summarized as follows:

1. The induced voltage of a beam must have a phase maximally opposite the motion of the charge, i.e. the phase angle $\chi = 0$.
2. $V_e = V_b/2$. The particle sees exactly $1/2$ of its own induced voltage.
3. $W_c = \alpha V_b^2 = q^2/4\alpha = kq^2$, where k is the loss factor, $k = V_b^2/(4W_c)$.
4. $V_b = 2kq$ or $V_e = kq$.

C. Steady state solution of multiple bunch passage

Consider an infinite train of bunches, separated by time T_b, passing through an rf cavity gap. When the cavity is on resonance, the induced voltage seen by the particle is

$$V_b = \frac{1}{2}V_{b0} + V_{b0}(e^{-(\lambda+j\phi)} + e^{-2(\lambda+j\phi)} + \cdots) = V_{b0}(-\frac{1}{2} + \frac{1}{1 - e^{-(\lambda+j\phi)}}), \quad (3.261)$$

where $\phi = (\omega - \omega_r)T_b$ is the relative bunch arrival phase with respect to the cavity phase at the rf gap, ω_r is the resonance frequency of the rf cavity, and $\lambda = T_b/T_f$ is the decay factor of the induced voltage between successive bunch passages, and $T_f = 2Q_L/\omega_r$ is the cavity time constant or the cavity filling time. Here Q_L is the loaded cavity quality factor, taking into account the generator resistance R_g in parallel with the RLC circuit of the cavity, i.e.

$$Q_L = \frac{R_{sh}R_g}{(R_{sh} + R_g)R_c} = \frac{Q_0}{1 + d}, \quad d = \frac{R_{sh}}{R_g}. \quad (3.262)$$

The filling time of the loaded cavity is reduced by a factor $1/(1 + d)$.

The cavity detuning angle ψ and the rf phase shift are

$$\psi = \tan^{-1}\left[\frac{2Q_L(\omega - \omega_r)}{\omega_r}\right] = \tan^{-1}\left[(\omega - \omega_r)T_f\right], \quad (3.263)$$

$$\phi = (\omega - \omega_r)T_b = +(T_b/T_f)\tan\psi = +\lambda\tan\psi, \quad (3.264)$$

where ω is the cavity operation frequency. For rf cavities used in accelerators, we have $\lambda = T_b/T_f = \omega_r T_b/2Q_L \ll 1$, and the induced voltage seen by the beam is

$$V_b = I_i R_{sh}\lambda(-\frac{1}{2} + \frac{1}{1 - e^{-(\lambda+j\phi)}}) \approx I_i \frac{R_{sh}}{(1 + d)}\cos\psi e^{-j\psi} \quad (\lambda \to 0), \quad (3.265)$$

where I_i is the rf image current, $V_{b0} = I_i R_{sh}T_b/T_f$, and the term $-1/2$ is neglected. *The beam induced voltage across the rf gap at the steady state is exactly the rf image current times the impedance of the rf cavity* (see Eq. (3.252)).

VI.4   Beam Loading Compensation and Robinson Instability

To provide particle acceleration in a cavity, we need a generator rf current $\tilde{I}_0 = I_0 e^{j\theta}$ with phase angle θ so that the voltage acting on the beam is $V_{\rm acc} = V_{\rm g} \cos\theta = V_{\rm g} \sin\phi_{\rm s}$, where $\phi_{\rm s}$ is the synchronous phase angle. It appears that the rf system would be optimally tuned if it were tuned to on-resonance so that it had a resistive load with $V_{\rm g} = I_0 R_{\rm sh}$. However, we will find shortly that the effect of beam loading would render such a scheme unusable.

When a *short* beam bunch passes through the rf system, the image rf current $I_{\rm i}$ generated by the beam is twice the DC current, as shown in Eq. (2.125). The beam will induce $I_{\rm i} R_{\rm sh}$ across the voltage gap (see dashed line in Fig. 3.33). The voltage seen by the beam is the sum of the voltage produced by the generator current and the beam induced current. Thus the stable phase angle $\phi_{\rm s}$ of the synchrotron motion will be changed by the induced voltage. This is shown schematically in Fig. 3.33 (left), where the required gap voltage $I_0 R_{\rm sh}$ and the synchronous phase angle $\phi_{\rm s}$ are altered by the voltage induced by the image current. The projection of the resultant vector V_0 on the real axis is negative, and results in deceleration of the beam.

One way to compensate the image current is to superimpose, on the generator current, current directly opposite to the image current. Such a large rf generator current at a phase angle other than that of the rf acceleration voltage is costly and unnecessary.
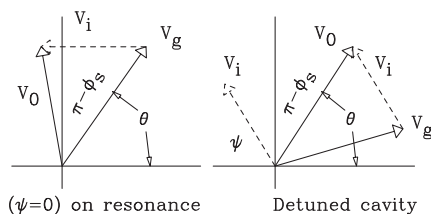

Figure 3.33: Phasor diagrams for beam loading compensation. Left: The beam loading voltage for a cavity tuned on resonance. The combination of generator voltage $V_{\rm g}$ and induced voltage $V_{\rm i}$ gives rise to a decelerating field V_0. Right: When the cavity is detuned to a detuning angle ψ, the superposition of the generator voltage $V_{\rm g}$ and the beam loading voltage $V_{\rm i}$ gives a proper cavity voltage V_0 for beam acceleration.

An alternative solution is to detune the accelerating structure.[47] The detuning angle and the generator current are adjusted so that the resultant voltage has a correct magnitude and phase for beam acceleration. This scheme will minimize the generator current. We define the following phasor currents and voltages for the analysis of this

---

[47]J.E. Griffin, *AIP Conf. Proc.* **87**, 564 (1981); F. Pedersen, *IEEE Tran. Nucl. Sci.* **NS-32**, 2138 (1985); D. Boussard, CERN 91-04, p. 294 (1991).

problem.

$$
\begin{cases}
\tilde{I}_0 = I_0 e^{j\theta} & \text{generator current necessary for accelerating voltage} \\
 & \quad \text{in the absence of beam} \\
\tilde{I}_g = I_g e^{j(\theta+\theta_g)} & \text{required generator current with beam} \\
\tilde{I}_i = -I_i = -I_b & \text{rf beam image current, } I_i \text{ is a positive quantity} \\
\tilde{V}_g = \tilde{I}_g R_{sh} \cos\psi\, e^{-j\psi} & \text{voltage induced by generator current} \\
\tilde{V}_0 = V_0 e^{j\theta} & \text{required rf accelerating voltage} \\
\psi = \tan^{-1}\left[\frac{2Q(\omega-\omega_r)}{\omega_r}\right] & \text{detuning angle} \\
Y = I_i/I_0 & \text{ratio of image current to unloaded generator current}
\end{cases}
$$

The equation for a proper accelerating voltage is

$$
\tilde{V}_0 = \tilde{V}_g + \tilde{V}_i
$$
$$
I_0 R_{sh} e^{j\theta} = [I_g e^{j(\theta+\theta_g)} - I_i] R_{sh} \cos\psi\, e^{-j\psi}. \tag{3.266}
$$

Here the induced voltage is derived from the steady state beam loading. By equating the real and imaginary parts, we obtain

$$
\tan\theta_g = \frac{\tan\psi - Y\sin\theta}{1 + Y\cos\theta}, \quad I_g = I_0 \frac{1 + Y\cos\theta}{\cos\theta_g}, \tag{3.267}
$$

where θ_g is the phase angle of the generator current relative to the ideal $\tilde{I}_0$. The optimal operating condition normally corresponds to $\theta_g = 0$, which minimizes I_g, i.e. the generator current is optimally chosen to be parallel to $\tilde{I}_0$, and Eq. (3.267) reduces to

$$
I_g = I_0(1 + Y\sin\phi_s), \quad \tan\psi = Y\cos\phi_s. \tag{3.268}
$$

Figure 3.33 (right) shows the beam loading phasor diagram with a detuned cavity angle ψ. The resultant vector of the generator voltage and the image current voltage is the effective accelerating voltage for the beam.

A. Robinson dipole mode instability

In accelerators, beams experience many sources of perturbation such as power supply ripple, mis-injection, mismatched beam profile, rf noise, voltage error, etc. Beam stability may sometimes need sophisticated active feedback systems. The topic of control and feedback is beyond the scope of this textbook. Here, we discuss only the dipole mode stability condition related to beam loading, studied by Robinson in 1964 [K.W. Robinson, CEA report CEAL-1010 (1964)].

We consider a small perturbation by shifting the arrival time of all bunches by a phase factor ξ. The accelerating rf voltage will be perturbed by the same phase factor,

$$
V_{acc} = V_0 \cos(\theta - \xi) = V_0 \cos\theta + \xi V_0 \sin\theta = V_0 \sin\phi_s + \xi V_0 \cos\phi_s. \tag{3.269}
$$

where the first term is the intended accelerating voltage and the second term is the effect of phase perturbation due to an error in arrival time.

The wrong arrival time shifts the image beam current by a phase angle ξ. The perturbation to the image rf current its induced rf voltage are

$$\Delta \tilde{I}_{\mathrm{i}} = j\xi \tilde{I}_{\mathrm{i}} = -j\xi I_{\mathrm{i}},$$
$$\Delta \tilde{V}_{\mathrm{i}} = -j\xi I_{\mathrm{i}} R_{\mathrm{sh}} \cos\psi \, e^{-j\psi},$$
$$\Delta V_{\mathrm{ir}} = \Re\{\Delta \tilde{V}_{\mathrm{i}}\} = -\xi Y V_0 \cos\psi \sin\psi,$$

where the beam sees real part ΔV_{ir} of the induced voltage or the projection of the phasor voltage onto the real axis. The net change in accelerating voltage seen by the *bunch* becomes

$$\Delta V_{\mathrm{acc}} = \xi V_0 \cos\phi_{\mathrm{s}} \left[1 - Y \frac{\sin\psi \cos\psi}{\cos\phi_{\mathrm{s}}} \right]. \tag{3.270}$$

A small perturbation in arrival time causes a perturbation in acceleration voltage proportional to the phase shift. If the voltage induced by the image charge is not significant, the bunches in the accelerator will execute synchrotron motion. Thus the equation of motion for the phasor error ξ is (see Exercise 3.6.7)

$$\ddot{\xi} = -\nu_{\mathrm{s}}^2 \left(1 - Y \frac{\sin\psi \cos\psi}{\cos\phi_{\mathrm{s}}} \right) \xi. \tag{3.271}$$

Using Eq. (3.268), we find that the Robinson stability condition becomes

$$1 - Y \frac{\sin\psi \cos\psi}{\cos\phi_{\mathrm{s}}} \geq 0 \quad \text{or} \quad 1 - \frac{\sin^2\psi}{\cos^2\phi_{\mathrm{s}}} \geq 0. \tag{3.272}$$

This means that Robinson stability requires $\psi < \theta = |\frac{1}{2}\pi - \phi_{\mathrm{s}}|$. In general, Eq. (3.272) is applicable to all high order modes. For those modes, Robinson stability can be described as follows.

Below transition energy, with $\cos\phi_{\mathrm{s}} > 0$, Robinson stability can be attained by choosing $\sin\psi < 0$, i.e. the cavity frequency is detuned with $\omega < \omega_{\mathrm{r}}$. Above transition energy, with $\cos\phi_{\mathrm{s}} < 0$, the cavity should be detuned so that $\sin\psi > 0$ or $\omega > \omega_{\mathrm{r}}$ in order to gain Robinson stability. Since the stability condition is a function of bunch intensity, instability is a self-adjusting process. Beam loss will appear until the Robinson stability condition can be achieved. Active feedback systems have been used to enhance the stability of bunched beam acceleration [See e.g. D. Boussard, CERN 87-03, p. 626 (1987); CERN 91-04, p. 294 (1991).]

B. Qualitative feature of Robinson instability

Robinson instability can be qualitatively understood as follows. The wakefield produced in a cavity by a circulating bunch is represented qualitatively in Fig. 3.34, where the impedance of the cavity is assumed to be real.
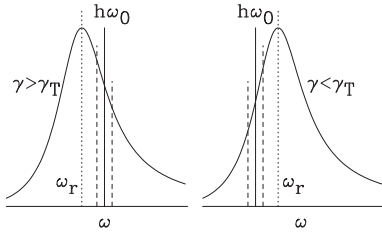
Figure 3.34: A schematic drawing of the real part of impedance arising from a wakefield induced by the circulating beam. To avoid Robinson instability, the cavity should be detuned to $h\omega_0 > \omega_r$ above transition energy and $h\omega_0 < \omega_r$ below transition energy. Above transition energy, higher energy particles have a smaller revolution frequency and thus lose more energy if the cavity detuning is $h\omega_0 > \omega_r$. A similar argument applies to rf cavities operating below transition energy.

Since the revolution frequency is related to the fractional momentum spread by

$$\frac{\Delta\omega}{\omega_0} = -\eta\frac{\Delta E}{\beta^2 E_0},$$

a higher beam energy has a smaller revolution frequency above the transition energy. If the cavity is detuned so that $h\omega_0 > \omega_r$, where ω_r is the resonance frequency of the cavity (Fig. 3.34, left), the beam bunch at higher energy sees a higher shunt impedance and loses more energy, and the beam bunch at lower beam energy sees a lower shunt impedance and loses less energy. Thus the centroid of the beam bunch will damp in the presence of beam loading, and the dipole mode of beam motion is Robinson damped. Similarly, if the cavity is detuned such that $h\omega_0 < \omega_r$, Robinson stability will be attained below transition energy.

Exercise 3.6

1. The skin depth δ_{skin} of an AC current with angular frequency ω traveling on a conductor of bulk conductivity σ is $\delta_{\text{skin}} = \sqrt{2/\mu\sigma\omega}$, where μ is the permeability.

   (a) Show that the surface resistivity defined as $R_s = 1/\sigma\delta_{\text{skin}}$ [in Ohm] is given by

   $$R_s = \sqrt{\frac{\mu\omega}{2\sigma}}.$$

   The surface resistivity does not depend on the geometry of the conductor.

   (b) Show that the resistance of a coaxial structure is given by Eq. (3.248) with

   $$R = \frac{R_s\ell}{2\pi}(\frac{1}{r_1} + \frac{1}{r_2}),$$

   where ℓ is the length of the structure and r_1, r_2 are the inner and outer radii of the coaxial wave guide.

2. Show that the solution of Maxwell's equation in the cylindrical coordinate is given by Eq. (3.237).

3. In a lossless transverse electromagnetic (TEM) wave transmission line, the equation for the current and voltage is

$$\frac{\partial V}{\partial s} = -\tilde{L}\frac{\partial I}{\partial t}, \quad \frac{\partial I}{\partial s} = -\tilde{C}\frac{\partial V}{\partial t},$$

where $\tilde{L}$ and $\tilde{C}$ are respectively the inductance and capacitance per unit length.

(a) Show that the general solution of the right/left traveling TEM wave is given by

$$V = f(t \mp \frac{s}{v}), \quad I = \pm\frac{1}{R_c}f(t \mp \frac{s}{v}),$$

where f is an arbitrary wave form, $v = \frac{1}{\sqrt{\tilde{L}\tilde{C}}}$ is the wave speed, $R_c = \sqrt{\tilde{L}/\tilde{C}}$ is the characteristic impedance of the line.

(b) For TEM sinusoidal waves in a transmission line, show that the current and voltage are related by

$$\begin{cases} I(s,t) = [I_0 \cos ks - j(V_0/R_c) \sin ks]e^{j\omega t} \\ V(s,t) = [V_0 \cos ks - jI_0 R_c \sin ks]e^{j\omega t} \end{cases}$$

where ω is the wave angular frequency, k is the wave number with wave speed $v = \omega/k$, and I_0 and V_0 are the amplitudes of current and voltage at $s = 0$.

4. Verify Eqs.(3.252) and plot Z vs ω for $\omega_r = 200$ MHz, $Q = 10^4$, and $R_{sh} = 25$ MΩ.

5. Consider the excitation of an RLC circuit with a current impulse $I(t) = q\delta(t)$, where $\delta(t)$ is the Dirac delta-function.

(a) Using Eq. (2.252) for pole decomposition of the RLC resonantor, Show that the induced voltage is

$$V(t) = \frac{1}{2\pi} \int \frac{q\,e^{j\omega t}}{j\omega C + \frac{1}{R} + \frac{1}{j\omega L}}d\omega = \frac{q\omega_r R_{sh}e^{-t/T_f}}{Q}\left[\cos\tilde{\omega}_r t - \frac{1}{\tilde{\omega}_r T_f}\sin\tilde{\omega}_r t\right]\Theta(t),$$

where $\omega_r = 1/\sqrt{LC}$, $R_{sh} = R$, $R_{sh}/Q = \sqrt{L/C}$, $\tilde{\omega}_r = \omega_r\sqrt{1 - (1/2Q)^2}$, $T_f = 2Q/\omega_r$, and $\Theta(t) = 1$ if $t \geq 0$ and 0 elsewhere.

(b) Evaluate the integral of Eq. (3.258) and show that the loss factor of a parallel RLC resonator is

$$k_r = \frac{\omega_r R_{sh}}{4\pi Q},$$

where R_{sh} is the shunt resistance, Q is the Q-factor, and ω_r is the resonance frequency.

6. Using the result of Exercise 3.6.5, show that $V_{b0} = I_i R_{sh}\lambda$ for a train of bunches separated by a time interval T_b, where $\lambda = T_b/T_f$, $I_i = 2q/T_b$, and $T_f = 2Q/\omega_r$. Verify Eq. (3.265)

7. Use the following steps to derive Eq. (3.271).

(a) Let ξ be the rf phase associated with the error in beam arrival time. Show that

$$\dot{\xi} = h\eta\delta_b,$$

where the overdot indicates the derivative with respect to orbiting angle θ, and δ_b is the momentum error of the beam centroid.

(b) Show that

$$\dot{\delta}_b = \frac{eV_0\cos\phi_s}{2\pi\beta^2 E}\left[1 - Y\frac{\sin 2\psi}{2\cos\phi_s}\right]\xi.$$

Thus you have arrived at Eq. (3.271).

(c) Draw the Robinson stability region, i.e. $1 \geq (\sin 2\psi/2\cos\phi_s)Y$, in (Y, ψ) for $\phi_s = 0°, 30°, 60°, 120°, 150°, 180°$.

8. The current for charged-particle beams in an accelerator is

$$I(t) = \sum_{\ell}\sum_{m=1}^{h} q_m\delta(t - m\frac{T_0}{h} - \ell T_0),$$

where T_0 is the revolution period, h is the harmonic number, and q_m is the charge in the mth bucket. Show that the amplitude of the Fourier harmonic is

$$I(\omega) = \sum_m I_m e^{-jm\omega T_0/h}$$

where $I_m = q_m/T_0$ is the current of the mth bucket. (1) If all buckets are filled with equal charge, what happens to the spectrum? (2) If there is only one bunch in the ring with harmonic number h, what is the beam spectrum? (3) Verify the symmetric properties: $I(-\omega) = I(\omega)^*$; $I(n\omega_0) = I((h-n)\omega_0)^*$, and $I(n\omega_0) = I((h+n)\omega_0)$.

VII Longitudinal Collective Instabilities

As the demand for beam brightness increases, the physics of collective instabilities becomes more important. Indeed, almost all accelerators and storage rings have suffered some type of collective instability that limits beam intensity or beam brightness. This section provides an introduction to the collective instability in synchrotron motion induced by wakefield, similar to the transverse collective dipole mode instability discussed in Chap. 2, Sec. VIII. A beam bunch can produce wakefield that affects the particle motion and change the beam distribution, the beam distribution can further enhance the wakefield to cause a run-away collective instability.

In the frequency domain, the collective motion is governed by the impedance, which is the Fourier transform of the wakefield. The impedance responsible for collective instabilities can be experimentally measured by the beam transfer function measurements,[48] or from passive measurements of beam loss, coherent and incoherent tune shift, and equilibrium momentum spread and emittance. Collective instabilities can cause bunch lengthening, beam brightness dilution, luminosity degradation, beam loss in machine operation.

Longitudinal collective instabilities have many modes. The collective synchrotron motion can be classified according to synchrotron modes, as discussed in Sec. III, where the phase space are split into resonance islands. On the other hand, since the growth rate of the microwave instability is very large, it can be classified according to the longitudinal mode with density fluctuation. This causes a beam bunch to form microbunches. Decoherence due to nonlinear synchrotron motion generates emittance dilution.

In this introduction text, we discuss only single bunch effects without mode coupling. In Sec. VII.1, we discuss the coherent frequency spectra of beams in a synchrotron. Knowledge of coherent synchrotron modes provides useful information about possible sources, and about the signature at the onset of collective instabilities. An experimental measurement of coherent synchrotron mode will be discussed. Detecting the onset of instabilities and measuring coherent synchrotron modes can help us understand the mechanism of collective instabilities. In Sec. VII.2, we study the linearized Vlasov equation with a coasting beam, and derive a dispersion relation for the collective frequency in single mode approximation. In Sec. VII.3, we list possible sources of the longitudinal impedance. In Sec. VII.4, we examine the microwave instability for a beam with zero momentum spread and for a beam with Gaussian momentum spread, and discuss the Keil-Schnell criterion and the turbulent bunch lengthening. Mode coupling and coupled bunch collective instabilities and other advanced topics can be found in a specialized advanced textbooks [5, 6, 7].

---

[48]A. Hofmann, *Proc. 1st EPAC*, p. 181 (World Scientific, Singapore, 1988).

VII.1 Beam Spectra of Synchrotron Motion

The current observed at a wall gap monitor or a BPM from a circulating charged particle is represented by a periodic δ-function in Eq. (2.125). The corresponding frequency spectra occur at all harmonics of the revolution frequency f_0. Similarly, the current of N equally spaced circulating particles is described by Eq. (2.130), where the Fourier spectra are separated by Nf_0. Since $N \sim 10^8 - 10^{14}$, Nf_0 is well above the bandwidths of BPMs and detection instruments, the coherent rf signal is invisible. Such a beam is called a coasting or DC beam because only the DC signal is visible. Nevertheless, the Schottky signal of each individual charged particle can produce high frequency resistive power loss proportional to the number of particles.[49]

The analysis above is applicable to a single short bunch or equally spaced short bunches. The frequency spectra of a single short bunch occur at all harmonics of the revolution frequency f_0. For B equally spaced short bunches, the coherent frequency spectra are located at harmonics of Bf_0. For bunches separated by T_0/h, the dominant harmonics are located at harmonics of hf_0.

A. Coherent synchrotron modes

The synchrotron motion of beam particles introduces a modulation in the periodic arrival time. Modifying Eq. (3.63) with a periodic linear synchrotron motion and expanding it in Fourier series, we obtain

$$
\begin{aligned}
I_e(t) &= e \sum_{\ell=-\infty}^{\infty} \delta(t - \tau \cos(\omega_s t + \psi) - \ell T_0) \\
&= \frac{e}{T_0} \sum_{n=-\infty}^{\infty} \sum_{m=-\infty}^{\infty} j^{-m} J_m(n\omega_0 \tau) e^{j[(n\omega_0 + m\omega_s)t + m\psi]},
\end{aligned}
\tag{3.273}
$$

where e is the charge, τ and ψ are the amplitude and phase of the synchrotron motion, $\omega_s = \omega_0 \sqrt{heV|\eta \cos\phi_s|/2\pi\beta^2 E}$ is the synchrotron angular frequency with ϕ_s as the rf phase of the synchronous particle, T_0 is the revolution period, and J_m is the Bessel function of order m. The resulting spectra of particle motion are classified into synchrotron modes, i.e. there are synchrotron sidebands around each orbital harmonic n. The amplitude of the mth synchrotron sideband is proportional to the Bessel function J_m.

For a beam with bunch length σ_τ, the coherent synchrotron mode frequency extends typically up to $\omega_{\text{roll off}} \sim 1/\sigma_\tau$ (see Eq. (2.129)), and thus $n\omega_0 \tau \leq \tau/\sigma_\tau$, where τ is the synchrotron oscillation amplitude, and σ_τ is the bunch length. For a stable beam with $\tau/\sigma_\tau \leq 0.1$, the power of the first order synchrotron sideband is about -26 dB below that of the revolution harmonic. However, the coherent mode frequency

---

[49]See A. Hofmann and T. Risselada, *Proc. of PAC 1983*, p. 2400 (1983).

may extend beyond the bunch-length roll-off $1/\sigma_\tau$ due to micro-bunching, residual coherent synchrotron motion, etc. The measurement of the synchrotron sideband power can be used to infer the residual coherent synchrotron motion of a beam and other coherent synchrotron modes. Figure 3.35 shows the coherent spectrum of a production beam in the Taiwan Light Source in Taiwan. There were 154 bunches in 200 buckets separated by 2.0 ns. The coherent mode frequencies are mainly located at revolution harmonics multiples of 499.6438 MHz. Because of the resolution bandwidth of spectrum analyzer (SA), the observed peak power of each harmonic appeared to roll-off faster than the prediction of a Gaussian distribution with a bunch length of 24 ps. The $m = 1$ synchrotron sideband around the 499.6438 MHz was about 82 dB below the revolution harmonic, indicating that the amplitude of coherent synchrotron oscillation was about $\tau \sim 0.05$ ps, a very stable beam.
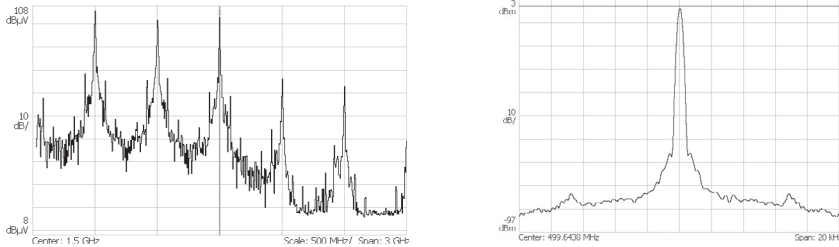
Figure 3.35: Beam power (10 dB/division) vs frequency. Left: The spectra (0-3 GHz) of a TLS production beam. There are 154 bunches in 200 buckets with $f_{\rm rf} = 499.6438$ MHz. The rms bunch length is about 24 ns. Right: The spectrum around the frequency $f_{\rm rf}$ with span 20 kHz. The power of the synchrotron mode is about 82 dB below that of the revolution harmonic (Graph courtesy of Yi-Chih Liu).

A bunch is made of particles with different synchrotron amplitudes and phases, the coherent synchrotron modes of the bunch can be obtained by averaging the synchrotron mode over the bunch distribution. For a ψ-independent beam distribution function $\rho(\tau, \psi) = \rho_0(\tau)$, the beam current becomes

$$I_0(t) = \int I_e(t)\rho_0(\tau)\tau d\tau d\psi = I_{\rm av} \sum_{n=-\infty}^{\infty} A_{n,0} e^{jn\omega_0 t}, \qquad (3.274)$$

$$A_{n,0} = 2\pi \int_0^\infty J_0(n\omega_0\tau)\rho_0(\tau)\tau d\tau,$$

where $I_{\rm av} = N_{\rm B} e f_0$ is the average current, and $A_{n,0}$ is the Hankel transformation of ρ_0. Equation (3.274) contains only orbital harmonics $n\omega_0$, i.e. all synchrotron sidebands of individual particles are averaged to zero. The inverse Hankel transformation can be used to determine the unperturbed distribution function $\rho_0(\tau)$.

Now, consider a coherent synchrotron mode in the bunch distribution, e.g. $\rho(\tau, \psi) = \rho_0(\tau) + \Delta\rho(\tau, \psi)$ with the mth synchrotron mode at the coherent frequency Ω_c, the coherent density becomes $\Delta\rho(\tau, \psi) = \rho_m(\tau)e^{j(\Omega_c t - m\psi)}$, and the current signal is

$$I(t) = I_0(t) + \int I_e(t)\Delta\rho(\tau, \psi)\tau d\tau d\psi = I_0(t) + I_{\text{av}} \sum_{n=-\infty}^{\infty} A_{n,m}e^{j(n\omega_0 + m\omega_s + \Omega_c)t},$$

$$A_{n,m} = 2\pi \int_0^{\infty} J_m(n\omega_0\tau)\rho_m(\tau)\tau d\tau, \tag{3.275}$$

where $A_{n,m}$ is the mth order Hankel transformation. The mth *coherent* synchrotron sideband appears around all coherent revolution harmonics. Using the inverse Hankel transformation, we can deduce the beam distribution function from the amplitudes of coherent modes integrals $A_{n,m}$, that form the kernel of the Sacherer integral equation to solve the coherent mode frequency of the longitudinal collective instability. The coherent synchrotron mode intensity can be obtain by taking the spectrum of a beam during the onset of coherent mode instability.[50] As an illustrative example, we measure the power of a synchrotron mode of a longitudinally kicked beam.

B. Coherent synchrotron modes of a kicked beam

We consider an initial Gaussian beam distribution (see Eq. (3.29) for the phase space coordinates) and a phase kick of time τ_{k}:

$$\begin{aligned}
\rho_0\left(\tau, \frac{\dot{\tau}}{\omega_s}\right) &= \frac{1}{2\pi\sigma_\tau^2} \exp\left(-\frac{\tau^2 + (\dot{\tau}/\omega_s)^2}{2\sigma_\tau^2}\right). \\
&\rightarrow \frac{1}{2\pi\sigma_\tau^2} \exp(-\frac{\tau_{\text{k}}^2}{2\sigma_\tau^2} - \frac{\hat{\tau}^2}{2\sigma_\tau^2} - \frac{\hat{\tau}\tau_{\text{k}}}{\sigma_\tau^2}\cos\psi), \\
&= \frac{1}{2\pi\sigma_\tau^2} \exp(-\frac{\tau_{\text{k}}^2}{2\sigma_\tau^2} - \frac{\hat{\tau}^2}{2\sigma_\tau^2}) \sum_{m=-\infty}^{\infty} (-1)^m I_m(\frac{\hat{\tau}\tau_{\text{k}}}{\sigma_\tau^2})e^{jm\psi}, \quad (3.276)
\end{aligned}$$

where τ_{k} is the amplitude of an initial phase kicked and the coherent mode amplitudes obey $I_{-m} = I_m$. Using formula 6.633.4 in Ref. [31], we obtain the coherent distribution and the coherent mode integral of Eq. (3.275) as

$$\begin{aligned}
\rho_m(\hat{\tau}) &= \frac{(-1)^m}{2\pi\sigma_\tau^2} \exp(-\frac{\tau_{\text{k}}^2}{2\sigma_\tau^2} - \frac{\hat{\tau}^2}{2\sigma_\tau^2})I_m(\frac{\hat{\tau}\tau_{\text{k}}}{\sigma_\tau^2}), \\
A_{n,m} &= e^{-\frac{1}{2}(n\omega_0\tau_{\text{k}})^2(\frac{\sigma_\tau}{\tau_{\text{k}}})^2} J_m(n\omega_0\tau_{\text{k}}). \tag{3.277}
\end{aligned}$$

---

[50]F. Sacherer, *IEEE Trans. Nucl. Sci.* **NS-20**, (1973), ibid **NS-24**, (1977); J.L. Laclare, CERN 87-03, p. 264 (1987). Because the measurement of $A_{n,m}$ peak power depends on the resolution bandwidth and the beam intensity, it is difficult to obtain these amplitudes in a single scan. Furthermore, for spectrum power in a very large frequency span, bandwidth limitation of amplifiers, attenuators, and other components should be carefully evaluated.

The power of the mth sideband of a kicked beam is proportional to the square of the mth order Bessel function. For non-Gaussian beams, the power spectrum is a weighted average of Bessel functions in Eq. (3.275). We describe below an experiment, measuring the coherent mode power at the IUCF Cooler.

C. Measurements of coherent synchrotron modes

The experiment started with a single bunched beam of about 5×10^8 protons at a kinetic energy of 45 MeV and harmonic number $h = 1$, revolution frequency $f_0 = 1.03168$ MHz, and phase slip factor $\eta = -0.86$. The cycle time was 5 s, while the injected beam was electron-cooled for about 3 s. The bunch length, could be adjusted by varying the rf voltage, was about 4.5 m (50 ns) FWHM, or $\sigma_\tau \approx 20$ ns. The bunched beam was kicked longitudinally by phase-shifting the rf cavity wave form (see Sec. III.3). A function generator was used to generate a 0 to 10 V square wave to control the phase kick. The rf phase lock feedback loop, which normally locks the rf cavity to the beam, was switched off. The resulting phase oscillations of the bunch relative to the rf wave form were measured by a phase detector, which was used to calibrate the control voltage for the phase shifters versus the actual phase shift. Both the phase error due to control nonlinearity and the parasitic amplitude modulation of the IUCF Cooler rf systems were kept to less than 10%. The response time of the step phase shifts was limited primarily by the inertia of the rf cavities, which had a quality factor Q of about 40. The magnitude of the phase shift was varied by the size of the applied step voltage.

The spectrum analyzer (SA), set at frequency span 0 Hz, video bandwidth 100 Hz, resolution bandwidth 100 Hz, was triggered about 5 ms before the phase shift. The power observed at a synchrotron sideband from the SA is shown in Fig. 3.36, where the top and bottom traces respectively show the SA responses at $f_0 - f_s$ and $6f_0 - f_s$ vs time. The kicked amplitude was 90 ns, or equivalently $\omega_0 \tau_k = 0.58$ rad. The resolution bandwidth of SA was 100 Hz, thus the measurement of the sideband power was taken at 10 ms after the phase kick. The sideband power shown in Fig. 3.37 was proportional to $|A_{1,1}|^2$ for the upper trace and $|A_{6,1}|^2$ for the lower trace.

Since $\omega_0 \tau_k \approx 0.58$ and $\sigma_\tau = 20$ ns for the case shown in Fig. 3.36, we find $A_{1,1} \sim e^{-0.0083} J_1(0.58)$, and $A_{6,1} \sim e^{-0.299} J_1(3.48)$. The initial power at the fundamental harmonic sideband, which is proportional to $|A_{1,1}|^2$, after the phase kick will be a factor of 6 larger than that of the 6th orbital harmonic. As the synchrotron phase amplitude decreases because of electron cooling, the power $A_{1,1}$ decreases because $J_1(\omega_0 \tau_a)$ decreases with decreasing $\omega_0 \tau_a$, where τ_a is the synchrotron amplitude. On the other hand, as $6\omega_0 \tau_a$ decreases, $J_1(6\omega_0 \tau_a)$ increases. Therefore the power spectrum shown in the lower plot of Fig. 3.36 increases with time. Figure 3.37 shows the power of the $m = 1$ sideband as a function of $\omega\tau = n\omega_0 \tau_k$, where n is the revolution
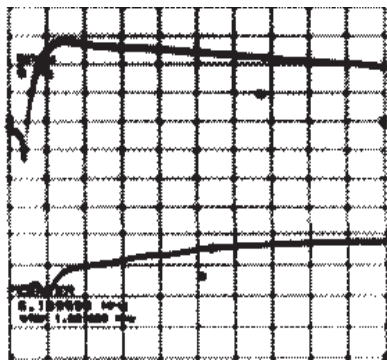
Figure 3.36: The synchrotron sideband power of a kicked beam observed from an SA tuned to the first revolution sideband (upper trace) and the 6th revolution sideband (lower trace) vs time. The revolution frequency was 1.03168 MHz. The setting of the SA was resolution bandwidth 100 Hz, video bandwidth 100 Hz, and frequency span 0 Hz. The sideband power decreased with time for the first harmonic and increased for the 6th harmonic, probably due to electron cooling in the IUCF Cooler. The vertical axis is coherent synchrotron power in dB per division, and the horizontal axis is time at 10 ms per division.

harmonic. For a kicked Gaussian beam, the power $P_{n,1}$ is proportional to $|A_{n,1}|^2$:

$$P_{n,1} \sim |A_{n,1}|^2 = e^{-(n\omega_0\tau_k)^2(\sigma_\tau/\tau_k)^2}|J_1(n\omega_0\tau_k)|^2. \tag{3.278}$$

Because the actual power depends on the beam intensity, all data are normalized at the first peak around $n\omega_0\tau_k \approx 1.8$. Solid curves are obtained from Eq. (3.278) normalized to the peak of experimental data. Finite bunch length suppresses the power of higher order harmonics is clearly seen in the experimental data of Fig. 3.37.
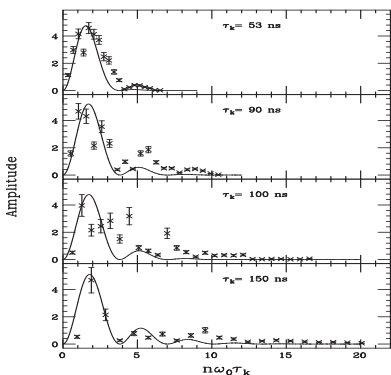
Figure 3.37: Measured $m = 1$ synchrotron sideband power vs frequency for different phase kicked amplitudes is compared with theory based on a Gaussian beam distribution. Plots from top to bottom correspond to a kicking amplitude (time) of 53, 90, 100 and 150 ns. These data were normalized to the peak of the theoretical predictions of Eq. (3.278) without other adjustable parameter.

When a bunched beam encounters collective instability, the observed sideband power $|A_{n,1}|^2$ is proportional to the weighted average of the coherent mode density $\rho(\hat{\tau})$ shown in Eq. (3.277). Measurement of $A_{n,1}$ for all orbital harmonics can be used to obtain the coherent mode distribution function. Similarly, setting up the central frequency at the second synchrotron harmonic, we can measure the $m = 2$ synchrotron modes for the kicked beam.

Difficulties of all spectra power measurements are (1) the measurement of power depends on the resolution bandwidth so that it can not be measured in one single

sweep; (2) BPMs or wall-gap monitors, amplifiers and attenuators are bandwidth limited; and (3) the coherent signal is proportional to $N_{\rm B}^2$, and thus sensitive to beam intensity during the measurement. However, the experiments can be parasitic without interfering regular machine operation.

VII.2   Collective Microwave Instability in Coasting Beams

For coasting beams, there is no rf cavity and the unperturbed distribution function is a function only of the off-momentum coordinate $\delta = \Delta p / p_0$. Let $\Psi_0(\delta)$ be the normalized distribution function with $\int \Psi_0 d\delta = 1$. Because of the impedance of the ring, the beam generates wakefields, which in turn perturb particle motion.

A self-consistent distribution function obeys the Vlasov equation

$$\frac{d\Psi}{dt} = \frac{\partial \Psi}{\partial t} + \dot{\theta}\frac{\partial \Psi}{\partial \theta} + \dot{\delta}\frac{\partial \Psi}{\partial \delta} = 0, \tag{3.279}$$

where the overdot is the derivative with respect to time t. In the presence of a wakefield, we assume a single longitudinal mode with the distribution function:

$$\Psi = \Psi_0(\delta) + \Delta\Psi_n e^{j(\Omega t - n\theta)}, \tag{3.280}$$

where Ψ_0 is the unperturbed distribution, Ω is the coherent frequency, θ is the orbiting angle, and $\Delta\Psi_n(\delta)$ is the perturbation amplitude for the longitudinal mode n. The perturbation causes density fluctuation along the machine, i.e. the collective instability of mode number n can cause a coasting beam into n microbunches. In general, the perturbing distribution function should be written as a linear superposition of all possible modes. The frequencies of the collective motion are eigenfrequencies of the coupled system.

By definition, the energy gain/loss per revolution due to the wakefield is equal to the current times the longitudinal broadband impedance, and the time derivative of the fractional off-momentum coordinate δ of a coasting beam become

$$\Delta E\Big|_{\rm per\ turn} = Z_\parallel \left(eI_0\int \Delta\Psi_n d\delta\right)e^{j(\Omega t - n\theta)},$$

$$\dot{\delta} = \frac{\omega_0}{2\pi\beta^2 E}\left(eI_0 Z_\parallel\int \Delta\Psi_n d\delta\right)e^{j(\Omega t - n\theta)}. \tag{3.281}$$

where the impedance is evaluated at the collective frequency Ω. Since $|\Delta\Psi_n| \ll \Psi_0$ at the onset threshold of collective instability, we linearize the Vlasov equation to obtain

$$j(\Omega - n\dot{\theta})\Delta\Psi_n = -\frac{\omega_0 e I_0 Z_\parallel}{2\pi\beta^2 E}\frac{\partial \Psi_0}{\partial \delta}\left(\int \Delta\Psi_n d\delta\right). \tag{3.282}$$

Using $\dot\theta = \omega$ and integrating Eq. (3.282), we obtain the dispersion relation

$$1 = j\frac{eI_0 n\omega_0\,(Z_\parallel/n)}{2\pi\beta^2 E}\int\frac{\partial\Psi_0/\partial\delta}{\Omega - n\omega}d\delta = j\frac{eI_0 n^2\omega_0\,(Z_\parallel/n)}{2\pi\beta^2 E}\int\frac{\Psi_0}{(\Omega - n\omega)^2}\frac{\partial\omega}{\partial\delta}d\delta, \quad (3.283)$$

where partial integration has been carried out in the second equality.

The eigenfrequency Ω of the collective motion is the solution of the dispersion relation. If the imaginary part of the coherent mode frequency is negative, i.e. $\mathrm{Im}\,\Omega < 0$, the perturbation amplitude grows exponentially, and the beam encounters the *collective microwave instability*, where the terminology is derived from the fact that the coherent frequency observed is in the microwave frequency range. With the relation $\omega = \omega_0 - \omega_0\eta\delta$, the dispersion integral can be analytically obtained for some distribution functions of the beam. First we examine possible sources of longitudinal impedance.

VII.3 Longitudinal Impedance

The impedance and the wake function are related by

$$Z_\parallel(\omega) = \int_{-\infty}^{\infty} W_\parallel(t)e^{-j\omega t}dt, \qquad W_\parallel(t) = \frac{1}{2\pi}\int_{-\infty}^{\infty} Z_\parallel(\omega)e^{j\omega t}d\omega. \qquad (3.284)$$

Because the wake function is real and obeys the causality $W_\parallel(t) = 0$ for $t < 0$, the impedance has the property: $Z_\parallel(-\omega) = Z_\parallel^*(\omega)$, i.e. the real part of the longitudinal impedance is positive and is a symmetric function of the frequency. In fact, the property of $Z_\parallel(\omega)/\omega$ is similar to that of $Z_\perp(\omega)$. Without making the effort to derive them, we list below some sources of commonly used impedance models. Since the wakefield obeys the causality principle, the impedance does not have singularities in the lower complex plane. The real and imaginary parts of the impedance are related by the Hilbert transform

$$\mathrm{Re}\,Z_\parallel(\omega) = -\frac{1}{\pi}\int_{\mathrm{P.V.}} d\omega'\frac{\mathrm{Im}\,Z_\parallel(\omega')}{\omega' - \omega}, \qquad \mathrm{Im}\,Z_\parallel(\omega) = +\frac{1}{\pi}\int_{\mathrm{P.V.}} d\omega'\frac{\mathrm{Re}\,Z_\parallel(\omega')}{\omega' - \omega},$$

where P.V. stands for the principal value integral.

A. Space-charge impedance

Let a be the radius of a uniformly distributed coasting beam, and let b be the radius of a beam pipe (Fig. 3.38). The electromagnetic fields of the coasting beam are

$$E_r = \begin{cases} \dfrac{e\lambda r}{2\pi\epsilon a^2} \\[2mm] \dfrac{e\lambda}{2\pi\epsilon r} \end{cases} \qquad B_\phi = \begin{cases} \dfrac{\mu_0 e\lambda\beta c r}{2\pi a^2} & r \le a \\[2mm] \dfrac{\mu_0 e\lambda\beta c}{2\pi r} & r > a \end{cases} \qquad (3.285)$$
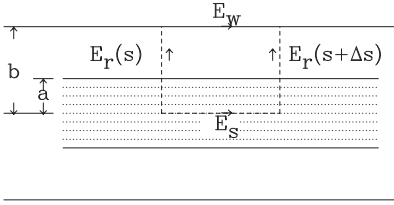
Figure 3.38: Geometry of a uniformly distributed beam with radius a in a beam pipe of radius b. The induced electric fields that arise from impedance are shown schematically. The rectangular loop is used for the path integral of Faraday's law.

where λ is the particle's line density, e is the charge, βc is the speed, and ϵ_0 and μ_0 are the permittivity and permeability of the vacuum.

Consider a small fluctuation in the line density $\lambda = \lambda_0 + \lambda_1 e^{j(\Omega t - n\theta)}$ and current $I = I_0 + I_1 e^{j(\Omega t - n\theta)}$, where $I_0 = e\beta c\lambda_0$ and $I_1 = e\beta c\lambda_1$. The perturbation generates an electric field on the beam. Using Faraday's law

$$\oint \vec{E} d\vec{\ell} = -\frac{\partial}{\partial t}\int \vec{B}\cdot d\vec{\sigma}$$

along the loop shown in Fig. 3.38, where $d\vec{\sigma}$ is the surface integral, we obtain

$$(E_s - E_{\mathrm{w}})\Delta s + \frac{eg_0}{4\pi\epsilon_0}[\lambda(s+\Delta s) - \lambda(s)] = -\Delta s \frac{\mu_0 e\beta cg_0}{4\pi}\frac{\partial\lambda}{\partial t},$$

where E_s and E_{w} are the electric fields at the center of the beam pipe and at the vacuum chamber wall, and the geometry factor $g_0 = 1 + 2\ln(b/a)$ is obtained from the integral along the radial paths from the beam center to the vacuum chamber wall. If the impedance is averaged over the beam cross section, the geometric factor becomes $g_0 = \frac{1}{2} + 2\ln(b/a)$. On the other hand, if the perturbation is on the surface of the beam, the geometry factor becomes $g_0 = 2\ln(b/a)$. Assuming that the disturbance is propagating at the same speed as the orbiting beam particles, i.e. $\partial\lambda/\partial t = -\beta c(\partial\lambda/\partial s)$, the electric field acting on the circulating beam becomes

$$E_s = E_{\mathrm{w}} - \frac{eg_0}{4\pi\epsilon_0\gamma^2}\frac{\partial\lambda}{\partial s}, \tag{3.286}$$

where the factor $1/\gamma^2$ arises from the cancellation of forces due to the electric and magnetic fields.

For most accelerators, the vacuum chamber wall is inductive at low and medium frequency range. Let $L/2\pi R$ be the inductance per unit length, then the induced wall electric field is

$$E_{\mathrm{w}} = \frac{L}{2\pi R}\frac{dI_{\mathrm{w}}}{dt} = \frac{e\beta^2 c^2 L}{2\pi R}\frac{\partial\lambda}{\partial s}. \quad \text{or} \quad E_s = -e\left[\frac{g_0}{4\pi\epsilon_0\gamma^2} - \frac{\beta^2 c^2 L}{2\pi R}\right]\frac{\partial\lambda}{\partial s}.$$

The total voltage drop in one revolution on the beam and the impedance are

$$\Delta U = -e\beta cR\frac{\partial\lambda}{\partial s}\left[\frac{g_0 Z_0}{2\beta\gamma^2} - \omega_0 L\right]; \qquad \frac{Z_\parallel}{n} = -\frac{\Delta U}{nI_1} = -j\left[\frac{g_0 Z_0}{2\beta\gamma^2} - \omega_0 L\right]. \tag{3.287}$$

where $\beta c = \omega_0 R$ is the speed of the orbiting particles, $Z_0 = 1/\epsilon_0 c = 377$ ohms is the vacuum impedance, and we use $R(\partial\lambda/\partial s) = (\partial\lambda/\partial\theta) = -jn\lambda_1$, and $e\beta c\lambda_1 = I_1$, The first term in Eq. (3.287) is the space-charge impedance and the second term is the inductance of the vacuum chamber wall. Typical values of the space-charge impedance at transition energy are listed in Table 3.7.

Table 3.7: Typical space-charge impedance at $\gamma = \gamma_{\mathrm{T}}$.

	AGS	RHIC	Fermilab BST	Fermilab MI	KEKPS
γ_{T}	8.7	22.5	5.4	20.4	6.8
$|Z_{\parallel,\mathrm{sc}}|/n$ $[\Omega]$	13	1.5	30	2.3	20

B. Resistive wall impedance

The vacuum chamber wall is normally not perfectly conducting, and E_{w} can also induce a resistive impedance part that depends on the conductivity, microwave frequency, and skin depth. Because the resistivity of the vacuum chamber wall is finite, part of the wakefield can penetrate the vacuum chamber and cause energy loss to the beam. Penetration of electromagnetic wave into the vacuum chamber can be described by Maxwell's equations

$$\nabla \times \vec{E} = -\mu\frac{\partial\vec{H}}{\partial t}, \qquad \nabla \times \vec{H} = \vec{J} = \sigma_c\vec{E}, \quad \implies \quad \nabla^2\vec{E} = \mu\sigma_c\frac{\partial\vec{E}}{\partial t}, \qquad (3.288)$$

where σ_c is the conductivity and μ is the permeability. Here we use Ohm's law, and neglect the contribution from the displacement current provided that the frequency of the electromagnetic wave is not very high.[51] The electric field inside the conductor becomes

$$\vec{E} = \hat{s}\, E_0 \exp\{j(\omega t - kx)\}, \qquad k = (1-j)\sqrt{|\omega|\sigma_c\mu/2}.$$

where x is the depth into the vacuum chamber wall and k is the wave number. The imaginary part of the wave number is the inverse of the penetration depth, or equivalently, the skin depth is $\delta_{\mathrm{skin}} = \sqrt{2/\mu\sigma_c\omega}$. The electromagnetic fields penetrate a skin depth inside the vacuum chamber wall. The resistance due to the electric field becomes

$$Z_{\parallel}^{\mathrm{real}} \approx \frac{2\pi R}{2\pi b\sigma_c\delta_{\mathrm{skin}}} = \frac{Z_0\beta}{2b}\left(\frac{|\omega|}{\omega_0}\right)^{1/2}\delta_{\mathrm{skin},0}, \qquad (3.289)$$

---

[51]For frequencies $\omega \ll \sigma_c/\epsilon \approx \sigma_c Z_0 c \approx 10^{19}$ Hz, where ϵ is the permittivity, the displacement current contribution to Maxwell's equation is small.

where Z_0 is the vacuum impedance, β is Lorentz's relativistic velocity factor, b is the vacuum chamber radius, $\delta_{\text{skin},0} = \sqrt{2/\mu\sigma_c\omega_0}$ is the skin depth at the revolution frequency ω_0. Since the magnetic energy is equal to the electric energy, the magnitude of the reactance is equal to the resistance. The resistive wall impedance becomes

$$Z_\parallel(\omega) = (1 + j\,\text{sgn}(\omega))\,\frac{Z_0\beta}{2b}\,\left(\frac{|\omega|}{\omega_0}\right)^{1/2}\delta_{\text{skin},0}, \tag{3.290}$$

where the sign function, $\text{sgn}(\omega) = +1$ if $\omega > 0$ and -1 if $\omega < 0$, is added so that the impedance satisfies the causality condition.

C. Narrowband and broadband impedance

Narrowband impedance arise from parasitic modes in rf cavities and cavity-like structures in accelerators. Broadband impedance arise from vacuum chamber breaks, bellows, and other discontinuities in accelerator components. The longitudinal narrowband and broadband impedance can conveniently be represented by an equivalent RLC circuit

$$Z(\omega) = \frac{R_{\text{sh}}}{1 + j\text{Q}(\omega/\omega_{\text{r}} - \omega_{\text{r}}/\omega)}, \tag{3.291}$$

where ω_{r} is the resonance frequency, R_{sh} is the shunt impedance, and Q is the quality factor. The high order mode (HOM) of rf cavities is a major source of narrowband impedance. Parameters for narrowband impedance depend on the geometry and material of cavity-like structures.

For a broadband impedance, the Q-factor is usually taken to be 1, and the resonance frequency to be the cut-off frequency $\omega_{\text{r,bb}} = \omega_0 R/b = \beta c/b$, where ω_0 is the revolution frequency, R is the average radius of the accelerator, and b is the vacuum chamber size. The magnitude of the broadband shunt impedance can range from 50 ohms for machines constructed in the 60's and 70's to less than 1 ohm for recently constructed machines, where the vacuum chamber is carefully smoothed.

To summarize, the longitudinal impedance $Z_\parallel(\omega)/\omega$ or $Z_\parallel/n$ are schematically shown in Fig. 3.39, where the solid and dashed lines correspond to the real and imaginary parts respectively. The symmetry of the impedance as a function of ω is also shown.

VII.4 Single Bunch Microwave Instability

The negative mass instability was predicted in 1960's. Experimental observations were obtained in the intersecting storage rings (ISR), where microwave signal was detected in the beam debunching process. Subsequently, it was observed in almost all existing high intensity accelerators.
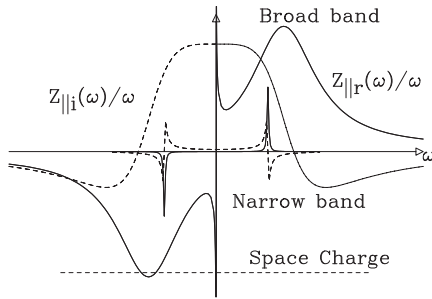
Figure 3.39: Schematic of a longitudinal impedance that includes broadband, narrowband, and space-charge impedance. Including the resistive wall impedance in the longitudinal impedance, we find that $|\mathrm{Re}(Z_\parallel/\omega)|$ becomes large at $\omega \approx 0$.

A. Negative mass instability without momentum spread

First, we consider negative mass instability. In the absence of momentum spread with $\Psi_0(\delta) = \delta_d(\delta)$, where $\delta = \Delta p/p_0$ and $\delta_d(x)$ is the Dirac δ-function, the solution of Eq. (3.283) is

$$\left(\frac{\Omega}{n\omega_0}\right)^2 = -j\frac{eI_0\,Z_\parallel/n}{2\pi\beta^2 E}\,\eta\ . \tag{3.292}$$

The condition for having a real Ω is $-j(Z_\parallel/n)\eta > 0$. This condition is only satisfied for a space-charge (capacitive) impedance below the transition energy, or an inductive impedance above the transition energy. If $Z_\parallel/n$ is capacitive, e.g. space-charge impedance, the collective frequency is a real number below the transition energy with $\eta < 0$. This results in a collective frequency shift without producing collective instabilities. On the other hand, if the impedance is inductive, the collective frequency becomes a complex number below the transition energy, and the solution with a negative imaginary part gives rise to collective instability. For resistive impedance, the beam with a zero momentum spread is unstable. Table 3.8 shows the characteristic behavior of microwave collective instability.

Table 3.8: Characteristic behavior of collective instability without Landau damping.

	$Z_\parallel/n$	capacitive	inductive	resistive
Below transition	$\eta < 0$	stable	unstable	unstable
Above transition	$\eta > 0$	unstable	stable	unstable

The terminology of "negative mass instability" is derived from a pure space charge effect. Above the transition energy with $\eta > 0$, a higher energy particle takes longer time to complete one revolution, or it appears to have a negative mass. Since the "microwave instability" resulting from the space-charge impedance occurs when $\eta > 0$, it is also called *negative mass instability*. However, a beam with a small frequency spread can also encounter microwave instability at $\gamma < \gamma_T$ if the impedance is inductive, or resistive.

B. Landau damping with finite frequency spread

For a beam with a finite momentum spread with $\eta \neq 0$, the coherent mode frequency can be obtained by solving the dispersion relation. In this case, there is a finite region of impedance value where the growth rate of collective instability is zero, and collective motion is Landau damped.

If the distribution function is a symmetric function of momentum deviation δ, the threshold impedance for microwave instability is reflectively symmetric with respect to the real part of the impedance. Depending on the actual distribution function, the threshold of collective instability can be estimated from the dispersion relation.

For example, we consider a Gaussian beam model of a coasting beam given by

$$\Psi_0 = \frac{1}{\sqrt{2\pi}\sigma_\delta} \exp\left\{-\frac{\delta^2}{2\sigma_\delta^2}\right\},$$

where $\delta = \Delta p/p_0$ and σ_δ is the rms momentum spread. In the limit of small frequency spread, the distribution becomes the Dirac δ-function. The rms frequency spread of the beam becomes $\sigma_\omega = \omega_0 \eta \sigma_\delta$. The dispersion relation can be integrated to obtain

$$\frac{Z_\parallel}{n} = j\frac{4\pi\beta^2 E\sigma_\delta^2 \eta}{eI_0}J_G^{-1}, \tag{3.293}$$

$$J_G = \sqrt{\frac{2}{\pi}} \int_{-\infty}^{\infty} \frac{xe^{-x^2/2}}{x + \tilde{\Omega}/(n\omega_0\eta\sigma_\delta)}dx = 2[1 + j\sqrt{\pi}yw(y)], \tag{3.294}$$

where $\tilde{\Omega} = \Omega - n\omega_0$, and $w(y)$ is the complex error function with $y = -\tilde{\Omega}/(\sqrt{2}n\omega_0\eta\sigma_\delta)$. Asymptotically, we have $J_G \to y^{-2}$ as $y \to \infty$. Thus in the limit of zero detuning (or zero frequency spread), Eq. (3.293) reduces to Eq. (3.292).

We usually define the effective U and V parameters, or U' and V' parameters as

$$U + jV = \frac{eI_0\ (Z_\parallel/n)}{2\pi\beta^2 E\sigma_\delta^2 \eta}, \qquad U' + jV' = \frac{eI_0\ (Z_\parallel/n)}{\beta^2 E\delta_{\text{FWHM}}^2 \eta}. \tag{3.295}$$

For the Gaussian beam, we find $\delta_{\text{FWHM}} = \sqrt{8\ln 2}\,\sigma_\delta$. In terms of U and V parameters, Eq. (3.293) becomes $-j(U + jV)J_G/2 = 1$.

The solid line in the left plot of Fig. 3.40 shows the threshold V' vs U' parameters of collective microwave instability with $\text{Im}(\Omega) = 0$. Dashed lines inside the threshold curve correspond to stable motion, and the dashed lines outside the threshold curve are unstable with growth rates $-(\text{Im}\,\Omega)/\sqrt{2\ln 2}\,\omega_0\eta\sigma_\delta = 0.1, 0.2, 0.3, 0.4$, and 0.5 respectively. The right plot of Fig. 3.40 shows the threshold V' vs U' parameters, from inside outward, for the normalized distribution functions $\Psi_0(x) = 3(1 - x^2)/4$, $8(1 - x^2)^{3/2}/3\pi$, $15(1 - x^2)^2/16$, $315(1 - x^2)^4/32$, and $(1/\sqrt{2\pi})\exp(-x^2/2)$. All distribution functions, except the Gaussian distribution, are limited to $x \leq 1$. Note that a distribution function with a softer tail, i.e. a less sudden cutoff, gives a larger stability region in the parametric space.
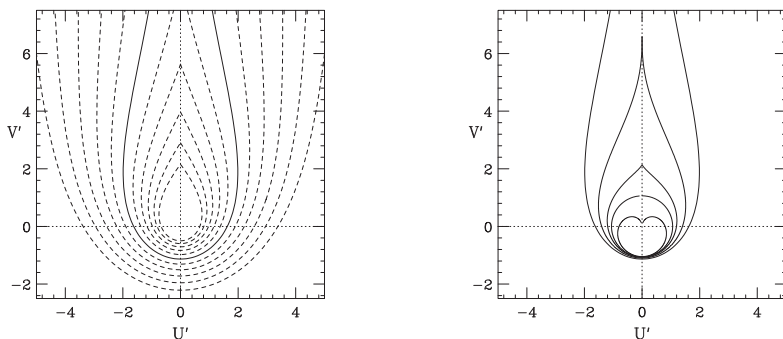
Figure 3.40: Left: The solid line shows the parameters V' vs U' for a Gaussian beam distribution at a zero growth rate. Dashed lines inside the threshold curve are stable. They correspond to $-\mathrm{Im}\,\Omega/(\sqrt{2\ln 2}\,\omega_0\eta\sigma_\delta) = -0.1, -0.2, -0.3, -0.4$, and -0.5. Dashed lines outside the threshold curve have growth rates $-\mathrm{Im}\,\Omega/(\sqrt{2\ln 2}\,\omega_0\eta\sigma_\delta) = 0.1, 0.2, 0.3, 0.4$, and 0.5 respectively. Right: The threshold V' vs U' parameters for various beam distributions.

C. Keil-Schnell criterion

Figure 3.40 show that the stability region depends on beam distribution. Based on experimental observations and numerical calculations of the dispersion relation, a simplified estimation of the stability condition is to draw a circle around the origin in the impedance plane, called the Keil-Schnell criterion:

$$\left|\frac{Z_\parallel}{n}\right| \leq \frac{2\pi\beta^2 E\sigma_\delta^2|\eta|F}{eI_0}, \tag{3.296}$$

where F is a form factor that depends on the distribution function. For a Gaussian beam, $F = 1$; and for a tri-elliptical distribution with $\Psi_0(x) = 8(1 - x^2)^{3/2}/3\pi$, $F \approx 0.94$ [5, 6, 7]. The total longitudinal energy drop from impedance, $eI_0|Z_\parallel|$, per unit frequency spread $n|\eta|/\sqrt{2\pi}\sigma_\delta$ for mode number n should be less than the total energy spread $\sqrt{2\pi}\beta^2 E\sigma_\delta$ of the beam. Since the microwave growth rate is usually fast, and the the wavelength of the coherent wave is usually small compared with the bunch length, the Keil-Schnell criterion at threshold of instability can be applied to the bunched beam by replacing the average current I_0 by the peak current $\hat{I}$:[52]

$$\left|\frac{Z_\parallel}{n}\right| \leq \frac{2\pi\beta^2 E\sigma_\delta^2|\eta|F}{e\hat{I}}, \tag{3.297}$$

[52]E. Keil and W. Schnell, CERN-ISR-TH-RF/69-48 (July 1969); A.G. Ruggiero and V.G. Vaccaro, CERN ISR TH/68-33 (1968); Since the growth rate of the microwave instability is normally very fast, the threshold condition can be obtained from the local peak current of the beam, called Boussard conjecture, which has been well tested in the Intersecting Storage Ring (ISR). See e.g. J.M. Wang and C. Pellegrini, *Proc. 11th HEACC*, p. 554 (1980).

where $I_0 = N_\mathrm{B} ef$ is the average bunch current, $\hat{I} = F_\mathrm{B} I_0$, and $F_\mathrm{B} = 2\pi/\sqrt{2\pi}\sigma_\theta$ is the bunching factor, where $\sigma_\theta = \omega_0 \sigma_{\Delta t}$ is the bunch length in orbiting angle.

D. Microwave instability near transition energy

Near the transition energy, Landau damping for microwave single bunch instability vanishes because of a small synchrotron frequency spread. The Keil-Schnell criterion is not applicable in this region. For a pure capacitive impedance, e.g. space-charge impedance, instability occurs when $\gamma \geq \gamma_\mathrm{T}$. For a pure inductance impedance, instability exists only below transition. Since the beam distribution function is non-adiabatic in the transition energy region, determination of microwave instability needs careful evaluation of the dispersion integral.

We assume a model of collective microwave instability such that the longitudinal modes are nearly decoupled and thus the coherent growth rate can be obtained by solving the dispersion relation Eq. (3.283). Furthermore, we assume a Gaussian beam model with the threshold impedance determined by the peak current. The peak current is located at the center of the bunch $\Delta\phi = 0$. The distribution function and the peak current become (see Sec. IV.1)

$$\Psi_0(\delta) = \sqrt{\frac{3\alpha_{\delta\delta}}{\pi}} e^{-3\alpha_{\delta\delta}\delta^2}, \qquad \hat{I} = I_0 \sqrt{\frac{3(\alpha_{\phi\phi}\alpha_{\delta\delta} - \alpha_{\phi\delta}^2)}{\pi\alpha_{\delta\delta}}} = I_0 \frac{\sqrt{3\pi}}{\tilde{A}\sqrt{\alpha_{\delta\delta}}}, \qquad (3.298)$$

where $\alpha_{\delta\delta}$ is given by Eq. (3.140), I_0 is the average current and $\tilde{A}$ is the rms phase-space area of the beam. The dispersion integral can be integrated to obtain the coherent mode frequency given by

$$1 = j\frac{3eI_0 \left(Z_\parallel/n\right)}{2\pi^{3/2}\beta^2 E\eta} \frac{\pi\sqrt{3\alpha_{\delta\delta}}}{\tilde{A}} J_\mathrm{G}^{-1}, \qquad (3.299)$$

$$J_\mathrm{G} = 2[1 + j\sqrt{\pi}yw(y)], \quad y = -\frac{\Omega}{n\omega_0\eta}\sqrt{6\alpha_{\delta\delta}}.$$

For a given broadband impedance model with constant $Z_\parallel/n$, we can find the eigenvalue of the growth rate Im $(\Omega(\mathrm{t}))$ by solving Eq. (3.299).[53]

The solution of Eq. (3.299) shows that the growth rate near the transition energy is nearly equal to the growth rate without Landau damping. This is easy to understand: at $\gamma = \gamma_\mathrm{T}$, the frequency spread of the beam becomes zero, and Landau damping vanishes. Fortunately, the growth rate is also small at $\gamma \approx \gamma_\mathrm{T}$.

---

[53]See e.g. S.Y. Lee and J.M. Wang, *IEEE Trans. Nucl. Sci.* **NS-32**, 2323 (1985). The impedance model $Z_\parallel/n = 5 - j(Z_{\parallel,\mathrm{sc}}/n)$ ohms was used to study the growth rate around the transition energy for RHIC. Microwave instability below transition may arise from the real impedance. Because of a large space-charge impedance, the growth rate appears to be larger above the transition energy.

The total growth factor across the transition energy region can be estimated by

$$G = \exp \left\{ \int (-\mathrm{Im}\Omega)_{\mathrm{unstable}} dt \right\}. \tag{3.300}$$

The total growth factor is a function of the scaling variable $|Z_\parallel/n|N_b/\tilde{A}$. Note that the growth factor is much smaller if the initial phase-space area is increased. Phase-space dilution below transition energy has become a useful strategy in accelerating high intensity proton beams through transition energy. The CERN PS and the AGS employ this method for high intensity beam acceleration. Bunched beam dilution can be achieved either by using a high frequency cavity as noise source or by mismatched injection at the beginning of the cycle.

The distribution function model Eq. (3.298) does not take into account nonlinear synchrotron motion near the transition energy. For a complete account of microwave instability, numerical simulation is an important tool near transition energy.[54] A possible cure for microwave instability is to pass through transition energy fast with a transition energy jump. Furthermore, blow-up of phase-space area before transition energy crossing can also alleviate the microwave growth rate.

We have discussed microwave instabilities induced by a broadband impedance. In fact, it can also be generated by a narrowband impedance. Longitudinal bunch shapes in the KEK proton synchrotron (PS) were measured by a fast bunch-monitor system, which showed the rapid growth of the microwave instability at the frequency of 1 GHz and significant beam loss just after transition energy.[55] Temporal evolution of the microwave instability is explained with a proton-klystron model. The narrowband impedance of the BPM system causes micro-bunching in the beam that further induces wakefield. The beam-cavity interaction produces the rapid growth of the microwave instability. This effect is particularly important near the transition energy, where the frequency spread of the beam vanishes, and the Landau damping mechanism disappears.

E. Microwave instability and bunch lengthening

When the current is above the microwave instability threshold, the instability can cause micro-bunching. The energy spread of the beam will increase until the stability condition is satisfied. For proton or hadron accelerators, the final momentum spread of the beam may be larger than that threshold value caused by decoherence of the synchrotron motion.

---

[54]W.W. Lee and L.C. Teng, *Proc. 8th Int. Conf. on High Energy Accelerators*, CERN, p. 327 (1971); J. Wei and S.Y. Lee, *Part. Accel.* **28**, 77-82 (1990); S.Y. Lee and J. Wei, *Proc. EPAC*, p. 764 (1989); J. McLachlan, private communications on ESME Program.

[55]See e.g. K. Takayama *et al., Phys. Rev. Lett.*, **78**, 871 (1997).

Due to synchrotron radiation damping in electron storage rings, the final momentum spread and the bunch length are determined by the microwave instability threshold of Eq. (3.297):

$$\sigma_\theta = \omega_0 \sigma_t = \frac{|\eta|}{\nu_s}\sigma_\delta = \left(\frac{eI_0|\eta Z_\parallel/n|}{(2\pi)^{3/2}F\nu_s^2\beta^2 E}\right)^{1/3}, \tag{3.301}$$

where ν_s is the synchrotron tune. Note that the bunch length depends only on the parameter $\xi = (I_0|\eta|/\nu_s^2\beta^2 E)$ provided that the impedance does not depend on the bunch length. Chao and Gareyte showed that the bunch lengths of many electron storage rings scaled as $\sigma_\theta \sim \xi^{1/(2+a)}$. This is called Chao-Gareyte scaling law. For a broadband impedance, we have $a = 1$. The scaling law is not applicable if the impedance depends on the beam current and bunch length.

F. Microwave instability induced by narrowband resonances

At low energy, the longitudinal space charge potential, shown as the first term in Eq. (3.287), can be large for high intensity beam bunch. It requires a costly large rf cavity potential to keep beam particles bunched inside the rf bucket. In particular, if it requires a beam gap for a clean extraction, and for minimizing the effect of the electron-cloud instability.

The longitudinal space charge potential can be compensated by the inductive impedance shown in the second term of Eq. (3.287). We consider a cavity with ferrite ring filling a pillbox. The inductance is

$$L = \frac{2\mu'\mu_0\ell}{4\pi}\ln\frac{R_2}{R_1}, \tag{3.302}$$

where μ' is the real part of the ferrite permittivity, R_1 and R_2 are the inner and outer radii of the ferrite rings, and ℓ is the length of the pillbox cavity. The inductive inserts carried out at PSR experiment employs coaxial pillbox cavity with 30 ferrite rings each with width 2.54 cm, 12.7 cm inner diameter (id), and 20.3 cm outer diameter (od). The Proton Storage Ring (PSR) at Los Alamos National Laboratory compresses high intensity proton beam from the 800 MeV linac into a bunch of the order of 250 ns. The parameters for PSR are $C = 90.2$ m, $\gamma_T = 3.1$, $\nu_x = 3.2$, $\nu_z = 2.2$, $\nu_s = 0.00042$, and $f_0 = 2.8$ MHz.

To cancel the space charge impedance at 800 MeV for PSR at the harmonic $h = 1$, one requires about 3 pillbox cavities. The experimental test for this experiment was indeed successful. Unfortunately, the beam also encounters collective microwave beam instability at high intensity. Figure 3.41 shows the microbunching of the beam under the action of three ferrite inserts when an initial bunched coasting beam injected into the ring. The instability is landau damped by heating up the ferrite core to change its permeability and lower the Q-value of the TM_010 mode.[56]

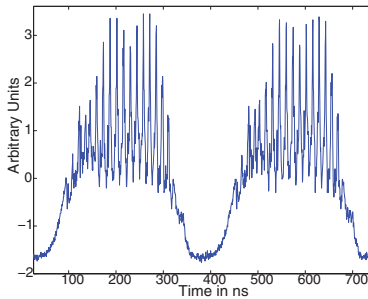[56]M.A. Plum, *et al.*, Phys. Rev. Special Topics, Accelerators and Beams, **2**, 064201 (1999); C.

Figure 3.41: The longitudinal beam profile at PSR encountered microwave instability caused by inductive inserts, where three 1-m long ferrite ring cavities were installed in the PSR ring. The injected beam was a uniformly distributed bunched-coasting beam with cavity off. After threshold intensity is encountered, the impedance causes microbunching in the beam. [Courtesy of R. Macek, LANL]

The microwave instability is induced by a narrowband impedance with $Q \approx 1$ at the center frequency of $f_{res} \approx 27 f_0$. Although the inductive inserts can be used to cancel the space charge impedance, the pillbox cavity can generate a narrowband impedance to cause microwave instability of the beam at higher harmonics. In order to alleviate this problem, it is necessary to broaden the narrowband impedance by either choosing different design geometries for different ferrite inserts, or by heating the ferrite so that the imaginary part (μ'') of the permittivity is larger at the cavity resonance frequency. At PSR, the cavities was heated to 125-150° C, so that the beam is below the microwave instability threshold.

Exercise 3.7

1. In synchrotrons, beam bunches are filled with a gap for ion-clearing, abort, extraction kicker rise time, etc. Show that the frequency spectra observed from a BPM for short bunches filled with a gap have a diffraction-pattern-like structure: $\sin(nM\pi/N)/\sin(n\pi/N)$ for M identical consecutive bunches in N buckets. Specifically, find the frequency spectra for 10 buckets filled with 9 equal intensity short bunches. The revolution frequency is assumed to be 1 MHz.

2. Show that the impedance of Eq. (3.291) has two poles in the upper half of the ω plane, and find their loci. Use the inverse Fourier transformation to show that the wake function of the RLC resonator circuit is ($\tilde{\omega}_r = \omega_r \sqrt{1 - 1/4Q^2}$)

$$ W_\parallel = \frac{R_{sh}\omega_r}{Q} e^{-\omega_r t/2Q} \left[\cos \tilde{\omega}_r t - \frac{1}{\sqrt{4Q^2 - 1}} \sin \tilde{\omega}_r t \right]. $$

3. The parameters of the SLC damping ring are $E = 1.15$ GeV, $\nu_x = 8.2$, $\nu_z = 3.2$, $\alpha_c = 0.0147$, $\gamma \epsilon_{x,z} = 15~\pi$ mm-mrad, $\sigma_{\Delta p/p} = 7.1 \times 10^{-4}$, $V_{rf} = 800$ kV, $C = 35.270$ m, $h = 84$, $f_{rf} = 714$ MHz, $\rho = 2.0372$ m, and the energy loss per revolution is $U_0 = 93.1$ keV. If the threshold of bunch lengthening is $N_B = 1.5 \times 10^{10}$, use the Keil-Schnell formula to estimate the impedance of the SLC damping ring.[57]

Beltran, Ph.D. thesis, Indiana University (2003).
[57]G.E. Fisher *et al.*, *Proc. 12th HEACC*, p. 37 (1983); L. Rivkin, *et al.*, *Proc. 1988 EPAC*, p. 634 (1988); see also P. Krejcik, *et al.*, *Proc. 1993 PAC*, p. 3240 (1993). The authors of the last paper observed sawtooth instability at the threshold current $N_B = 3 \times 10^{10}$.

4. Assuming that the microwave instability growth rate is equal to the damping rate at equilibrium, find the tolerable impedance as a function of the machine parameters. Use Eq. (3.292) for The growth rate of microwave instability in a quasi-isochronous electron storage ring and the damping rate $\tau_s = 2ET_0/\mathcal{J}_s U_0$, where E is the energy of the particle, T_0 is the revolution period, the damping partition $\mathcal{J}_s \approx 2$, $U_0 = C_\gamma E^4/\rho$, $C_\gamma = 8.85 \times 10^{-5}$ m/(GeV^3), and ρ is the bending radius.

5. Consider a pillbox-like cavity with length ℓ (see Sec. VII.4). The cavity is filled with ferrite rings with inner and outer radii a and b respectively. Show that the longitudinal impedance for TM$_{010}$ mode is[58]

$$\frac{Z_\parallel}{\ell} = j\frac{Z_0}{2\pi a}\sqrt{\frac{\mu' - j\mu''}{\epsilon_r}}\,\frac{H_0^{(1)}(k_c a)H_0^{(2)}(k_c b) - H_0^{(1)}(k_c b)H_0^{(2)}(k_c a)}{H_1^{(1)}(k_c a)H_0^{(2)}(k_c b) - H_0^{(1)}(k_c b)H_1^{(2)}(k_c a)}.$$

where $H_m^{(n)}$ are Hankel functions which represent incoming and outgoing waves, $Z_0 = 377\Omega$ is the impedance of free space. $k_c = \omega\sqrt{\mu\epsilon} = k\sqrt{\epsilon_r(\mu' - j\mu'')}$, $k = \frac{\omega}{c} = \omega\sqrt{\mu_0\epsilon_0}$ in vacuum, ϵ_r is the relative permittivity and μ' and μ'' are the real and complex parts of the relative complex permeability.

6. The equation of motion for the fractional off-momentum deviation of a particle is

$$\frac{d\delta}{dt} = \frac{\omega_0}{2\pi\beta^2 E}\left[eV(\sin\phi - \sin\phi_s) + \Delta U\right],$$

where the second term in the bracket is the effect of voltage drop due to impedance of the accelerator. Using the voltage drop of the space charge in Eq. (3.287), show that the synchrotron Hamiltonian is

$$H(\phi,\delta) = \frac{h\eta\omega_0}{2}\delta^2 + \frac{\omega_0 eV}{2\pi\beta^2 E}[\cos\phi - \cos\phi_s + (\phi - \phi_s)\sin\phi_s] + \frac{h\omega_0 e^2 cg_0 Z_0 N_B}{4\pi\beta^2\gamma^2 RE}\rho(\phi),$$

where $\rho(\phi)$ is the normalized beam distribution in the synchrotron phase-angle, N_B is the number of particles in a bunch, $g_0 = 1 + 2\ln(b/a)$ is the geometric factor, R is the mean radius of the accelerator. For a Gaussian normalized distribution function, $\rho(\phi) = \frac{1}{\sqrt{2\pi}\sigma_\phi}\exp\{-\frac{(\phi-\phi_s)^2}{2\sigma_\phi^2}\}$. Show that the Hamiltonian becomes

$$H(\phi,\delta) \approx \frac{h\eta\omega_0}{2}\delta^2 - \frac{\omega_0 e}{4\pi\beta^2 E}\left[V\cos\phi_s - \frac{hecg_0 Z_0 N_B}{2\gamma^2 R\sigma_\phi^3}\right](\phi - \phi_s)^2.$$

Note that the space charge produce potential well distortion, and synchrotron detuning. At energies below the transition energy, where $\cos\phi_s \geq 0$, the space charge force tends to push particles away from the center. At energies above the transition energy, the space charge force tends to focus the beam. As the beam bunch is accelerated through the transition energy, the mis-match in the matched bunch length will set off quadrupole mode oscillations. This phenomenon is called Sorenssen effect.[59]

---

[58]The general formula to calculate the shunt impedance is $\Delta V = -IZ_\parallel = -E_s\ell$, with E_s the longitudinal electric field, ℓ the total length, and I obtained by Ampere's law: $I = \oint Hdl = 2\pi a H_\phi$.

[59]A. Sorrenssen, Particle Accelerators **6**, 141 (1975).

VIII   Introduction to Linear Accelerators

By definition, any accelerator that accelerates charged particles in a straight line is a linear accelerator (linac).[60] Linacs includes induction linacs; electrostatic accelerators such as the Cockcroft-Walton, Van de Graaff and Tandem; radio-frequency quadrupole (RFQ) linacs; drift-tube linacs (DTL); coupled cavity linacs (CCL); coupled cavity drift-tube linacs (CCDTL); high-energy electron linacs, etc. Modern linacs, almost exclusively, use rf cavities for particle acceleration in a straight line. For linacs, important research topics include the design of high gradient acceleration cavities, control of wakefields, rf power sources, rf superconductivity, and the beam dynamics of high brightness beams.

Linacs evolved through the development of high power rf sources, rf engineering, superconductivity, ingenious designs for various accelerating structures, high brightness electron sources, and a better understanding of high intensity beam dynamics. Since electrons emit synchrotron radiation in synchrotron storage rings, high energy e^+e^- colliders with energies larger than 200 GeV per beam can be effectively attained only by high energy linacs. Current work on high energy linear colliders is divided into two camps, one using superconducting cavities and the other using conventional copper cavities. In conventional cavity design, the choice of rf frequency varies from S band to millimeter wavelength at 30 GHz in the two beam acceleration scheme. Research activity in this line is active, as indicated by bi-annual linac, and annual linear collider conferences.

Since the beam in a linac is adiabatically damped, an intense electron beam bunch from a high brightness source will provide a small emittance at high energy. The linac has also been used to generate coherent synchrotron light. Many interesting applications will be available using high brilliance coherent photon sources.

This section provides an introduction to a highly technical and evolving branch of accelerator physics. In Sec. VIII.1 we review some historical milestones. In Sec. VIII.2 we discuss fundamental properties of rf cavities. In Sec. VIII.3 we present the general properties of electromagnetic fields in accelerating cavity structures. In Sec. VIII.4 we address longitudinal particle dynamics and in Sec. VIII.5, transverse particle dynamics. Since the field is evolving, many advanced school lectures are available.

VIII.1   Historical Milestones

In 1924 G. Ising published a first theoretical paper on the acceleration of ions by applying a time varying electric field to an array of drift tubes via transmission lines; subsequently, in 1928 R. Wideröe used a 1 MHz, 25 kV rf source to accelerate potassium ions up to 50 keV. The optimal choice of the distance between acceleration

---

[60]See Ref. [4]; G.A. Loew and R. Talman, *AIP Conf. Proc.* **105**, 1 (1982); J. Le Duff, CERN 85-19, p. 144 (1985).

gaps is $d = \beta\lambda/2 = \beta c/2f$, where d is the distance between drift tube gaps, βc is the velocity of the particle, and λ and f are the wavelength and frequency of the rf wave. A Wideröe structure is shown in the top plot of Fig. 1.4. In 1931–34 E.O. Lawrence, D. Sloan $et\ al.$, at U.C. Berkeley, built a Wiederöe type linac to accelerate Hg ions to 1.26 MeV using an rf frequency of about 7 MHz.[61] At the same time (1931-1935) K. Kingdon at the General Electric Company and L. Snoddy at the University of Virginia, and others, accelerated electrons from 28 keV to 2.5 MeV.

The drift tube distance could be minimized by using a high frequency rf source. For example, the velocity of a 1 MeV proton is $v = \beta c = 4.6 \times 10^{-2} c$, and the length of drift space in a half cycle at rf frequency $f_{\rm rf} = 7$ MHz is $\frac{1}{2}v f_{\rm rf}^{-1} \approx 1$ m. As the energy increases, the drift length becomes too long. The solution is to use a higher frequency system, which became available from radar research during WWII. In 1937 the Varian brothers invented the klystron at Stanford. Similarly, high power magnetrons were developed in Great Britain.[62]

However, the accelerator is almost capacitive at high frequency, and it radiates a large amount of power $P = IV$, where V is the accelerating voltage, $I = \omega C V$ is the displacement current, C is the capacitance between drift tubes, and ω is the angular frequency. The solution is to enclose the gap between the drift tubes in a cavity that holds the the electromagnetic energy in the form of a magnetic field by introducing an inductive load to the system. To attain a high electric field, the cavity is designed to have a resonant frequency that synchronizes with the particle motion. An acceleration cavity is a structure in which the longitudinal electric field can be stored at the gap for particle acceleration, as shown in Fig. 3.42.
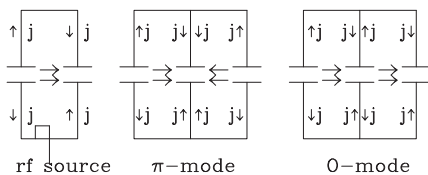

Figure 3.42: Left: Schematic drawing of a single gap cavity fed by an rf source. The rf currents are indicated by j on the cavity wall. Middle: A two-gap cavity operating at π-mode, where the electric fields at two gaps have opposite polarity. Right: A two-gap cavity operating at 0-mode, where the electric fields at all gaps have the same polarity. In 0-mode (or 2π-mode) operation, the rf currents on the common wall cancel, and the wall becomes unnecessary.

When two or more cavity gaps are adjacent to each other, the cavity can be operated at π-mode or 0-mode, as shown in Fig. 3.42. In 0-mode, the resulting current is zero at the common wall so that the common wall is useless. Thus a group of drift tubes can be placed in a single resonant tank, where the field has the same

---

[61]G. Ising, $Arkiv\ f\ddot{u}r\ Matematik\ o.\ Fisik$ **18**, 1 (1924); R. Wideröe, $Archiv\ f\ddot{u}r\ Electrotechnik$ **21**, 387 (1928); D.H. Sloan and E.O. Lawrence, $Phys.\ Rev.$ **32**, 2021 (1931); D.H. Sloan and W.M. Coate, $Phys.\ Rev.$ **46**, 539 (1934).

[62]The power source of present day household microwave ovens is the magnetron.

phase in all gaps. Such a structure (see Fig. 1.4) was invented by L. Alvarez in 1945.[63] In 1945–47 L. Alvarez, W.K.H. Panofsky, *et al.*, built a 32 MeV, 200 MHz proton drift tube linac (DTL). Drift tubes in the Alvarez structure are in one large cylindrical tank and powered at the same phase. The distances between the drift tubes, $d = \beta\lambda$,[64] are arranged so that the particles, when they are in the decelerating phase, are shielded from the fields.

In 1945 E.M. McMillan and V.I. Veksler discovered the phase focusing principle, and in 1952 J. Blewett invented electric quadrupoles for transverse focusing based on the alternating gradient focusing principle. These discoveries solved the 3D beam stability problem, at least for low intensity beams. Since then, Alvarez linacs has commonly been used to accelerate protons and ions up to 50–200 MeV kinetic energy.

In the ultra relativistic regime with $\beta \to 1$, cavities designed for high frequency operation are usually used to achieve a high accelerating field. At high frequencies, the klystron, invented in 1937, becomes a powerful rf power source. In 1947-48 W. Hansen *et al.*, at Stanford, built the MARK-I *disk loaded linac* yielding 4.5 MeV electrons in a 9 ft structure powered by a 0.75 MW, 2.856 GHz magnetron.[65] On September 9, 1967, the linac at Stanford Linear Accelerator Center (SLAC) accelerated electrons to energies of 20 GeV. In 1973 P. Wilson, D. Farkas, and H. Hogg, at SLAC, invented the rf energy compression scheme SLED (SLAC Energy Development) that provided the rf source for the SLAC linac to reach 30 GeV. In 1990's, SLAC has achieved 50 GeV in the 3 km linac.

Another important idea in high energy particle acceleration is acceleration by traveling waves.[66] The standing wave cavity in a resonant structure can be decomposed into two traveling waves: one that travels in synchronism with the particle, and the backward wave that has no net effect on the particle. Thus the shunt impedance of a traveling wave structure is twice that of a standing wave structure except at the phase advances 0 or π. To regain the factor of two in the shunt impedance for standing wave operation, E. Knapp and D. Nagle invented the side coupled cavity in 1964.[67] In 1972 E. Knapp *et al.* successfully operated the 800 MHz side coupled cavity linac (CCL) to produce 800 MeV energy at Los Alamos. In 1994 the last three tanks of

---

[63]L. Alvarez, *Phys. Rev.* **70**, 799 (1946).

[64]It appears that the distance between drift tubes for an Alvarez linac is twice that of a Wideröe linac, and thus less efficient. However, the use of a high frequency rf system in a resonance-cavity more than compensates the requirement of a longer distance between drift tubes.

[65]E.L. Ginzton, W.W. Hanson and W.R. Kennedy, *Rev. Sci. Instrum.* **19**, 89 (1948); W.W. Hansen *et al., Rev. Sci. Instrum.* **26**, 134 (1955).

[66]J.W. Beams at the University of Virginia in 1934 experimented with a traveling-wave accelerator for electrons using transmission lines of different lengths attached to a linear array of tubular electrodes and fed with potential surges generated by a capacitor-spark gap circuit, similar to the system proposed by Ising. Burst of electrons were occasionally accelerated to 1.3 MeV. See J.W. Beams *et. al., Phys. Rev.* **44**, 784 (1933); *Phys. Rev.,* **45**,849 (1934).

[67]E. Knapp *et al., Proc. 1966 linac Conf.*, p. 83 (1966).

the DTL linac at Fermilab were replaced by CCL to upgrade its proton energy to 400 MeV. Above $\beta \geq 0.3$, CCL has been widely used for proton beam acceleration. A combination of CCL with DTL produces the CCDTL structure suitable for high gradient proton acceleration.

For the acceleration of ions, the Alvarez linac is efficient for $\beta > 0.04$. The acceleration of low energy protons and ions relies on DC accelerators such as the Cockcroft-Walton or Van de Graaff. In 1970 I. Kapchinskij and V. Teplyakov at ITEP Moscow invented the radio-frequency quadrupole (RFQ) accelerator. In 1980 R. Stokes *et al.* at Los Alamos succeeded in building an RFQ to accelerate protons to 3 MeV. Today RFQ is commonly used to accelerate protons and ions for injection into linacs or synchrotrons.

Since the first experiment on a superconducting linear accelerator at SLAC in 1965, the superconducting (SC) cavity has become a major branch of accelerator physics research. In the 1970's, many SC post linear accelerators were constructed for the study of heavy ion collisions in nuclear physics.[68] Recently, more than 180 m of superconducting cavities have been installed in CEBAF for the 4 GeV continuous electron beams used in nuclear physics research. More than 400 m of SC cavities at about 7 MV/m were installed in LEP energy upgrade, and reached 3.6 GV rf voltage for the operation of 104.5 GeV per beam in 2000.[69] The TESLA project had also successfully achieved an acceleration gradient of 35 MV/m.

VIII.2   Fundamental Properties of Accelerating Structures

Fundamental properties of all accelerating structures are the transit time factor, shunt impedance, and Q-value. These quantities are discussed below.

A. Transit time factor

We consider a standing wave accelerating gap, e.g. the Alvarez structure, and assume that the electric field in the gap is independent of the longitudinal coordinate s. If $\mathcal{E}$ is the maximum electric field at the acceleration gap, the accelerating field and the energy gain in traversing the accelerating gap are

$$\mathcal{E}_s = \mathcal{E} \cos \omega t, \tag{3.303}$$

$$\Delta E = e \int_{-\frac{g}{2}}^{\frac{g}{2}} \mathcal{E} \, \cos \frac{\omega s}{v} \, ds = e \mathcal{E} g T_{\text{tr}} = e V_0, \quad T_{\text{tr}} = \frac{\sin(\pi g / \beta \lambda)}{\pi g / \beta \lambda},$$

where $V_0 = \mathcal{E} g T_{\text{tr}}$ is the effective voltage of the gap, T_{tr} is the transit time factor, $\lambda = 2\pi c/\omega$ is the rf wavelength, and $\pi g / \beta \lambda$ is the rf phase shift across the gap. If the

---

[68]See e.g., H. Piel, CERN **87-03**, p. 376 (1987); CERN **89-04**, p. 149 (1994), and references therein. These low energy SC cavities are essentially drift-tube type operating at $\lambda/4$ or $\lambda/2$ modes.

[69]P. Brown *et al.*, Proceedings of PAC2001, p. 1059 (IEEE, 2001).

gap length of a standing wave structure is equal to the drift tube length, i.e. $g = \beta\lambda/2$, the transit time factor is $T_{\mathrm{tr}} = \sin(\pi/2)/(\pi/2) = 0.637$. This means that only 63% of the rf voltage is used for particle acceleration. To improve the efficiency, the gap length g should be reduced. However, a small g can lead to sparking at the gap. Since there is relatively little gain for $g < \beta\lambda/4$, the gap g is designed to optimize linac performance. The overall transit time factor for standing wave structures in DTL is about 0.8. The transit time factor of Eq. (3.303) is valid for the standing wave structure. The transit time factor for particle acceleration by a guided wave differs from that of Eq. (3.303). An example is illustrated in Exercise 3.8.7.

B. Shunt impedance

Neglecting power loss to the transmission line and reflections between the source and the cavity, electromagnetic energy is consumed in the cavity wall and beam acceleration. The shunt impedance for an rf cavity is defined as

$$R_{\mathrm{sh}} = V_0^2/P_{\mathrm{d}}, \tag{3.304}$$

where V_0 is the effective acceleration voltage, and P_{d} is the dissipated power. For a multi-cell cavity structure, it is also convenient to define the shunt impedance per unit length r_{sh} as

$$r_{\mathrm{sh}} = \frac{R_{\mathrm{sh}}}{L_{\mathrm{cav}}} = \frac{\mathcal{E}^2}{P_{\mathrm{d}}/L_{\mathrm{cav}}} \qquad \text{or} \qquad \frac{dP_{\mathrm{d}}}{ds} = -\frac{\mathcal{E}^2}{r_{\mathrm{sh}}}, \tag{3.305}$$

where $\mathcal{E}$ is the effective longitudinal electric field that includes the transit time factor, and dP_{d}/ds is the fraction of input power loss per unit length in the wall. The power per unit length needed to maintain an accelerating field $\mathcal{E}$ is $P_{\mathrm{d}}/L = \mathcal{E}^2/r_{\mathrm{sh}}$ and the accelerating gradient for low beam intensity is $\mathcal{E} = \sqrt{r_{\mathrm{sh}}P_{\mathrm{d}}/L_{\mathrm{cav}}}$.

For a 200 MHz proton linac, we normally have $r_{\mathrm{sh}} \approx 15-50$ MΩ/m, depending on the transit time factors. For an electron linac at 3 GHz, $r_{\mathrm{sh}} \approx 100$ MΩ/m. For high frequency cavities, the shunt impedance is generally proportional to $\omega^{1/2}$ (see Exercise 3.8.4). A high shunt impedance with low surface fields is an important guideline in rf cavity design. For example, using a 50 MW high peak power pulsed klystron, the accelerating gradient of a 3 GHz cavity can be as high as 70 MV/m. The working SLC S-band accelerating structure delivers about 20 MV/m.[70]

C. The quality factor Q

The quality factor is defined by $Q = \omega W_{\mathrm{st}}/P_{\mathrm{d}}$, and thus we obtain

$$dW_{\mathrm{st}}/dt = -P_{\mathrm{d}} = -\omega W_{\mathrm{st}}/Q; \qquad W_{\mathrm{st}} = W_{\mathrm{st},0}e^{-2t/t_{\mathrm{F,sw}}}, \qquad t_{\mathrm{F,sw}} = 2Q_{\mathrm{L}}/\omega, \tag{3.306}$$

---

[70]P. Raimondi, *et al.*, Proceedings of the EPAC2000, (EPAC, 2000).

where W_{st} is the maximum stored energy, Q_{L} is the loaded Q-factor that includes the resistance of the power source, and $t_{F,\text{sw}}$ is the filling time for the standing wave operation, which is the time for the field to decay to $1/e$ of its initial value. The Q-factor of an accelerating structure is independent of whether it operates in standing wave or traveling wave modes.

For a traveling wave structure, the stored energy per unit length, the power loss per unit length, and the filling time for a traveling wave structure are respectively[71]

$$w_{\text{st}} = W_{\text{st}}/L_{\text{cav}}; \qquad \frac{dP_{\text{d}}}{ds} = -\frac{\omega w_{\text{st}}}{Q}, \quad \text{or} \quad Q = -\frac{\omega w_{\text{st}}}{dP_{\text{d}}/ds}; \qquad (3.307)$$

$$t_{F,\text{tw}} = L_{\text{cav}}/v_{\text{g}}, \qquad\qquad\qquad\qquad\qquad\qquad\qquad\qquad\qquad (3.308)$$

where L_{cav} is the length of the cavity structure and v_{g} is the velocity of the energy flow. A useful quantity is the ratio R_{sh}/Q:

$$\frac{R_{\text{sh}}}{Q} = \frac{V_0^2}{\omega W_{\text{st}}}, \quad \text{or} \quad \frac{r_{\text{sh}}}{Q} = \frac{(V_0/L_{\text{cav}})^2}{\omega(W_{\text{st}}/L_{\text{cav}})} = \frac{\mathcal{E}^2}{\omega w_{\text{st}}}, \qquad (3.309)$$

which depends only on the cavity geometry and is independent of the wall material, welds, etc.

VIII.3   Particle Acceleration by EM Waves

Charged particles gain or lose energy when the velocity is parallel to the electric field. A particle traveling in the same direction as the plane electromagnetic (EM) wave will not gain energy because the electric field is perpendicular to the particle velocity. On the other hand, if a particle moves along a path that is not parallel to the direction of an EM wave, it can gain energy. However, it will quickly pass through the wave propagation region unless a wiggler field is employed to bend back the particle velocity vector.[72] Alternatively, a wave guide designed to provide electric field along the particle trajectory at a phase velocity equal to the particle velocity is the basic design principle of rf cavities.

The rf cavities for particle acceleration can be operated in standing wave or traveling wave modes.[73] Standing wave cavities operating at steady state are usually used in synchrotrons and storage rings for beam acceleration or energy compensation of synchrotron radiation energy loss. The standing wave can also accelerate oppositely charged beams traveling in opposite directions. Its high duty factor can be used to

---

[71]We will show that the velocity of the energy flow is equal to the group velocity, $v_{\text{g}} = P_{\text{d}}/w_{\text{st}}$. The conventional definition of standing wave filling time in Eq. (3.306) is twice that of the traveling wave in Eq. (3.308).

[72]This scheme includes inverse free electron laser acceleration and inverse Cerenkov acceleration.

[73]See G.A. Loew, R.H. Miller, R.A. Early, and K.L. Bane, *Proc. 1979 Part. Acc. Conf.*, p. 3701 (IEEE, 1979); R.H. Miller, SLAC-PUB-3935 (1988); see also Exercise 3.8.7.

accelerate long pulsed beams such as protons, and continuous wave (CW) electron beams in the Continuous Electron Beam Accelerator Facility (CEBAF). On the other hand, employing high power pulsed rf sources, a traveling wave structure can attain a very high gradient for the acceleration of an intense electron beam pulse.

In this section we study the properties of electromagnetic waves in cavities. These waves are classified into transverse magnetic (TM) or transverse electric (TE) modes. The phase velocity of the EM waves can be slowed down by capacitive or inductive loading. We will discuss the choice of standing wave vs traveling wave operation, the effect of shunt impedance, and the coupled cavity linac.

A. EM waves in a cylindrical wave guide

First we consider the propagation of EM waves in a cylindrical wave guide. Since there is no ends for the cylindrical wave guide, the EM fields can be described by the traveling wave component in Eq. (3.237) in Sec. VI.1 (see Appendix B Sec. IV). The EM fields of the lowest frequency TM_{01} mode, traveling in the $+\hat{s}$ direction, are

$$
\begin{aligned}
E_s &= E_0 J_0(k_r r) e^{-j[ks-\omega t]}, \\
E_r &= j\frac{k}{k_r} E_0 J_1(k_r r) e^{-j[ks-\omega t]}, \\
H_\phi &= j\frac{\omega}{cZ_0 k_r} E_0 J_1(k_r r) e^{-j[ks-\omega t]}, \\
E_\phi &= 0, \quad H_s = 0, \quad H_r = 0,
\end{aligned}
\tag{3.310}
$$

where $Z_0 = \sqrt{\mu_0/\epsilon_0}$ is the vacuum impedance, (r, ϕ) is the cylindrical coordinate, s is the longitudinal coordinate, k is the propagation wave number in the $+\hat{s}$ direction, and k_r is the radial wave number:

$$
k^2 = (\omega/c)^2 - k_r^2 \qquad k_{r,mn} = j_{mn}/b,
\tag{3.311}
$$

where the propagation modes are determined by the boundary condition for $E_s = E_\phi = 0$ at the pipe radius $r = b$ with j_{mn} are zeros of the Bessel functions $J_m(j_{mn}) = 0$ listed in Table B.1 in Appendix B Sec. IV.

The frequency of the TM_{01} mode is $\omega/c = \sqrt{k^2 + (2.405/b)^2}$, shown in Fig. 3.43. The subscript 01 stands for $m = 0$ in ϕ-variation, 1 radial-node at the boundary of the cylinder [see Eq. (3.237)]. This mode is a free propagation mode along the longitudinal $\hat{s}$ direction. We define $\omega_c = k_r c = 2.405c/b$. The wave number of the TM_{01} wave and the corresponding phase velocity v_p become

$$
k = \frac{\omega}{c}\left[1 - \left(\frac{\omega_c}{\omega}\right)^2\right]^{1/2}, \qquad v_p = \frac{\omega}{k} = \frac{c}{[1 - (\omega_c/\omega)^2]^{1/2}} > c.
\tag{3.312}
$$

Unattenuated wave propagation at $\omega < \omega_c$ is not possible. Since the phase velocity propagates faster than the speed of light, the particle can not be synchronized with

the EM wave during acceleration. At low frequency, the wave travels forward and backward with a very large phase velocity; it is not useful for particle acceleration. At high frequency, the phase velocity approaches c. However, the electromagnetic field is transverse; it becomes the transverse TEM wave, i.e.

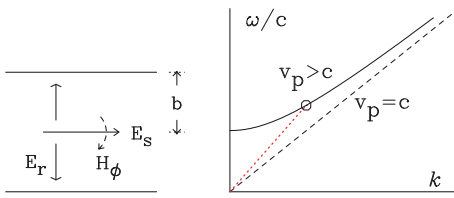$$\frac{E_s}{E_r} = j\frac{k_r}{k} \to 0, \qquad \frac{H_\phi}{E_r} = \frac{\omega}{ckZ_0} \to \frac{1}{Z_0}.$$

Figure 3.43: Left: Schematic drawing of a cylindrical cavity. Right: Dispersion curve $(\omega/c)^2 = k^2 + (2.405/b)^2$ for the TM$_{01}$ wave. The phase velocity ω/k for a wave without cavity load is always greater than the velocity of light. At high frequencies, where $k_r \to 0$, the phase velocity approaches the speed of light. However, the longitudinal component of the EM wave vanishes.

B. Phase velocity and group velocity

Equation (3.310) represents an infinitely long pulse of EM waves in the cylindrical wave guide. The phase of the plane wave, $ks - \omega t$, travels at a phase velocity of $v_p = ds/dt = \omega/k$. In reality, we have to discuss a short pulse formed by a group of EM waves. Since the Maxwell equation is linear, the pulse can be decomposed in linear superposition of Fourier series.

For a quasi-monochromatic pulse at frequency ω_0 in free space, the electric field can be represented by

$$\begin{aligned}
E(t,s) &= A(t)e^{j(\omega_0 t - ks)} = \frac{1}{2\pi}\int\int A(\xi)e^{j[\omega t - ks - \omega\xi + \omega_0\xi]}d\xi d\omega \\
&= \frac{1}{2\pi}\int\int A(\xi)e^{j[\omega t - k(\omega)s - \omega\xi + \omega_0\xi]}d\xi d\omega,
\end{aligned} \tag{3.313}$$

where $A(t)$ is the amplitude with a short time duration and we include the dispersion of the wave number in Eq. (3.311). For a quasi-monochromatic wave at the angular frequency ω_0, we expand the dispersion wave number around ω_0:

$$k(\omega) = k(\omega_0) + \left.\frac{dk}{d\omega}\right|_{\omega_0}(\omega - \omega_0) = k_0 + k'(\omega - \omega_0). \tag{3.314}$$

Substituting Eq. (3.314) into Eq. (3.313), we obtain $E(t,s) = A(t - k's)\,e^{j(\omega_0 t - k_0 s)}$. Note that the phase of the pulse propagates at a "phase velocity" of $v_p = \omega_0/k_0$, and the amplitude function of the EM pulse propagates at the "group velocity"

$$v_g = \frac{1}{k'} = \left.\frac{d\omega}{dk}\right|_{\omega_0}. \tag{3.315}$$

Using Eq. (3.312) for single-mode wave propagation, we obtain $v_{\mathrm{g}} = kc^2/\omega$, or $v_{\mathrm{p}}v_{\mathrm{g}} = c^2$. From Fig. 3.43 we see that the group velocity is zero at $k = 0$.

In fact, the group velocity is equal to the velocity of energy flow in the wave guide to be shown as follows: The power of the TM wave, the total energy per unit length stored, and the velocity of the energy flow are

$$P = \frac{1}{2}Re \int_S E_r H_\phi^* dS = \frac{1}{2}E_0^2 \frac{k\omega}{cZ_0 k_r^2} \int_0^b J_1^2(k_r r) 2\pi r dr,$$

$$W = 2W_{\mathrm{m}} = \frac{1}{2}E_0^2 \frac{\mu\omega^2}{c^2 Z_0^2 k_r^2} \int_0^b J_1^2(k_r r) 2\pi r dr,$$

$$v_{\mathrm{e}} = \frac{P}{W} = \frac{k}{\omega}c^2 = v_{\mathrm{g}},$$

where H_ϕ^* is the complex conjugate of H_ϕ, W_{m} is the magnetic energy. The *velocity of energy flow* is equal to the *group velocity*.

C. TM modes in a cylindrical pillbox cavity

Now we consider a cylindrical pillbox cavity, where both ends of the cylinder are nearly closed. The cylinder has a beam hole for the passage of particle beams (Fig. 3.44). Here we discuss the standing wave solution of Maxwell's equation for a "closed pillbox cavity," and the effect of beam holes. The effect of a chain of cylindrical cells on the propagation of EM waves is discussed in the next section.
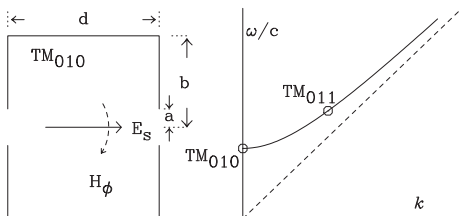
Figure 3.44: Left: Schematic of a cylindrical cavity. Right: Dispersion curve $(\omega/c)^2 = (p\pi/d)^2 + (2.405/b)^2$ for TM_{01p} resonance waves (marked as circles) for a closed cylindrical pillbox without beam holes. With proper design of pillbox geometry, the phase velocity of the TM_{010} mode can be slowed to the particle speed for beam acceleration.

We first discuss the standing wave solution of a closed pillbox cavity without beam holes. With a time dependent factor $e^{j\omega t}$, the TM mode solution of Eq. (3.237) in the closed cylindrical pillbox cavity is reproduced as follows:

$$\begin{cases} E_s = C k_r^2 \, J_m(k_r r) \cos m\phi \cos ks, \\ E_r = -C k k_r \, J'_m(k_r r) \cos m\phi \sin ks, \\ E_\phi = C n k \dfrac{1}{r} J_m(k_r r) \sin m\phi \sin ks, \end{cases} \qquad \begin{cases} H_s = 0, \\ H_r = -jC \dfrac{m\omega\epsilon_0}{r} \, J_m(k_r r) \sin m\phi \cos ks, \\ H_\phi = -jC\omega\epsilon_0 k_r \, J'_m(k_r r) \cos m\phi \cos ks, \end{cases}$$

where the longitudinal magnetic field is zero for TM modes, ω is the angular frequency, and k_r and k are wave numbers of the radial and longitudinal modes. The dispersion

relation is $\omega/c = \sqrt{k_r^2 + k^2}$. Similarly, there are also TE modes where the longitudinal electric field is zero.

Using the boundary conditions that $E_r = 0$ and $E_\phi = 0$ at $s = 0$ and d, we obtain $kd = p\pi$ ($p = 0, 1, 2, \cdots$), where d is the length of the pillbox, kd is the phase advance of the EM wave in the cavity cell. We also use the boundary conditions $E_s = 0$ and $E_\phi = 0$ at the pipe radius $r = b$ to obtain the radial modes $k_{r,mn}b = j_{mn}$, where b is the inner radius of the cylinder, and j_{mn} are zeros of the Bessel functions $J_m(j_{mn}) = 0$ listed in Table B.1 (Appendix B Sec. IV).

In summary, the resonance frequency ω for the TM$_{mnp}$ mode is

$$\frac{\omega_{mnp}}{c} = \sqrt{\frac{j_{mn}^2}{b^2} + \frac{p^2\pi^2}{d^2}}. \tag{3.316}$$

For the TM$_{010}$ mode, we have $k = 0$ and $\omega/c = k_r = 2.405/b$ shown as a circle on Fig. 3.44. The electromagnetic fields for this mode are

$$E_s = E_0 J_0(k_r r), \quad B_\phi = j\frac{E_0}{c}J_1(k_r r). \tag{3.317}$$

Figure 3.44 (right) show also the mode frequency of TM$_{011}$ on the dispersion curve. Both these modes have phase velocities greater than c.

To lower the phase velocity, beam hole radius a and cylinder radius b are tailored to provide matched phase advance kd and phase velocity ω/k for the structure. Analytic solution of Maxwell's equations for an actual cavity geometry is difficult. The EM wave modes can be calculated by finite element or finite difference EM codes with a periodic boundary (resonance) condition and a prescribed phase advance kd across the cavity gap.

The solid lines in Fig. 3.45 are the dispersion curves of frequency f vs phase shift kd for TM$_{0np}$ modes of a SLAC-like pillbox cavity with $a = 18$ mm, $b = 43$ mm, and $d = 34.99$ mm.[74] Because of the coupling between adjacent pillbox-cavities, the discrete mode frequencies become a continuous function of the phase advance kd, and the phase-velocity is effectively lowered. The dashed lines show the world line $v_p = c$. The details of the TM$_{010}$ mode are shown in the right plot. At $f = 2.856$ GHz, the phase shift per cell is about $120°$, and the phase velocity v_p is equal to c.

The frequencies of the TM modes 010, 011, 020, 021, 030 for a closed cylindrical pillbox are shown as circles in the left plot of Fig. 3.45. Increasing the size of the beam

---

[74]The calculation was done by Dr. D. Li using MAFIA in 2D monopole mode. The wall thickness chosen was 6.027 mm. The wall thickness slightly influences the mode frequencies of TM$_{0n1}$ modes, where the effective d parameter is reduced for a single cell structure. The actual SLAC structure is a constant gradient structure with frequency of $f = 2.856$ GHz, phase advance of $2\pi/3$, length of the structure of $L = 3.05$ m, inner diameter of $2b = 83.461 - 81.793$ mm, disk diameter of $2a = 26.22 - 19.24$ mm, and disk thickness of 5.842 mm. See also C.J. Karzmark, Xraig S. Nunan, and Eiji Tanabe, *Medical Electron Accelerators*, (McGraw-Hill, New York, 1993).
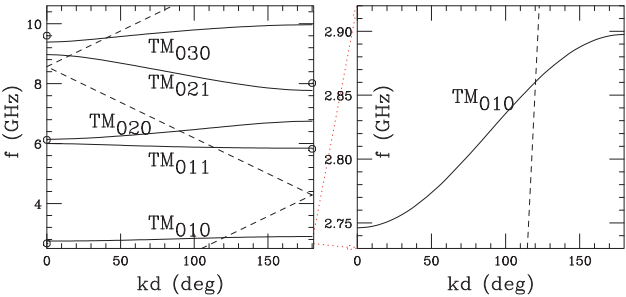
Figure 3.45: Left: Dispersion curves, f vs kd, for TM$_{01p}$ modes for a pillbox cavity with $a = 18$ mm, $b = 43$ mm, and $d = 34.99$ mm. Circles show the TM$_{0np}$ mode frequencies for a closed pillbox cavity. The dashed lines show the world line $v_p = c$. Right: Dispersion curve of TM$_{010}$ mode.

hole decreases the coupling capacitance and increases the TM$_{010}$ mode frequency. More importantly, it provides a continuous TM mode frequency as a function of wave number k. When the beam hole radius decreases, all mode frequencies become horizontal lines. When the beam hole is completely closed, the mode frequencies become discrete points, the circles in the left plot of Fig. 3.45.

Table 3.9: Parametric dependence of the SLAC cavity geometry

b (mm)	d (mm)	kd (deg)	f (GHz)	R_{sh} (MΩ)	Q	r_{sh} (MΩ/m)
42.475	17.495	60	2.8579	0.5107	7713	29.2
42.000	26.24	90	2.853	1.2	10947	45.73
41.805	30.616	105	2.857	1.559	12413	50.92
41.685	34.99	120	2.854	1.874	13700	53.56
41.580	39.36	135	2.857	2.14	14848	54.37
41.415	46.653	160	2.857	2.416	16507	51.79
41.290	52.485	180	2.857	2.466	17646	46.98

Table 3.9 shows parametric dependence of a SLAC-like pillbox cavity at $f = 2.856$ GHz. Note that the shunt impedance per unit length is maximum at a phase advance of about 135°. The phase advance per cell at a given frequency is mainly determined by the cell length.

D. Alvarez structure

The Alvarez linac cavity resembles the TM$_{010}$ standing wave mode (see Table 3.10). The tank radius and other coupling structures, such as rods and slugs inside the cavity, are designed to obtain a proper resonance frequency for the TM$_{010}$ mode, and thus we have $b \approx 2.405c/\omega$. The resulting electric field of Eq. (3.317) is independent of s. The total length is designed to have a distance $\beta\lambda$ between two adjacent drift tubes (cells), where βc is the speed of the accelerating particles. Since β increases

along the line, the distance between drift tubes increases as well. Table 3.10 shows some properties of an Alvarez linac, the SLAC cavity, and the CEBAF cavity.

Table 3.10: Some parameters of basic cylindrical cavity cells

Machine	f (MHz)	b (cm)	d (cm)	N_{cell}	$\mathcal{E}$ (MV/m)
Alvarez linac	201.25	57.0	$\sum_i \beta_i \lambda$		
Fermilab (cavity1)		47	744	55	1.60
Fermilab (cavity2)		45	1902	59	2.0
CEBAF SC cavity	1497	7.66	10.	5	$5-10$
SLAC linac	2856	4.2	3.5	≈ 100	20

E. Loaded wave guide chain and the space harmonics

The phase velocity must be brought to the level of the particle velocity, i.e. $v_{\text{p}} \approx c$. A simple method of reducing the phase velocity is to load the structure with disks, or washers. Figure 3.45 shows, as an example, frequency f vs phase advance kd of the loaded SLAC-like pillbox cavity. Loaded cavity cells can be joined together to form a cavity module. Opening a beam hole at the center of the cavity is equivalent to a capacitive loading for attaining continuous bands of resonance frequencies. The question is, what happens to the EM wave in a chain of cavity cells?

If the wave guide is loaded with wave reflecting structures such as iris, nose-cone, etc., shown in Fig. 3.46 (top), the propagating EM waves can be reflected by obstruction disks. The size of the beam hole determines the degree of coupling and the phase shift from one cavity to the next. When the a, b parameters of the disk radii are tailored correctly, the phase change from cavity to cavity along the accelerator gives an overall phase velocity that is equal to the particle velocity. The reflected waves for a band of frequencies interfere destructively so that there is no radial field at the irises. Since the irises play no role in wave propagation, this gives rise to a minor perturbation in the propagating wave. The dispersion relation in this case resembles that in Fig. 3.43. At some frequencies the reflected waves from successive irises are exactly in phase so that the irises force a standing wave pattern. At these frequencies, unattenuated propagation is impossible, so that the EM wave becomes a standing wave and the group velocity again becomes zero, i.e. the phase advance $kd = \pi$. Such a chain of loaded wave guides can be used to slow the phase velocity of EM waves.

With the Floquet theorem for the periodic wave guide, the EM wave of an infinitely long disk loaded wave guide is

$$\tilde{E}_s(r, \phi, s, t) = e^{-j[k_0 s - \omega t]} E_s(r, \phi, s), \quad \tilde{H}_\phi(r, \phi, s, t) = e^{-j[k_0 s - \omega t]} H_\phi(r, \phi, s),$$
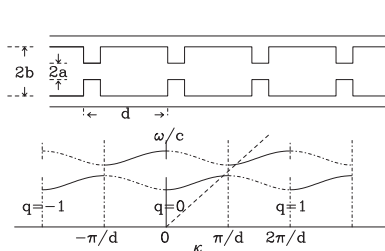$$E_s(r, \phi, s + d) = E_s(r, \phi, s), \quad H_\phi(r, \phi, s + d) = H_\phi(r, \phi, s),$$

Figure 3.46: Top: Schematic of a chain of cylindrical cavities. Bottom: Dispersion curve (ω/c) vs k. The phase velocity ω/k with a cavity load is equal to the speed of light at a specific point of the dispersion curve, shown as the intersection of the dashed diagonal line and the solid dispersion curve. The solid line branches correspond to forward traveling waves and the dashed line branches are associated with backward traveling waves. The $q = 0$ space harmonic corresponds to $kd \in (-\pi, \pi)$, and the $q = 1$ space harmonic to $kd \in (\pi, 3\pi)$, etc.

$$\tilde{E}_s(r, \phi, s, t) = e^{-j[k_0 s - \omega t]} \sum_{q=-\infty}^{\infty} E_{s,q}(r, \phi) e^{-j2q\pi s/d} = e^{j\omega t} \sum_{q=-\infty}^{\infty} E_{s,q}(r, \phi) e^{-jk_q s},$$

where d is the period of the wave guide, the propagation wave number is $k_q = k_0 + \frac{2\pi q}{d}$ (q = integer) for the qth "space harmonic", and k_0 is the propagation wave number of the "fundamental space harmonic." These space harmonics are shown in Fig. 3.46. We note further that as $k_0 d \to 0$ or π, forward and backward traveling branches coincide and they will contribute to enhance the electric field.

The field components of the lowest TM_{0n} mode with cylindrical symmetry become

$$\tilde{E}_s = \sum_q E_{0q} J_0(k_{r,q} r) e^{-j[k_q s - \omega t]}, \tag{3.318}$$

$$\tilde{E}_r = j \sum_q \frac{k_q}{k_{r,q}} E_{0q} J_1(k_{r,q} r) e^{-j[k_q s - \omega t]}, \tag{3.319}$$

$$\tilde{H}_\phi = j \frac{1}{Z_0} \sum_q \frac{k_0}{k_{r,q}} E_{0q} J_1(k_{r,q} r) e^{-j[k_q s - \omega t]}, \tag{3.320}$$

where the wave number and the phase velocity at a given frequency ω are

$$k_q^2 = (\omega/c)^2 - k_{r,q}^2, \qquad v_{p,q} = \frac{\omega}{k_q} = \frac{\omega}{k_0 + 2\pi q/d}. \tag{3.321}$$

Note that $k_{r,q} = 0$ and $J_0(k_{r,q} r) = 1$ for $v_{p,q} = c$. This indicates that the electric field of the qth space harmonic is independent of the transverse position.[75]

The dispersion curve of a periodic loaded wave-guide structure (or slow wave structure) is a typical Brillouin-like diagram shown in Fig. 3.46, where the branches with solid lines correspond to forward traveling wave, and the branches with dashed

---

[75]One may wonder how to reconcile the fact that the tangential electric field component E_s must be zero at $r = b$. The statement that the electric field is independent of transverse position is valid only near the center axis of loaded wave-guide structures.

dots are backward traveling wave. Because the dispersion curve is a simple translation of $2\pi/d$, and these curves must join, they must have zero slope at the lower frequency ω_0/c, where $k_0d = 0$, and at the upper frequency ω_π/c, where $k_0d = \pi$ (see also Fig. 3.45). The range of frequencies $[\omega_0, \omega_\pi]$ is called the *pass band*, or the propagation band. The extreme of the pass band is $k_0d = \pi$, where the group velocity is zero. At $k_0d = \pi$, the cavity has lowest rf loss,[76] making this a favorable mode of operation for accelerator modules.

The electric field at a snapshot is shown schematically in Fig. 3.47. At an instant of time, it represents a traveling wave or the maximum of a standing wave. The upper plot shows the snapshot of an electromagnetic wave. The lengths of $kd = \pi, 2\pi/3$, and $\pi/2$ cavities are also shown. The arrows indicate the maximum electric field directions. The lower plot shows a similar snapshot for $kd = 0, \pi/2, 2\pi/3$ and π cavities.
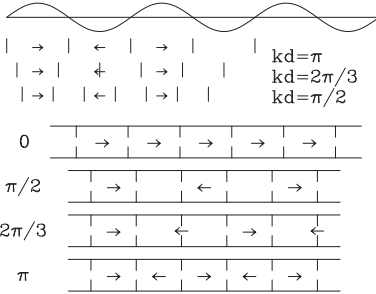

Figure 3.47: Top: Snapshot of a sinusoidal wave for phase advances $kd = \pi/2, 2\pi/3$, and π. Bottom: Snapshot at the maximum electric field configuration across each cell for $kd = 0, \pi/2, 2\pi/3$, and π phase shift structures. The actual electromagnetic fields must satisfy the periodic boundary conditions. The snapshot represents the field pattern of a traveling wave guide or the maximum field pattern of a standing wave. Note that only half of the $kd = \pi/2$ mode has longitudinal electric field in the standing wave mode. The resulting shunt impedance is half of that in traveling wave operation.

The condition for wave propagation is $-1 \leq \cos k_0d \leq 1$. If we draw a horizontal line in the dispersion curve within the pass band of the frequency, there are infinite numbers of crossings between the horizontal line and the dispersion curve. These crossings are separated into space harmonics. Higher order space harmonics have no effect on a beam because they have very different phase velocity. Each point corresponds to the propagation factor k_q, which has an identical slope in the ω/c vs k curve, i.e. an identical group velocity:

$$v_{g,q} = \frac{d\omega}{dk_q} = \frac{d\omega}{dk_0} = v_g. \tag{3.322}$$

A module made of N cells resembles a chain of N weakly coupled oscillators. There are $N + 1$ resonances located at

$$k_{0m}d = m\pi/N \quad (m = 0, 1, 2, \cdots, N). \tag{3.323}$$

_____

[76]The rf loss is proportional to $|H_\phi|^2$ on the cavity wall.

In the coupled RLC circuit model, the resonance frequency of the electric coupled cavity is[77]

$$\omega_m = \omega_0 \left[1 + \kappa(1 - \cos k_{0m}d)\right]^{1/2}, \tag{3.324}$$

where ω_0 is the resonance frequency without beam hole coupling, and κ is the coupling coefficient. The resonance frequency can be more accurately calculated from powerful finite difference, or finite element, programs such as 2D URMEL, SUPER-FISH, LALA, and 3D MAFIA. The size and the length of cavity cells are also tailored to actual rf sources for optimization.

The operating condition $v_{\mathrm{p}} = c$ is equivalent to

$$k_0 = \omega/c, \quad \text{or} \quad k_{r,0} = 0$$

for the fundamental space harmonic [see Eq. (3.321)]. Since $J_0(k_{r,0}r) = 1$, *the energy gain of a charged particle is independent of its transverse position*, i.e. the longitudinal electric field of the fundamental space harmonic is independent of the radial position within the radius of the iris. This implies that the transverse force on the particle vanishes as well (see Sec. VIII.5).

F. Standing wave, traveling wave, and coupled cavity linacs

We have shown that the Alvarez linac operates at the standing wave TM_{010} mode, with drift tubes used to shield the electric field at the decelerating phase. The effective acceleration gradient is reduced by the transit time factor and the time the particle spends inside the drift tube. On the other hand, a wave guide accelerator, where the phase velocity is equal to the particle velocity, can effectively accelerate particles in its entire length. A wave guide accelerator is usually more effective if the particle velocity is high. There are two ways to operate high-β cavities: standing wave or traveling wave.

The filling time of a standing wave structure is a few times the cavity filling time $2Q_{\mathrm{L}}/\omega$, where Q_{L} is the loaded Q-factor, to allow time to build up its electric field strength for beam acceleration. Standing wave cavities are usually used to accelerate CW beams, e.g. the CEBAF rf cavity at the Jefferson Laboratory (see Table 3.10), and long pulse beams, e.g. in the proton linacs and storage rings. In a storage ring, a standing wave can be used to accelerate beams of oppositely charged particles moving in opposite directions.

Standing wave operation of a module made of many cells may have a serious problem of many nearby resonances. For example, if a cavity has 50 cells, it can have standing waves at

$$kd = \pi, \ \frac{49}{50}\pi, \ \frac{48}{50}\pi, \ \cdots.$$

---

[77]See Exercise 3.8.6. For magnetically coupled cavity, the resonance frequency is given by $\omega_0 = \omega\left[1 + \kappa(1 - \cos k_0 d)\right]^{1/2}$.

Since $d\omega/dk = 0$ for a standing wave at $kd = 0$ or π, these resonances are located in a very narrow range of frequency. A small shift of rf frequency will lead to a different standing wave mode. This problem can be minimized if the standing wave operates at the $kd = \pi/2$ condition, where $d\omega/dk$ has its highest value. However, the shunt impedance in $kd = \pi/2$ mode operation is reduced by a factor of 2, because only half of the cavity cells are used for particle acceleration. Similarly, the forward traveling wave component of a standing wave can accelerate particles, the resulting shunt impedance is $1/2$ of that of a traveling wave structure except for the phase advance $kd = 0$ or π (see Fig. 3.48).
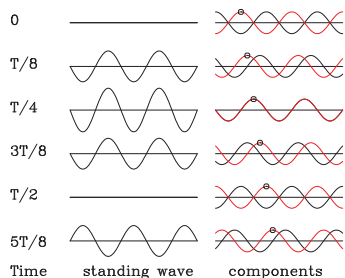

Figure 3.48: A standing wave (left) can be decomposed into forward and backward traveling waves (right). Since only the forward traveling wave can accelerate the beam, the shunt impedance is $1/2$ of that of the traveling wave structure except for $kd = 0$ and π standing wave modes, where two neighboring space harmonics contribute to regain the factor of two in the shunt impedance. Note that the particle riding on top of the right-going wave that has the phase velocity equal to the particle velocity will receive energy gain

Since every other cavity cell has no electric fields in $kd = \pi/2$ standing wave operation, these empty cells can be shortened or moved outside. This led to the invention of the coupled cavity linac (CCL) by E. Knapp and D. Nagle in 1964. The idea is schematically shown in Fig. 3.49.
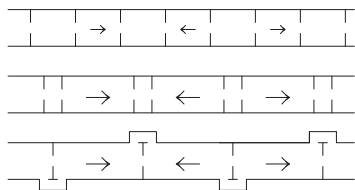

Figure 3.49: A schematic drawing of the $\pi/2$ phase shift cavity structure (top), where the field free regions are shortened (middle), and moved outside to become a coupled cavity structure (bottom).

The CCL cavities operate at $\pi/2$ mode, where field free cells are located outside the main cavity cells. These field free cells are coupled to the main accelerating cavity in the high magnetic field region. The electric field pattern of the main accelerating cavity cells looks like that of a π-mode cavity. Such a design regains the other half of the shunt impedance and provides very efficient proton beam acceleration for $\beta > 0.3$.

The high-β linac can also be operated as a traveling wave guide. There are divided into "constant gradient" and "constant impedance" structures (see Exercise 3.8.8). The accelerating cavities of a constant impedance structure are identical and the power attenuation along the linac is held constant. On the other hand, the geometry of accelerating cavities of a constant gradient structure are tapered to maintain a

constant accelerating field along the linac. The filling time for a traveling wave guide is $L_{\text{cav}}/v_{\text{g}}$, where L_{cav} is the length of a cavity and v_{g} is the group velocity. Typical group velocity is about $0.05c$. Table 3.10 lists the properties of SLAC linac cavity, that is a constant gradient structure operating at a phase advance of $2\pi/3$. With a high peak power rf source, a traveling wave cavity can provide a high acceleration gradient for intense electron beams.

G. High Order Modes (HOMs)

So far we have discussed only the fundamental mode of a cavity. In reality, high order modes (HOMs) can be equally important in cavity design. Efforts are being made to design or invent new cavity geometries with damped HOMs or detuned and damped HOMs. Such efforts are instrumental for future linear colliders operating at high frequencies.

These HOMs, particularly TM_{11p}-like modes, can affect the threshold current of a linac. When a beam is accelerated in cavities, it also generates long range and short range wakefields. A long range wake can affect trailing bunches, and a short range wake can cause a bunch tail to break up. These instabilities are called BBU (beam break up, or beam blow up) instabilities, observed first in 1957.[78] The BBU is a transverse instability. Its threshold current can be increased by a quadrupole focusing system. It also depends strongly on the misalignment of accelerating structure and rf noise. Operation of the SLAC linac provides valuable information on transverse instability of intense linac beams.[79]

VIII.4   Longitudinal Particle Dynamics in a Linac

Phase focusing of charged particles by a sinusoidal rf wave provides longitudinal stability in a linac. Let t_{s}, ψ_{s} and W_{s} be the time, rf phase, and energy of a synchronous particle, and let t, ψ, and W be the corresponding physical quantities for a non-synchronous particle. We define the synchrotron phase space coordinates as

$$\Delta t = t - t_{\text{s}}, \quad \Delta\psi = \psi - \psi_{\text{s}} = \omega(t - t_{\text{s}}), \quad \Delta W = W - W_{\text{s}}. \tag{3.325}$$

The accelerating electric field is

$$\mathcal{E} = \mathcal{E}_0 \sin \omega t = \mathcal{E}_0 \sin(\psi_s + \Delta\psi), \tag{3.326}$$

where the coordinate s is chosen to coincide with the proper rf phase coordinate. The change of the phase coordinate is

$$\frac{d\Delta\psi}{ds} = \omega\left(\frac{dt}{ds} - \frac{dt_{\text{s}}}{ds}\right) = \omega\left(\frac{1}{v} - \frac{1}{v_{\text{s}}}\right) \approx -\frac{\omega}{mc^3\beta_{\text{s}}^3\gamma_{\text{s}}^3}\Delta W, \tag{3.327}$$

[78]T.R. Jarvis, G. Saxon, and M.C. Crowley-Milling, *IEEE Trans. Nucl. Sci.* **NS-112**, 9 (1965).
[79]See J.T. Seeman, p. 255 in Ref. [19].

where $v = ds/dt$ and $v_s = ds/dt_s$ are the velocities of a particle and a synchronous particle, and the subscript s is used for physical quantities associated with a synchronous particle. This equation is in fact identical to Eq. (3.13), where $\omega/\beta_s c$ is equivalent to the harmonic number per unit length, $\Delta W/\beta_s^2 E$ is the fractional momentum spread, and $-1/\gamma_s^2$ is the equivalent phase slip factor. Since the momentum compaction in a linac is zero, the beam in a linac is always below transition energy.

The energy gain from rf accelerating electric fields is[80]

$$\frac{d\Delta W}{ds} = e\mathcal{E}_0 \left[\sin(\psi_s + \Delta\psi) - \sin\psi_s\right] \approx e\mathcal{E}_0 \cos\psi_s \, \Delta\psi. \qquad (3.328)$$

The Hamiltonian for the synchrotron motion becomes

$$H = -\frac{\omega}{2mc^3\beta^3\gamma^3}(\Delta W)^2 + e\mathcal{E}_0\left[\cos(\psi_s + \Delta\psi) + \Delta\psi\sin\psi_s\right]. \qquad (3.329)$$

Hereafter, β_s and γ_s are replaced by β and γ for simplicity. The linearized synchrotron equation of motion is simple harmonic:

$$\frac{d^2\Delta W}{ds^2} = -k_{syn}^2 \, \Delta W, \qquad k_{syn} = \sqrt{\frac{e\mathcal{E}_0\omega\cos\psi_s}{mc^3\beta^3\gamma^3}}, \qquad (3.330)$$

where k_{syn} is the wave number of the synchrotron motion. For medium energy proton linacs, k_{syn} is about 0.1 to 0.01 m^{-1}, which is equal to the wave number of transverse motion. Synchro-betatron coupling can be an important beam dynamics issue. For high energy electrons, $k_{syn} \sim 1/\sqrt{\gamma^3}$ is small. The beam particles move rigidly in synchrotron phase space, and thus the synchronous phase angle is normally chosen as $\phi_s = \frac{\pi}{2}$, i.e. electron bunches are riding on top of the crest of the rf wave. The beam will get the maximum acceleration and a minimum energy spread.

In contrast to synchrotrons, the linac usually do not have repetitive periodic structures, the concept of synchrotron tune is not necessary. However, if there is a quasi-periodic external focusing structures such as periodic solenoidal focusing systems, FODO focusing systems, or periodic doublet focusing systems, etc., the synchrotron tune can be defined as the $\nu_{syn} = k_{syn}L/(2\pi)$, where L is the length of the periodic focusing system. Parametric synchrotron resonances can occur if $m\nu_{syn} = \ell$ is satisfied, where m and ℓ are integers. Near a parametric synchrotron resonance, the longitudinal phase space will form islands as discussed in Sec. III.

A. The capture condition in an electron linac with $v_p = c$

Since $\beta_s\gamma_s$ changes rapidly in the first few sections of electron linac, the Hamiltonian contour is not a constant of motion. Tori of phase space ellipses form a golf-club-like

---

[80]Note that the convention of the rf phase used in the linac community differs from that of the storage ring community by a phase of $\pi/2$. In this textbook, we use the rf phase convention of the storage ring community.

shape, shown in Fig. 3.3. This section will show that all captured particles ride on top of the rf wave.

In an electron linac operating at a phase velocity equal to c, what happens to the injected electrons with velocities less than c? Let ψ be the phase angle between the wave and the particle. Assuming constant gradient acceleration, the electric field seen by the electron is $\mathcal{E}_0 \sin \psi$. Since the phase velocity and the particle velocity are different, the path length difference between the EM wave and the particle in time interval dt is

$$d\ell = (c-v)dt = \frac{\lambda}{2\pi}d\psi, \qquad \frac{d\psi}{dt} = \frac{2\pi c}{\lambda}(1-\beta), \qquad (3.331)$$

where $\lambda = 2\pi c/\omega$ is the rf wavelength, $d\ell/\lambda = d\psi/2\pi$, and $\beta = v/c$. The particle gains energy through the electric field, i.e.

$$\frac{d(\gamma m v)}{dt} = mc \frac{d}{dt}\left[\frac{\beta}{(1-\beta^2)^{1/2}}\right] = e\mathcal{E}_0 \sin\psi, \qquad \text{or} \qquad \frac{d\zeta}{dt} = -\frac{e\mathcal{E}_0}{mc}\sin\psi \sin^2\zeta,$$

where $\beta = \cos\zeta$. Using the chain rule $d\psi/dt = (d\psi/d\zeta)(d\zeta/dt)$, we can integrate the equation of motion to obtain

$$\cos\psi_2 - \cos\psi_1 = \frac{2\pi mc^2}{e\mathcal{E}_0\lambda}\tan\frac{\zeta}{2}\bigg|_1^2 = -\frac{2\pi mc^2}{e\mathcal{E}_0\lambda}\left(\frac{1-\beta_1}{1+\beta_1}\right)^{1/2} = -Y_{\text{inj}}, \qquad (3.332)$$

where the indices 1 and 2 specify the injection and the captured condition respectively, and we have used $\beta_2 = 1$ and the relation

$$\tan(\zeta/2) = ((1-\cos\zeta)/(1+\cos\zeta))^{1/2} = [(1-\beta)/(1+\beta)]^{1/2} = \gamma - \sqrt{\gamma^2-1}.$$

The capture condition, Eq. (3.332), favors a linac with a higher acceleration gradient $\mathcal{E}_0$. If $Y_{\text{inj}} = 1.5$, particles within an initial phase $-\pi/3 < \psi_1 < \pi/3$ will be captured inside the phase region $\pi > \psi_2 > 2\pi/3$. If the factor $Y_{\text{inj}} = 1$, all particles within $-\pi/2 < \psi_1 < \pi/2$ will be captured into the region $\pi > \psi_2 > \pi/2$. In particular, particles distributed within the range $\Delta > \psi_1 > -\Delta$ will be captured into the range $\pi/2 \leq \psi_2 \leq \pi/2 + \Delta^2/2$ ($\Delta \ll 1$). For example, all injected beam with phase length $20°$ will be compressed to a beam with a phase length $3.5°$ in the capture process.

The capture efficiency and energy spread of the electron beam can be optimized by a prebuncher. A prebuncher is usually used to prebunch the electrons from a source, which can be thermionic or rf gun. We assume a thermionic gun with a DC gun voltage V_0, which is usually about 80–150 kV. Let the electric field and the gap width of the prebuncher be $\mathcal{E}\sin(\omega t)$ and g. Electrons that arrive earlier are slowed and that arrive late are sped up. At a drift distance away from the prebuncher, the faster electrons catch up the slower ones. Thus electrons are prebunched into a smaller phase extension to be captured by the buncher and the main linac (see Exercise 3.8.9). All captured high energy electrons can ride on top of the crest of the rf wave in order to gain maximum energy from the rf electric field.

B. Energy spread of the beam

In a multi-section linac, individual adjustment of each klystron phase can be used to make a bunch with phase length Δ ride on top of the rf crest, i.e. $\psi_{\rm s} = \frac{\pi}{2}$. The final energy spread of the beam becomes

$$\frac{\Delta W}{W_{\rm s}} = 1 - \cos \frac{\Delta}{2} = \frac{\Delta^2}{8}. \tag{3.333}$$

This means that a beam with a phase spread of 0.1 rad will have an energy spread of about 0.13 %. Thus the injection match is important in minimizing the final energy spread of the beam. Other effects that can affect the beam energy are beam loading, wakefields, etc. A train of beam bunches extracts energy from the linac structure and, at the same time, the wakefield induced by the beam travels along at the group velocity. Until an equilibrium state is reached, the energies of individual beam bunches may vary.

C. Synchrotron motion in proton linacs

Since the speed of protons in linacs is not highly relativistic, the synchronous phase angle $\psi_{\rm s}$ can not be chosen as $\frac{\pi}{2}$. The synchrotron motion in ion linac is adiabatic. The longitudinal particle motion follows a torus of the Hamiltonian flow of Eq. (3.329). Table 3.11 lists bucket area and bucket height for longitudinal motion in proton linacs (see also Table 3.2 for comparison), where $\alpha_{\rm b}(\psi_{\rm s})$ and $Y(\psi_{\rm s})$ are running bucket factors shown in Eqs. (3.35) and (3.38). The rf phase region for stable particle motion can be obtained from $\psi_{\rm u}$ and $\pi - \psi_{\rm s}$ identical to those in the second the third columns of Table 3.1.

Table 3.11: Properties of rf bucket in conjugate phase space variables

	$(\psi, \frac{\Delta E}{\omega})$	(ψ, δ)
Bucket Area	$16 \left(\frac{m\beta^3\gamma^3 c^3 e\mathcal{E}_0}{\omega^3} \right)^{1/2} \alpha_{\rm b}(\psi_{\rm s})$	$16 \left(\frac{\gamma e\mathcal{E}_0}{\omega\beta mc} \right)^{1/2} \alpha_{\rm b}(\psi_{\rm s})$
Bucket Height	$2 \left(\frac{mc^3\beta^3\gamma^3 e\mathcal{E}_0}{\omega^3} \right)^{1/2} Y(\psi_{\rm s})$	$2 \left(\frac{\beta c\gamma^2 e\mathcal{E}_0}{\omega\beta^2 E} \right)^{1/2} Y(\psi_{\rm s})$

The equilibrium beam distribution must be a function of the Hamiltonian, i.e. $\rho[H(\Delta W/\omega, \Delta\psi)]$. In small bunch approximation, the Hamiltonian becomes

$$H = -\frac{\omega^3}{2mc^3\beta^3\gamma^3}(\frac{\Delta W}{\omega})^2 - \frac{1}{2}e\mathcal{E}_0 \cos \psi_{\rm s} \, (\Delta\psi)^2. \tag{3.334}$$

A Gaussian beam distribution with small bunch area becomes

$$\rho(\frac{\Delta W}{\omega}, \Delta\psi) = \frac{1}{2\pi\sigma_{\Delta W/\omega}\sigma_{\Delta\psi}}e^{H/H_0}, \tag{3.335}$$

$$\sigma_{\Delta W/\omega} = \sqrt{\frac{H_0 mc^3\beta^3\gamma^3}{\omega^3}} = \sqrt{\frac{\mathcal{A}_{\mathrm{rms}}}{\pi}}\left(\frac{mc^3\beta^3\gamma^3 e\mathcal{E}_0\cos\psi_{\mathrm{s}}}{\omega^3}\right)^{1/4},$$

$$\sigma_{\Delta\psi} = \sqrt{\frac{H_0}{e\mathcal{E}_0\cos\psi_{\mathrm{s}}}} = \sqrt{\frac{\mathcal{A}_{\mathrm{rms}}}{\pi}}\left(\frac{\omega^3}{mc^3\beta^3\gamma^3 e\mathcal{E}_0\cos\psi_{\mathrm{s}}}\right)^{1/4},$$

where H_0 is related to the thermal energy of the beam and the rms energy spread and bunch width are given by where $\mathcal{A}_{\mathrm{rms}}$ is the rms phase space area in (eVs), i.e. $\mathcal{A}_{\mathrm{rms}} = \pi\sigma_{\Delta W/\omega}\sigma_{\Delta\psi}$. The bunch length in τ-coordinate is given by $\sigma_\tau = \sigma_{\Delta\psi}/\omega$. Note that, for a constant phase space area $\mathcal{A}_{\mathrm{rms}}$, we find $\sigma_{\Delta W} \sim (\omega\mathcal{E}_0)^{1/4}(\beta\gamma)^{3/4}$, and $\sigma_\tau \sim (\omega\mathcal{E}_0)^{-1/4}(\beta\gamma)^{-3/4}$. However, the fractional momentum spread will decrease when the beam energy is increased:

$$\sigma_{\Delta p/p} = \sqrt{\frac{\mathcal{A}_{\mathrm{rms}}}{\pi}}\left(\frac{\omega e\mathcal{E}_0\cos\psi_{\mathrm{s}}}{m^3c^5\beta^5\gamma}\right)^{1/4}. \tag{3.336}$$

Examples for beam properties in the Fermilab DTL linac and SNS linacs are available in Exercises 3.8.3 and 3.8.10 respectively.

VIII.5 Transverse Beam Dynamics in a Linac

Figure 3.50 shows the electric field lines between electrodes in an acceleration gap, e.g., the drift tubes of an Alvarez linac or the irises of a high-β linac. In an electrostatic accelerator, the constant field strength gives rise to a global focusing effect because the particle at the end of the gap has more energy so that the defocusing force is weaker. This has been exploited in the design of DC accelerators such as the Van de Graaff or Cockcroft-Walton accelerators.
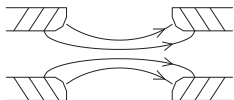

Figure 3.50: A schematic drawing of electric field lines between electrodes of acceleration cavities. Note that the converging field lines contribute to a focusing effect in electrostatic accelerators. For rf accelerators, the field at the exit end increases with time so that the defocusing effect due to the diverging field lines is larger than the focusing effect at the entrance end of the cavity gap. E.O. Lawrence placed a screen at the end of the cavity gap to straighten the electric field line. The screen produces a focusing force, but unfortunately it also causes nuclear and Coulomb scattering.

For rf linear accelerators, phase stability requires $\pi/2 > \psi_{\mathrm{s}} > 0$ (below transition energy), and field strength increases with time during the passage of a particle. Thus

the defocusing force experienced by the particle at the exit end of the gap is stronger than the focusing force at the entrance of the gap.

Using Eq. (3.310), the EM field of TM$_{010}$ mode is

$$E_s = \mathcal{E}_0 \sin \psi, \quad E_r = +\frac{\omega r}{2v_{\rm p}}\mathcal{E}_0 \cos \psi, \quad B_\phi = +\frac{\omega r}{2c^2}\mathcal{E}_0 \cos \psi, \tag{3.337}$$

where $\psi = \left(\omega t - \omega \int ds/v_{\rm p}\right)$. The transverse force on particle motion is

$$\frac{d(\gamma m \dot{r})}{dt} = +eE_r - evB_\phi = +\frac{er\omega\epsilon_0}{2v_{\rm p}}(1 - \frac{vv_{\rm p}}{c^2})\cos \psi \xrightarrow{v=v_{\rm p}} \frac{|e|\omega\epsilon_0 \cos \psi}{2\beta\gamma^2 c}\, r. \tag{3.338}$$

For a relativistic particle with $\gamma \gg 1$, the transverse defocusing force is highly reduced because the transverse electric force and the magnetic force cancel each other. Assuming a zero defocusing force, Eq. (3.338) becomes

$$\frac{dp_x}{dt} = 0 \quad \text{or} \quad \frac{d}{ds}\gamma\frac{dx}{ds} = 0 \quad \Longrightarrow \quad \gamma\frac{dx}{ds} = \text{constant} = \gamma_0 x_0'. \tag{3.339}$$

Assuming $\gamma = \gamma_0 + \gamma's$, where $\gamma' = d\gamma/ds$, we obtain

$$x - x_0 = \left(\frac{\gamma_0}{\gamma'}\ln\frac{\gamma}{\gamma_0}\right)x_0'. \tag{3.340}$$

Thus the orbit displacement increases only logarithmically with distance along a linac (Lorentz contraction), if no other external force acts on the particle. In reality quadrupoles are needed to focus the beam to achieve good transmission efficiency and emittance control in a linac.

Transverse particle motion in the presence of quadrupole elements is identical to that of betatron motion. The linear betatron equation of motion is given by

$$\frac{d^2}{ds^2}x(t,s) + K_x(s)x(t,s) = 0, \qquad \frac{d^2}{ds^2}z(t,s) + K_z(s)z(t,s) = 0, \tag{3.341}$$

where $K_x(s)$ and $K_z(s)$ are focusing functions. Since there is no repetitive focusing elements, the betatron motion in linac is an initial value problem. It should be designed from a known initial or desired betatron amplitude function and matched through the linac. A mismatched linac will produce quadrupole mode oscillations along the linac structure.

In smooth approximation, the linear betatron motion can be described by

$$\frac{d^2}{ds^2}y(t,s) + k_y^2(s)y(t,s) = 0, \tag{3.342}$$

where y is used to represent either x or z, and k_y is the wave number. Since there is no apparent periodic structure, the concept of betatron tune is not necessary. However, many linacs employ periodic focusing systems. In this case, one can *define* the betatron tune per period as $\nu_y = k_y L/2\pi$, where L is the length of a period. Betatron resonances may occur when the condition $m\nu_x + n\nu_z = \ell$ is satisfied, where m, n, and ℓ are integers. Furthermore, synchrobetatron resonances may occur when the condition $m\nu_x + n\nu_z + l\nu_{\rm syn} = \ell$ is satisfied, where l is also an integer.

Wakefield and beam break up instabilities

Applying the Panofsky-Wenzel theorem [29], we find the transverse force:

$$\nabla_\perp \int ds \, F_\parallel = \frac{\partial}{\partial s} \int ds \, \vec{F}_\perp \,, \qquad \vec{F}_\perp = \int ds \, \nabla_\perp F_\parallel = \frac{ce}{\omega} \nabla_\perp E_s \,. \tag{3.343}$$

Thus the transverse force on a charged particle is related to the transverse dependence of the longitudinal electric field; it vanishes if the longitudinal electric field is independent of the transverse positions. This is the basic driving mechanism of synchro-betatron coupling resonances.[81] Since TE modes have zero longitudinal electric field, its effect on the transverse motion vanishes as well. Thus we are most concerned with HOMs of the TM waves. These HOMs are also called wakefields. The design of cavities that minimize long range wakefields is an important task in NLC research.[82]

In the presence of a wakefield, the equation of motion is [5]

$$\frac{d^2}{ds^2}x(t,s) + k^2(t,s)x(t,s) = \frac{r_0}{\gamma(t,s)} \int_t^\infty d\tilde{t}\rho(\tilde{t})W_\perp(\tilde{t}-t)x(\tilde{t},s), \tag{3.344}$$

where t describes the longitudinal position of a particle, s is the longitudinal coordinate along the accelerator, $x(t,s)$ is the transverse coordinate of the particle, $k(t,s)$ is the betatron wave number (also called the focusing function), $\rho(t)$ is the density of particle distribution, and $W_\perp(t'-t)$ is the transverse wake function. Detailed properties of the wake function and its relation to the impedance and the transverse force can be found in Ref. [5]. We will examine its implications on particle motion in a simple macro-particle model.

We divide an intense bunch into two macro-particles separated by a distance $\ell = 2\sigma_z$. Each macro-particle represents half of the bunch charge. They travel at the speed of light c. The equation of motion in the smoothed focusing approximation is

$$x_1'' + k_1^2 x_1 = 0, \tag{3.345}$$

$$x_2'' + k_2^2 x_2 = \frac{e^2 N W_\perp(\ell)}{2E} x_1 = G x_1, \tag{3.346}$$

where $eN/2$ is the charge of the leading macro-particle, x_1 and x_2 are transverse displacements, $W_\perp(\ell)$ is the wake function evaluated at the position of the trailing particle, and k_1 and k_2 are betatron wave numbers for these two macro-particles.

If, for some reason, the leading particle begins betatron oscillation; the trailing particle can be resonantly excited, i.e.

$$x_1 \;\; = \;\; \hat{x}_1 \sin k_1 s,$$

---

[81]See e.g., S.Y. Lee, *Phys. Rev.* **E 49**, 5706 (1994).
[82]See R. Ruth, p. 562 in Ref. [19].

$$x_2 = \frac{k_1}{k_2}\hat{x}_1 \sin k_2 s + \frac{G\hat{x}_1}{k_2^2 - k_1^2}\left(\sin k_1 s - \frac{k_1}{k_2}\sin k_2 s\right).$$

$$\rightarrow \hat{x}_1 \sin k_1 s + \hat{x}_1\left(\Delta k - \frac{G}{2k_1}\right)s\cos k_1 s, \tag{3.347}$$

where $\Delta k = k_2 - k_1$. In the limit $\Delta k \to 0$, The amplitude of the trailing particles can grow linearly with s. This is the essence of BBU instability. If the beam bunch is subdivided into many macro-particles, one would observe nonlinear growth for trailing particles.[83]

An interesting and effective method to alleviate the beam break up instabilities is BNS damping.[84] If the betatron wave number for the trailing particle is higher than that for the leading particle by

$$\Delta k = \frac{G}{2k_1} = \frac{e^2 N W_\perp(\ell)}{4Ek_1}, \tag{3.348}$$

the linear growth term in Eq. (3.347) vanishes. This means that the dipole kick due to the wakefield is exactly canceled by the extra focusing force. The bunch will perform rigid coherent betatron oscillations without altering its shape. Note that BNS damping depends on the beam current.

The BNS damping of Eq. (3.348) can be achieved either by applying rf quadrupole field across the bunch length or by lowering the energy of trailing particles. The SLC linac uses the latter method by accelerating the bunch behind the rf crest early in the linac, and then ahead of the rf crest downstream, to restore the energy spread at the end of the linac. Since the average focusing function is related to the energy spread by the chromaticity

$$\frac{\Delta k}{k_1} = C_x \frac{\Delta E}{E}, \tag{3.349}$$

and the chromaticity $C_x \approx -1$ for FODO cells, the energy spread is equivalent to a spread in focusing strength. This method can also be used to provide BNS damping. It is also worth pointing out that the smooth focusing approximation of Eq. (3.345) provides a good approximation for the description of particle motion in a linac.

Exercise 3.8

1. Show that the phase shifts per cell for the CEBAF and SLAC linac cavities listed in Table 3.10 are $kd = \pi$ and $2\pi/3$ respectively.

---

[83]Including beam acceleration, the amplitude will grow logarithmically with energy (distance), as in Eq. (3.340) [5].

[84]V. Balakin, A. Novokhatsky, and V. Smirnov, *Proc. 12th HEACC*, p. 119 (1983).

2. Show that the peak rf magnetic flux density on the inner surface of a pillbox cylindrical cavity in TM_{010} mode is

$$\hat{B}_\phi \approx \frac{\pi\mu_0}{2Z_0}\,\mathcal{E} \quad \text{or} \quad \hat{B}_\phi\ [\text{T}] \approx 50\times 10^{-4}\,\mathcal{E}\ [\text{MV/m}],$$

where $Z_0 = \mu_0 c$ is the impedance of the vacuum.

3. In an Alvarez linac, the longitudinal equations of motion (3.327) and (3.328) can be expressed as mapping equations:

$$\Delta\psi_{n+1} = \Delta\psi_n - \frac{L_{\text{cell}}\omega}{mc^3\beta^3\gamma^3}\,\Delta E_n,$$
$$\Delta E_{n+1} = \Delta E_n + eV\cos\psi_s\,\Delta\psi_{n+1},$$

where $\psi_n, \Delta E_n$ are the synchrotron phase space coordinates at the nth cell, L_{cell} is the length of the drift tube cell, and eV is the energy gain in this cell.

(a) Using the Courant–Snyder formalism, we can derive the amplitude function for synchrotron motion similar to that for betatron motion. Show that the synchrotron phase advance per cell is

$$\Phi_{\text{syn}} = 2\,\arcsin\left(\frac{\pi eV\cos\psi_s}{2\beta^2\gamma^2 E}\right)^{1/2},$$

where $E = \gamma mc^2$ is the beam energy, $\mathcal{E}_{\text{av}} = V/L_{\text{cell}}$ is the average acceleration field, λ is the rf wave length, and ψ_s is the synchronous phase.

(b) Using the table below, calculate the synchrotron phase advance per cell for the first and last cells of cavities 1 and 2, where the synchronous phase is chosen to be $\cos\psi_s = 1/2$. Estimate the total synchrotron phase advance in a cavity.

Fermilab Alvarez linac

Cavity Number	1	2
Proton energy in (MeV)	0.75	10.42
Proton energy out (MeV)	10.42	37.54
Cavity length (m)	7.44	19.02
Cell length (cm) (first/last)	6.04/21.8	22.2/40.8
Average field gradient (MV/m) (first/last)	1.60/2.30	2.0
Average gap field (MV/m) (first/last)	7.62/7.45	10.0/6.45
Transit time factor (first/last)	0.64/0.81	0.86/0.81
Number of cells	55	59

4. In a resonance circuit, Q is expressed as

$$Q = \frac{\frac{1}{2}\omega LI^2}{\frac{1}{2}RI^2} = \frac{\omega L}{R} = 2\pi\frac{\text{stored energy}}{\text{energy dissipation per period}},$$

where $\omega = (LC)^{-1/2}$. The energy stored in the cavity volume is

$$W_{\text{st}} = \frac{\mu}{2}\int_V |H_\phi|^2 dV = \frac{\epsilon}{2}\int_V |\mathcal{E}|^2 dV.$$

The power loss in the wall is obtained from the wall current,

$$P_{\rm d} = \frac{1}{2}\int_S R_{\rm s}|H|^2 dS = \frac{\mu\delta_{\rm skin}\omega}{4}\int_S |H|^2 dS,$$

where $R_{\rm s} = 1/\sigma\delta_{\rm skin}$ is the surface resistance,[85] $\delta_{\rm skin} = \sqrt{2/\mu\sigma\omega}$ is the skin depth, and σ is the conductivity. The total energy loss in one period becomes

$$\Delta W_{\rm d} = \frac{2\pi}{\omega}P_{\rm d} = \frac{\pi\mu\delta_{\rm skin}}{2}\int_S |H|^2 dS.$$

(a) Using the identity $\int_0^b J_1^2(k_r r)2\pi r\,dr = \pi b^2 J_1^2(k_r b)$, show that the quality factor for a pillbox cavity at TM$_{010}$ mode is

$$Q = \frac{2\int_V |H|^2 dV}{\delta_{\rm skin}\int_S |H|^2 dS} = \frac{d}{\delta_{\rm skin}}\frac{b}{d+b} = \frac{2.405 Z_0}{2R_{\rm s}(1+b/d)},$$

where b and d are the radius and length of a cavity cell, $R_{\rm s}$ is the surface resistivity, and $Z_0 = 1/\mu_0 c \approx 377\Omega$. The Q-factor depends essentially on geometry of the cavity. Since $\delta_{\rm skin} \sim \omega^{-1/2}$, we find Q $\sim \omega^{+1/2}$. Find the Q-value for the SLAC copper cavity at $f = 2.856$ GHz.

(b) Show that the shunt impedance is

$$R_{\rm sh} = \frac{Z_0^2 d^2}{R_{\rm s}\pi b(b+d)J_1^2(k_r b)}\quad\text{or}\quad \frac{r_{\rm sh}}{Q} = \frac{2\omega\mu}{\pi(k_r b)^2 J_1^2(k_r b)} = 0.41\omega\mu,$$

where $k_r b = 2.405$. Note here that the shunt impedance behaves like $r_{\rm sh} \sim \omega^{1/2}$. At higher frequencies, the shunt impedance is more favorable; however, the diameter of the cavity will also be smaller, which may limit the beam aperture.

5. The average power flowing through a transverse cross-section of a wave guide is

$$P = \frac{1}{2}\int E_\perp \times H_\perp dS$$

where only transverse components of the field contribute. For TM mode, The energy stored in the electric and magnetic fields are

$$\frac{\mathcal{E}_\perp}{H_\perp} = Z_0\frac{\lambda}{\lambda_{\rm g}},\quad P = \frac{1}{2Z_0}\int \frac{k}{\beta}|\mathcal{E}_\perp|^2 dS$$

$$W_{\rm st,m} = \frac{\mu}{4}\int |H_\perp|^2 dS = \frac{\mu}{4}\frac{k^2}{Z_0^2\beta^2}\int |\mathcal{E}_\perp|^2 dS$$

$$W_{\rm st} = W_{\rm st,e} + W_{\rm st,e} = 2W_{\rm st,m}.$$

---

[85] In the limit that the mean free path ℓ of conduction electrons is much larger than the skin depth $\delta_{\rm skin}$, the surface resistance becomes $R_{\rm s} = (8/9)(\sqrt{3}\mu_0^2\omega^2\ell/16\pi\sigma)^{1/3}$. Since the conductivity is proportional to the mean free path ℓ, the resulting surface resistance is independent of the mean free path, and is proportional to $\omega^{2/3}$. There is little advantage to operating copper cavities at very low temperature. See G.E.H. Reuter and E.H. Sonderheimer, *Proc. Roy. Soc.* **A195**, 336 (1984).

(a) Show that the energy flow, defined by $v_e = P/W_{st}$, is $v_e = \beta c/k$.

(b) Verify that $v_g = d\omega/d\beta = v_e$.

6. The disk-loaded linac acceleration structure can be modeled by LC resonant circuits coupled with capacitors $2C_p$ shown in the figure below. The model describes only the qualitative narrowband properties of a loaded wave guide. Thus the equivalent circuit does not imply that a coupled resonator accurately represents a disk loaded structure. In the limit of large C_p, these resonators are uncoupled, which corresponds to a pillbox without holes, or equivalently, a small beam hole in a pillbox cavity corresponds to $C_p \gg C_s$.
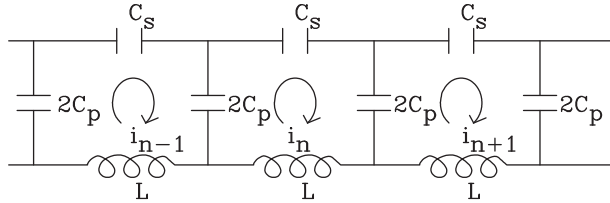
(a) Applying Kirchoff's law, show that

$$i_{n+1} - 2\cos(kd)\, i_n + i_{n-1} = 0, \quad \cos(kd) = 1 + \frac{C_p}{C_s} - \omega^2 C_p L.$$

(b) Show that the solution of the above equation is

$$i_n = e^{\pm j[nkd + \chi_0]}, \quad n = 0, 1, 2, \cdots.$$

We identify kd as the phase advance per cell, and k as the wave number. Show that the frequency is
$$\omega^2 = \omega_0^2 \left[1 + \kappa(1 - \cos kd)\right],$$
where $\omega_0 = 1/\sqrt{LC_s}$ is the natural frequency without coupling at $kd = 0$, and $\kappa = C_s/C_p$ is the coupling constant between neighboring cavities.

(c) Show that the condition for an unattenuated traveling wave is $\omega_0 \leq \omega \leq \omega_\pi$, where
$$\omega_\pi = \omega_0 \left(1 + 2\frac{C_s}{C_p}\right)^{1/2} \approx \omega_0 \left(1 + \frac{C_s}{C_p}\right)$$
is the resonance frequency at phase advance $kd = \pi$. Draw the dispersion curve of ω vs k. In a realistic cavity, there are higher frequency modes, which give rise to another passband (see Fig. 3.45).

(d) Find k such that the phase velocity $v_p = c$.

(e) Cavities can also be magnetically coupled. The magnetically coupled-cavity chain can be modeled by replacing $2C_p$ in the LC circuit with $L_p/2$. Show that the dispersion curve of a magnetically coupled cavity is
$$\omega_0^2 = \omega^2 \left[1 + \kappa(1 - \cos kd)\right],$$
where $\omega_0 = 1/\sqrt{LC_s}$ is the natural frequency without coupling at $kd = 0$, and $\kappa = L_p/L$ is the coupling constant between neighboring cavities. Discuss the differences between the electric and magnetic coupled cavities.

7. Using Eq. (3.318), the electric field of a standing wave rf cavity structure that consists of N cells is

$$\mathcal{E}_s = \mathcal{E}_0 \, \cos ks \, \cos \omega t,$$

where $s \in [0, Nd]$ is the longitudinal coordinate, k is the wave number, d is the cell length of one period, and ω is the frequency. The resonance condition is

$$kd = m\pi/N, \quad m = 0, 1, \cdots, N,$$

where kd is the rf phase advance per cell.

(a) For a particle traveling at velocity v, show that the total voltage gain in passing through the cavity is

$$\Delta V = \frac{1}{2}N \, d \, \mathcal{E}_0 \left[\frac{\sin\left(k - (\omega/v)\right)Nd}{(k - (\omega/v))Nd} + \frac{\sin\left(k + (\omega/v)\right)Nd}{(k + (\omega/v))Nd} \right].$$

Show that the energy gain is maximum when the phase velocity k/ω is equal to the particle velocity v. Show that the maximum voltage gain of the standing wave is $(\Delta V)_{\max} = Nd\,\mathcal{E}_0/2$, i.e. the energy gain of a standing wave structure is only $1/2$ that of an equivalent traveling wave structure.

(b) For a sinusoidal electric field, the power consumed in one cell is

$$|\mathcal{E}_0 d|^2 / 2R_{\text{sh,cell}},$$

where $R_{\text{sh,cell}}$ is the shunt impedance per cell for the traveling wave. For an rf structure composed of N cells, the power is

$$P_{\text{d}} = N|\mathcal{E}_0 d|^2 / 2R_{\text{sh,cell}}.$$

Using the definition of shunt impedance, show that the shunt impedance of a standing wave rf structure is

$$R_{\text{sh}} = \frac{1}{2}N R_{\text{sh,cell}}.$$

Thus the shunt impedance for a standing wave structure is equal to $1/2$ that of an equivalent traveling wave structure.[86]

8. There are two types of traveling wave structures. A constant impedance structure has a uniform multi-cell structure so that the impedance is constant and the power decays exponentially along the structure. A constant gradient structure is tapered so that the longitudinal electric field is kept constant. The electric field is related to the shunt impedance per unit length by [see Eq. (3.305)]

$$\mathcal{E}^2 = -r_{\text{sh}}\frac{dP_{\text{d}}}{ds} = 2\alpha \, r_{\text{sh}} \, P_{\text{d}}(s) \qquad \text{where} \qquad \alpha = -\frac{1}{2P_{\text{d}}}\frac{dP_{\text{d}}}{ds}.$$

The total energy gain for an electron in a linac of length L is

$$\Delta E = e \int_0^L \mathcal{E}\,ds.$$

---

[86]The above calculation for voltage gain in the cavity structure is not applicable for an standing wave structure with $kd = 0$ and π, where two space harmonics contribute to the electric field so that $\mathcal{E}_s = 2\mathcal{E}_0 \, \cos ks \, \cos \omega t$. This means that the voltage gain in the rf structure is $\Delta V = Nd\mathcal{E}_0$, and the shunt impedance is $R_{\text{sh}} = N R_{\text{sh,cell}}$.

(a) In a constant impedance structure, show that the energy gain is

$$\Delta E(L) = eL(2r_{\mathrm{sh}}P_0\alpha)^{1/2}\frac{1 - e^{-\alpha L}}{\alpha L},$$

where P_0 is the power at the input point.

(b) Assuming that r_{sh} and Q are nearly constant in a constant gradient structure, show that

$$P_{\mathrm{d}} = P_0 \left(1 - \frac{s}{L}(1 - e^{-2\tau})\right),$$

where $\tau = \int_0^L \alpha(s)ds$. The group velocity is equal to the velocity of energy flow. Show that the group velocity of a constant gradient structure [see Eq. (3.307)] and the energy gain are

$$v_{\mathrm{g}} = \omega L \left(1 - \frac{s}{L}(1 - e^{-2\tau})\right) \left(\mathrm{Q}(1 - e^{-2\tau})\right)^{-1},$$
$$\Delta E = e\mathcal{E}L = e\sqrt{P_0 r_{\mathrm{sh}}L\left(1 - e^{-2\tau}\right)}.$$

9. The design of the 2 MW spallation neutron source uses a chain of linacs composed of ion source, RFQ, DTL, CCL, and SCL to accelerate 2.08×10^{14} particles per pulse at 60 Hz repetition rate. An accumulator compresses the 1 ms linac pulse into a 695 ns high intensity beam pulse with 250 ns beam gap. The following table lists linac and beam parameters. Calculate the longitudinal bucket and bunch areas in (eVs). Compare the rms bunch length in (ns) and in (m) with the rms transverse beam size at exit points of linacs. Each microbunch has about $N_B = 8.70 \times 10^8$ protons, what is the longitudinal brightness of the beam in number of particles per (eVs)?

	RFQ	DTL	CCL	SRFL
L (m) length of the structure	3.723	38.7	55.12	206.812
f_{rf} (MHz)	402.5	402.5	805	805
ψ_{s} (differ from linac convention by $-\pi/2$)	60°	45-65°	60-62°	20°
$\mathcal{E}_0 T$ (MV/m)		3.0	3.37	10.6
$\mathrm{KE}_{\mathrm{inj}}$ (MeV)	0.065	2.5	86.8	185
$\mathrm{KE}_{\mathrm{ext}}$ (MeV)	2.5	86.8	185	1001.5
$\epsilon_{\parallel}$ (π-MeV-deg) emittance at exit point	0.108	-	-	0.60
$\epsilon_{\perp}$ (π-mm-mrad) emittance at exit point	0.21	-	-	0.45
$\sigma_{\Delta W}$ (MeV)	0.0092			0.33
$\mathcal{A}_{\mathrm{bucket}}$ (eVs) at injection energy				
$\mathcal{A}_{\mathrm{rms}}$ (eVs)				
σ_τ (ns)				
k_{syn} (m^{-1})				
$\beta_{x/z}$ at exit (m)	0.2/0.2	-	-	10.1/5.3

10. A prebuncher is usually used to prebunch the electrons from a source, which can be thermionic or rf gun. We assume a thermionic gun with a DC gun voltage V_0, which is usually about 80–150 kV. Let the electric field and the gap width of the prebuncher be $\mathcal{E}\sin(\omega t)$ and g. Electrons that arrive earlier are slowed and that arrive late are

sped up. At a drift distance away from the prebuncher, the faster electrons catch up the slower electrons. Thus electrons are prebunched into a smaller phase extension to be captured by the buncher and the main linac. Assuming a small prebuncher gap with $V_1 = \mathcal{E}g \ll V_0$, find the drift distance as a function of the V_0 and V_1. Discuss the efficiency of prebunching as a function of relevant parameters.